ENERGY REDISTRIBUTION THROUGH TIDAL AND INERTIAL WAVE INTERACTION

A DISSERTATION SUBMITTED TO THE GRADUATE DIVISION OF THE UNIVERSITY OF HAWAI‘I IN PARTIAL FULFILLMENT OF THE REQUIREMENTS FOR THE DEGREE OF

DOCTOR OF PHILOSOPHY

IN

OCEANOGRAPHY

MAY 2009

By
Martin D. Guiles

Dissertation Committee:

Douglas Luther, Chairperson
Eric Firing
Mark Merrifield
Axel Timmermann
John Learned

We certify that we have read this dissertation and that, in our opinion, it is satisfactory in scope and quality as a dissertation for the degree of Doctor of Philosophy in Oceanography.

DISSERTATION COMMITTEE

_____
Chairperson

_____

_____

_____

_____

©Copyright 2009

by

Martin D. Guiles

Acknowledgments

I would like to thank the National Science Foundation for its full support of this work.

Abstract

Evidence for an interaction between inertial internal waves and semi-diurnal internal tides is described from oceanic velocity records. The resulting motions at the difference frequency between M_2 and f, termed Internal Wave Induced Sub/Super-inertial Currents, or IWISC, are complicated structures whose existence suggests a new energy path from tidal and inertial internal waves directly to dissipative structures, independent of the assumed cascade of energy through the internal wave field from large to small scales.

We have observed an accumulation of energy in cyclonic rotary power spectral densities at the frequency of $M_2 - f$ (the IWISC frequency) over a broad range of depths and in numerous geographic locations throughout the worlds oceans. Poleward of the critical latitude (where $f = M_2/2$), IWISC is outside of the freely propagating internal wave band. Bulk observations of IWISC cyclonic energy poleward of the critical latitude show a positive correlation (though not strong, R < .5) with the corresponding anti-cyclonic $M_2 + f$ energy peak. The relationships between IWISC energy and the semi-diurnal and inertial interactant energies do not appear to be simple, since the correlations between IWISC and M_2 and f are small, although significant for the IWISC vs. inertial correlation.

IWISC energy in mid-latitude records exhibits a depth dependence, with normalized maximum energy above a mesoscale background occurring near 1500 meters depth. IWISC energy has been observed to vary considerably on quite small vertical scales, on the order of 30 meters. Even equatorward of the critical latitude, IWISC energy appears predominantly in the cyclonic component, commonly distorting the expected relationship between cyclonic and anti-cyclonic currents for free internal waves.

A significant focus in our study of IWISC is the differentiation between reversible vertical advection and irreversible non-linear interaction. A hierarchy of vertical advection models has been created to establish if, when, and how vertical advection is a satisfactory explanation of IWISC. A simple model of single sinusoid semi-diurnal internal tide displacement of an inertial internal wave, as is commonly employed in the literature, replicates properties of the Eulerian oceanic observations such as a power spectral density (PSD) peak at the IWISC frequency. However, this model always yields an additional PSD peak at the sum ($M_2 + f$) frequency. Such a tight correlation between PSD at IWISC and $M_2 + f$

frequencies is not commonly observed, as noted above. When we extended the displacement model to include multiple semi-diurnal vertical modes and frequency constituents, the result was a temporal and spatial variability of IWISC and $M_2 + f$ energies, which consequently decorrelated those energies. This result is consistent with observed variability.

Bispectra and bicoherence analysis were tested on the complex displacement model velocities to determine if these methodologies can distinguish between reversible vertical advection and energy exchanging non-linearity. In fact, they cannot. Due to the frequently short duration of the inertial wave energy and even the internal tide energy a wavelet rotary bispectral analysis technique was created in an attempt to improve the identification of interactions. While the methodology appears to have great promise, its utility for this problem has yet to be demonstrated.

An analysis of vertical profiles of horizontal currents from ADCP instruments deployed in the Hawaii Ocean Mixing Experiment revealed IWISC PSD peaks for both horizontal currents and their vertical shear. Semi-diurnal internal tide displacement was derived from the well-instrumented HOME mooring A2 ADCP vertical velocity record, after application of our new method for correcting for biases due to diel migrators. The semi-diurnal displacement was used to project the ADCP horizontal velocities into a semi-Lagrangian coordinate system. This Semi-Lagrange inversion revealed that there are depth ranges where interaction peak energy (at IWISC and $M_2 + f$) is diminished by the inversion, thus implying that those signals were dominated by reversible advection, and depth ranges where the energy peaks remained unaffected or were amplified. This leads to the conclusion that both periodic, reversible advection and other energy redistribution processes are present at this location. Bispectral and bicoherence analysis of the Semi-Lagrange inverted ADCP velocities suggests the presence of irreversible non-linear interaction at IWISC.

Table of Contents

Acknowledgments . . . iv
Abstract . . . v
List of Tables . . . ix
List of Figures . . . x
1 Introduction . . . 1
1.1 The Problem . . . 1
1.2 What is Known? . . . 3
1.3 Summary of Work and Significant Results . . . 5
2 Historical Data Reanalysis . . . 8
2.1 Introduction . . . 8
2.1.1 Motivation . . . 9
2.1.2 Relevance . . . 16
2.1.3 Historical Data Analysis . . . 16
2.2 Data Sets . . . 18
2.2.1 Scope of Data Coverage . . . 18
2.2.2 Overview of Data . . . 19
2.2.3 Quantify Existence . . . 21
2.3 Analysis of IWISC Evidence . . . 21
2.3.1 Difference Frequency Peak ($M_2 - f$) . . . 22
2.3.2 Geographical Extent . . . 23
2.3.3 Energy Correlation and Comparison . . . 26
2.3.4 Variability of Interactant Energy . . . 31
2.3.5 Intermittency of IWISC Energy . . . 36
2.3.6 Horizontal Structures . . . 42
2.3.7 Vertical Structure . . . 53
2.4 Discussion of Variability . . . 61
2.5 Summary of Historical Data Analysis . . . 62
3 Advection Analysis and Simulation . . . 64
3.1 Single Sinusoid Vertical Advection Model . . . 64
3.1.1 Introduction . . . 64
3.1.2 Deterministic Single Sinusoid Model Description . . . 66
3.2 Extension of the Deterministic Displacement Advection Model . . . 71
3.3 Description of Multiple Deterministic Advection Model . . . 79
3.4 Evaluation of Bispectra and Bicoherence for Delineating Non-linear Interactions . . . 91
3.4.1 HOME C2 Mooring . . . 93

3.4.2 Plane Wave Summation Model . . . 99
3.4.3 Case II . . . 103
3.4.4 Case III . . . 108
3.4.5 Summary of Bispectra and Bicoherence Evaluation . . . 108
3.5 Rotary Wavelet Decomposition . . . 109
3.6 Summary of Advection Analysis and Simulation . . . 117
4 Analysis of HOME A2 Moored ADCP Velocities . . . 120
4.1 HOME Experiment and Data . . . 120
4.1.1 Impact of Observations . . . 122
4.2 Observational Context . . . 125
4.2.1 Background and Diurnal Flow Structures . . . 126
4.2.2 Vertical Time Series of Band-passed Velocity . . . 129
4.2.3 Power Spectra and Shear Spectra . . . 144
4.2.4 Summary of General Observations at HOME Mooring A2 . . . 146
4.3 Vertical Velocity at A2 . . . 153
4.3.1 Diel Migrator Contamination . . . 153
4.3.2 Coherence of Vertical Velocity Through Depth Range . . . 161
4.4 Displacement and Semi-Lagrange Inversion . . . 166
4.4.1 Displacement Series . . . 166
4.4.2 Inverted Horizontal Velocities . . . 167
4.4.3 Summary of A2 Semi-Lagrange Inversion . . . 170
4.5 Vertical Profile of Interactant Peaks . . . 171
4.6 Rotary Bispectra and Bicoherence . . . 176
4.6.1 Analysis at 424 Meters . . . 179
4.6.2 Analysis at 784 Meters . . . 185
4.6.3 Wavelet Rotary Bispectra and Bicoherence . . . 194
4.7 Summary of HOME Results . . . 197
5 Conclusion . . . 200
5.1 Discussion . . . 200
5.1.1 Observational Results . . . 204
5.1.2 Analysis Tools . . . 205
5.2 Hypothetical Non-linear Process Producing IWISC . . . 206
5.3 Hypothetical Energy Transfer . . . 207
Bibliography . . . 210

List of Tables

Table Page

2.1 Sample of Major Data Sets Analyzed 19

4.1 Spring Neap Peak Times 132

List of Figures

Figure Page

2.1 Rotary PSD of current meter velocity recorded at 1075m depth on the TW mooring during BEMPEX/RTE87. This record stimulated investigation of the sub-inertial peak at the IWISC ($M_2 - f$) frequency. The record length is 200 days long. 95% confidence intervals for each independent PSD estimate are indicated by the dashed green lines at the bottom; the diamond symbols indicate the frequency intervals between independent PSD estimates. 10

2.2 Comparison of rotary PSD from a number of representative locations exhibiting a sub-inertial IWISC peak (latitudes > crit). Black arrows indicate the exact $M_2 - f$ frequency. There is clear enhancement of counter-clockwise energy (clockwise for the Southern Hemisphere SWINDEX site) in the neighborhood of the difference ($M_2 - f$) frequency. Note that inertial wave energy is usually maximum at a slightly super-inertial frequency; this would account for the IWISC peaks occurring at slightly lower frequencies than the exact $M_2 - f$ frequency. Enhanced energy at the IWISC frequency is not unique to these records, nor extreme (see Figure 2.27 below). TW and CM are moorings from the RTE87 and BEMPEX experiments, respectively. 95% confidence intervals for each independent PSD estimate are indicated by the dashed green lines at the bottom; the diamond and cross symbols indicate the frequency intervals between independent PSD estimates. 11

2.3 Map of North Pacific mooring locations for all but one of the rotary PSD shown in figure 2.2. 12

2.4 Temperature PSD ($(degC^2)(rad/s)$) for the instrument at 1075m on the TW RTE87 mooring, first deployment. The record length is 200 days long. 95% confidence intervals for each independent PSD estimate are indicated by the dashed green lines at the bottom; the diamond symbols indicate the frequency intervals between independent PSD estimates. 23

2.5 Rotary PSD ($(m^2/s^2)(rad/s)$) of current meter velocity recorded at 200m depth for the SW mooring of ACM25. This mooring was located at 18° N, 33° W. The record length is 134 days long. 95% confidence intervals for each independent PSD estimate are indicated by the dashed green lines at the bottom; the diamond symbols indicate the frequency intervals between independent PSD estimates. 25

2.6 Scatter plot of energy in the anti-cyclonic rotary PSD ($(m^2/s^2)(rad s)$) for the frequency sum band (M2 + f) vs. the energy in the cyclonic IWISC band (M2 - f) for multiple 22 day segments within the records shown in Figure 2.2. Red symbols are for the 50% of records with highest semi-diurnal tidal energy. P values less than 0.05 indicate significance. 27
2.7 Time series of rotary PSD for the TW mooring of BEMPEX/RTE87. The depth of the instrument is 1075m. The temperature spectra are indicated for the M_2 band. The frame labeled $M_2 - f$ shows the cyclonic (CCW) rotary PSD. The frames labeled $M_2 + f$, f and M_2 show the anti-cyclonic (CW) rotary PSD. The color scales are different for each frame, and so indicate only relative strengths of the energies within each separate frequency band. See the text for a discussion of the events and for further details of how the time series of PSD were calculated. Number of independent points per band (from the top): 4, 3, 3, 3, and 5. 29
2.8 Rotary PSD ($(m^2/s^2)(rad s)$) of horizontal currents from the RTE87 mooring TW, first deployment, showing two 22 day records centered at 85 days and 135 days. These time segments are indicated in Figure 2.7 as Event One and Event Two. The 95% confidence intervals for each independent PSD estimate is indicated by the dashed green lines at the bottom; the diamond symbols indicate the frequency intervals between independent PSD estimates. See the text for an explanation. 30
2.9 Ratio of cyclonic/anti-cyclonic rotary PSD for the RTE87 mooring TW for two 22 day records centered at 85 days and 135 days. Event One is on the top (see Figure 2.7) and Event two on the bottom. Though not exceeding the confidence interval in its deviation from the theoretical curve ($(\omega - f)/(\omega + f)$), the sum ($M_2 + f$) frequency band in the bottom panel is noticeable. Dashed green lines indicate 95% confidence interval. . . . 32
2.10 Scatter plot of rotary power spectral peak amplitudes at the cyclonic IWISC and anti-cyclonic inertial frequencies. Red symbols are for the 50% of records with highest semi-diurnal mean log amplitude PSD. Both red and green sets have P values less than 0.05 indicating a significant correlation, though very weak. 33
2.11 Scatter plot of IWISC anti-cyclonic rotary PSD versus total semi-diurnal horizontal current PSD (here designated as just M2). Red symbols are for the 50% of records with highest semi-diurnal mean log amplitude PSD. Both red and green sets have P values greater than 0.05 indicating non-significant correlation. 34
2.12 Scatter plot of sum (cyclonic M2 + f) PSD and semi-diurnal (total horizontal current) PSD. Red symbols are for the 50% of records with highest semi-diurnal mean log amplitude PSD. Both red and green sets have P values greater than 0.05 indicating non-significant correlation. 36
2.13 Scatter plot of PSD log amplitudes corresponding to the IWISC (cyclonic $M_2 - f$), M_2 (sum of cyclonic and anti cyclonic energy), and inertial frequency bands. Red indicates those amplitudes representing the upper half of data with greater than mean log amplitude PSD at the M_2 frequency band, and green the lower. Regression lines corresponding to the IWISC vs. M_2 and IWISC vs. inertial are indicated for the respective data. Confidence intervals are indicated by vertical lines with circle markers at the end of each regression line. 37

2.14 IWISC frequency band vertical time series for STORMS mooring located at 47.42° N and 139.29° W. Band energy is from the anti-cyclonic component of rotary velocity PSD $((cm^2/s^2)/(rad/s))$; although IWISC exists outside the free internal wave band, since the assumed energy source for IWISC is believed to be free internal waves the IWISC PSD was normalized according to the expected WKB linear dependence of free internal wave horizontal current PSD on the buoyancy frequency, using WOA mean stratification. Frequency axis is in $rads$ normalized by the local inertial with dotted white line indicating calculated IWISC frequency. Vertical white lines show thirty day separation. Days axis begins with deployment on August 21, 1987. See Figure 2.7 and its accompanying description for further details of how the PSD time series were constructed. 38
2.15 Time series of inertial band cyclonic rotary PSD $((cm^2/s^2)/(rad/s))$ for instruments from the STORMS experiment mooring. Local inertial frequency is indicated by the dotted white line at each depth. See Figure 2.14 caption for specific details. 39
2.16 Semi-diurnal frequency band PSD $((cm^2/s^s)/(rad/s))$ time series of total horizontal energy for the STORMS mooring. White dotted lines indicate principal semi-diurnal constituents M2 (lower line) and S2. See Figure 2.14 caption for specific details. . . . 40
2.17 Semi-diurnal temperature frequency band PSD $((degC^2)(rads))$ vertical time series for STORMS mooring. White dotted lines indicate principal semi-diurnal constituents M2 (lower line) and S2. See Figure 2.14 caption for specific details. 41
2.18 Rotary PSD $((m^2/s^2)/(rad/s))$ for the deep water central mooring of EBC with a depth of 598m and a latitude of 37.11°. Although the IWISC frequency is near the frequencies of the diurnal and inertial bands, there is distinct separation of the energy in those bands from the IWISC energy, which is elevated. There is energy at the sum $(M_2 + f)$ frequency as well. The record length is 740 days long. 95% confidence intervals for each independent PSD estimate are indicated by the dashed green lines at the bottom; the diamond symbols indicate the frequency intervals between independent PSD estimates. 44
2.19 Semi-diurnal total current PSD (sum of cyclonic and anti-cyclonic) time series for the deep water central mooring of EBC. Dotted white lines indicate M_2 and S_2 frequencies. There are four independent points in each band. Days axis begins with deployment on August 9, 1992. White vertical lines are separated by 60 days. See Figure 2.7 and its accompanying description for further details of how the PSD time series were constructed. 45
2.20 Inertial frequency anti-cyclonic rotary PSD time series for the four depths of the deep water central mooring of EBC. See Figure 2.19 caption for specific details. 46
2.21 The cyclonic current PSD around the IWISC frequency is shown. This record is from the deep water central mooring of EBC. See Figure 2.19 caption for specific details. . . 47
2.22 PSD time series at 600m for the North, South, and Central moorings for EBC. The top three are the cyclonic difference frequency $(M_2 - f)$, next is the anti-cyclonic inertial period, and the last three are the total energy semi-diurnal internal tide. Arrows indicate a specific frequency (top to bottom: $M_2 - f$, f, M_2) along the vertical axis of each bar; frequency scale on left is normalized by f. Mooring location is noted with (N)orth, (C)entral, and (S)outh. See Figure 2.7 and its accompanying description for further details of how the PSD time series were constructed. 48

2.23 Frequency band PSD vs. time for the (N)orth, (C)enter, and (S)outh moorings of the EBC offshore group. Time segment is the later period identified in figure 2.22. See Figure 2.7 and its accompanying description for further details of how the PSD time series were constructed. 50
2.24 Coherence between moorings in four frequency bands for the first time period indicated in figure 21 from day 220 to day 280. The top panel is between the North mooring and the South. Next is North vs. Center, then Center vs. South. The horizontal light blue line indicates the 95% level of no significance. 51
2.25 Coherence between moorings in four frequency bands for the second time period indicated in figure 2.22 from day 440 to day 500. The top panel is between the North mooring and the South. Next is North vs. Center, then Center vs. South. The horizontal light blue line indicates the 95% level of no significance. 52
2.26 Narrow band rotary PSD of current meter velocity recorded at 1075m depth on the TW mooring during BEMPEX/RTE87. Selection bands for the peak IWISC and broad cyclonic mesoscale are indicated by red and blue dotted lines, respectively. Respective values correspond to those used in the difference calculation, ΔPSD. The record length is 200 days long. 95% confidence intervals for each independent PSD estimate are indicated by the dashed green lines at the bottom; the diamond symbols indicate the frequency intervals between independent PSD estimates. 55
2.27 Depth distribution of IWISC cyclonic rotary PSD peak height above a near IWISC frequency band mesoscale anti-cyclonic rotary PSD average. Thin red lines indicate 95% confidence intervals. Green depth profile is a third order polynomic fit to all data points. Dark blue circles indicate instrument records with little or no IWISC peak, where the actual values are much less than the plot range. Blue squares correspond to those records used in figure 2.2. 56
2.28 Time series of clockwise rotary PSD for the IWISC frequency band of the moored ADCP instrument as part of the Deep Basin (ACM13 WOCE component) experiment. Dotted white line indicates IWISC frequency. During the time period of 160 to 210 days enhanced IWISC energy is seen at lower depths. Other peak energy (days 220 to 300) is likely associated with inertial events, and is not peaked at the IWISC frequency. See Figure 2.7 and its accompanying description for further details of how the PSD time series were constructed. 58
2.29 Time series counterclockwise rotary PSD for the inertial frequency band of the moored ADCP instrument as part of the ACM13 WOCE component. See Figure 2.7 and its accompanying description for further details of how the PSD time series were constructed. 59
2.30 Time series of total (cyclonic and anti-cyclonic) PSD for the M_2 frequency band of the moored ADCP instrument as part of the ACM13 WOCE component. Dotted lines indicate M_2 (lower) and S_2 within each depth band. See Figure 2.7 and its accompanying description for further details of how the PSD time series were constructed. 60

3.1 Vertical profile of PSD ($(m^2/s^2)/(rad/s)$) for simple inertial frequency vertical plane wave ($L_z = 140m$) under periodic vertical coordinate displacement. The top panel has M_2 coordinate displacement structure with $L_z = 1000m$ and 75 meter amplitude. Bottom panel displacements are M_2 and S_2 vertical plane wave structures. Bottom panel M_2 has L_z = 1000m and 70m amplitude; S_2 has L_z = 600m and 50m amplitude. The inclusion of multiple frequencies in the displacement results in a vertical modulation envelope for the interaction frequencies and a relative broadening of the interaction bands. This figure only depicts the coordinate shifted inertial signal. 77
3.2 Single depth (600m) PSD for the spectral depth profiles in figure 3.1 with the original signal in red. Indicated in the upper left is the sum PSD across all frequencies. The top panel, with only M_2 displacement, has narrow peaks at interaction and harmonic frequencies. The bottom panel, with both M_2 and S_2 displacement, has broader, less defined peaks especially at the difference frequency $M_2 - f$. 95% confidence intervals for each independent PSD estimate are indicated by the dashed green lines at the bottom; the diamond symbols indicate the frequency intervals between independent PSD estimates. 78
3.3 Wavenumber and frequency values for the inertial wave packet reconstruction utilized in the model are depicted in the top two panels. Amplitude and phase for each are indicated in the lower panels. 80
3.4 Internal wave vertical group velocity (cm/s) with inertial wavenumbers used in the synthetic model indicated with black stars located near $k_h = 1 * 10{-}4$ and $k_z = 3 * 10{-}2$. Lines of constant frequency are indicated in green. Constant total wavenumber is indicated in red. The buoyancy period for this simulation is 20 minutes. 81
3.5 In the top panel amplitudes of horizontal velocity are Fourier reconstructed for the inertial and semi-diurnal bands at a selection depth of 500m for the plane wave summation model. A snapshot of the indicated time period for each band is shown in the bottom panel. See text for further description. 82
3.6 Spectra for two latitude ranges of the Synthetic Model. On the top is the model corresponding to the HOME mooring A2 at 21 degrees north. On the bottom is a model for 40 degrees north. Notice that for latitudes equator-ward of +/- 28.9 degrees latitude, the IWISC (difference frequency $M_2 - f$) interaction band occurs in the internal wave range. The record lengths are 90 days long. Independent PSD estimate 95% confidence intervals are indicated by the dashed green lines at the bottom; the diamond symbols indicate the frequency intervals between independent PSD estimates. 84
3.7 Consistency relation for the simulated velocity record created for 21° N latitude. Both sum ($M_2 + f$) and difference ($M_2 - f$) advection signature frequencies occur in the free internal wave regime. These two frequencies bands show deviation from theoretically predicted consistency ($(\omega - f)/(\omega + f)$). Independent PSD estimate 95% confidence intervals are indicated by the dashed green lines; the diamond symbols indicate the frequency intervals between independent PSD estimates. 85

3.8 Rotary PSD ($(m^2/s^2)/(rad/s)$) for the plane wave summation model at 21° N latitude. On the top is the PSD from the plane wave summation model with semi-diurnal displacement of the inertial motion. The bottom panel is the result of Semi-Lagrange (S-L) inversion of the modeled data. The S-L inversion is described in the text. Independent PSD estimate 95% confidence intervals are indicated by the dashed green lines at the bottom; the diamond symbols indicate the frequency intervals between independent PSD estimates. 89
3.9 Rotary shear spectra ($(1/s^2)/(rad/s)$) for the plane wave summation model at 40 degrees corresponding to the data used in figure 3.8 displaying PSD. In the bottom panel, after the S-L inversion, the shear associated with the IWISC interaction band has been diminished. Dashed green lines indicate 95% confidence interval. 90
3.10 Selected time segment with IWISC energy of ADCP horizontal velocities from the HOME C2 mooring at 520 meters. Velocity data is in the upper series, with reconstructed, band passed, inertial and semi-diurnal signals below. Days begin January 1, 2002 with day 480 being April 24, 2003. 94
3.11 Rotary PSD ($(m^2/s^2)/(rad/s)$) for the horizontal velocity time series depicted in figure 3.10 of the HOME C2 mooring at a depth of 520 meters. Of note is the significant enhancement of cyclonic energy at the IWISC ($M_2 - f$) frequency. Independent points identified with diamond symbols. Dashed green lines indicate 95% confidence intervals. 95
3.12 Rotary bispectrum of the HOME C2 ADCP horizontal velocities at a depth of 520 meters for the time period indicated in figure 3.10. SD indicates average semi-diurnal frequency. There are three frequency axis which range from cyclonic (red) through zero frequency to anti-cyclonic (blue). Elevated bispectrum indications are then associated with the three frequencies indicated on the respective axis. Labeled interaction points are described in the text. 97
3.13 Rotary bicoherence of the horizontal ADCP velocities at HOME mooring C2 with a depth of 520 meters for the time period indicated in figure 3.10. There are coherent indications at the interaction points of interest. These points are discussed in the text. There are three frequency axis which range from cyclonic (red) through zero frequency to anti-cyclonic (blue). Elevated bicoherence indications are then associated with the three frequencies indicated on the respective axis. 98
3.14 Plane wave summation model with vertical displacement of inertial currents at 21° latitude. Modeled data is in the upper series, with reconstructed, band passed, inertial and semi-diurnal signals below. 100
3.15 Rotary PSD ($(m^2/s^2)/(rad/s)$) for the 21° plane wave model time series indicated in figure 3.14. There are significant peaks at the interaction frequencies between the inertial horizontal currents and the semi-diurnal internal tide. This is a result of the vertical displacement of the inertial by the semi-diurnal. Independent points identified with diamond symbols. Dashed green lines indicate 95% confidence intervals. 101
3.16 Bispectrum of the selected time series indicated in figure 3.14. There are peaks at the interaction triple points associated with the inertial and semi-diurnal internal waves in the modeled record. There are three frequency axes which range from cyclonic (red) through zero frequency to anti-cyclonic (blue). Elevated bispectrum indications are then associated with the three frequencies indicated on the respective axis. 102

3.17 Bicoherence of the selected time series indicated in figure 3.14. The principal frequency triples associated with the vertical displacement of inertial horizontal currents by the semi-diurnal internal tide all show high bicoherence. There are three frequency axes which range from cyclonic (red) through zero frequency to anti-cyclonic (blue). Elevated bispectrum indications are then associated with the three frequencies indicated on the respective axis. 104
3.18 Rotary PSD ($(m^2/s^2)/(rad/s)$) for the time series indicated in figure 3.14 after Semi-Lagrange inversion of the vertical coordinate. Spectral peaks indicating the reversible advection of the inertial wave by the semi-diurnal displacement, as indicated in Figure 3.15, have been removed by the S-L inversion. Independent points identified with diamond symbols. Dashed green lines indicate 95% confidence intervals. 105
3.19 Bispectrum of the 21° semi-diurnal displacement model after Semi-Lagrange inversion. As compared with Figure 3.16, the magnitude of the interaction triple points has been significantly reduced (notice the multi-decadal drop in scale maximum). There are three frequency axis which range from cyclonic (red) through zero frequency to anti-cyclonic (blue). Elevated bispectrum indications are then associated with the three frequencies indicated on the respective axis. 106
3.20 Bicoherence of the 21° semi-diurnal displacement model after Semi-Lagrange inversion. In comparison to Figure 3.17, the bicoherence before S-L inversion, there is very little bicoherence. There are three frequency axes which range from cyclonic (red) through zero frequency to anti-cyclonic (blue). Elevated bicoherence indications are then associated with the three frequencies indicated on the respective axis. 107
3.21 Bispectrum of the 21° model with no displacement of the inertial by the semi-diurnal. Compare with Figure 3.19 which is the bispectrum of the S-L inverted model with displacement. There are three frequency axes which range from cyclonic (red) through zero frequency to anti-cyclonic (blue). Elevated bispectrum indications are then associated with the three frequencies indicated on the respective axis. 109
3.22 Rotary wavelet PSD ($(m^2/s^2)/(rad/s)$) for the 21° latitude model with inertial waves displaced by the semi-diurnal waves as described in section 3.3. Spectral peaks indicating the reversible advection of the inertial wave by the semi-diurnal displacement, as indicated in Figure 3.15, have been removed by the S-L inversion. Independent points identified with diamond symbols. Dashed green lines indicate 95% confidence intervals. 111
3.23 Consistency relation (cyclonic/anti-cyclonic) using wavelet analysis for the 21° latitude model corresponding to Figure 3.22. Near the IWISC frequency there is significant deviation from the theoretical curve ($(\omega - f)/(\omega + f)$). Independent points identified with diamond symbols. Dashed green lines indicate 95% confidence intervals. 112
3.24 Frequency B-Spline wavelet decomposition of velocity for the plane wave summation model as described in the text for 21° latitude with displacement of the inertial waves by the semi-diurnal. The top panel is the clockwise wavelet time series and the bottom panel is the counter-clockwise. Contour color levels are indicated on the left. Transform times used in the rotary wavelet PSD (Figure 3.22) and wavelet bispectral analysis (Figures 3.28 and 3.28) are indicated by red dotted vertical lines. 113

3.25 Anti-cyclonic rotary wavelet amplitudes of inertial frequency at depth over a 14 day section of the plane wave sum model at 21° with the inertial displaced by semi-diurnal waves. A single time vertical structure is overlaid on the left. The theoretical group velocity indicated upper center. Model description is in section 3.3 114
3.26 Anti-cyclonic and cyclonic rotary wavelet amplitudes at the semi-diurnal frequency at depth for the plane wave sum model at 21° with the inertial displaced by semi-diurnal waves. Curve on the bottom is the lowpass amplitude envelope of the barotropic tide values used in the model for setting the semi-diurnal properties. Model description is in section 3.3 115
3.27 Rotary wavelet bispectrum for the inertial displacement model at 21° described in the text (section 3.3). There are peaks at the interaction triple points associated with the inertial and semi-diurnal internal waves in the modeled record. There are three frequency axes which range from cyclonic (red) through zero frequency to anti-cyclonic (blue). Elevated bispectrum indications are then associated with the three frequencies indicated on the respective axis. 117
3.28 Rotary wavelet bicoherence for the inertial displacement model at 21° described in the text (section 3.3). The frequency triple associated with IWISC shows significant elevated bicoherence. There are three frequency axes which range from cyclonic (red) through zero frequency to anti-cyclonic (blue). Elevated bispectrum indications are then associated with the three frequencies indicated on the respective axis. 118

4.1 Location of Hawaii Ocean Mixing Experiment (HOME) moorings in the Kauai channel. The focus of this chapter is on ADCP data from the A2 mooring. Mooring C2 data was used as well. Map courtesy of D. Luther. 121
4.2 Horizontal rotary velocity PSD $((m^2/s^2)/(rad/s))$ from the HOME mooring A2 upper long range ADCP for the 7 bin depth range between 696m and 640m. There is enhanced energy at the IWISC $(M_2 - f)$ and $M_2 + f$ frequencies. Dashed green lines indicate 95% confidence interval, diamonds indicate frequency intervals between independent PSD estimates. 122
4.3 Companion display to figure 4.2 showing shear PSD $((1/s^2)/(rad/s))$ for the 7 bin depth range between 696m and 640m. There is significantly enhanced shear at the IWISC $(M_2 - f)$ frequency. Dashed green lines indicate 95% confidence interval, diamonds indicate frequency intervals between independent PSD estimates. 123
4.4 Shear PSD $((1/s^2)/(rad/s))$ for the 7 bin depth range between 696m and 640m after the data has been Semi-Lagrange inverted using the semi-diurnal displacement (see text for details). In comparison to Figure 4.3, there remains significantly enhanced shear at the IWISC $(M_2 - f)$ frequency. This suggests there are other processes than simple vertical advection of inertial waves by the semi-diurnal tide. Dashed green lines indicate 95% confidence interval, diamonds indicate frequency intervals between independent PSD estimates. 124

4.5 Frequency of the maximum PSD in the inertial wave band for an anti-cyclonic Fourier decomposition with double taper window applied daily to the A2 mooring ADCP data for two depths, 440 meters and 776 meters. At the two respective depths, the rotary PSD is averaged across three adjacent depth bins. Dotted reference lines indicate the frequencies of the Fourier constituents. Colored crosses represent the frequencies of the peak energies in the inertial band at both depths for the whole record . In the top frame is the 15 day average meridional velocity (m/s) for the two depths. Days are measured from Jan 1, 2002, 0000 GMT. 127
4.6 Vertical time series of ADCP fifteen day mean velocity (m/s) in the meridional direction for the A2 HOME mooring. Shaded regions represent ratios of blanked data in the calculation of the average at that point. Semi-diurnal barotropic tide amplitudes are indicate at the top, as calculated from TPXO6.2 model. Positive (red) indicates northward flow in meters per second. Days are measured from Jan 1, 2002, 0000 GMT. 130
4.7 Time series of ADCP semi-diurnal band velocity PSD $((m^2/s^2)/(rad/s))$ sum of cyclonic and anti-cyclonic components vs. depth for the A2 HOME mooring. Above the thin blue contour is time depth location of southward background 15 day average meridional velocity that exceeds an amplitude of 5 cm/s. The solid white line represents the barotropic semi-diurnal sea level tide derived from TPXO 6.2 for this location. Dotted white curve is a scaled single rms time series of semi-diurnal horizontal current amplitude from depth 632 meters. First right hand panel indicates tidal ellipse major axis direction versus depth, with scale lines at 180° and 225° degrees indicated (South and Southwest, respectively). 131
4.8 Semi-diurnal total PSD $((m^2/s^2)/(rad/s))$ from figure 4.7 after applying a 28 day moving average. Solid white curves indicate 100 meter depth averages plotted in their respective depth ranges. Bottom dotted curve is average of all depths. 135
4.9 Major axis direction verses depth for each peak in the semi-diurnal spring neap cycle for the A2 mooring. There are eleven periods, with the center of the spring/neap envelope peak indicated by the day location of the red bar. The red bar indicates relative peak height of the spring neap envelopes corresponding to the main beam near 600 meters depth. The background field is smoothed eccentricity with darker colors indicating a more circular flow. The two green lines correspond to the major axis direction of the leftmost phase. Subsequent phases have the same relative angle. 136
4.10 Time series of ADCP diurnal band velocity PSD $((m^2/s^2)/(rad/s))$ component sum vs. depth for the A2 HOME mooring. Above the thin blue contour is time depth location of southward background 15 day average meridional velocity that exceeds an amplitude of 5 cm/s. First right hand panel indicates tidal ellipse major axis direction verses depth, with scale lines at 180° and 270° indicated (South and West). 139
4.11 Time series of ADCP diurnal band cyclonic PSD $((m^2/s^2)/(rad/s))$ vs. depth for the A2 HOME mooring. Above the thin blue contour is time depth location of southward background 15 day average meridional velocity that exceeds an amplitude of 5 cm/s. First right hand panel indicates tidal ellipse major axis direction verses depth, with scale lines at 180° and 270° indicated (South and West). Color contour limits are independent for each figure. 140

4.12 Vertical time series of ADCP inertial band anti-cyclonic rotary velocity PSD $((m^2/s^2)/(rad/s))$ for the A2 HOME mooring. Above the thin blue contour is time depth location of southward background 15 day average meridional velocity that exceeds an amplitude of 5 cm/s. First right hand panel indicates inertial ellipse major axis direction verses depth. Yellow shaded area shows depths where inertial eccentricity exceeds .66, indicating more elliptic motion. 142
4.13 Vertical time series of ADCP inertial band cyclonic rotary velocity PSD $((m^2/s^2)/(rad/s))$ for the A2 HOME mooring. First right hand panel indicates inertial ellipse major axis direction verses depth. Yellow shaded area shows depths where inertial eccentricity exceeds .66, indicating more elliptic motion. 143
4.14 Rotary PSD $((m^2/s^2)/(rad/s))$ of the upper 75kHz ADCP from mooring A2 of the HOME experiment is in the top panel and rotary shear spectrum $((1/s^2)/(rad/s))$ is in the lower. The major tidal frequencies are indicated as well as the interaction frequencies. Sample is whole record encompassing data range between day 329 to day 500. Vertical average is 13 bins between 400m and 504m depth. 148
4.15 Internal wave consistency relation (ratio of cyclonic/anti-cyclonic) for the spectra in figure 4.14. 149
4.16 Expanded focus on the semi-diurnal band and the summation frequency band $(M_2 + f)$ from figure 4.14. There are now four separate interaction frequencies identified in this figure. There is a band associated with diurnal constituents containing three nearby components, $\frac{2}{2}M_2$, $M_2 + K_1$, and $3K_1$. Visible but not distinct are other semi-diurnal components, N_2, and K_2. The black horizontal line beneath the sum frequency indicator is the bandwidth used for amplitude comparison between this data and a similar set that has been Semi-Lagrange inverted in the vertical. 150
4.17 Rotary PSD $((m^2/s^2)/(rad/s))$ of the lower 75kHz ADCP from mooring A2 of the HOME experiment is in the top panel and rotary shear spectrum $((1/s^2)/(rad/s))$ is in the lower. The major tidal frequencies are indicated, as well as the interaction frequencies. Sample is whole record encompassing data range between day 329 to day 500. Vertical average is 13 bins between 832m and 936m depth. 151
4.18 Internal wave consistency relation (ratio of cyclonic/anti-cyclonic) for the spectra in figure 4.17. There is significant deviation from the theoretical curve at the inertial band and higher near inertial frequencies. The sum $(M_2 + f)$ interaction frequency has deviated as well. 152
4.19 Comparison of raw vertical velocity (cm/s) and that with the zooplankton spike removed for HOME mooring C2 ADCP data. In the top figure, raw vertical velocity is shown for the 352m depth. On the bottom is the vertical velocity record with zooplankton removed. In both figures the times series of zooplankton vertical motion from the sunrise/sunset model is shown. 155
4.20 Vertical velocity PSD $((m^2/s^2)/(rad/s))$ for the zooplankton model and model M_2+S_2 semi-diurnal tides in the top panel. On the bottom is a section of the same spectra constrained to the semi-diurnal band showing the uncontaminated semi-diurnal peaks and the level of the modeled zooplankton energy. 157

4.21 PSD $((m^2/s^2)/(rad/s))$ of vertical velocity from the C2 mooring 75kHz ADCP with the zooplankton removed and without from a depth of 408 meters. The second panel is expanded around the semi-diurnal tidal constituents. There is a good qualitative comparison with the modeled spectra in figure 4.20. 158
4.22 Comparison of times series in velocity (cm/s) and temperature (normalized, C°) that has band band-passed narrowly about the semi-diurnal tide for the 352m depth bin of the HOME C2 mooring. The upper panel is horizontal velocity. In the middle panel are the displacement (m) time series. On the bottom is a temperature time series from 680m. 159
4.23 Comparison of times series in velocity (cm/s) derived from a simple model of semi-diurnal tide and zooplankton vertical migration. The top panel is horizontal velocity. The bottom panel is the vertical velocity, the green curve indicating the addition of the zooplankton signal. 160
4.24 PSD $((m^2/s^2)/(rad/s))$ of vertical velocity from the 714m bin of the ADCP on HOME mooring A2. This is the upper instrument on the mooring located at 746m, and is upward looking. It is clear that the signal with the diel migrators removed is diminishing energy equally across bands, and is not selectively removing diurnal constituent harmonics. The remaining harmonics do not seem to be associated with the zooplankton harmonic 'spikes' in depths above this. This figure illustrates 'over' removal at a depth below most migration. 161
4.25 Coherence chart for the semi-diurnal band passed vertical velocity at the A2 HOME mooring for the time period of day 449 to 479 (beginning Jan 1, 2002). The separation of upper and lower ADCP coverage is indicated by the black line. This time period encompasses the highest vertical velocity coherence with depth in the A2 data. 163
4.26 Coherence chart for the semi-diurnal band passed vertical velocity at the A2 HOME mooring for the time period of day 372 to 411 (beginning Jan 1, 2002). The separation of upper and lower ADCP coverage is indicated by the black line. The time period is indicative of the lowest vertical velocity coherence with depth from the A2 data. 165
4.27 Wavelet decomposition of vertical velocity coherence in the semi-diurnal band for the A2 HOME mooring. The separation of upper and lower ADCP coverage is indicated by the black line. This figure is indicative of the second section of the deployment in regards to background mean flow, and corresponds to the Fourier coherence figure 4.25. 167
4.28 Calculated displacement vs. depth for a peak tidal spring/neap envelope during the time segment of the total A2 record with low large scale background shear. Shaded region represents area of poor data. Center line indicates depth where velocity coverage switches between instruments. Days from January 1, 2002. 168
4.29 Semi-Lagrangian meridional velocities (blue curves) calculated with the displacements indicated in the previous figure. Original data in red. Velocities have been smoothed with a 1.33 hour moving average and increased in amplitude by 200 to match the depth scale. Shaded region represents area of poor data. Center line indicates a switch between instruments. 169
4.30 Horizontal velocity rotary PSD $((m^2/s^2)/(rad/s))$ of the single internal tide enhanced period selected for the previous figures of displacement. The solid curves are data that has been Semi-Lagrange inverted. The dotted curve is the original data. 170

4.31 Horizontal velocity rotary PSD ($(m^2/s^2)/(rad/s)$) of the single internal tide enhanced period selected for the previous figures of displacement. There is a significant diminishment of the energy in the $M_2 + f$ band. The depth is 928 meters on the A2 mooring. The solid curves are data that has been Semi-Lagrange inverted. The dotted curve is the original data. 171
4.32 Vertical profile of the normalized difference in peak values at the interaction bands between the S-L inverted data and the original data. Blue indicates the difference band ($M_2 - f$) and red is the sum band ($M_2 + f$). Negative values of the main curves indicate regions where the S-L inversion has removed energy from the band, indicating vertical advection as the source of the observed band energy. Filled diamonds represent values exceeding 95% confidence. On the left is the depth smothed curve of maximum displacement over the entire record. The curves on the right indicate the relative strength of the band peak vs. depth. The far right colorbar is the clockwise bandpassed semi-diurnal energy vs. depth, with the peak value identifying the topographically generated internal tide beam at this location. 173
4.33 Vertical profile of the normalized difference in peak values at the interaction bands between the S-L inverted data and the original data. This figure represents data from the last third of the A2 mooring time coverage, and is constructed like figure 4.32. . . . 178
4.34 Horizontal velocity time series at a depth of 424 meters on the A2 mooring. The reconstructed, demodulated inertial and semi-diurnal horizontal velocities are depicted beneath the original data. 180
4.35 Rotary PSD for A2 at 424 meters of the time series shown in figure 4.34. 181
4.36 Rotary PSD for A2 at 424 meters of the S-L inverted data for the time period corresponding to figure 4.34. Peaks at the sum ($M_2 + f$) and difference ($M_2 - f$) frequencies have higher energy after the S-L inversion. 182
4.37 Rotary bispectrum for A2 at 424 meters. There are peaks in bispectrum associated with the two interaction frequencies. The IWISC ($M_2 - f$) is located at the intersection of cyclonic $SD - f$, anticyclonic SD, and anticyclonic f. The difference ($M_2 + f$) is located at the intersection of anti-cyclonic $SD + f$, anticyclonic SD, and anticyclonic f. Further discussion is in the text. Analysis technique described in section 3.4. 183
4.38 Rotary bispectra for A2 at 424 meters for the S-L inverted data. Enhanced energy remains at the interaction points as indicated in figure 4.37. Analysis technique described in section 3.4. 185
4.39 Rotary bicoherence for A2 at 424 meters. Significant coherence is indicated at the interaction point identified by cyclonic IWISC ($M_2 - f$) frequency, anti-cyclonic inertial frequency, and anti-cyclonic semi-diurnal frequency. Analysis technique described in section 3.4. 186
4.40 Rotary bicoherence for A2 at 424 meters for the S-L inverted data. Significant coherence remains at the location associated with the IWISC frequency as in figure 4.37. Analysis technique described in section 3.4. 187
4.41 Rotary PSD for A2 at 784 meters. Peaks are evident at the interaction frequencies. The inertial is diminished as compared to the corresponding spectra for 424 meters (figure 4.35) 188

4.42 Rotary PSD for A2 at 784 meters for the S-L inverted data. The inversion has removed some of the energy at the sum ($M_2 + f$) frequency. There is not a corresponding drop in the IWISC energy. 189
4.43 Rotary bispectra for A2 at 784 meters. There is enhanced bispectra at the IWISC and sum ($M_2 + f$) interaction frequencies. Time period and method correspond to the previous analysis at 424 meters. Analysis technique described in section 3.4. 190
4.44 Rotary bispectra for A2 at 784 meters for the S-L inverted data. Bispectra at the sum ($M_2 + f$) interaction frequency has diminished as compared to figure 4.43. Time period and method correspond to the previous analysis at 424 meters. Analysis technique described in section 3.4. 191
4.45 Rotary bicoherence for A2 at 784 meters. Elevated bicoherence is indicated at the IWISC and sum ($M_2 + f$) interaction frequencies. Time period and method correspond to the previous analysis at 424 meters. Analysis technique described in section 3.4. . . 192
4.46 Rotary bicoherence for A2 at 784 meters for the S-L inverted data. Elevated bicoherence is indicated at the IWISC frquency. This indication supports a conclusion that reversible advection is not the source of the IWISC interaction at this depth. Analysis technique described in section 3.4. 193
4.47 Wavelet rotary amplitude coefficient time series from the HOME A2 mooring at a depth of 424 meters. Temporal range is selected from within the time period of the corresponding bispectral analysis. Vertical red lines indicate center time of wavelet transforms used in bispectral/bicoherence analysis. Analysis technique described in section 3.4. 195
4.48 Wavelet rotary bicoherence utilizing the two transforms indicated in figure 4.47. There is elevated coherence associated with the IWISC interaction located at the frequencies $SD - f$ (cyclonic), SD (anti-cyclonic), and f (cyclonic). Analysis technique described in section 3.4. 196
4.49 Wavelet rotary bispectrum utilizing the two transforms indicated in figure 4.47. There is an elevated bispectrum value associated with the IWISC interaction located at the frequencies $SD-f$ (cyclonic), SD (anti-cyclonic), and f (cyclonic). Analysis technique described in section 3.4. 197

5.1 Visual representation of inertial energy lost at 200 meter intervals to a process with a three percent conversion rate. Within 1400 meters, one third of the inertial energy has been removed. 207

Chapter 1

Introduction

1.1 The Problem

The study of internal waves continues to be a major focus of physical oceanography due to the impact of the flow of internal wave energy. For example, internal wave energy is believed to be an important source of the energy required to mix heat downward at low- to mid-latitudes, contributing to, if not dominating, the maintenance of the abyssal stratification against the upwelling of the cold abyssal waters originating in high latitude convection regions. Understanding how the stratification is supported, and by what means it can change, is important for our understanding of the Meridional Overturning Circulation.

The dominant energy-containing components of the internal wave field are near-inertial waves and internal tides, with inertial waves traditionally receiving the most attention as sources of energy for both other internal waves (through non-linear interactions) and turbulence. Only in the last decade has there been a shift in the collective understanding regarding the importance of internal tides to the internal wave continuum. Researchers have been revisiting conventional ideas established in the 1970s as new data has become available. Areas in which internal tide theory has seen significant changes are as follows:

- internal tides were considered marginally important in global oceanic tide budgets (see Wunsch [91], Schott [78]); and,
- internal tides were not believed to be an important source of energy supporting the internal wave continuum (e.g., Olbers and Pomphrey [63]).

The significance of internal tide energy in the global tide budget was revealed by several analyses whose results show a considerable amount of internal tide energy originating from mid ocean

topographic features (e.g., Sjoberg and Stigebrandt [81]; Morozov [53]; Ray and Mitchum [73] [74]; Egbert and Ray [21]; Ray and Cartwright [72]; Niwa and Hibiya [60]). Although it has not been well determined globally, the total flux of energy from external tides into internal tides at topographic features is estimated to be of first order significance in the neighborhood of 25% (e.g., Munk [57]; Munk and Wunsch [58]; Alford [3]).

The idea that internal tides contribute to the broad continuum of internal wave energy is more difficult to demonstrate. Researchers are moving beyond the simple empirical models begun by Garrett and Monk (early review [28]) in the 1970's that have dominated internal wave energetics for three decades. New ideas have followed advances in observational resolution and extent.

The principal difficulty in establishing the mechanisms of energy flux through frequency and wavenumber space is a lack of data sets which resolve specific free internal waves interacting in a non-linear exchange. Some researchers continue to emphasize the importance of weak nonlinear interaction, but with the addition of internal tides as a major source of energy (e.g., Hibiya et al. [35], Levine [42], van Haren et al. [88]). Others emphasize the impact of internal tides as a simple means to advect smaller scale motions, thus yielding an apparent re-distribution of energy that seems to explain many of the spectral characteristics of internal waves derived from Eulerian data (Pinkel [67]).

In either case, whether through increased involvement of inertial wave and internal tide energies in weakly non-linear processes, or distortions of reference frame, the description of internal wave energetics needs to evolve. A pertinent anchor to any new description will include the interaction between inertial waves and internal tides, which are by far the most energetic and continually forced internal wave components in the ocean.

The frequency band containing the inertial and internal tide waves constitutes roughly eighty percent of the total internal wave energy in many regions. The specific interactions involving these sources is a natural place to investigate internal wave non-linearity. This is the case, for instance, with the Parametric Subharmonic Instability (PSI) mechanism, hypothesized in the seventies to be one of the three dominant resonant non-linear interactions re-distributing internal wave energy in frequency-wavenumber space to yield what appeared to be a canonical spectral form. No conclusive evidence has been found supporting the existence of the PSI process. However, carefully designed numerical simulations have suggested that it can be an important energy conversion mechanism at the critical PSI latitude (e.g. MacKinnon and Winters [47]).

1.2 What is Known?

The vertical scale at which diapycnal mixing occurs is short, and the associated frequency is rapid compared with most of the internal wave structures in the ocean. To transfer energy to the scales of mixing, a classic theory exists where energy at large scales and/or lower frequency interacts via weak non-linear processes with structures at higher frequencies and/or smaller scales. This dynamic relationship has been the established theory for more than three decades (reviewed in Müller et al. [55]).

Internal wave dynamics have their roots in the non-linear interactions of surface gravity waves first discussed by Phillips [65]. Hasselmann [31] extended the theory of fluid dynamics, which opened a vast and continuing field of wave interactions studies in geophysical fluids. Each of the principal 'modern' weakly non-linear resonant processes can be seen (with hindsight) in the various example interactions of Hasselmann. A concise development of the equations applicable to the internal wave system is presented by Olbers [61].

From the general interaction theory a set of weakly non-linear resonant interactions came to prominence in internal wave dynamics. The primary weakly non-linear triad interactions in the theory are induced diffusion, elastic scattering, and parametric sub-harmonic instability. An 'interim' review of the three can be found in McComas and Bretherton [48]. The weakly non-linear theory was subsequently extended to include interaction between waves and vortical modes, reviewed in Müller et. al. [55].

The development of the theory continues today. For instance, modern numerical simulations seem to strongly support the inclusion of vortical structures. Waite and Bartello [90] argue forcefully in favor of this interaction, "Any explanation of the energy spectrum involving resonant interactions must take into account the effect of vortical motion."

The primary goal for many investigating these interactions has been to elucidate the presumably universal mechanism supporting many of the features observed in oceanic velocity record spectra, and more specifically the transfer of energy within the internal wave frequency-wavenumber spectrum (the "cascade"). Of high importance for the work presented here, the critical spectral features that are universal, yet not well represented by existing non-linear theory (or empirical spectra descriptions) include the peak of energy at the semi-diurnal tidal band, and the very near inertial band.

Internal tide and inertial input energies contain the bulk of total energy in the internal wave band. These waves have the potential to interact in non-resonant ways. There is a possibility that these peaks could directly force other motion, without it being detected by our limited observations. As an example

of how difficult it is to observationally account for the flow of energy of even the strongest internal waves, Hebert and Moum [33] carefully observed the propagation of an inertial wave packet and could not account for more than half of the energy loss within the study region.

Data analysed in this work shows evidence of an irreversible interaction between inertial internal waves and semi-diurnal internal tides that cannot be classified as one of the main weakly non-linear resonant triad interactions. Other evidence supports spectral contamination by an Eulerian reference frame. Distinguishing these phenomena is the primary focus of this work. In an excellent review of internal wave models, Olbers [62] makes this highly applicable statement: "An accurate identification of reversible (wave induced) fine structure and irreversible fine structure is needed to determine the dissipation rate of the wave field and the mixing rates of the ocean."

Olbers statement is true to this day, and applies to more than just fine structure. It is possible that a significant part of the observed internal wave spectrum is a result of reversible advection; Pinkel [67] has recently provided evidence and modeling in support of that conjecture. It is also possible that there are some direct irreversible exchanges that are not described by conventional theory. Determining the nature of these processes and differentiating between them is as important a question now as it was thirty years ago.

Part of the reason no suitable answer has come forward is the lack of observational evidence indicating internal wave weakly non-linear interactions. Direct evidence in support of the energy cascade has not been abundant. For example, in a review of the deep ocean mixing problem, Garrett and St. Laurent [29] indicate the lack of direct evidence identifying the energy transfer as significant source of concern. In terms of general internal wave observations, the wave field in the ocean remains as vertically symmetric and horizontally isotropic today as in the 1970's, when analysed with similar techniques that led to the weakly non-linear interaction theories. However, the focus in this paper is on a previously overlooked feature which provides unique evidence of internal wave interaction.

This feature represents a short circuit to the traditional energy cascade establishing the internal wave field, whereby energy could be moved from the low-frequency waves directly into dissipative structures. In this research there is evidence that indicates a shift in understanding may be warranted to explain large scale, low frequency internal wave dynamics.

Consider the current excitement and interest surrounding PSI at its critical latitude. Many efforts have been made to identify and establish what is happening in the ocean in regards to this possible interaction (e.g., Young et al. [96], Alford et al. [4], MacKinnon and Winters [47]). Yet despite the effort, there is no conclusive evidence to support the existing theory. The research in this paper uses

abundant evidence to analyze the interaction between inertial internal waves and the semi-diurnal tide. Based on these observational results, possible physical mechanisms are examined and proposed.

1.3 Summary of Work and Significant Results

The investigation in this work has led to the following results, organized in order of appearance beginning with the reanalysis of historic moored current meter data:

- A peak in spectral energy has been observed at the frequency of $M_2 - f$ (which is dubbed the Internal Wave Induced Sub-Inertial Current - IWISC - frequency) over a broad range of depths and in numerous geographic locations throughout the worlds oceans.
- The IWISC energy is almost entirely in the cyclonic rotary component, rather than the anti-cyclonic component that dominates free internal waves.
- IWISC energy poleward of the critical (where $f = M_2/2$) frequency is outside of the free internal wave band.
- There is a corresponding energy peak at the frequency $M_2 + f$ in many of the records where IWISC is observed, but this peak is dominantly in the anti-cyclonic rotary component (as appropriate for free internal waves).
- Energy at the IWISC frequency is episodic and in general is not directly correlated with observed energy at the semi-diurnal frequency.
- There is a weak (R < .2) positive correlation between bulk observations of IWISC peak energy and inertial peak energy, with the strongest IWISC events usually associated with enhanced inertial energy.
- All interactant frequency bands (M_2, f, $M_2 - f$, $M_2 + f$) were found to exhibit horizontal correlation scales less than 10 km in one experiment where spatially-distributed time series were available.
- IWISC peak energy for mid-latitude records exhibit a depth structure, with maximum peak energy above a mesoscale background occurring near 1500 meters depth.

Given the characteristics of IWISC derived from the historical data, which suggest the possibility of the existence of an irreversible non-linear interaction between semi-diurnal internal tides and near-inertial internal waves, both simple and sophisticated analysis tools were tested on simple models

of reversible advection to determine whether these tools would be able to definitively discriminate reversible advection from irreversible non-linear interaction in existing oceanic data. The tests yielded the following results:

- A hierarchy of vertical advection models was created to establish if, when, and how vertical advection is a satisfactory explanation of IWISC.
- The simplest model of a single sinusoid semi-diurnal internal tide displacement of an inertial internal wave replicates properties of the Eulerian observations of IWISC, such as a power spectral density (PSD) peak at the IWISC frequency; however, this model always yields an additional PSD peak at the sum ($M_2 + f$) frequency. Such a tight correlation between PSD at IWISC and $M_2 + f$ frequencies is not observed.
- Extending the displacement model to include multiple semi-diurnal vertical modes and frequency constituents results in temporal and spatial variability of IWISC not inconsistent with observed variability.
- Several analysis techniques were applied to the output of the model that employed multiple plane waves (simulating multiple vertical modes and frequency constituents) to vertically advect inertial currents, in order to provide insight into the utility of applying these techniques to real data.
- Bispectra and bicoherence analyses, used to identify non-linear interactions in many disciplines, **do not** distinguish between periodic Doppler shifting (reversible advection) and energy exchanging non-linear interaction.
- Semi-Lagrangian inversion is commonly used to remove reversible advection signals from Eulerian data. Applying such an inversion to the model output yielded the expected result, i.e., absence of any indication of the original advection, e.g., Semi-Lagrange inversion of modeled currents eliminated interaction frequency energy so that there were no longer IWISC or M2+f peaks in power spectra, bispectra or bicoherence.
- Wavelet rotary bispectral analysis was created here in an attempt to improve the identifications of interactions where one of the signals appears as a relatively short event.

With the calibrated tools and techniques, and the insight gained in the historic data analysis, high resolution (in depth and time) horizontal current data from the Hawaii Ocean Mixing Experiment (HOME) was analysed with the following results:

- ADCP records revealed IWISC frequency peaks in power spectra of horizontal currents and their vertical shear.
- The vertical velocity from the well-instrumented A2 mooring ADCP records was corrected for diel migrator contamination at the semi-diurnal frequency. Vertical velocity at this band was extracted. Validation was possible due to the existence of two long-range ADCP's on the mooring with overlapping fields of view.
- The vertical velocities were used in a Semi-Lagrange inversion of ADCP horizontal velocity.
- The Semi-Lagrange inversion revealed both depth ranges where interaction peak energy (at IWISC and M2+f) is diminished by the inversion thus implying that reversible advection dominated those signals, and depth ranges where the energy peaks remained unaffected. This leads to the conclusion that both periodic Doppler advection and other energy redistribution processes are present at this location.
- Bispectral and bicoherence analysis of Semi-Lagrange-corrected ADCP velocity suggest the presence of irreversible non-linear interaction at IWISC.

The results indicate that more than one process is responsible for the observed energy peak at the IWISC frequency. This is indicative of a fundamental change in how the internal wave band energy is viewed. One process, periodic Doppler shifting, implies that the origin of the internal wave continuum must be re-evaluated (as demonstrated recently by Pinkel [67]); and, especially, Eulerian data must be evaluated much more carefully than has been the norm. Another process, direct forcing of non-free wave motions by non-linear internal wave interactions, represents a new pathway for the flow of energy out of free internal waves which has not been previously considered. The conclusion of this work in Chapter 5 discusses these scenarios.

Chapter 2

Historical Data Reanalysis

2.1 Introduction

The phenomena of Internal Wave Induced Sub- and Super-Inertial Currents (IWISC) is evident in many historical current meter records. This chapter reports on the effort to characterize the IWISC (observed energy at a frequency of $M_2 - f$) phenomenon and explore its depth and geographic extent in existing repositories of historical moored current records. The work began with a reanalysis of the coincident BEMPEX (Luther et al. [46]) and RTE87 data (Dushaw et al. [19]) in which the sub-inertial $M_2 - f$ peak was first noticed by Luther (private communication). The analysis expanded to cover over three decades of moored current meter experiments from many regions. The IWISC energy signature was found at many depths from moorings located throughout the globe. This search highlighted the need for more spatial resolution to identify interaction processes and structures, so the data analysis was enlarged to include relevant historical ADCP data that provides higher vertical resolution.

Utilizing the records containing an interaction signal, characteristics such as the following were sought: depth dependence, vertical correlation, temporal correlation, relationships among the energies of M_2 and f and the interaction frequencies, etc. The primary spectral features are the sum ($M_2 + f$) and difference (IWISC, $M_2 - f$) frequency peaks that occur in the anti-cyclonic and cyclonic (respectively) rotary power spectral density (PSD). It could be argued that these peaks are simply the result of vertical advection of inertial waves by the semi-diurnal internal tide waves. However, the bulk of the records do not exhibit temporal coincidence of high values of the IWISC, $M_2 + f$, M_2, and f energies. Even more interesting was the discovery that there were many time periods in individual records when the sum and difference frequency energies had relative maxima that were not coincident in time. Any vertical advection mechanism that is reversible, i.e., the heaving of mostly horizontal inertial waves by

a low mode semi-diurnal tide, would be expected to lock these two signals (although, this assumption is re-examined in the next chapter).

The occurrence of IWISC PSD peaks is not ubiquitous in the records we have examined (for a variety of reasons), but neither is it uncommon or evident in only one small region or in one dataset. Whether the IWISC phenomenon is the result of a simple vertical advection of inertial wave shear by semi-diurnal tide displacements, or whether it is the result of a significant energy-exchanging non-linear interaction, or whether it can be both at different times or different places, its presence in oceanic current meter datasets cannot be denied and must be explained in order for us to understand the origins of the full spectrum of internal wave energy and the consequences of the magnitude and structure of that spectrum, e.g., for diapycnal mixing. Sections 1.1 and 1.2 address these issues, and more, as a necessary motivation for this study of what some may consider to be an esoteric sideline.

2.1.1 Motivation

A significant sub-inertial peak was identified in the spectra from current meters deployed during BEMPEX/RTE87. This dramatic feature can be seen in figure 2.1 at the difference between the semi-diurnal tide and inertial frequencies. The peak in the counter-clockwise rotary PSD exceeds one order of magnitude above the 'background' mesoscale energy observed in this sub-inertial band.

The most energetic feature in Figure 2.1 is the peak of inertial energy in the clockwise rotary velocity component. Following this are the tidal energy peaks, then the two peaks at interaction frequencies between the inertial internal waves and the semi-diurnal internal tide. The IWISC ($M_2 - f$) peak energy in this figure is 3.4% of the peak inertial energy. This cyclonic signal has 30% more kinetic energy than the clockwise sum ($M_2 + f$) interaction energy. Peak energy values were determined from the maximal independent point within the respective frequency band with a ±5% width selected from the smoothed rotary PSD.

We have found numerous Eulerian observations of oceanic currents that contain energy at the difference frequency of the semi-diurnal internal tides and inertial internal waves. This resultant energy containing frequency is outside of the internal wave band for locations north of the critical frequency ($\approx 29°$), indicating that it is not a free wave. Peaks in the near sub-inertial could arise from many possible sources for mesoscale energy in this range, but usually have periods longer than a few days. The IWISC signature (cyclonic rotary PSD peaks at the difference frequency $M_2 - f$), however, was discovered at multiple locations that have relatively weak mesoscale energy.

The principal motivating factor driving this examination of IWISC is the possibility that the IWISC spectral peaks imply that energy is actually being drained from the inertial and internal tide wave fields

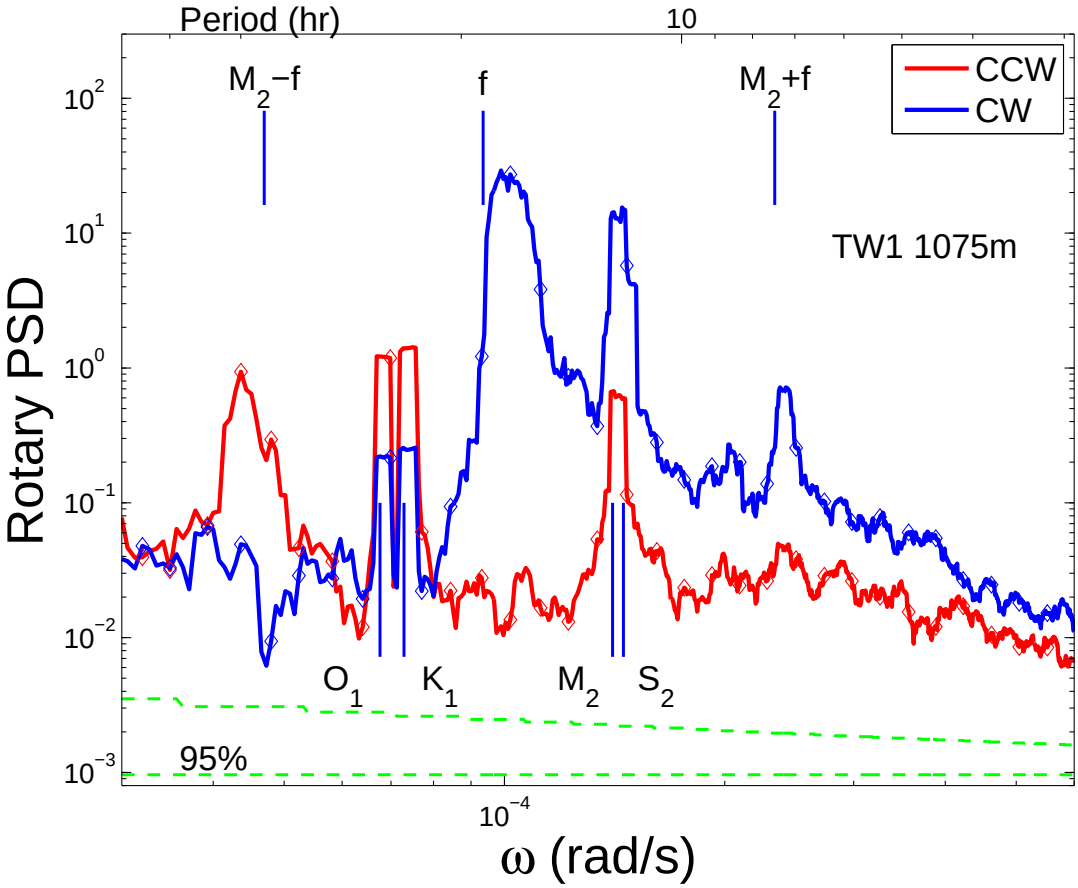

Figure 2.1. Rotary PSD of current meter velocity recorded at 1075m depth on the TW mooring during BEMPEX/RTE87. This record stimulated investigation of the sub-inertial peak at the IWISC ($M_2 - f$) frequency. The record length is 200 days long. 95% confidence intervals for each independent PSD estimate are indicated by the dashed green lines at the bottom; the diamond symbols indicate the frequency intervals between independent PSD estimates.

as the inertial waves propagate downward from the surface mixed layer. There is no cascade, energy is simply extracted into non-free oscillations. This energy pathway has not been considered in internal wave energy budgets (Muller and Briscoe [54]). Not only might IWISC represent a significant energy loss pathway for the inertial waves and internal tides, but the subsequent short-circuiting of the inertial wave energy would have implications for the speculation that nearly all wind-generated inertial wave energy is needed to maintain the abyssal stratification below 1 km depth through boundary-catalyzed diapycnal mixing (e.g., Munk and Wunsch, [58]).

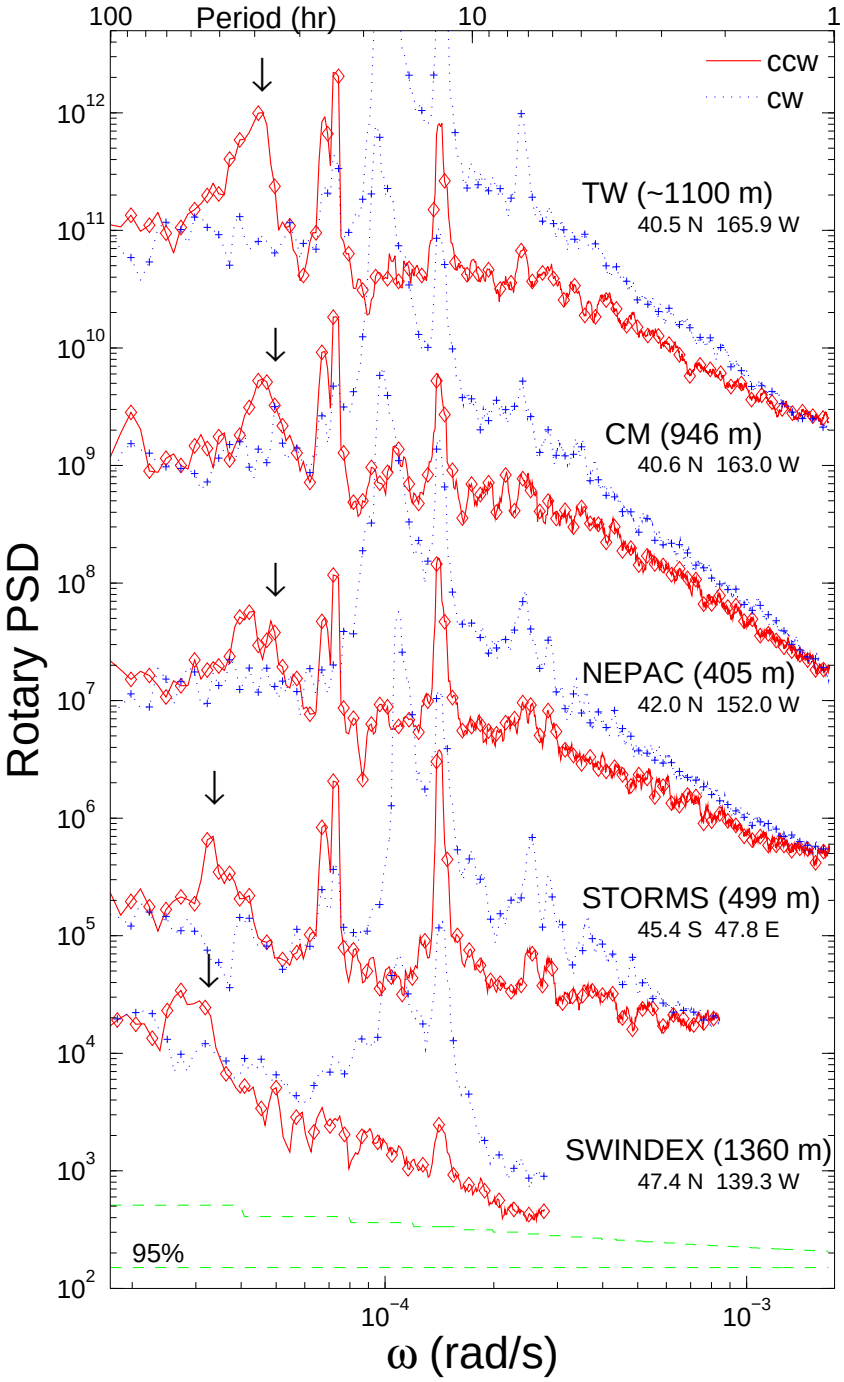

Figure 2.2. Comparison of rotary PSD from a number of representative locations exhibiting a sub-inertial IWISC peak (latitudes > crit). Black arrows indicate the exact $M_2 - f$ frequency. There is clear enhancement of counter-clockwise energy (clockwise for the Southern Hemisphere SWINDEX site) in the neighborhood of the difference $(M_2 - f)$ frequency. Note that inertial wave energy is usually maximum at a slightly super-inertial frequency; this would account for the IWISC peaks occurring at slightly lower frequencies than the exact $M_2 - f$ frequency. Enhanced energy at the IWISC frequency is not unique to these records, nor extreme (see Figure 2.27 below). TW and CM are moorings from the RTE87 and BEMPEX experiments, respectively. 95% confidence intervals for each independent PSD estimate are indicated by the dashed green lines at the bottom; the diamond and cross symbols indicate the frequency intervals between independent PSD estimates.

If there is no exchange of energy (that is, if IWISC is simply the result of reversible advection), this fact would be important in its own right for understanding past and future Eulerian current measurements, and therefore it needs to be established in a positive definite manner. The assumption that there is no energy exchanging mechanism implies that advection contamination is a significant feature across much of the internal wave frequency band, a hypothesis now receiving renewed attention (Pinkel [67]).

In Figure 2.2, the peak energy at the $M_2 - f$ difference frequency is clearly seen for a number of locations. These records have been chosen for their reduced near inertial mesoscale energy, which permits clear delineation of the sub-inertial IWISC peak. This case occurs in mid-latitude records. The IWISC acronym can be used to specify a similar phenomenon at tropical latitudes, equator-ward of the critical latitudes at which the inertial frequency is half of the semi-diurnal tide frequency, by substituting "Super-Inertial for "Sub-Inertial. Since the moored current meters provide Eulerian measurements, a simple hypothetical question was formulated: What part of the observed IWISC energy can be accounted for by non-linear energy transfer vs. periodic Doppler shifting (e.g., from vertical advection)? This is a simple question at first glance, yet leads to layers of complexity when analyzed in the context of low frequency oceanic internal waves.

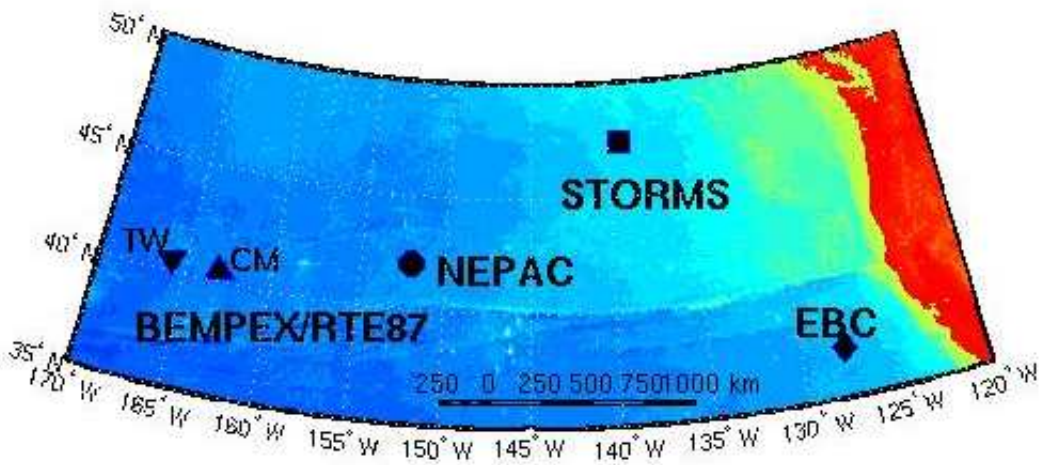

Figure 2.3. Map of North Pacific mooring locations for all but one of the rotary PSD shown in figure 2.2.

The inertial interaction with the semi-diurnal tide has the potential to yield motions at sum (M_2+f) and difference ($M_2 - f$) frequencies. The sum interaction has been identified by Mihaly et al. [51]. Mihaly et al. utilized observations from 23 current meter records deployed over a ten year period near the Endeavor ridge in the northeast Pacific from depths below 2000 meters. A peak in the anti-cyclonic rotary PSD at the $M_2 + f$ frequency was found which exceding the $2M_2$ harmonic in magnitude.

In the time series of energy, they did not find coincident elevated energy between interacting bands, but a 'seasonal' correspondence was surmised. In Figure 2, the authors have a time series of anti-cyclonic velocity from one current meter which has three clear events with elevated $M_2 + f$ band energy. One of these corresponds with a inertial event, both bands during this coincident feature having duration in excess of twenty days. There is no clear relationship in elevated energy from $M_2 + f$ or the inertial corresponding to elevated semi-diurnal tide energy. The semi-diurnal tide does not have a clear spring/neap cycle in the figure.

Bispectra were calculated by the authors, but did not yield results. A possible explanation for this lack of results was interpreted by the authors as the point measurements used in the analysis not 'observing' all three of the interacting waves (or wave packets) at the time and place of interaction. Lack of phase coupling during elevated $M_2 + f$ event is deemed evidence of a resonant interaction.

The generation mechanism proposed by Mihaly et al. for the $M_2 + f$ interaction is classic weakly nonlinear theory (Müller et al. [55]). As the analysis did not identify the mechanism, the authors speculate on possible spatial structures and propagation of wave packets as an explanation. In other words, the interaction is occurring non-locally, then moving into the range of the point observation. During this movement, the features become decoupled in phase.

During a strong $M_2 + f$ event, Mihaly et al. observed that the frequency band was predominantly anti-cyclonic. They comment that during this event the interaction mechanism may be forced non-resonant. The authors do not comment on a potential PSD peak at the difference frequency or the possibility of reversible vertical advection as a mechanism.

The $M_2 + f$ sum peak has been commented upon subsequently by van Haren et al. [88], van Haren [84] [85] [86], Lavelle [40], Garrett [27] [29], Alford [2], Xing and Davies [92] [15] [93], van Aken et al. [83], as well as others.

Of interest among these investigations is van Haren et al. [88] where there is indication of a spectral peak at the $M_2 - f$ frequency. The measurements were taken from seven moorings in the Bay of Biscay, over a time period of 11 months. Moorings were deployed on and near the continental slope.

In Figure 1, the authors display the kinetic energy PSD from two depths, 3810 m and 1450 m, with numerous harmonics of the internal tide and inertial bands indicated and with a few interaction

frequencies between the two bands and their harmonics likewise identified. Among the interactions is the $M_2 - f$ frequency, however this is not described in the text.

Most notably in the van Haren et al. work is the statement that part of the universal nature of highly smoothed internal wave spectra is due to nonlinear forced harmonics of the inertial and semi-diurnal bands. Additionally, and of equal importance in characterizing the smoothed spectra, were nonlinear interactions between the inertial waves and internal tide. Specifically mentioned are the interactions $M_2 + f$ and $2M_2 - f$.

The authors accentuate their conclusions in the abstract with the statement that "... the first half decade of the internal wave band is dominated by motions at localized frequencies determined by strong non-linear interactions between waves at the fundamental tidal and atmospherically induced inertial frequencies." This statement represents a view where reversible vertical advection is negligible.

Investigation into baroclinic tidal advection encompasses a wide scope of problems from internal wave generation to sediment flux. The physical process of barotropic advection has also been well studied, but is different from the vertical advection (periodic vertical Doppler shifting) of baroclinic structures we are interested in. A thorough literature search did not identify any discussion of a specific attempt to delineate wave-wave interaction from periodic Doppler shifting of near inertial energy by the semi-diurnal internal tide.

There is however, a long history of investigating the source of fine-scale "contamination" of internal wave spectra, including the vertical advection of near-inertial fine-scale shear by internal tides. Pinkel [66] introduces high resolution data of the upper ocean and reviews the possible nature of the contamination. Subsequently (1997), Pinkel and Anderson [68] discuss a semi-Lagrangian approach, whereby the vertical coordinate moves vertically with the isopycnals, for removing some of the shear contamination occurring in Eulerian measurements. The principle is consistent with periodic vertical Doppler shifting (reversible advection) to explain peaks in rotary PSD derived from Eulerian current meter data sets. Alford [2] deals specifically with the problem of identifying Doppler shifted energy by internal tidal mechanisms in the context of fine-scale contamination.

The data used by Alford was collected at 6.5° S in the Banda Sea. Diurnal interaction with inertial internal waves was evident in rotary PSD. Shear at the same interaction frequencies ($K_1 + f$ and $K_1 - f$) was observed. After a Semi-Lagrange inversion of the data, these interaction indications were reduced to below significance. The results were consistent with a two wave simple model of reversible vertical coordinate displacement described by Alford. At this low latitude, the IWISC interaction between the inertial and semi-diurnal tide bands would be at a frequency near the semi-diurnal, and is not evident in

the analysis, though both $M_2 + f$ and $M_2 - f$ are labeled in Alfords Figure 3, where in the shear spectra there appears to be a significant reduction at the $M_2 + f$ frequency after the Semi-Lagrange inversion.

An important aspect to consider in the results of Alford is the length of record. There appears to be approximately twelve days of data, which is less than a spring/neap cycle. Without characterizing the internal tide variability at this location, it is difficult to attribute specific results to a more general application. However, even with this limited sample, the simple two wave model of Alford predicts shear at both the $M_2 + f$ and $M_2 - f$, yet there is only shear observed at the sum frequency ($M_2 + f$). This shear asymmetry raises questions about what process is active, and how that mechanism can result in observations like these. For the data presented by Alford, there is not enough spectral resolution to separate the inertial and semi-diurnal interaction bands from the semi-diurnal band.

A plausible reason the evidence of a spectral peak at the ($M_2 - f$) frequency, as an indicator of inertial wave interaction with the semi-diurnal internal tides, was not 'discovered in the data from many prior experiments is that the result of the interaction produced sub-inertial variability that was hidden by mesoscale processes of other origins. (Indeed, for a long time, most current meter moorings were placed in regions where the study of the mesoscale variability was primary, e.g., the western Atlantic, and the study of the internal wave field was secondary.) It is natural that the only clearly observed interaction, as evidenced by the ($M_2 - f$) spectral peak, occurs in records with relatively low sub-inertial variability. For latitudes nearer the equator, the resulting interaction is detected in the super-inertial band, with the same caveat, except it is free internal waves hiding the product of the interaction (which is not a free wave) instead of mesoscale currents.

With the level of energy of the observed interaction product near that of 'background' processes, a natural question to ask is "Why would this process be of interest?" Consider that the process may be an active energy flux pathway, such that even a small fraction of the peak inertial and semi-diurnal energy transferred quickly and continuously could represent a significant sink in the total energy budget. The implication is that this transfer is not part of a 'cascade' but moves energy directly out of the internal wave regime and into forced rotary motion. Part of the decay of such rotary motion would likely result in increased mixing at many depths where other mixing processes are weak. The IWISC process takes on additional significance when it is realized that there is probably no reason why the interaction should not occur between internal waves at other frequencies. However, such interaction will be very difficult to prove, considering what weve learned from the current study of the interaction between the stochastically narrow-band inertial and semi-diurnal waves.

A very important point about investigating IWISC with available data sets concerns the required resolution to definitively address kinematic and dynamic characteristics within the flow. The majority of

data investigated does not have the spatial resolution to determine conclusively what process dominates the interaction between the inertial internal waves and the semi-diurnal internal tide. This chapter describes an exploration of the characteristics of the IWISC, and is an attempt to understand enough about IWISC observationally both to define experimental requirements to better observe IWISC, and to design analytical and numerical models to better understand IWISC and predict its consequences on the internal wave field.

2.1.2 Relevance

A permanent, non-linear flux of internal wave energy out of the internal wave band has consequences on where, when and how internal wave energy dissipates and diapycnal mixing occurs, with potential implications for maintenance of the abyssal stratification and climate variability. Well established arguments have been developed requiring that a very large portion of the wind generated internal wave energy that flows into the deep ocean be utilized for abyssal mixing in order to maintain the observed abyssal stratification (Munk and Wusch [58], St. Laurent and Garrett [82]). Identifying the IWISC energy path, along with quantitative estimates of energy lost to IWISC, could have significant impacts on the origin of required mixing needed to maintain abyssal stratification.

In addition to the specific relevance in regard to mixing and climate variability, the existence of IWISC, if it truly is the result of a non-linear energy-transferring process, impacts the more general theory of internal wave energetics. The flow of energy in wavenumber space within the internal wave band has been investigated extensively; a brief overview is presented in Müller and Briscoe [54]. The conventional view is that the bulk of internal wave energy is input at inertial and tidal frequencies, which then interacts with other free waves to transfer energy to smaller scales, eventually ending in dissipation. IWISC represents a potential short circuit of that conventional view in that it immediately transfers energy from the peak input frequencies to decaying and dissipative structures at interaction frequencies.

2.1.3 Historical Data Analysis

In this chapter, a large number of observations are examined in varying degrees of detail. The general course of discovery leads from the coarsest identification to very specific analyses of selected time periods and depths. The following list details the course of presentation:

- Section 2.2 - discussion of data sets
- Section 2.3 - presentation of Eulerian observational evidence of IWISC

- Section 2.4 - discussion of the variability in Section 2.3 with a focus on reversible advection and energy exchanging non-linearity
- Section 2.5 - summary of Historical Data Reanalysis

The analysis of historical records has generated important results in the study of IWISC and the possible underlying mechanisms. These significant results include the following:

- A peak in spectral energy has been observed at the frequency of $M_2 - f$ over a broad range of depths and in numerous geographic locations throughout the worlds oceans.
- The IWISC energy is almost entirely in the cyclonic rotary component, rather than the anti-cyclonic component that dominates free internal waves.
- IWISC energy poleward of the critical frequency (where $f = M_2/2$) is outside of the free internal wave band.
- There is a corresponding anti-cyclonic rotary component energy peak at the frequency $M_2 + f$ in many of the records.
- Bulk observations of IWISC cyclonic peak energy poleward of the critical frequency ($f = M_2/2$) show a positive correlation (though not strong with R < .5) with the corresponding anti-cyclonic $M_2 + f$ energy peak.
- Energy at the IWISC frequency is episodic and in general is not directly correlated with observed energy at the semi-diurnal frequency.
- There is a weak (R < .2) positive correlation between bulk observations poleward of the critical frequency ($f = M_2/2$) of IWISC peak energy and inertial peak energy, with the strongest IWISC events usually associated with enhanced inertial energy.
- All interactant frequency bands (M_2, f, $M_2 - f$, $M_2 + f$) were found to exhibit horizontal correlation scales less than 10 km in one experiment where spatially-distributed time series were available.
- IWISC peak energy for mid-latitude records exhibits a depth structure, with maximum peak energy above a mesoscale background occurring near 1500 meters depth.

These significant results suggest the possible existence of an irreversible non-linear interaction between semi-diurnal internal tides and near-inertial internal waves.

2.2 Data Sets

Many historical data sets were investigated to determine IWISCs presence and characteristics. Evidence accumulated quickly across a broad range of regions and depths. It was realized that to fully characterize all the differing properties and variability of IWISC that were observed regionally would require much more detailed observations (especially with respect to spatial resolution) than are available. With this insight, the intention turned to examining a handful of locations that exhibited significant IWISC indications and had the best spatial resolution (e.g., multiple moorings close together; or, ADCP data). Through this process a good understanding of the problem was achieved.

This investigation is not to be construed as an exhaustive analysis of historical data to study IWISC. The work on this phenomenon has only just begun. Given the implications of IWISC, further historical analysis is warranted. For instance, if an estimate of actual non-linear energy transfer can be achieved based on observed rotary PSD, it would be possible to create a global estimate of the energy transferred from free internal waves to the interaction frequency structures. Before that can be achieved, the energy transfer needs to be established and quantified. This situation motivated the approach here. A winnowing to specific data sets that had high relevance to IWISC and unique information made the problem more tractable.

2.2.1 Scope of Data Coverage

The bulk of records scanned for evidence of IWISC are in the OSU Buoy Group repository of deep water records. This data bank has grown to nearly 5000 records. For specific usefulness in the characterization of IWISC, a few narrow subsets of records have been used. Most of the pertinent velocity records come from specific experiments with clear reference and documentation. A list of some major moorings used in this study and the associated experiments is given in table 2.1.

Table 2.1. Sample of Major Data Sets Analyzed

Project	Moor	Insts	Depth Range	Lat	Lon	Year	Ref
BEMPEX							Luther et al. [46]
	CM	6	75 5649 m	40.65	-163.02	1986	
RTE87							Dushaw et al. [19]
	TE1	2	1081, 2431 m	40.47	-157.15	1986	
	TW1	2	1075, 2525 m	40.5	-165.9	1986	
	TW2	1	1159 m	40.5	-165.9	1987	
	TS	2	1114, 2364 m	31.47	-157.06	1986	
NEPAC							Hu and Niiler [37]
	1	7	281 3756 m	41.97	-152	1982	
	2	7	270 3980 m	42	-152.05	1983	
	3	6	167 2468 m	41.93	-151.91	1984	
STORMS		13	199 3999 m	47.42	-139.29	1987	Qi et. al. [70]
NEADS 6		5	547 3109 m	52.4	-17.7	1982	Dickson [18]
SCM9							Pollard & Read [69]
	A	6	330 2818 m	-45.42	47.82	1993	
	B	3	311 1529 m	-44.7	45.73	1993	
	F	3	382 4174 m	-43.39	36.06	1993	
ACM13							Zenk et al. [97]
	906	4	509 3532 m	-28.47	-44.47	1991	
	907	4	496 3850 m	-29.04	-43.49	1991	
	909	4	514 3714 m	-30.08	-41.73	1991	
PCM11							Rudnick [76]
	S1	3	2990 4230 m	-9.68	-170.47	1992	
	S3	4	2890 5103 m	-9.92	-169.73	1992	
EBC							Chereskin [11]
	OW	5	106 605 m	37.05	-127.7	1992	
	ON	5	102 601 m	37.21	-127.61	1992	
	OE	5	107 600 m	37.14	-127.41	1992	
	OS	5	106 605 m	36.98	-126.49	1992	
	OC	5	98 597 m	37.11	-125.53	1992	

2.2.2 Overview of Data

The scope and direction of the data analysis in the search for IWISC characteristics evolved as more information became available. An initial proposed comparison was to identify a statistically sound sample of single records with clear peaks in cyclonic rotary PSD at the IWISC frequency. It quickly became apparent that this signature was intermittent, depth variable, regionally variable,

and separated in frequency regime by latitude. A different approach was crafted, with targeted goals matched to more restricted sets of data.

As a bulk description, more than 300 individual moored velocity records have been processed, covering over thirty years of data beginning in the mid 1970's. This does not include records that had no particular IWISC indication. However, the threshold for claiming IWISC signature is necessarily vague and situational. Additionally, the identification of elevated energy in the cyclonic rotary PSD in a moored current meter at a given depth promotes the other instruments on that mooring into the bulk data set of locations exhibiting IWISC. This can lead to confusion when discussing raw numbers of records that have this signature.

Since the criteria for designating a particular record or mooring as useful in characterizing IWISC depends on the location, depths, length of record, strength of inertial activity, plus many other possible details, broad statements about the preponderance of IWISC are misleading. A choice was made to focus on specific regions that help define the IWISC phenomena instead of an attempt to assess global significance.

The records in the Oregon State University (OSU) Buoy Group database originated from a wide range of sources, and represent varying degrees of quality. Detailed information can be found online [1], though the status of ongoing maintenance is unknown. Maintainers of the mooring database exercised care and considerable effort in preparing each record for general use in the community. The following is a partial list of quality control issues addressed in the data collection:

- Compass irregularity
- Rotorcounter failure
- Speed sensor fouling
- Sensor drift

Bad segments were addressed with different degrees of interpolation depending upon the length of the corrupted portion. Very corrupt records were not included based on the OSU group's decision of 'usefulness', whether the data represents true oceanic variability.

BEMPEX/RTE87

The mooring component of the BEMPEX experiment combined with the concurrent RTE87 project and its moorings provided the initial unique spectra illuminating IWISC, primarily due to the regions

very low near-inertial mesoscale activity (a design criterion sought by the BEMPEX investigators). An overview and synopsis of current meter data from these moorings can be found in Luther et al. [46].

WOCE data

Many records utilized here were components of the World Ocean Circulation Experiment (WOCE [13]). The mooring data from these experiments was handled by the OSU Buoy Group who were contracted to maintain the WOCE Current Meter Data Assembly Center. Quality control of these records follows the same standards as other data in the OSU Buoy Group moored current meter database.

One particular WOCE component (PCM2 - Eastern Boundary Current - EBC) provided unique horizontal information relevant to IWISC. The data is described in Chereskin et al. [11] with a summary of instruments and quality control.

2.2.3 Quantify Existence

To gain a global view of the IWISC phenomenon is a difficult problem. For perspective, this view would require a global quantification of both the inertial and semi-diurnal internal wave bands. Both of these phenomena are currently the focus of substantial empirical and modeling research. Given a future characterization of the energy transferred to IWISC relative to the energy that simply appears at IWISC frequencies as a result of periodic Doppler shifting, estimates of IWISC global energy could be made based on modeled inertial and semi-diurnal internal waves.

Ample evidence has been found supporting the global nature of IWISC. However, it is an intermittent feature. That fact, coupled with the sparse coverage of the major ocean regions by long term current meter deployments, means that little can be determined conclusively about the global impact of IWISC. More high spatial resolution data is necessary to answer the question of global impact.

2.3 Analysis of IWISC Evidence

The initial evidence of IWISC consisted of cyclonic rotary PSD energy peaks in a frequency band bracketing the difference frequency, $M_2 - f$. Records with this indication can be examined in more detail and with other standard techniques. This section presents specific further examinations of records where IWISC is evident. The approach is one of identifying a question or characteristic and then analyzing subsets of the available data that contain IWISC signatures in order to answer the question or define the characteristic.

2.3.1 Difference Frequency Peak ($M_2 - f$)

The rotary PSD peak at the difference frequency was the first indication of IWISC and became the criterion for further analysis of an existing current meter record. A power spectral peak, nominally at frequency $M2 - f$, has been found in the spectra of cyclonic rotating currents in the northern and southern hemispheres (e.g., Figure 1). For these locations in latitudes poleward of the critical latitude, the indicated peak can not represent a free internal gravity wave. They can be forced motions that are evanescent away from their generation location, while adjusting and decaying in place.

It is possible that sub-inertial PSD peaks in oceanic currents might occur as a response to narrow band atmospheric forcing (e.g., Easterly Waves in the tropical Pacific). One such possibility is atmospherically generated motion. However, in Chave et. al. [10] an analysis of wind stress curl over the North Pacific during the BEMPEX/RTE87 deployment period found no narrow band signals near the frequency of IWISC.

For the bulk identification of records that show indications of IWISC, the evidentiary criterion of a difference peak in rotary PSD at the IWISC frequency was utilized. This is not a criterion of absolute exclusion, but one of practical investigation. Many records are in geographical locations with significant sub-inertial mesoscale energy that can easily exceed the expected peak values of any IWISC activity.

There are many other factors which can result in the exclusion of a historical record for the purposes of bulk IWISC characterization, yet do not represent absolute exclusion of IWISC from that depth or location. Intermittency of inertial events is a contributing factor. Many records may not be of sufficient length to capture a particular locations maximum inertial activity. By this we mean the seasonal increase in wind energy. Furthermore, many historic records have sparse depth coverage. If, for example, the process depends heavily upon semi-diurnal vertical motion, an instrument near a null in vertical velocity may not have any IWISC rotary PSD signature.

In instances of slowly varying background flow and fairly uniform distribution of density (with a tight T/S relation) above and below a current meter instrument, it is common to consider observed temperature spectra as a proxy for vertical displacement spectra under the assumption that temperature variations are solely the result of vertical advection of the background temperature field. In figure 2.4 the temperature PSD is shown for the TW mooring of RTE87 at 1075 m depth. Note the multi-decadal drop in signal just below the inertial frequency. This is a clear indication of low mesoscale current activity with respect to the internal wave field. There are enhanced signals at the interaction frequencies, though they are only nominally significant.

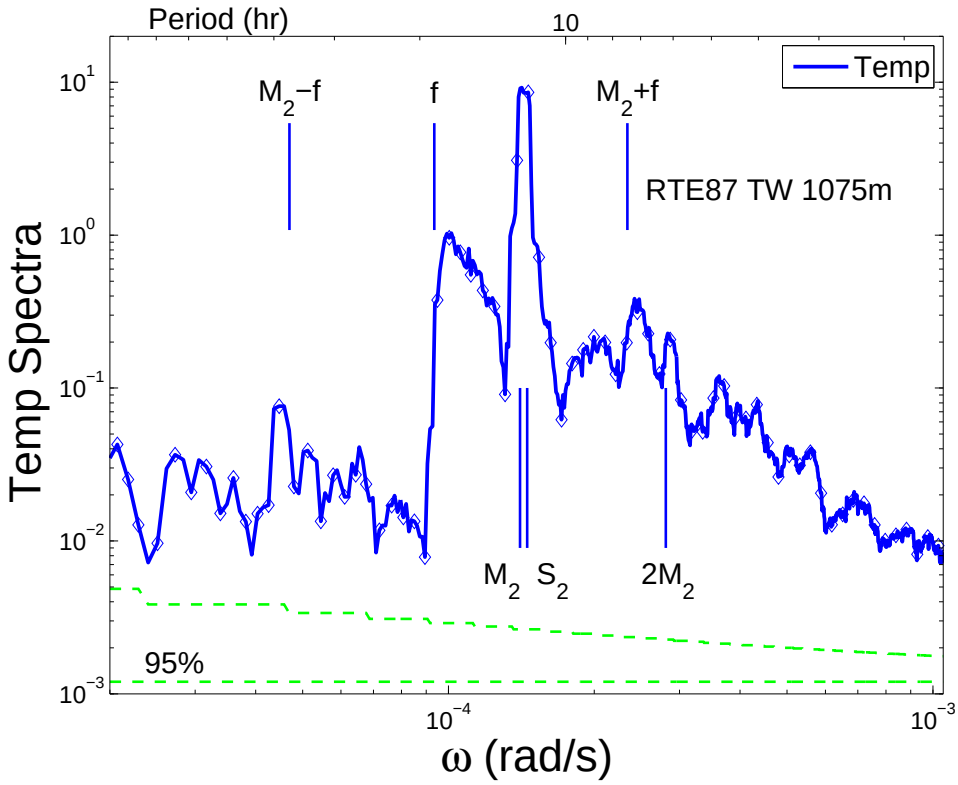

Figure 2.4. Temperature PSD ($(degC^2)(rad/s)$) for the instrument at 1075m on the TW RTE87 mooring, first deployment. The record length is 200 days long. 95% confidence intervals for each independent PSD estimate are indicated by the dashed green lines at the bottom; the diamond symbols indicate the frequency intervals between independent PSD estimates.

If the situation at TW was one of pure vertical advection, and the conditions were such that temperature could be considered an analogue to vertical displacement, there should be no significant signal at the interaction frequencies. This would be the result because the vertical periodic Doppler shifting of a primarily horizontal inertial oscillation that has no vertical strain variations would not produce Doppler shifted temperature signals. A simple explanation like this is, however, far removed from the complexity of the observed currents.

2.3.2 Geographical Extent

IWISC are not confined to a particular location, topographic environment or oceanographic experiment. The initial observations that indicated some type of process involving an inertial and semi-diurnal tide interaction were from a region in the North Pacific with certain conditions conducive to identify-

ing this phenomena, notably a relatively low energy sub-inertial mesoscale eddy band. Once some of the characteristics of the difference frequency ($M_2 - f$) phenomenon were identified, a search of other regions was initiated.

As additional records revealed the same characteristic peak, specific differences became apparent in the analysis. Pertaining to the geographical extent, it became evident that three latitudinal bands were appropriate to search for the difference frequency interaction ($M_2 - f$).

- **Sub-inertial** (Latitude $\approx 33°$ to $55°$) The difference frequency occurs in the sub-inertial mesoscale eddy gap, facilitating detection of a PSD peak. Poleward of $\approx 55°$ the IWISC period is greater than 3.2 days.
  - The PSD of horizontal currents is generally red, so that at higher latitudes it is more likely that mesoscale eddy energy will dominate at the IWISC frequency.
  - Furthermore, as the IWSIC period lengthens, it is unlikely that an interaction will occur because the period begins to exceed the duration of inertial current events and the spring-neap cycle.
- **Near Critical** (Latitude $\approx 25°$ to $33°$) The difference frequency is now close to the inertial frequency.
  - Distinguishing IWISC from the multiplicity of other processes (e.g., diurnal internal tides, inertial waves, Parametric Sub-harmonic instability) that can occur in this latitude band becomes nearly impossible with existing low-spatial-resolution datasets.
- **Sub-tropic** (Latitude $\approx 10°$ to $25°$) The difference frequency is always within the free internal wave band.
  - IWISC PSD peaks are more difficult to clearly identify due to internal wave activity.
  - IWISC is still identifiable by its occurrence in the cyclonic PSD, which then produces a deviation from the expected internal wave consistency relations.

The latitude limits are all approximate as they depend upon other factors as well. For instance, in regions with relatively "quiet" mesoscale energy, the difference frequency may be observed at higher latitudes. In the near critical range, longer records will facilitate the separation of frequency peaks, and the difference frequency could be more readily observed. For short records, it is unlikely that energies from the inertial, diurnal, and other processes can be distinguished unambiguously.

In terms of historical data mining for the signature of the IWISC phenomenon, the sub-tropics present other difficulties. There are few long term mooring records suitable in this latitude range. Even with this limitation, provocative indications of the IWISC phenomena have been found.

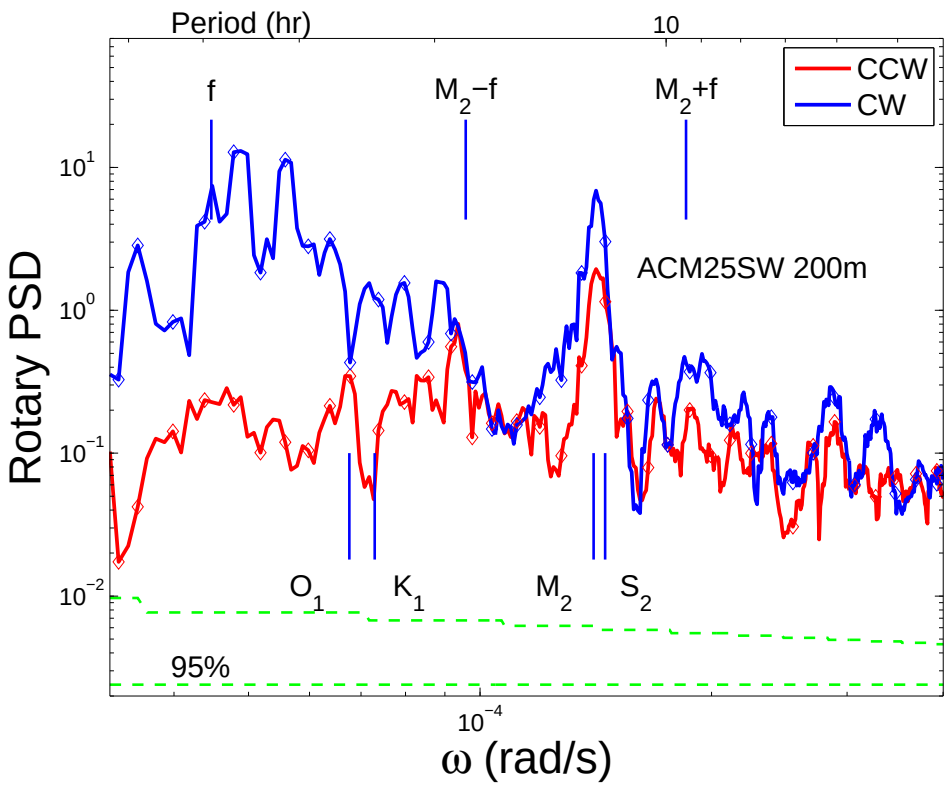

Figure 2.5. Rotary PSD ($(m^2/s^2)(rad/s)$) of current meter velocity recorded at 200m depth for the SW mooring of ACM25. This mooring was located at 18° N, 33° W. The record length is 134 days long. 95% confidence intervals for each independent PSD estimate are indicated by the dashed green lines at the bottom; the diamond symbols indicate the frequency intervals between independent PSD estimates.

Figure 2.5 depicts the rotary PSD from a moored current meter at 200 m depth from the WOCE ACM25 experiment. The latitude is 18° N in the Atlantic. There is a significant peak at the IWISC frequency in the cyclonic (counter-clockwise - CCW) spectrum. This CCW energy meets or exceeds the corresponding energy in the clockwise rotary velocity component thus violating free internal wave consistency. The counter-clockwise IWISC peak exceeds all other counter-clockwise signals except the semi-diurnal tides. Evidence such as this motivates future analysis of sub-tropical data or the acquisition of new data in this latitude range.

There is a unique situation not yet investigated with respect to IWISC and latitude. Two latitudes exist where the IWISC frequency coincides with the principal diurnal tides.

- At a latitude of 27.99° the IWISC frequency is the same as the K_1 diurnal tide. At this latitude the K_1 constituent is in the internal wave band, but just a few degrees south of its turning latitude of 30.41°.
- For the O_1 diurnal constituent, the coincident latitude with IWISC is 30.41°. This is poleward of 27.99°, the turning latitude for the O_1 diurnal constituent.

There are numerous intriguing possibilities for energy exchange at these latitudes between various high energy internal wave interactants, even given just the well-studied non-linear triad interactions like PSI. However, plausible scenarios are predominantly speculative due to the lack of detailed observations. To investigate these unique situations, high-resolution data in multiple spatial dimensions is probably necessary.

The existence of IWISC evidence has been established for multiple basins and in each of the latitude ranges described, excluding the very near critical latitude. However, identification of IWISC based on location remains highly variable. This is expected for any process that depends upon sources which are variable in space and time.

2.3.3 Energy Correlation and Comparison

Is there a relationship between IWISC energy and the energy at the M2+f frequency? The spectra in figure 2.2 suggest that the two interaction frequencies have similar energies, at least when averaged over long time periods. To determine a possible link between the two bands the data from the records in figure 2.2 has been analysed in this way:

- Each data set has been processed identically.
- Data has been divided by 10% cosine taper windows with length of 22 days.
- Windows overlap by one third.
- Band-passed rotary PSD is recorded for each window for both interaction frequencies.
- Rotary PSD from the two interaction frequency bands is compared for each segment.

This process represents a comparison of energy between the interaction bands at coincident times for many independant time periods. The scatter of IWISC vs. $M_2 + f$ is shown in figure 2.6 with separate symbols indicating which mooring the data represents. There is an additional separation between relatively high energy semi-diurnal internal tide segments in red, and lower energy segments in green.

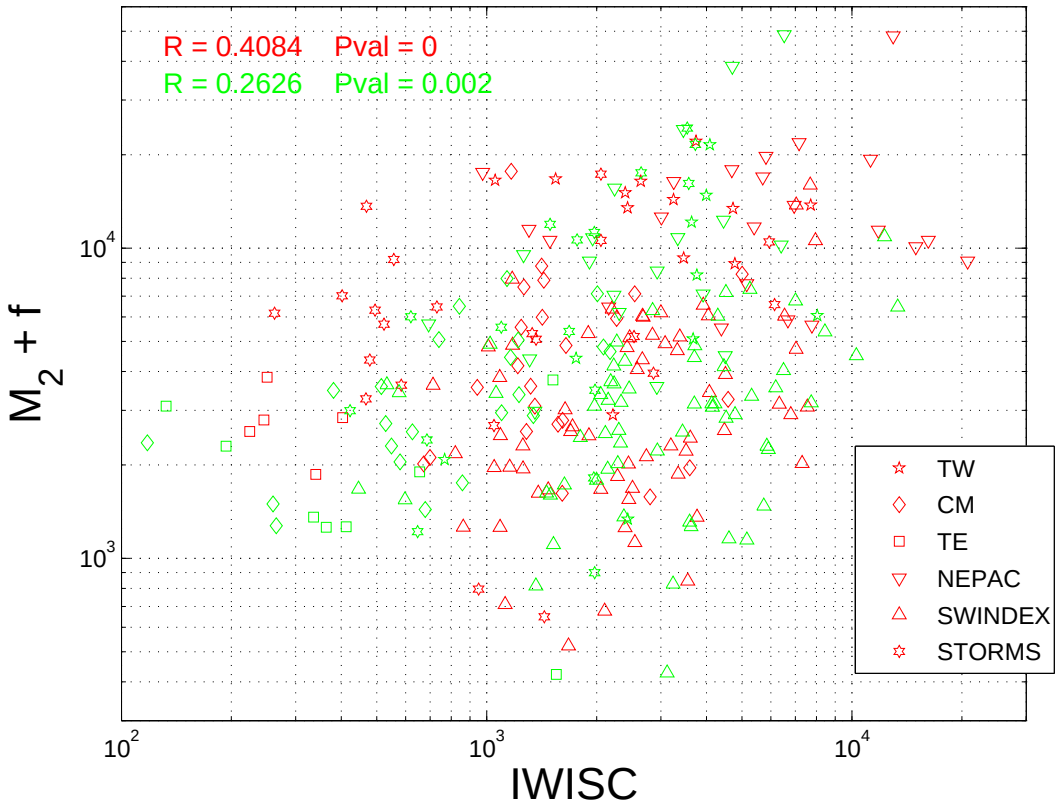

Figure 2.6. Scatter plot of energy in the anti-cyclonic rotary PSD ($(m^2/s^2)(rad s)$) for the frequency sum band (M2 + f) vs. the energy in the cyclonic IWISC band (M2 - f) for multiple 22 day segments within the records shown in Figure 2.2. Red symbols are for the 50% of records with highest semi-diurnal tidal energy. P values less than 0.05 indicate significance.

There is a statistically significant positive correlation between IWISC and $M_2 + f$ for both the values associated with higher semi-diurnal energy (red) and those with lower (teal). No single data set stands out as having a separate distinct correspondence between the two interaction energy bands. In other terms, the individual geographical regions are not visually apparent as having higher (more oval distribution) or weaker (circular distribution) relationships between the energy at the frequencies of interaction.

There does not appear to be a strong dependence of the corresponding energies upon the intensity of the semi-diurnal internal tide. The observations associated with the higher energy semi-diurnal tides have a bit higher correlation (i.e., 0.41 vs. 0.26), but do not indicate a strong dependence on the strength of the semi-diurnal tides.

This bulk correspondence motivates looking at specific time periods where there is a distinct lack of correspondence and investigating possible reasons. There is one record that has two periods of time in which the correspondence is low. In the velocity record for the TW mooring at a depth of 1075 meters, one time period exists where IWISC is elevated with respect to the sum frequency, and another time period where there is a clear sum peak with little IWISC energy.

To visualize the interaction frequency energies and their relationships to inertial and semi-diurnal tide energies, time series of rotary PSD are shown in Figure 2.7. The figure is constructed in the following way:

- Compute rotary PSD from 14-day-long pieces of horizontal currents and temperature centered at noon GMT each day.
- A double tapered Hanning window is applied to each 14 day data piece.
- Narrow frequency bands of PSD, centered around appropriate frequencies (e.g., M2-f, M2, f, etc.), are plotted vs time in separate frames.
- Plots are smoothed with 2x2 box interpolation in frequency-time.

The ordinates display the frequency bands. The IWISC ($M_2 - f$) time series are from the counter-clockwise (cyclonic) rotary PSD. The $M_2 + f$, f and M_2 time series show the clockwise (anti-cyclonic) rotary PSD. Peak colors are not fixed between frames in this representation, and so indicate only relative strengths of the energies within each separate frequency band.

There are two specific periods in Figure 2.7 that exhibit clear cases of non-correspondence of the energies at the interaction frequencies. Centered at 85 days in the record is a situation where there is low inertial energy and a pronounced IWISC. This is broken out into a 22 day rotary PSD in Figure 2.8 (upper frame). Complementary to this is a 22 day selection centered at day 135 (PSD spectrum shown in the lower frame of Figure 8). At that time, there is very little IWISC and a significant peak in the sum frequency $M_2 + f$. These two examples highlight a question about how an advective mechanism would be able to select intermittently between energy production at one frequency over another.

To further identify the difference between the two time periods, the ratio of counterclockwise to clockwise rotary PSD is shown in Figure 2.9. One possible signature (see chapter 3 for discussion)

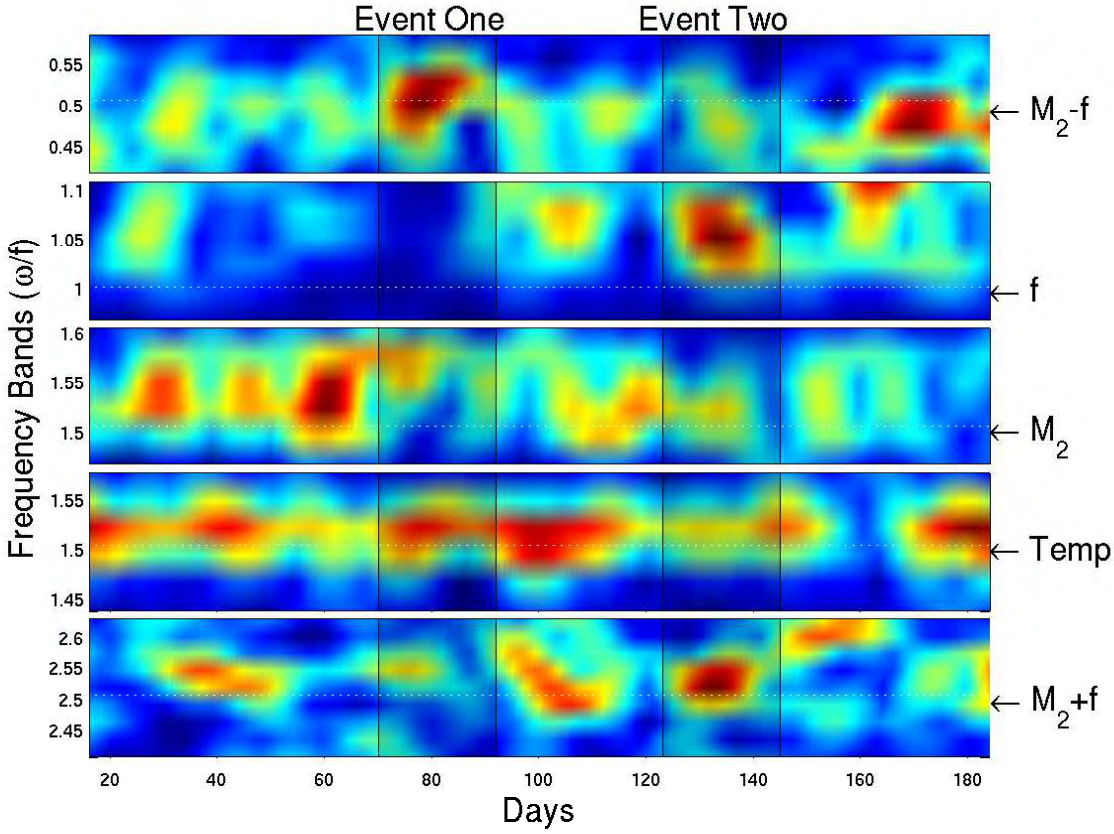

Figure 2.7. Time series of rotary PSD for the TW mooring of BEMPEX/RTE87. The depth of the instrument is 1075m. The temperature spectra are indicated for the M_2 band. The frame labeled $M_2 - f$ shows the cyclonic (CCW) rotary PSD. The frames labeled $M_2 + f$, f and M_2 show the anti-cyclonic (CW) rotary PSD. The color scales are different for each frame, and so indicate only relative strengths of the energies within each separate frequency band. See the text for a discussion of the events and for further details of how the time series of PSD were calculated. Number of independent points per band (from the top): 4, 3, 3, 3, and 5.

of advection as the mechanism responsible for the Eulerian rotary PSD peaks at the $M_2 \pm f$ interaction frequencies is the disruption of the theoretical free internal wave consistency relationship between anti-cyclonic and cyclonic energies. In the second event, when there is a higher peak in the summation frequency, a small deviation from linear internal wave consistency can be seen in Figure 2.9. The deviation is marginally statistically significant, yet qualitatively appears to match the consistency breaking seen in the simple advection model in the next chapter. At the IWISC frequency there is no freely propagating internal waves for this latitude, so the internal wave consistency relation is not a relevant

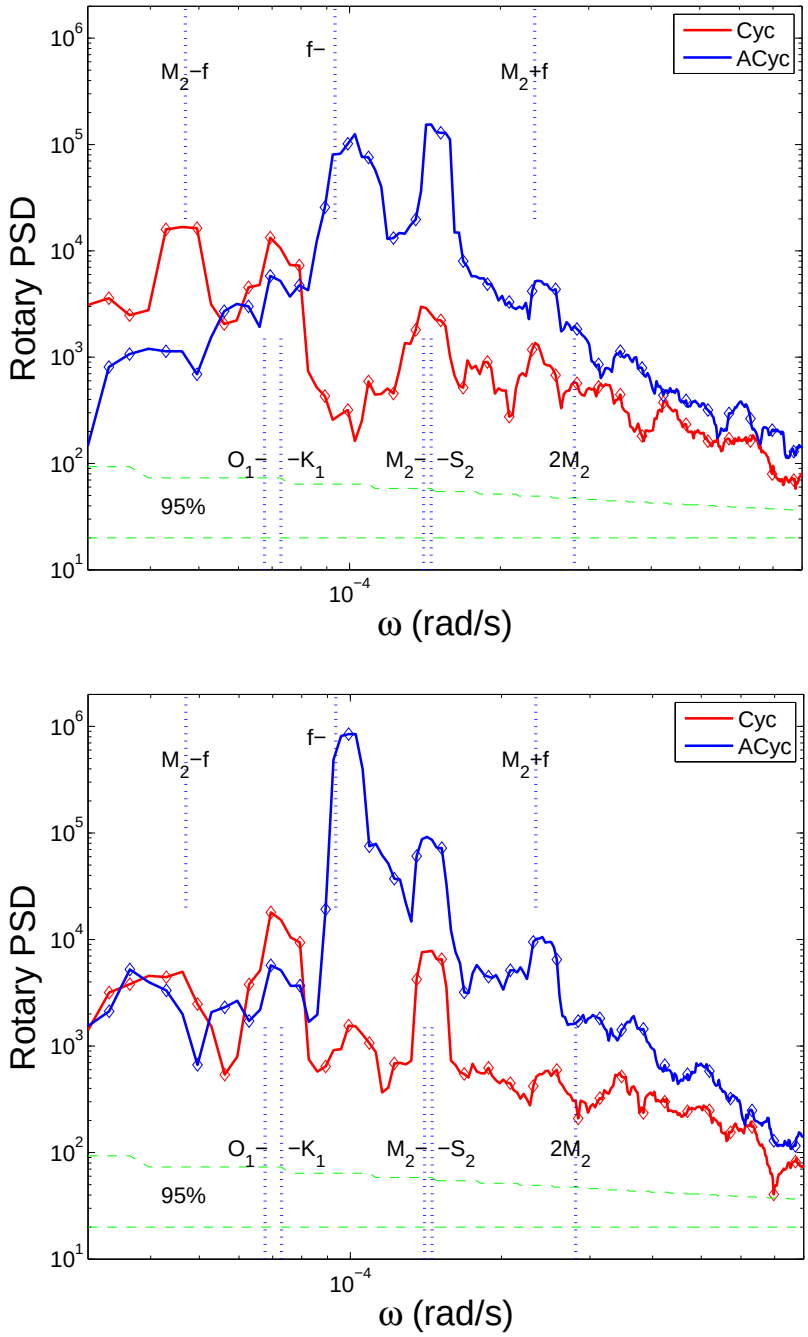

Figure 2.8. Rotary PSD $((m^2/s^2)(rad s))$ of horizontal currents from the RTE87 mooring TW, first deployment, showing two 22 day records centered at 85 days and 135 days. These time segments are indicated in Figure 2.7 as Event One and Event Two. The 95% confidence intervals for each independent PSD estimate is indicated by the dashed green lines at the bottom; the diamond symbols indicate the frequency intervals between independent PSD estimates. See the text for an explanation.

test for the presence of an advection mechanism. However, between the two events in Figure 2.9 it is clear that the IWISC dominated event (top) has a larger value for the ratio at the IWISC frequency.

If the region is characterized by a near sub-inertial mesoscale with equal distribution of energy between cyclonic and anti-cyclonic horizontal rotary velocities, a ratio indication like the top panel of Figure 2.9, showing the IWISC with a larger cyclonic signal, may be helpful. For the ratio outside of the free internal wave band to be a reliable measure, more information about the flow structures is necessary.

Although neither the IWISC band ratio in the top panel of Figure 2.9 or the $M_2 + f$ band low ratio (in comparison to the theoretical curve) exceed the significance level, there is a significant result in the assymetric observation. As stated previously, a single sinusoid displacement will produce equal deviations at the IWISC and sum frequencies. In chapter 3 a discussion is made about multiple frequency and structure displacements and how they can lead to assymetric indications at the interaction frequencies. The case here, with Event One and Event Two, strongly suggests at a minimum multiple displacements if not full non-linearity.

2.3.4 Variability of Interactant Energy

In each record containing IWISC evidence, a high variability of peak energy has been seen both in depth on moorings with multiple instruments, and in time. To establish this variability quantitatively a comparison has been made between IWISC energy and the energies at the inertial and semi-diurnal forcing frequencies. The processing is the same as the previous section, with the further step taking the log of the amplitudes and subtracting the mean log amplitude. In figure 2.10 there is very weak correlation between cyclonic IWISC and anti-cyclonic inertial rotary PSD energies, although it is significant. This is an interesting result, as it was expected that there would be a stronger relationship here. This assumption was based on some observations in time series of the coincidence of high IWISC amplitudes and strong inertial events. There is little difference in the correlation value between the red and green data points. This would indicate that the IWISC dependence on inertial amplitude is not impacted by the relative strength of the semi-diurnal internal tide.

A possible explanation for the lack of a stronger relationship between IWISC and inertial wave energy levels may be that other characteristics of the inertial (and semi-diurnal) internal waves besides amplitude are important for determining the magnitude of the interaction. For instance, the vertical structure of the inertial waves or the semi-diurnal vertical velocity could be an important factor determining the strength of the energy exchange, yet it is clear from some of the data we have examined that the vertical structures of the inertial and internal tide waves can vary strongly in time. The historical

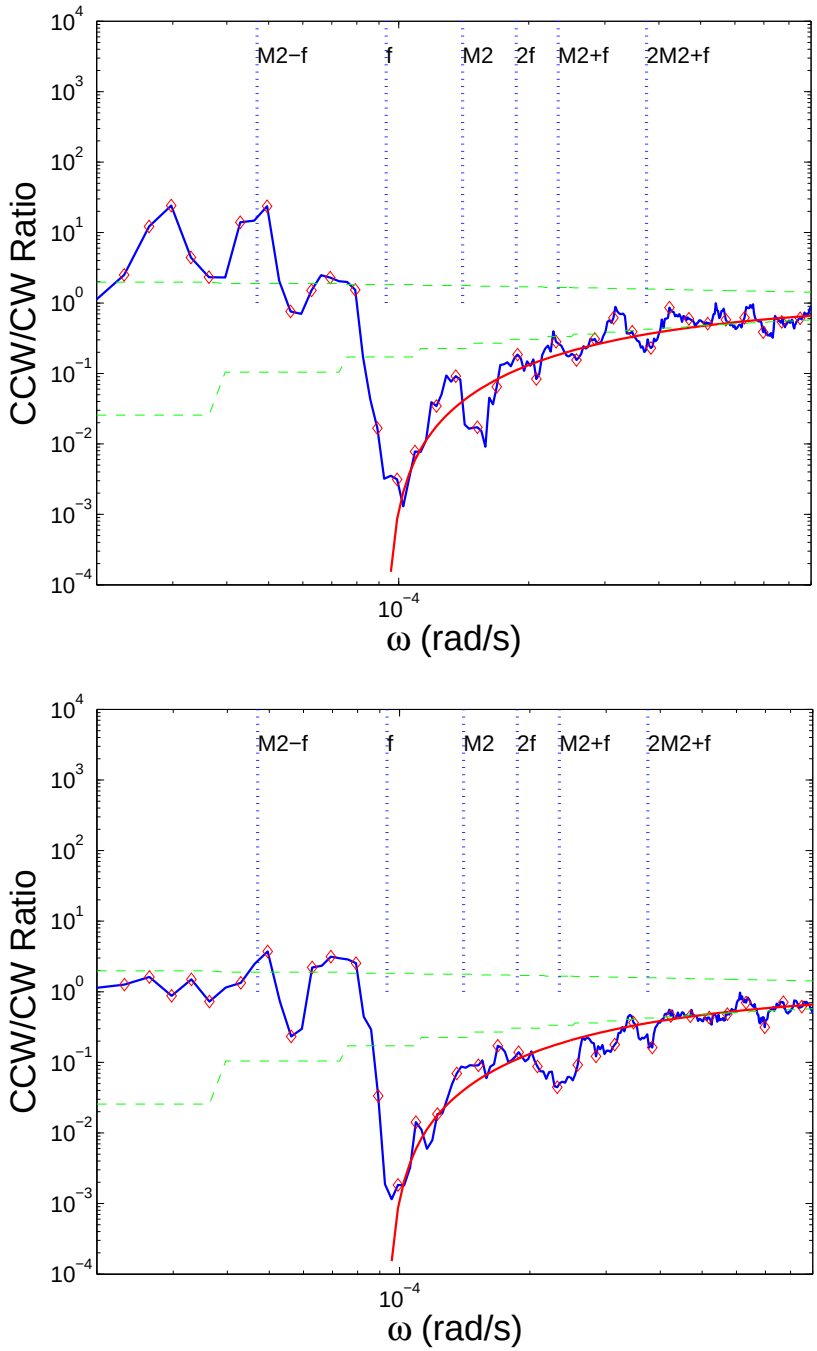

Figure 2.9. Ratio of cyclonic/anti-cyclonic rotary PSD for the RTE87 mooring TW for two 22 day records centered at 85 days and 135 days. Event One is on the top (see Figure 2.7) and Event two on the bottom. Though not exceeding the confidence interval in its deviation from the theoretical curve $((\omega - f)/(\omega + f))$, the sum $(M_2 + f)$ frequency band in the bottom panel is noticeable. Dashed green lines indicate 95% confidence interval.

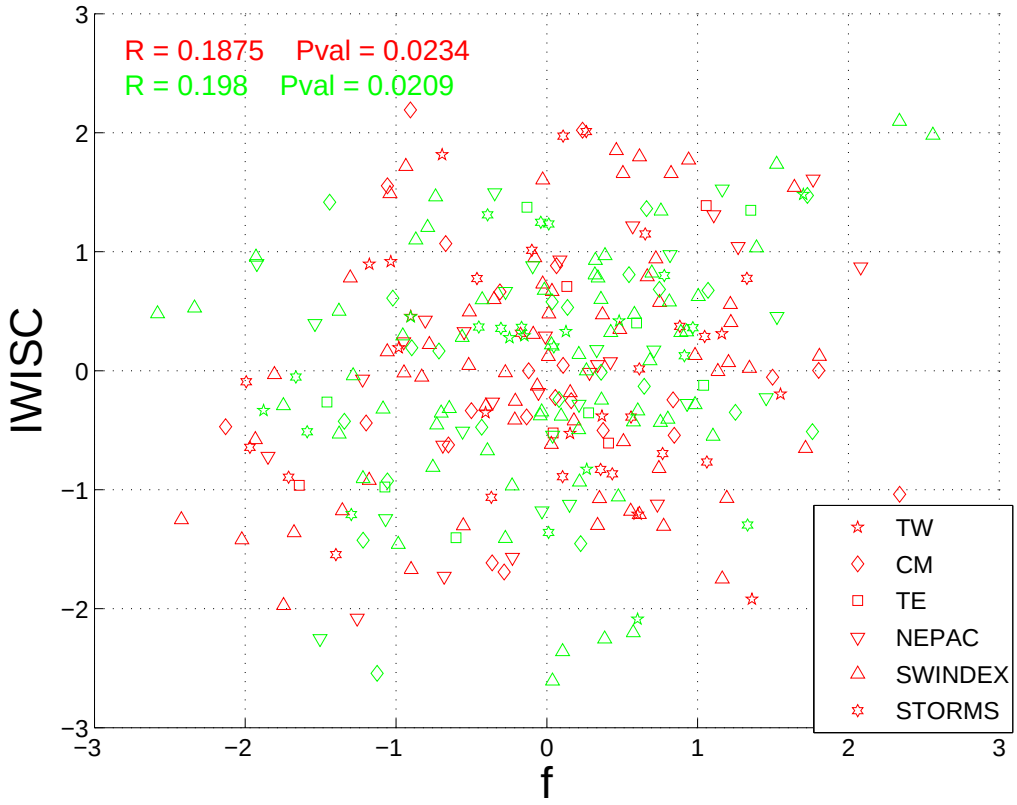

Figure 2.10. Scatter plot of rotary power spectral peak amplitudes at the cyclonic IWISC and anti-cyclonic inertial frequencies. Red symbols are for the 50% of records with highest semi-diurnal mean log amplitude PSD. Both red and green sets have P values less than 0.05 indicating a significant correlation, though very weak.

data used here to illuminate IWISCs bulk characteristics do not provide enough detailed information about vertical structure, so further analysis will require new data.

One plausible scenario that fits the results indicated by figure 2.10 is that a few significant IWISC energy time periods are closely associated with high inertial energy, but that the bulk remainder of time periods has a predominantly random association. This explanation fits the observed time series of inertial energy in most of these records in that a few events of short duration (< 20 days) dominate the total inertial energy of the whole record.

These events, corresponding to elevated inertial energy at unique locations, have inherent variability when compared globally. Some regions and latitudes have higher peak storm activity. Additionally,

different depths on the same mooring represent inertial energy that has propagated from separate source regions.

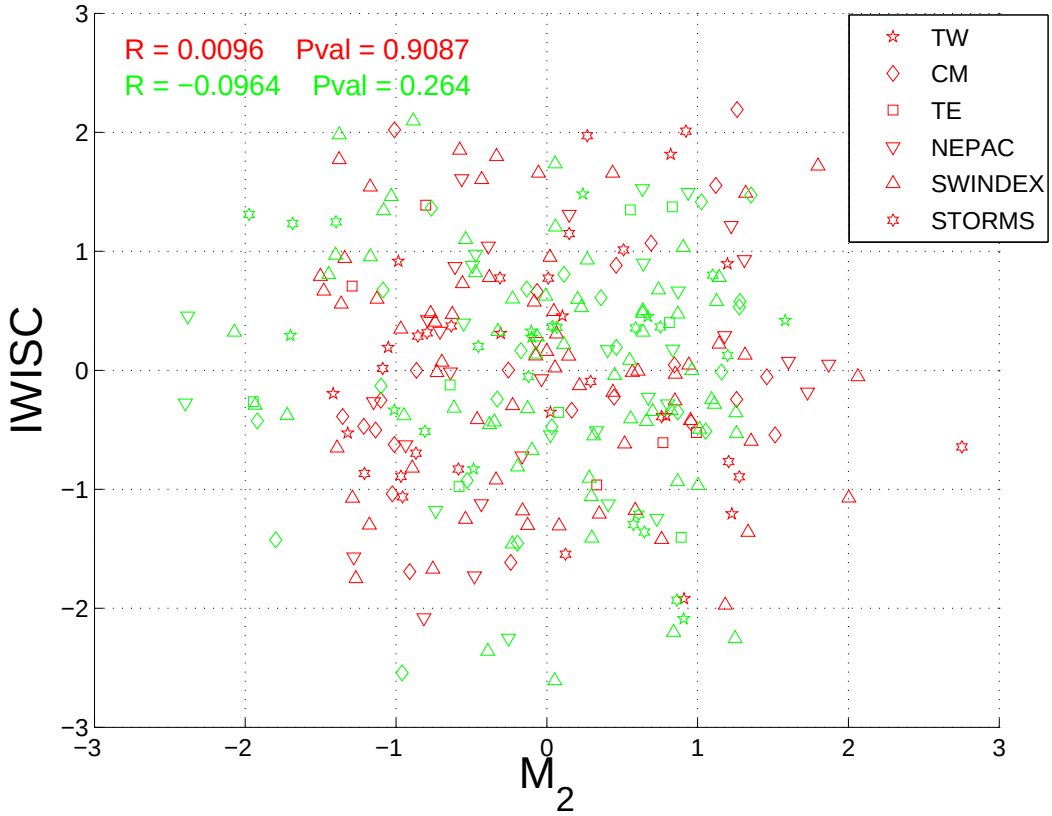

Figure 2.11. Scatter plot of IWISC anti-cyclonic rotary PSD versus total semi-diurnal horizontal current PSD (here designated as just M2). Red symbols are for the 50% of records with highest semi-diurnal mean log amplitude PSD. Both red and green sets have P values greater than 0.05 indicating non-significant correlation.

There is even less of a suggestion of a bulk relationship between IWISC cyclonic energy and the total horizontal energy of the semi-diurnal internal tide (Figure 2.11), than found for IWISC versus inertial wave energy. Furthermore, the correlation P values indicate non-significant results.

There are many possible explanations for this lack of correspondence; a few of the principal ones are as follows:

- If the process depends heavily on semi-diurnal vertical velocity, it will not be seen at nodes of the vertical velocities vertical structure;

- IWISC peak energy could originate from nearby (vertical, horizontal) semi-diurnal forcing not correlated with the specific M_2 energy found at the observation point; and,
- Existence of IWISC could depend upon local semi-diurnal M_2 energy, yet the amplitude is determined by other factors besides amplitude of the semi-diurnal internal tide, e.g., as discussed for the IWISC versus inertial wave energy relationship, the vertical structure (wavenumber) of the semi-diurnal internal tide could be important.

There is one more comparison that was initially expected to yield some weak correspondence, that is, the comparison between the anti-cyclonic rotary PSD energy peak at the sum frequency (M_2+f) and the total horizontal current semi-diurnal internal tide energy. The latitude for each of the observations here is such that the IWISC is sub-inertial and not in the internal wave band, but the sum frequency is. If the sum frequency energy were directly linked to the energy of the semi-diurnal internal tide by a wave-wave exchange mechanism, it could be expected to show up as some bulk characteristic.

As can be seen in Figure 2.12, there is no significant bulk correspondence between the sum frequency and the semi-diurnal tide band. This further reinforces the conclusion that whatever the process is that creates the observed rotary PSD peaks at the sum frequency (and likewise the IWISC frequency), it is not solely a function of observed total semi-diurnal tide velocities. The same explanations can be postulated here as for the IWISC correspondence to M2, with the additional observation that whatever the process is, it does not appear to be a locally harmonic internal wave interaction.

A similar comparison was made between the sum frequency energies and the inertial wave energies, with no significant result. Additional comparisons with individual rotary components of the semi-diurnal tide did not modify the bulk correlation in either the IWISC or sum ($M_2 + f$) cases.

There is a further possibility in relation to the weak, significant correlation between IWISC and the inertial. This relationship would represent increased inertial energy and increased tidal energy in the same sampled data segment contributing to increased IWISC energy. In figure 2.13, a three dimensional scatter plot of the log amplitudes of all three frequencies (IWISC, M_2, and f) is shown. There is no strong tendency for elevated IWISC energy towards the axis location of higher semi-diurnal and inertial energy.

The corresponding linear regression lines are indicated. Colored bars with circle markers indicate the 95% confidence interval at the endpoints of the regression lines. For the red regression line, calculated from the set of all M_2 energies above the mean, there is a weak trend matching the scenario of increased semi-diurnal and inertial yielding higher IWISC energy. For the set of data with

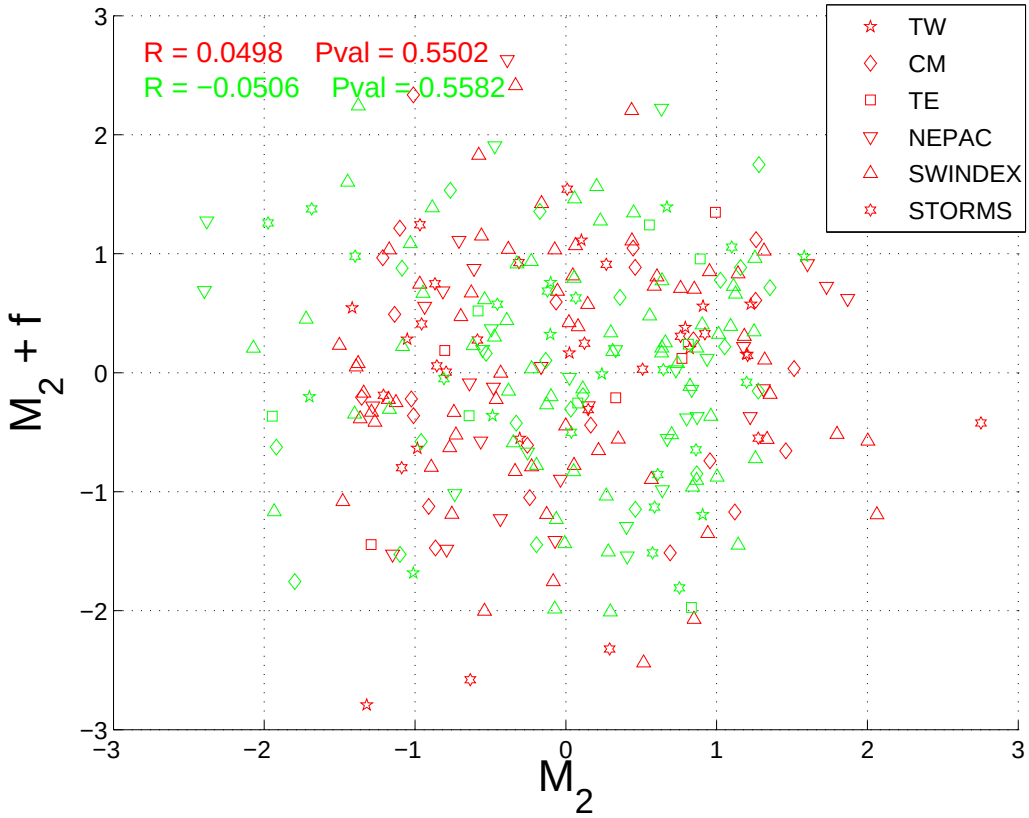

Figure 2.12. Scatter plot of sum (cyclonic M2 + f) PSD and semi-diurnal (total horizontal current) PSD. Red symbols are for the 50% of records with highest semi-diurnal mean log amplitude PSD. Both red and green sets have P values greater than 0.05 indicating non-significant correlation.

weaker semi-diurnal energy, the regression line indicating IWISC dependence on the semi-diurnal has a negative trend.

As was demonstrated in figure 2.11, neither the red or green sets had significant correlation coefficients between the IWISC and semi-diurnal. Though not significant, it is perhaps interesting that the elevated semi-diurnal energy set (red) has a positive contribution between the IWISC and semi-diurnal, as would be expected by a rudimentary conjecture.

2.3.5 Intermittency of IWISC Energy

In all records where elevated energy at the IWISC frequency has been observed, significant intermittency of that energy exists. A particularly good example of this is found in the current meter

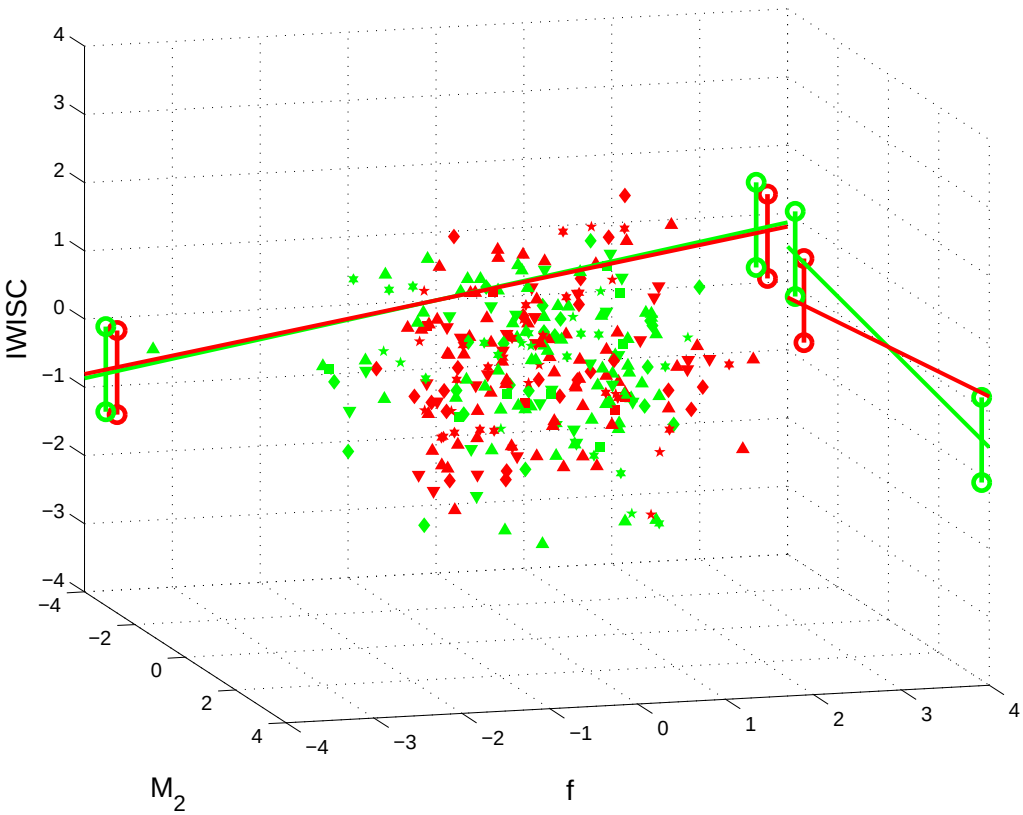

Figure 2.13. Scatter plot of PSD log amplitudes corresponding to the IWISC (cyclonic M_2-f), M_2 (sum of cyclonic and anti cyclonic energy), and inertial frequency bands. Red indicates those amplitudes representing the upper half of data with greater than mean log amplitude PSD at the M_2 frequency band, and green the lower. Regression lines corresponding to the IWISC vs. M_2 and IWISC vs. inertial are indicated for the respective data. Confidence intervals are indicated by vertical lines with circle markers at the end of each regression line.

measurements from the STORMS experiment ([70]). The experiments mooring design provided good depth coverage of horizontal currents over a considerable time period. In figure 2.14 a time series of PSD in the IWISC band is shown for each instrument depth.

During the first hundred days, each depth level has some IWISC activity, with little evidence of vertical association. At 90 to 100 days there is elevated energy at 999m but not at 1999m. From day 100 to day 200, two or three events contribute heavily to the observed IWISC at many depths, some of which appear to have some vertical association, suggesting a vertical extent of the IWISC events

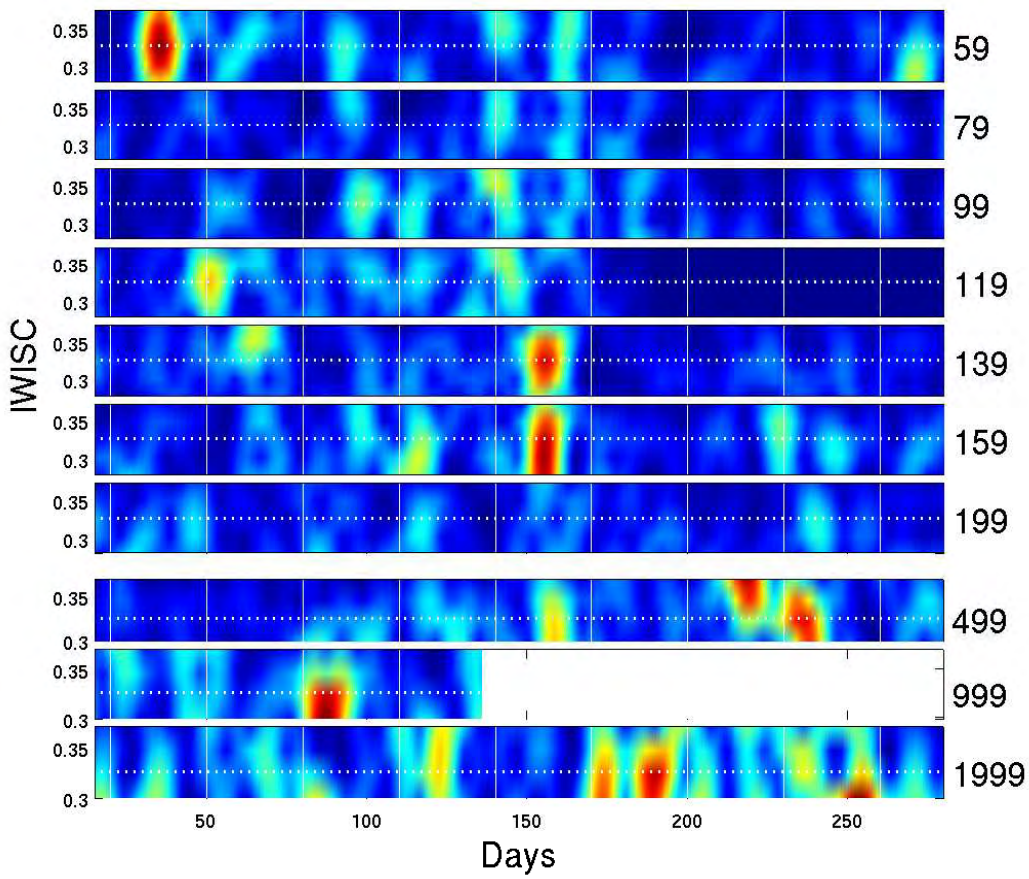

Figure 2.14. IWISC frequency band vertical time series for STORMS mooring located at 47.42° N and 139.29° W. Band energy is from the anti-cyclonic component of rotary velocity PSD $((cm^2/s^2)/(rad/s))$; although IWISC exists outside the free internal wave band, since the assumed energy source for IWISC is believed to be free internal waves the IWISC PSD was normalized according to the expected WKB linear dependence of free internal wave horizontal current PSD on the buoyancy frequency, using WOA mean stratification. Frequency axis is in *rads* normalized by the local inertial with dotted white line indicating calculated IWISC frequency. Vertical white lines show thirty day separation. Days axis begins with deployment on August 21, 1987. See Figure 2.7 and its accompanying description for further details of how the PSD time series were constructed.

on the order of 50 m. The final third of the time period has limited IWISC activity above 499m and intermittent elevated events below. These have no apparent visual vertical association.

For the inertial energy during the STORMS experiment shown in figure 2.15, there are five or six events which dominate the energy in the upper 500m. These events exhibit a vertical extent of order 100 m or more, and are clearly more vertically correlated than the IWISC events. At deeper depths the

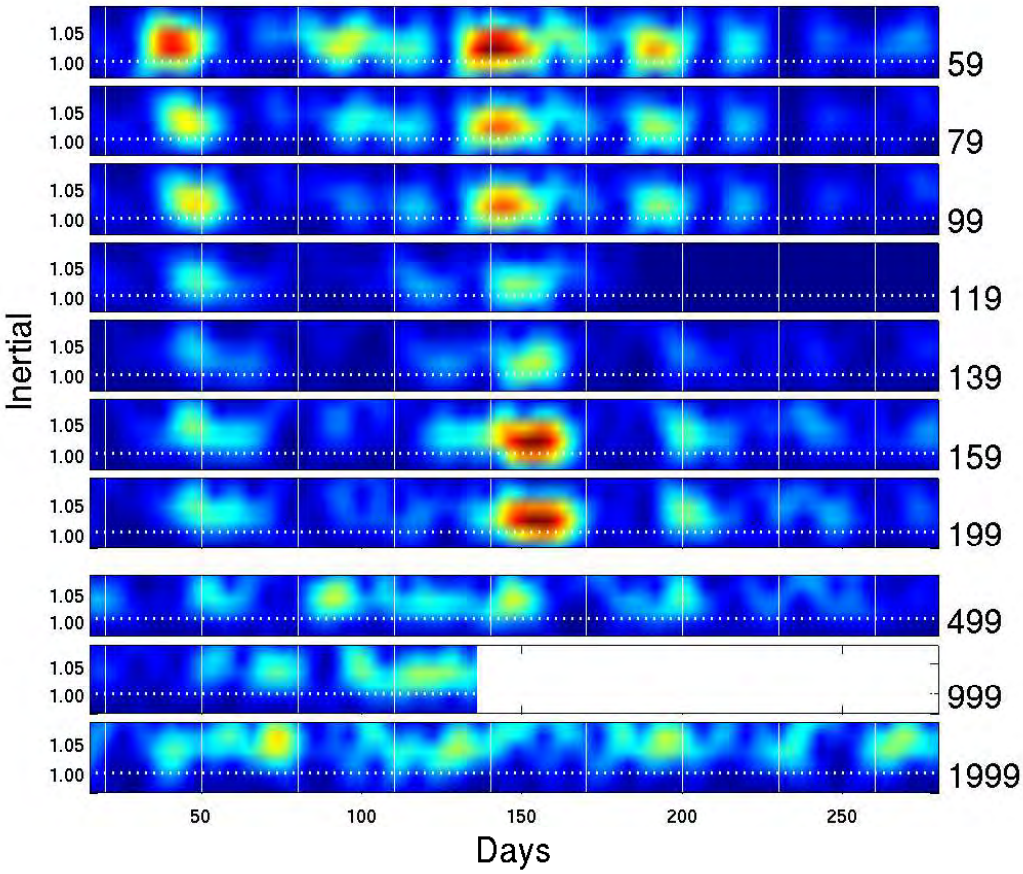

Figure 2.15. Time series of inertial band cyclonic rotary PSD ($(cm^2/s^2)/(rad/s)$) for instruments from the STORMS experiment mooring. Local inertial frequency is indicated by the dotted white line at each depth. See Figure 2.14 caption for specific details.

events become less distinct due to the larger instrument separations. There is a visual blue shift of peak inertial energy with depth, as expected (e.g., Fu [25]).

For the events during the time period of 140 days to 160 days, there is corresponding peak energy in the anti-cyclonic IWISC PSD in the upper 500m (figure 2.14). The time periods coincide, and show some corresponding depth relationship. However, the precise IWISC peaks do not 'line up exactly with inertial energy in this depth presentation, which could be the result of mis-matched temporal dependence of the semi-diurnal and inertial waves, or could be due to a finite growth time for the inertial-tidal interaction, and so forth.

Total semi-diurnal band PSD for each depth is shown in Figure 2.16. Buoyancy frequency scaling of the horizontal current energy for this band does not appear to yield more uniform energy levels

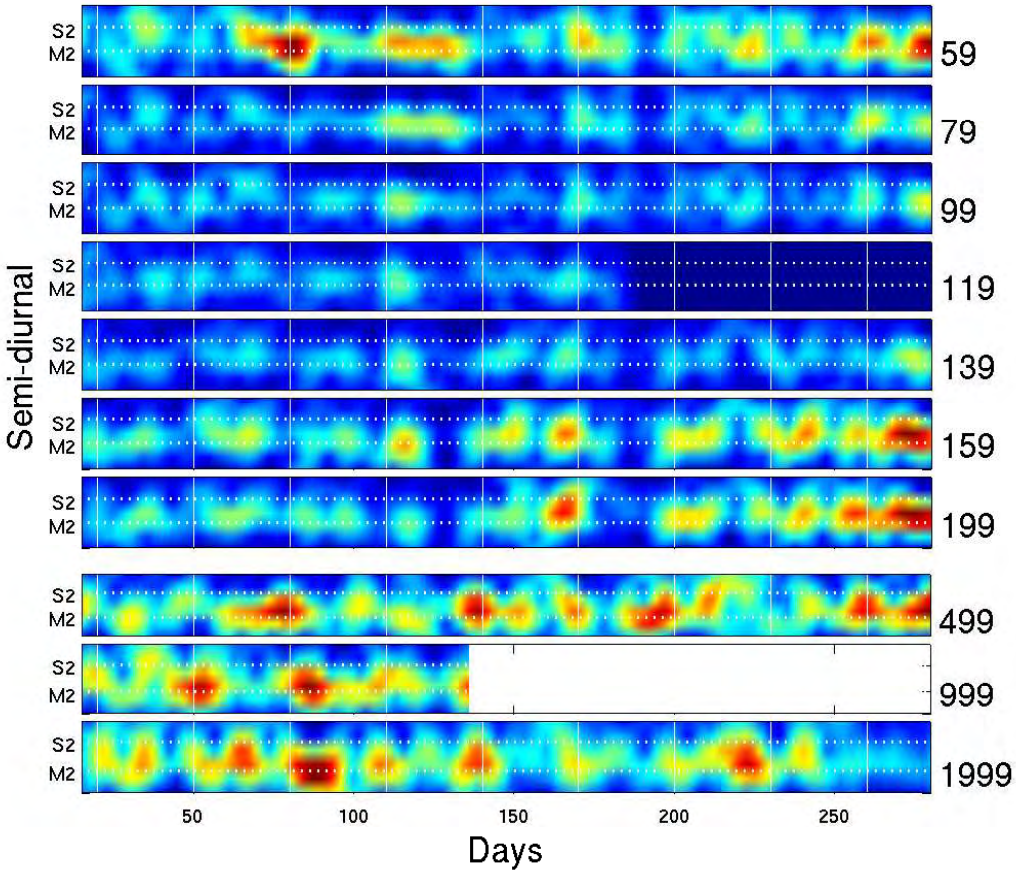

Figure 2.16. Semi-diurnal frequency band PSD $((cm^2/s^s)/(rad/s))$ time series of total horizontal energy for the STORMS mooring. White dotted lines indicate principal semi-diurnal constituents M2 (lower line) and S2. See Figure 2.14 caption for specific details.

between the upper 1000m and below, suggesting that the WKB scaling is not entirely appropriate. There are clear spring/neap cycles at many depths. However, changes in amplitude are apparent with depth for associated cycles.

It is particularly interesting to note that at some depths and time periods, there is a shift between energy predominance within the band between M_2 and S_2. The specific cause(s) of this and the other kinds of variability seen in Figure 2.16 will require effort that goes far beyond the scope of the present work. At the very least, figures such as this provide us with a better understanding of the lack of temporal uniformity of the internal tides, which will be important in devising simulations of interactions between the internal tides and inertial waves.

In relation to IWISC energy, there appear some spring/neap cycles in the semi-diurnal tide temporally located near elevated IWISC energies (for instance, days 150 to 170). However, no specific feature in the IWISC record (figure 2.14) shows a strong spring/neap affinity.

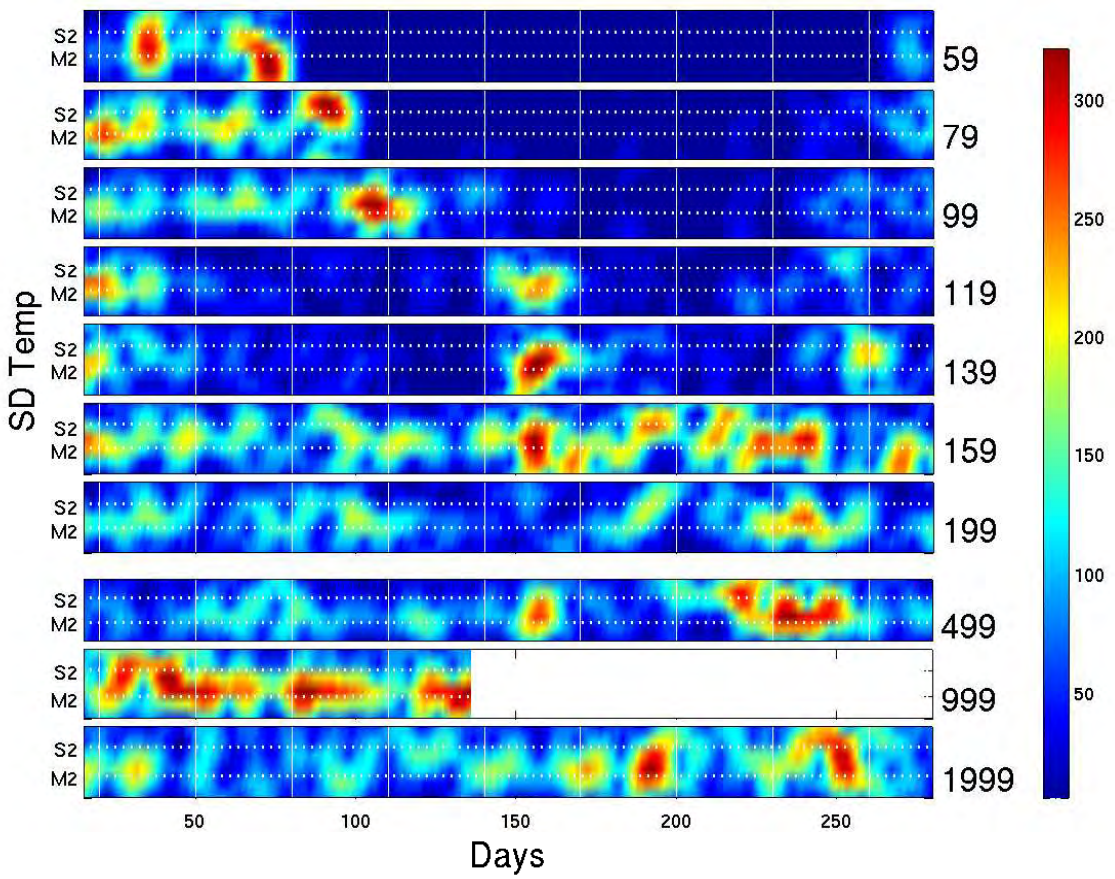

Figure 2.17. Semi-diurnal temperature frequency band PSD ($(degC^2)(rads)$) vertical time series for STORMS mooring. White dotted lines indicate principal semi-diurnal constituents M2 (lower line) and S2. See Figure 2.14 caption for specific details.

Under specific conditions, temperature can have a high correlation with vertical displacement (e.g., van Haren [87]). If it were consistantly the case, temperature could be used as a proxy for displacement, which has been historically dificult to measure accurately. In figure 2.17 the semi-diurnal band temperature signal is presented at each depth from the STORMS mooring. There is a clear deepening seasonal thermocline from day 75 to day 200.

There are some time periods with visually close association of high temperature PSD with high semi-diurnal horizontal current PSD (Figure 2.16). Specifically the first 75 days have relatively good

correspondence. However there are many other depths and time periods where the correspondence is not clear.

Of interest are the two apparent spring/neap cycles during the interval of 140 to 160 days. The first cycle does not show considerable temperature fluctuation in Figure 2.17 except at the 159m instrument. The second cycle has significant temperature signals at depths 119m, 139m, 159m, and 499m. The IWISC PSD peaks in Figure 2.14 during this time match very closely the 139m, 159m, and 499m temperature peaks.

At the same time, during the second spring/neap cycle (roughly 150 to 160 days) of the time period, there is highly elevated inertial PSD (Figure 2.15). This is not the case for the preceding cycle (roughly 140 to 150 days). This presents the odd situation that observed energetic temperature fluctuations match well with a confluence of IWISC, inertial, and semi-diurnal energy, while just two weeks before there is no IWISC, no inertial, and only weak temperature variability.

Clearly, making an assumption about the underlying process based on this data is problematic due to the very intermittent nature of both the IWISC and inertial energies. Such intermittency is a ubiquitous characteristic of the historical records weve examined. Also, there was a unexpected high variability in temperature, not having much association with semi-diurnal observed horizontal energy. Yet, even with this lack of overall visual correspondence in energy time series between the semi-diurnal temperature and horizontal velocities, there is a very positive relationship during the unique event from day 150 to day 160.

2.3.6 Horizontal Structures

A major need exists in the description of oceanic internal waves for data that reveals both the mean values and temporal variability of the horizontal wavenumbers of the inertial waves and semi-diurnal tide. There are however, some observations that provide pieces of information about horizontal scales and structures for these IWISC progenitors, as well as for IWISC itself.

The first indication of the horizontal extent of IWISC came from the cotemporal current records during BEMPEX/RET87, all of which were at approximately the same latitude. There is a distinct decrease in specific IWISC event energy from mooring TW to CM (about 250km apart), and again from CM to TE (about 500 km apart) (see Figure 2.3). This observation engendered speculation about regional variation in the strength of the semi-diurnal tide, especially in light of modern internal tide models (e.g., see Simmons et al. [80] for a simulation of internal tide propagation from the Hawaiian and Aleutian Islands to the BEMPEX/RTE87 area).

The mooring separations in BEMPEX/RTE87, while revealing a significant spatial variation of IWISC energy, are too large to delineate the detailed spatial variability of inertial wave energy or even internal tides that may have a much finer scale, and as indicated by current internal tide models (for instance, Carter et al. [8]). Therefore, a search was instituted to find records that could provide more detail about the horizontal scales of open ocean inertial waves and internal tides. One experiment that provides such records is the WOCE Eastern Boundary Current (EBC) experiment.

EBC Spectra

The EBC experiment had three separate arrays deployed off the Northern California coast, one of which was in deep water. Details of the experiment and instrumentation can be found in Chereskin [11]. The arrangement of the five moorings in the array was in a cross with the points of the compass and a central mooring. Four depth levels were sampled with each mooring. The record is unfortunately incomplete due to instrument failure, but some spatial characteristics can be interpreted. Each mooring was roughly ten kilometers from the next in the zonal and meridional directions.

From the central mooring rotary PSD (Figure 2.18) at 598m there is a clear elevation in the anti-cyclonic rotary velocity at the IWISC frequency. Also of note are the semi-diurnal tidal harmonics, often seen in other records near a continental slope (for instance see van Haren [88]). This record is at a latitude (37°) where the frequency separation between the IWISC, diurnal, and inertial structures is relatively narrow. But, for the EBC time period, there is little contamination of nearby sub-inertial bands by the inertial.

EBC Vertical Time Series

While describing the horizontal structures of IWISC, inertial and tidal currents from EBC (next section), an inevitable question arises concerning what we know about the vertical variation of these currents. This sub-section provides an answer to that question via a brief analysis of the data from the offshore central (OC) mooring of EBC, even though the EBC instruments do not provide as much vertical resolution as the Ocean Storms mooring discussed previously, or the Deep Basin experiment mooring discussed later in this chapter.

For the presentation of the rotary PSD time series in the next several figures, there has not been a normalization with the buoyancy frequency at any depth. Normalization with the buoyancy frequency calculated using the WOA data for this location results in very reduced PSD at the shallower depths. So, to simplify the comparison of temporal changes in energy between depths we have not scaled the

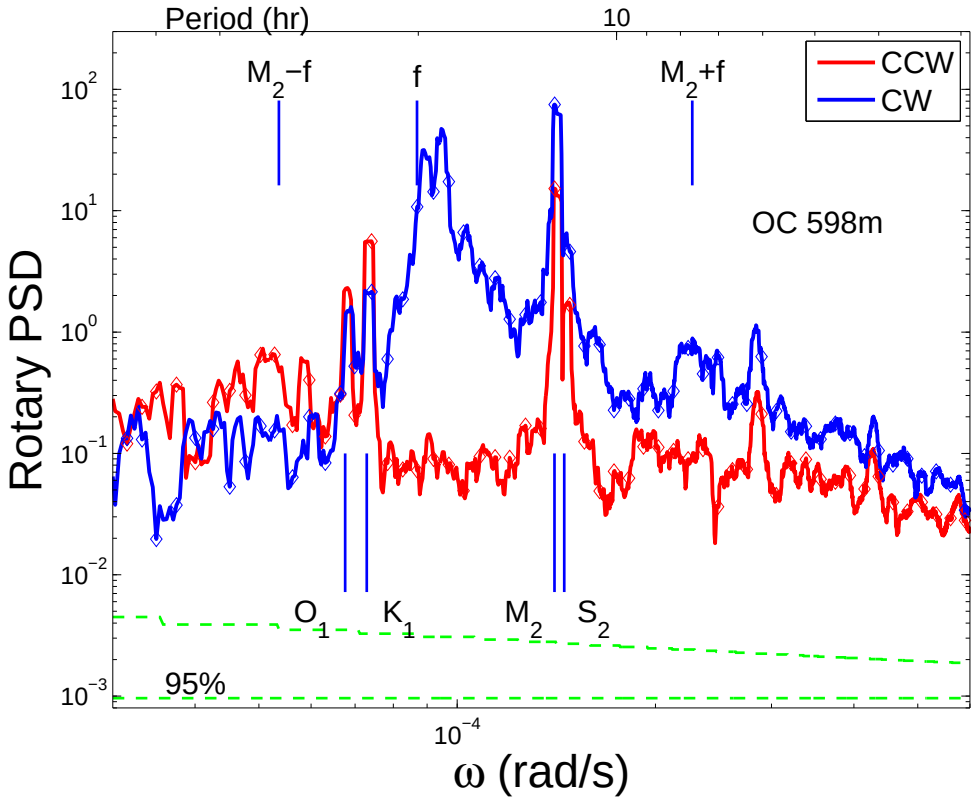

Figure 2.18. Rotary PSD $((m^2/s^2)/(rad/s))$ for the deep water central mooring of EBC with a depth of 598m and a latitude of 37.11°. Although the IWISC frequency is near the frequencies of the diurnal and inertial bands, there is distinct separation of the energy in those bands from the IWISC energy, which is elevated. There is energy at the sum $(M_2 + f)$ frequency as well. The record length is 740 days long. 95% confidence intervals for each independent PSD estimate are indicated by the dashed green lines at the bottom; the diamond symbols indicate the frequency intervals between independent PSD estimates.

PSDs. The characteristics of the vertical variations in the PSD seen at OC are similar to the other four moorings in the offshore EBC array.

A plot of total semi-diurnal current PSD versus time is shown in Figure 2.19. The temporal variability of peak energy is typical of that seen at other locations (e.g., Ocean Storms, Figure 2.16). But, note the quite variable vertical structure, which appears to be substantially more pronounced than was found in the shallower records from the Ocean Storms experiment (Figure 2.16). Also noteworthy is the general long term variability in peak energies of spring/neap cycles; that is, at each depth the strongest patterns of spring/neap cycles rarely correspond to nearby depths. This location does not

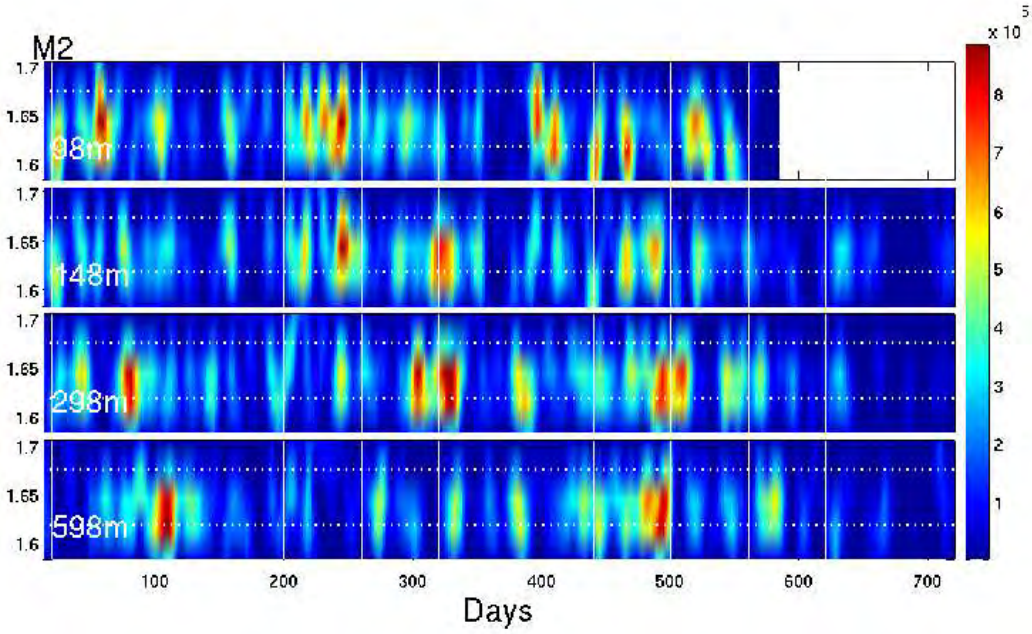

Figure 2.19. Semi-diurnal total current PSD (sum of cyclonic and anti-cyclonic) time series for the deep water central mooring of EBC. Dotted white lines indicate M_2 and S_2 frequencies. There are four independent points in each band. Days axis begins with deployment on August 9, 1992. White vertical lines are separated by 60 days. See Figure 2.7 and its accompanying description for further details of how the PSD time series were constructed.

appear to be dominated by a time invariant phase relationship between the mix of modes. This is evidenced by the changing depths of the maximum peak energy.

This variability of the vertical structure of the semi-diurnal tide is provocative. An expected source in this region for internal tide generation would be from the nearby continental slope to the east ($\approx$ 400 km), and therefore would have a more uniform time dependence of amplitude and structure. However, observations now show that strong internal tides are generated by the Mendocino Escarpment (Althaus et al. [5]), just 300 km north of the EBC offshore mooring array.

Projected semi-diurnal ray paths from the Mendocino Escarpment would have multiple reflections at the surface and seafloor before arriving near the EBC location. The evolution of these generated beams as distance from the source increases is not well observed. It is entirely plausible to construct the high variability observed at EBC with a few low mode semi-diurnal internal waves generated 300 km to the north. Levine and Richman [43] analysed data from 35.5° N, 126.5° W which is roughly 600 km south of the Mendocino Escarpment (300 km south of EBC). They found evidence supporting semi-diurnal tides propagating southward.

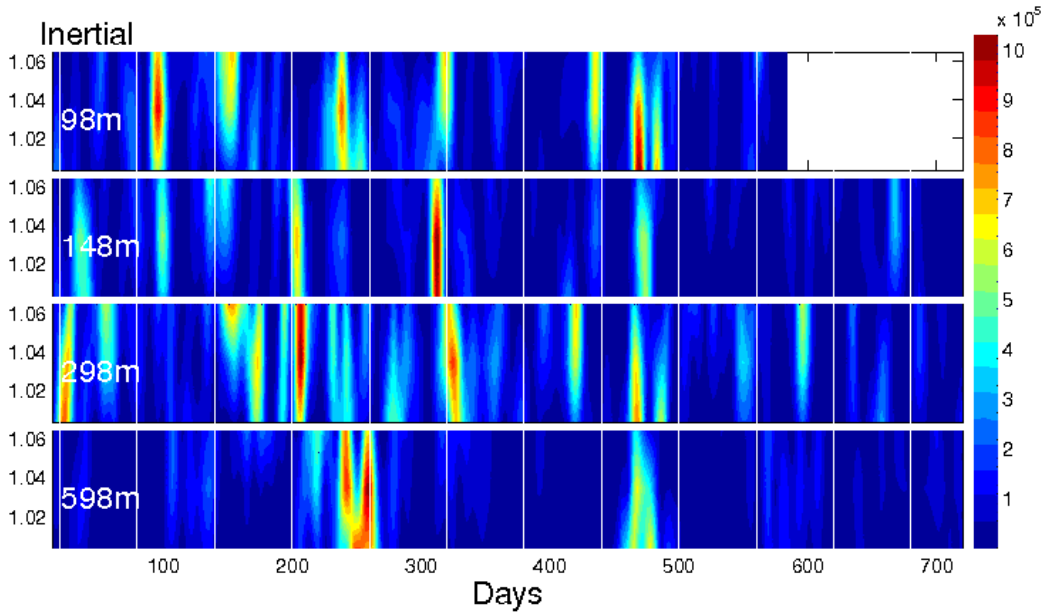

Figure 2.20. Inertial frequency anti-cyclonic rotary PSD time series for the four depths of the deep water central mooring of EBC. See Figure 2.19 caption for specific details.

The inertial current PSD time series for this mooring (Figure 2.20) reveal a few robust events that penetrated to the 600m instrument. In the upper two instruments, there are many more events, and most seem to be coincident at both the 100m and 150m instruments, with a few exceptions. The high temporal variability of inertial wave energy is well known, being the result of the high temporal variability of surface winds. The strong, and time-varying, depth dependence of the inertial current energy is also well known, being a consequence of both the limited vertical extent of inertial current beams emanating from the base of the mixed layer and the horizontal variation of inertial current energy created by a particular wind event. In the Ocean Storms data (Figure 2.15) the vertical extent of inertial wave events appears to be on the order of a 100 m, which is consistent with the results from the more widely spaced instruments in the EBC (Figure 2.20).

At the IWISC frequency in the cyclonic current PSD component (Figure 2.21), most of the activity appears to be at the upper two depths. If the PSD is appropriately scaled with the buoyancy frequency, however, the 598m peaks are much more prominent. We can still see those peaks without the scaling in Figure 2.21, and some events appear to be nearly co-temporal with the 598m inertial time series (Figure 2.20). The IWISC energy is seen to have a high variability in time, comparable to the temporal variability of the inertial wave energy. The vertical extent of the IWISC events appears to be smaller

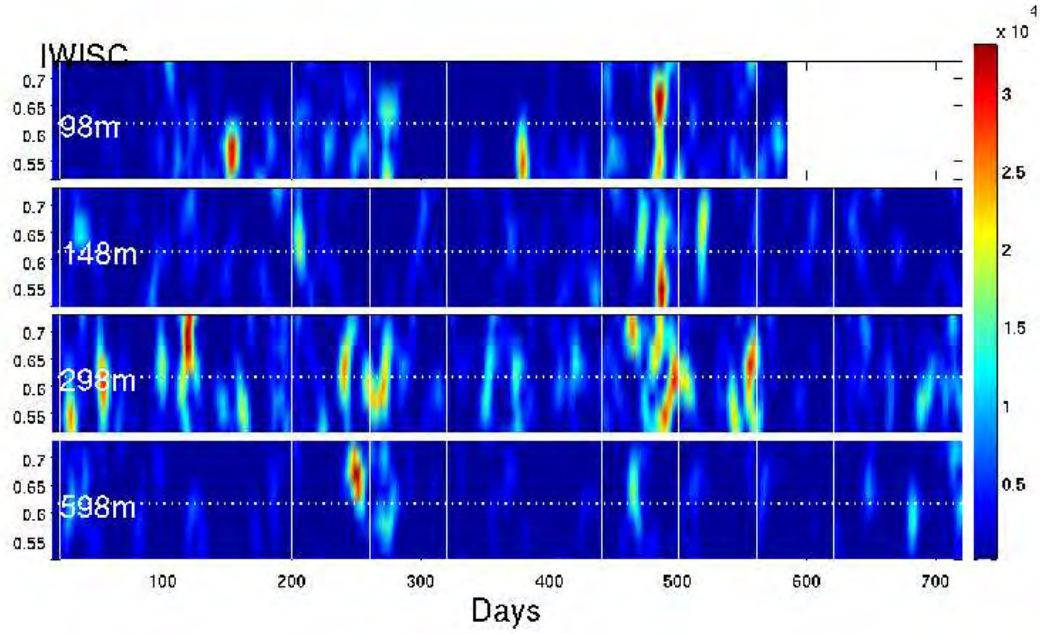

Figure 2.21. The cyclonic current PSD around the IWISC frequency is shown. This record is from the deep water central mooring of EBC. See Figure 2.19 caption for specific details.

than the inertial wave events, consistent with the Ocean Storms data in which the IWISC events appear to have a depth extent of order 50 m or less (Figure 2.14). This motivates the question of how coherent are these signals and is there any signature that extends from one mooring to the next.

EBC Horizontal Current Comparison

An ideal data set for the identification of horizontal structures would have a grid of velocity and vertical displacement at multiple depths covering an area on the scale of the longest horizontal wavelength. For IWISC, this would be on the order of a hundred kilometers to capture inertial and internal tide horizontal wavenumbers. Grid points would be separated by only a few kilometers to maximize coherence. Such data does not exist yet. Fortunately, at the EBC location there is enough data at a short enough grid spacing to get a sense of the horizontal scales of all relevant motions. The EBC records described here come from the north, central, and south moorings at 598m. This is roughly in line with the probable source of semi-diurnal internal tide variability at the Mendocino Escarpment to the north.

The 598m records were chosen for display here because they have a minimum of "contamination by mesoscale variability at the IWISC frequency compared to instruments closer to the surface. There is a roughly seven kilometer separation between each mooring. In Figure 2.22 the time series of PSD

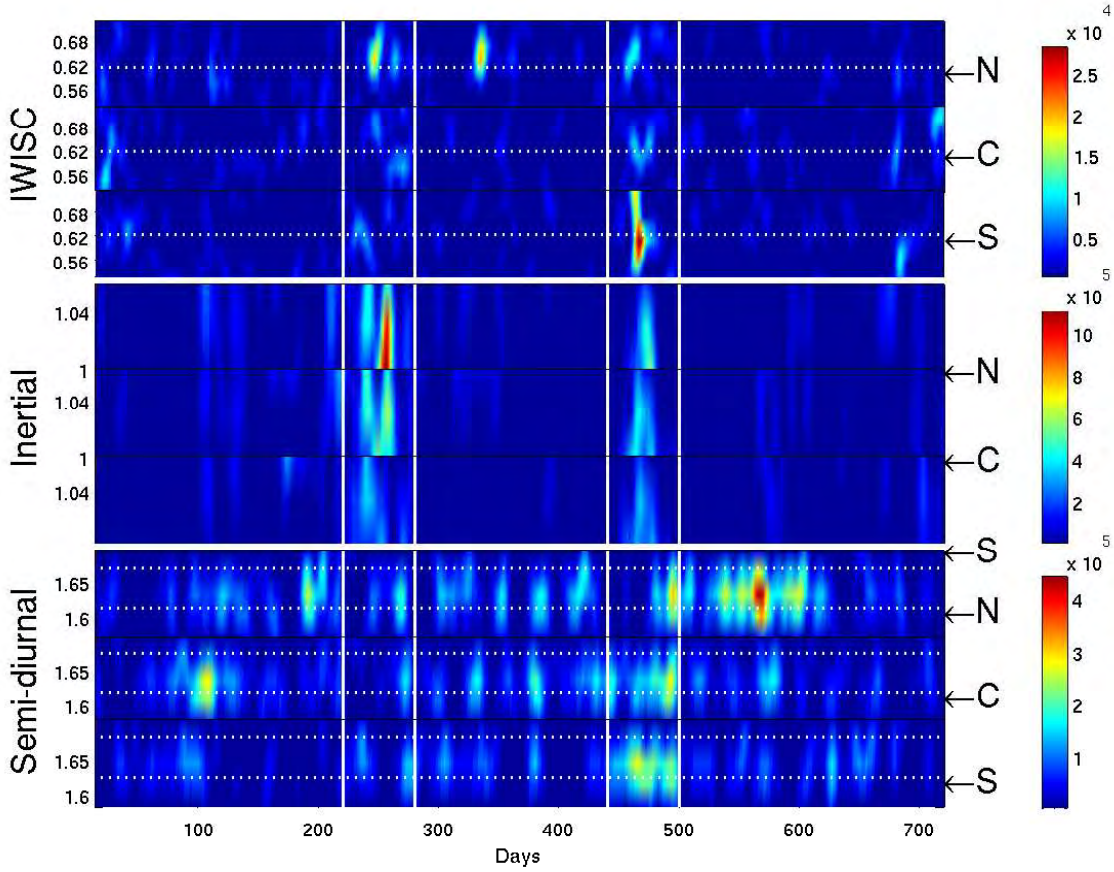

Figure 2.22. PSD time series at 600m for the North, South, and Central moorings for EBC. The top three are the cyclonic difference frequency ($M_2 - f$), next is the anti-cyclonic inertial period, and the last three are the total energy semi-diurnal internal tide. Arrows indicate a specific frequency (top to bottom: $M_2 - f$, f, M_2) along the vertical axis of each bar; frequency scale on left is normalized by f. Mooring location is noted with (N)orth, (C)entral, and (S)outh. See Figure 2.7 and its accompanying description for further details of how the PSD time series were constructed.

is compared at the three frequencies for each of the three mooring locations. Note the distinct events at both the IWISC and inertial frequencies that appear at multiple locations. Also, there are events that are seen only at one location. We can begin to make some inferences about the ranges of the horizontal scales based on these data. However, unlike the inertial peaks for which we have internal wave theory to estimate and compare the wave structures, motions at the IWISC frequency are outside the free internal wave regime at this latitude, and as such the horizontal nature is indeterminate with limited horizontal data points.

The inertial events are very interesting in their own right. The first event time period shows a strong fall off of inertial peak energy from north to south. This is significant variability considering the short horizontal scale. For a southward, downward beam of near-inertial waves at a frequency of 1.02f, the expected increase in depth from N to C to S is approximately 30 meters at each step. It seems unlikely that the vertical structure of the beam would have such strong gradients as to account for the differences in energy from N to C to S. More likely, this beam has a substantial east-west propagation component such that the more southerly moorings are farther out on the edge of the beam. During the second time period the inertial energy appears evenly distributed across each mooring.

In the semi-diurnal internal tide band, there is more temporal regularity of PSD than for the inertial waves, with clear sequences of spring-neap tide variations apparent, but there is also strong variability in energy from one mooring to the next despite the closeness of the moorings. This is somewhat surprising; however, there are many possible constructions of internal tide structures that could produce such a result even with predominantly low vertical mode waves. To restate, the horizontal variability is high, but not inconsistent with the conventional understanding of internal tides. Further research is warranted to fully understand what is causing this distribution of energy, but such an effort goes beyond the scope of this work.

When plotting data with intermittent signals of varying amplitude, events of lesser magnitude may become more difficult to evaluate, especially when using color scale plots such as those presented above. The peak inertial energy in figure 2.22 sets the scale for all other events., which visually diminishes the variability in the second time period. In figure 2.23 the second time period is isolated.

Now, in relation to all inertial activity during just this time period, there appears to be a fall off of inertial peak energy from North to South, as was clear for the first event in Fig. 2.22. Also, peak inertial activity is not entirely aligned in time.

There is a good correspondence between IWISC energy and inertial energy at the Center and South moorings. There is even a suggestion that the frequency of the maximum IWISC PSD varies in time in accordance with the time variability of the maximum inertial PSD. This is most easily seen in the Center mooring record, where the IWISC event starts with a slightly higher frequency, drops to a lower frequency for a few days, then returns to a higher frequency, in accordance with the inertial PSD which begins with a peak very near the inertial frequency, that then migrates to a higher frequency for a few days, followed by a return to a very near-inertial maximum.

The apparent horizontal variability at the IWISC frequency does not match the horizontal variability at the inertial frequency. The cyclonic energy at the IWISC frequency appears to diminish towards

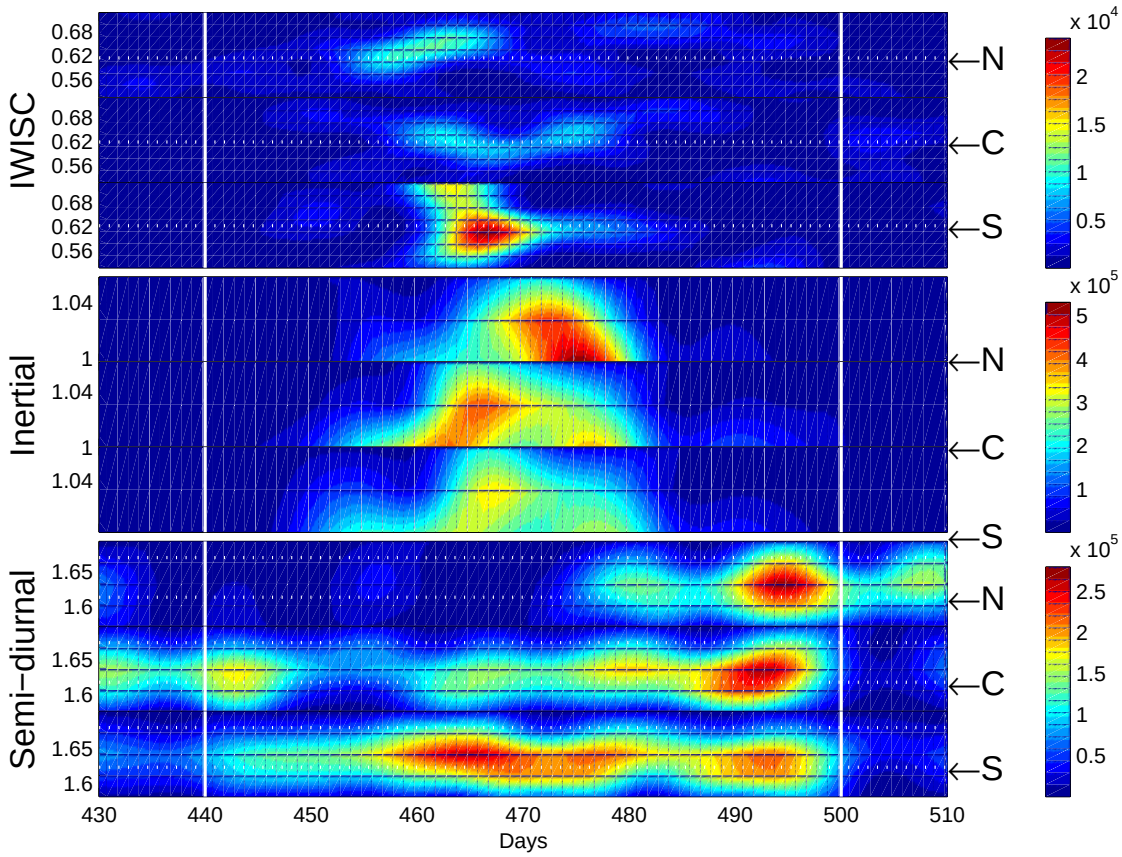

Figure 2.23. Frequency band PSD vs. time for the (N)orth, (C)enter, and (S)outh moorings of the EBC offshore group. Time segment is the later period identified in figure 2.22. See Figure 2.7 and its accompanying description for further details of how the PSD time series were constructed.

the North, opposite the spatial dependence of the inertial PSD. The peak inertial energy seen in the North has little associated IWISC energy.

With the display in Fig. 2.23, spring/neap cycles in the semi-diurnal PSD are easily identifiable. It is clear that from cycle to cycle there is high variability in the internal tide energy across this relatively small horizontal scale (just 14 km from N to S). An explanation for this variability is a subject for future investigation. In comparison with IWISC energy, it is notable that the largest IWISC PSD - which occurs at the southern mooring at about day 468 - coincides with very high tidal PSD and moderately high inertial wave PSD. At the other two moorings at this time, while there is still high inertial PSD, the tidal PSD is moderate to weak; the concomitant IWISC PSD is at a moderate value.

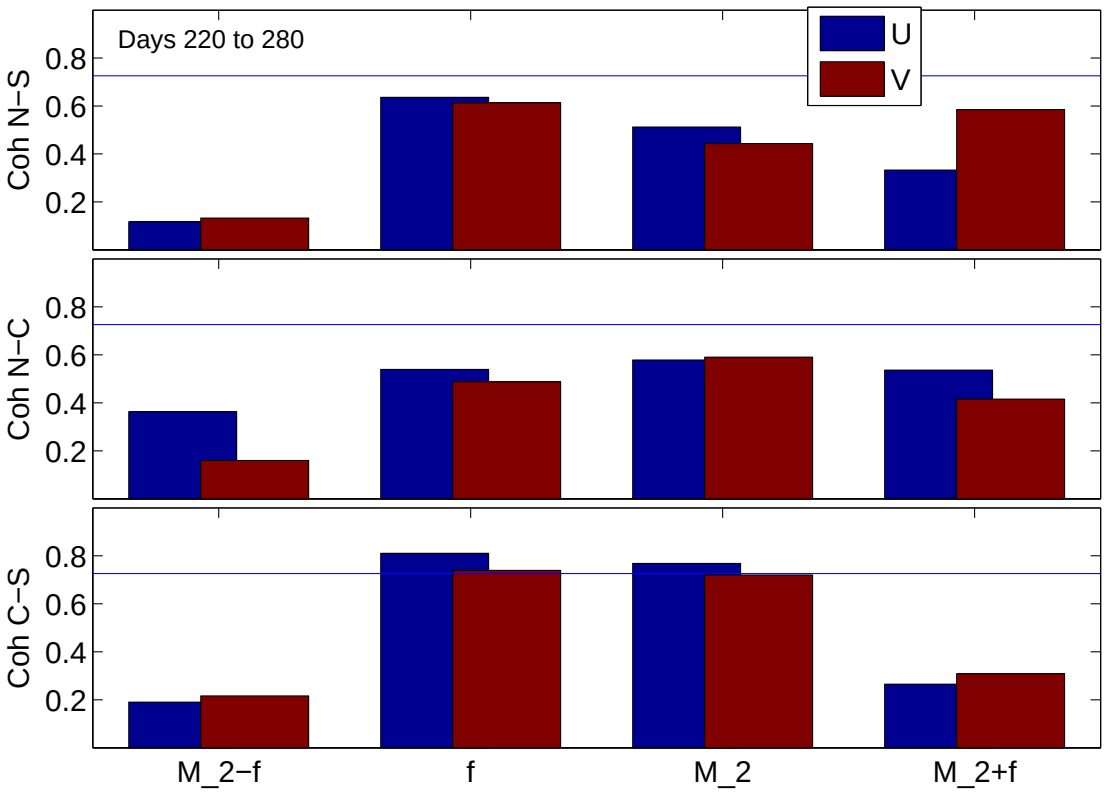

Figure 2.24. Coherence between moorings in four frequency bands for the first time period indicated in figure 21 from day 220 to day 280. The top panel is between the North mooring and the South. Next is North vs. Center, then Center vs. South. The horizontal light blue line indicates the 95% level of no significance.

Coherence was calculated between observed velocities at each mooring for the data used in figure 2.22 and identified by the two time periods of inertial and IWISC energy enhancement. The coherence values for the interacting frequency bands are displayed in figures 2.24 and 2.25.

During the first time period between day 220 and day 280 the only significant coherence occurs between the Center mooring and the South mooring at the inertial and semi-diurnal frequencies. Both velocity components are coherent in these bands.

The second time period from day 440 to day 500 reveals a different set of coherences. For the inertial frequency band, there is coherence between the North and Center, and between the Center and South. However, across the longer separation of North to South the coherence is not significant.

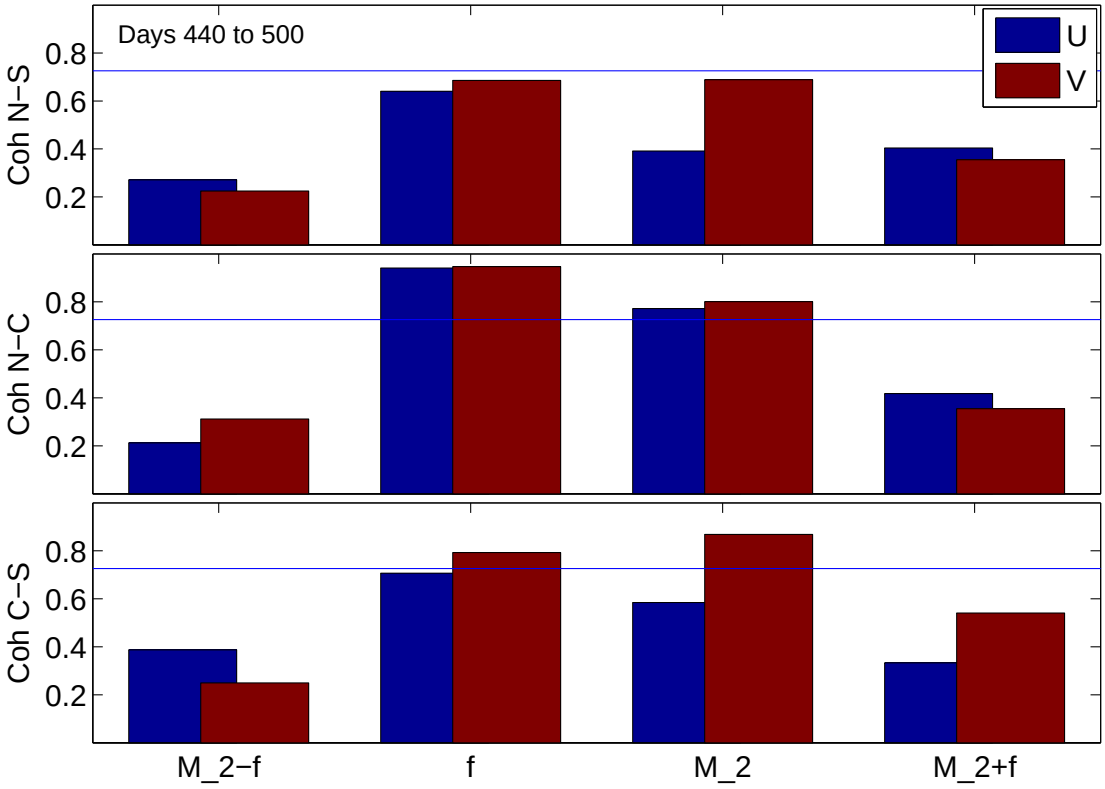

Figure 2.25. Coherence between moorings in four frequency bands for the second time period indicated in figure 2.22 from day 440 to day 500. The top panel is between the North mooring and the South. Next is North vs. Center, then Center vs. South. The horizontal light blue line indicates the 95% level of no significance.

At the semi-diurnal frequency, there is coherence in the meridional velocity between the North and Center moorings, and between the Center and South moorings. The zonal velocity is significant between the North and Center mooring. This may be an indication of predominantly meridional orientation of the semi-diurnal internal tide, which would be consistent with the nearby studies of Althaus et al. [5]) and Levine and Richman [43] commented upon earlier. Further investigation is warranted.

What is very clear from the coherence analysis of the EBC data, of which only a subset is shown here, is the lack of coherence at the IWISC and sum frequencies. These structures are not mirroring directly either the inertial internal waves or the semi-diurnal internal tide.

This lack of coherence is not unexpected. If the two interacting internal waves are coherent at 5 km or less, as indicated by the data here, any product between them would certainly have a reduced coherence length if the resulting structure were not locked to one input or the other.

This observation emphasizes the need for detailed horizontal resolution to determine more about how this interaction is occurring. With such high variability in peak energy horizontally, new data sets with high resolution in the horizontal will be necessary to determine how peak energy at inertial and semi-diurnal frequencies evolves.

The analysis of horizontal energy distribution motivates a reconsideration of observed energy at a single point. Even with excellent vertical resolution, a single Eulerian point in the horizontal will not likely yield representative views of energy variability for a particular region.

At the semi-diurnal frequency, the waves may be completely deterministic and linear in the Lagrangian frame, yet mesoscale variability on top of background flow coupled with the summation of a few low vertical modes at semi-diurnal tidal constituent frequencies results in highly variable Eulerian observations (for instance, Rainville and Pinkel [71]). Using deterministic reconstructions to analyze this Eulerian data masks the source of variability. Furthermore, these waves have the potential to interact non-linearly in many different ways, which significantly changes any assignment of energy variability based on such limited observations.

For inertial frequencies, the result is less unexpected. Inertial packets in three dimensions are known to have small vertical scales. Observing the evolution of such a wave packet will be a future concern.

What the EBC data tells us is that, at least at this location, the horizontal distribution of PSD of the internal tide and inertial wave progenitors of the IWISC and sum frequency motions are not at all homogeneous, and that the IWISC motions are even more variable horizontally. Even at a relatively small distance (about 300 km) from the probable source of the internal tide variability the temporal dependence of internal tide energy can depart substantially from the expected regular spring-neap cycle variations. All these characteristics, though just crudely determined here, will be required for the eventual construction of a theory of the generation of IWISC.

2.3.7 Vertical Structure

In the initial analysis of historic data, the focus was on records well below the thermocline, thus avoiding surface-enhanced mesoscale energy which can obscure IWISC peak indications. Once it was established that IWISC occurred in many geographic regions, the depth range of records to analyse was expanded. It was found that many experiments with multiple instrument depths had evidence

of IWISC at more than one depth. A significant question became "Is there a depth dependence to IWISC?" Enough data was available from experiments with multiple instruments to reveal a intriguing distribution of IWISC activity in depth.

To examine this depth dependence a method was devised which represents the relative energy peak in the IWISC counter-clockwise (clockwise for the Southern Hemisphere) rotary PSD above the mesoscale background. This method is applicable to latitude ranges poleward of approximately 33° for two reasons: one, the IWISC rotary PSD peak is not in the internal wave band, and two, it is not close enough in frequency to the inertial period to be contaminated by inertial wave energy. The data records have been processed as follows:

- 98 horizontal velocity records were selected from 11 moorings with multiple instrument depths
- All records below 50 meters were included from each experiment, regardless of IWISC signature
- Each record was split into two windows, each of which was tapered with a 10% cosine taper at its ends
- Rotary PSD was computed from averaged fft
- Rotary PSD was appropriately scaled with a WOA buoyancy profile at the mooring location
- A narrow-band IWISC peak PSD value was obtained
- A broader band (with IWISC center frequency) mesoscale energy average was calculated from the opposing rotary PSD
- The difference between IWISC and mesoscale background PSDs (ΔPSD) was calculated along with its confidence interval.

To better illustrate the how the energy differences are calculated a spectrum from the RTE87 TW mooring is shown in figure 2.26. The cyclonic (CCW) IWISC signal is the highest PSD value within the red dotted frequency range. This occurs after smoothing, typically a two point smoothing filter. From this is subtracted an average value derived from the anti-cyclonic rotary velocity within the blue dotted frequency range. The confidence intervals indicated in the figure are appropriate for the cyclonic IWISC value. The bands are calculated as a percentage gap centered on a local IWISC frequency with a four percent blue shifted inertial.

The estimated ΔPSD produces the depth dependent structure shown in figure 2.27. Each diamond and square symbol indicate the depth vs. ΔPSD for a single record with its associated 95% confidence

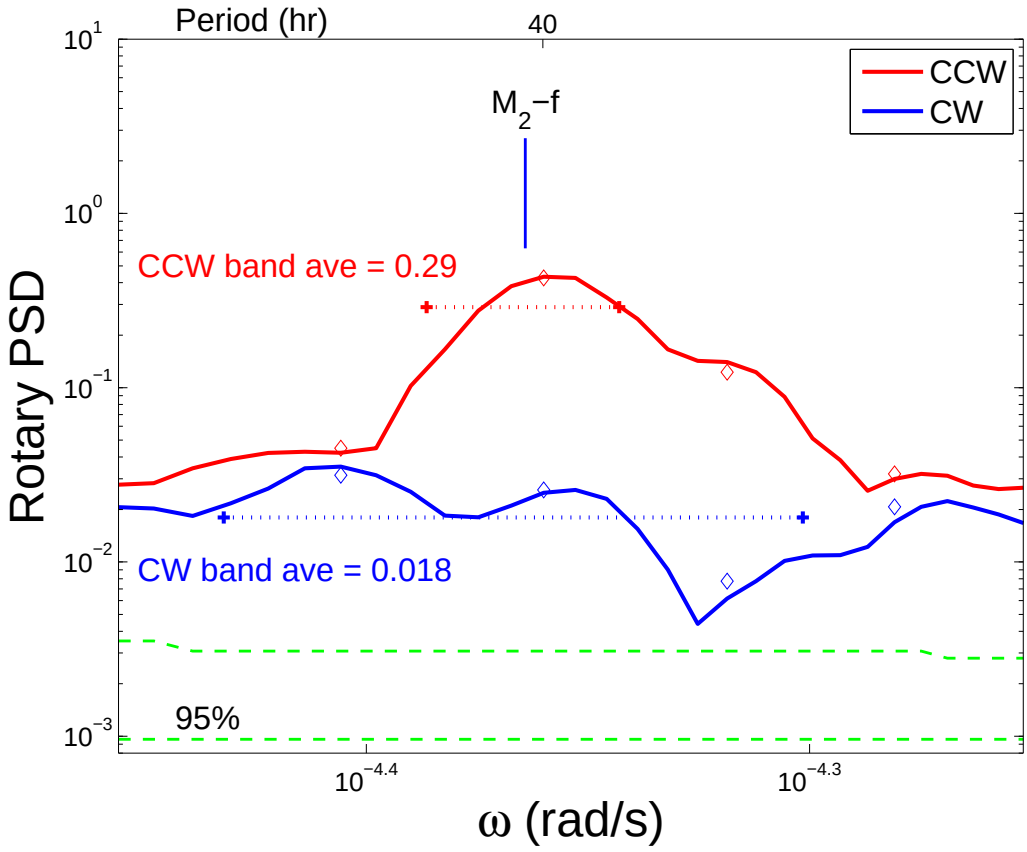

Figure 2.26. Narrow band rotary PSD of current meter velocity recorded at 1075m depth on the TW mooring during BEMPEX/RTE87. Selection bands for the peak IWISC and broad cyclonic mesoscale are indicated by red and blue dotted lines, respectively. Respective values correspond to those used in the difference calculation, ΔPSD. The record length is 200 days long. 95% confidence intervals for each independent PSD estimate are indicated by the dashed green lines at the bottom; the diamond symbols indicate the frequency intervals between independent PSD estimates.

interval indicated by a thin red horizontal line. The green profile is a third order polynomic fit to the data points. The fit is simply a potential reference line and is not intended to represent a specific underlying relationship.

There are a few observations with little or no ΔPSD, these are not in the range of the figure, but are indicated on the left ordinate as dark blue dots. The confidence intervals for some small off-figure estimates can be seen. All estimates are included in the polynomic fit for consistency. Higher resolution observations have narrower confidence intervals.

There is a clear increase in IWISC proceeding down from the surface to approximately 1500 meters. After this the peak difference begins to diminish. There is a weakening trend in ΔPSD below 1500 meters. However, there are far fewer data points supporting this observed weakening trend. A

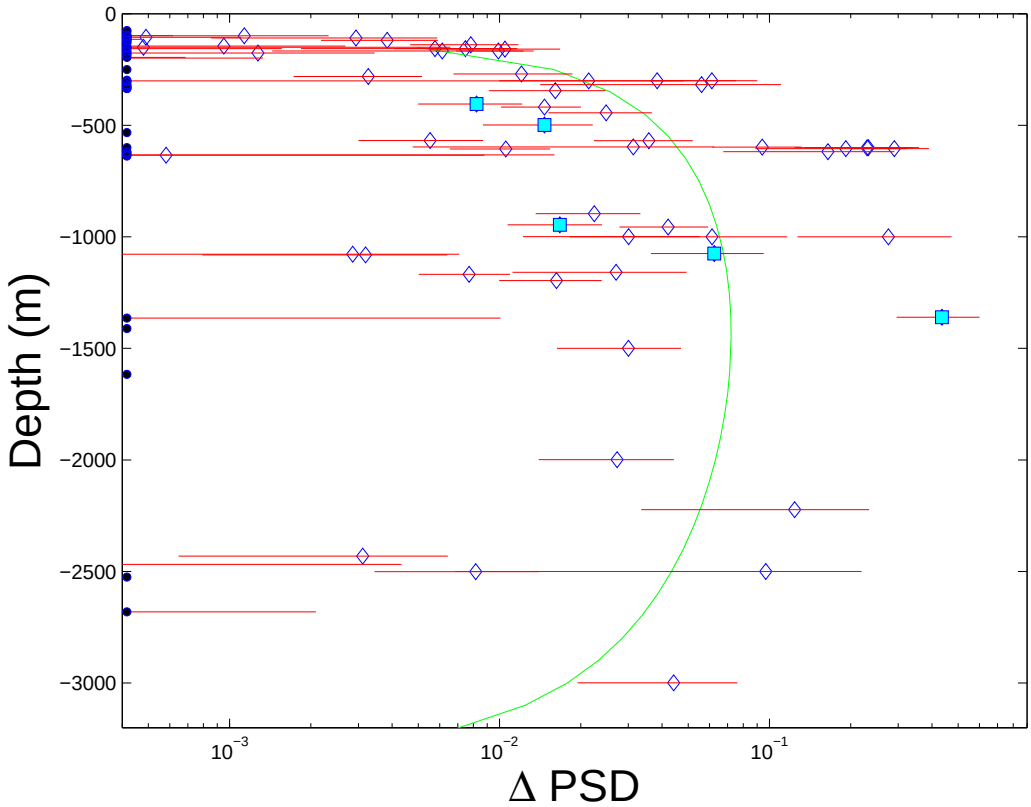

Figure 2.27. Depth distribution of IWISC cyclonic rotary PSD peak height above a near IWISC frequency band mesoscale anti-cyclonic rotary PSD average. Thin red lines indicate 95% confidence intervals. Green depth profile is a third order polynomic fit to all data points. Dark blue circles indicate instrument records with little or no IWISC peak, where the actual values are much less than the plot range. Blue squares correspond to those records used in figure 2.2.

few data points exist at depths below 3000 meters. These points, though not erroneous, do not scale appropriately with the WOA buoyancy profile, and are not shown.

The most intriguing overt implication of this figure 2.27 is the possible IWISC dependence on the vertical structure of the internal tide vertical velocity. If the principal mechanism generating IWISC observations depends heavily on vertical velocity, IWISC would be expected to have observed maxima at depths with vertical velocity maxima. Making the assumption that the primary vertical velocities involved are from the first few semi-diurnal internal tide modes, a distribution in depth of vertical velocity amplitude similar to Figure 2.27 could be established easily.

This leads to the limitation of Figure 2.27; few of the moorings included there have any information from which to establish accurately the semi-diurnal tide vertical velocity structure in depth. As a bulk observation, the vertical structure in Figure 2.27 supports the argument in favor of a dependence of IWISC on semi-diurnal tide vertical velocity, but does not conclusively establish the argument. To confidently establish such a dependence, the semi-diurnal internal tide vertical structure would have to be observed at high resolution over multiple spring/neap cycles.

The need for more precise observations of the vertical structures of IWISCs progenitor waves motivated the inclusion of ADCP records into this analysis. A moored ADCP from the Deep Basin (WOCE component ACM13) experiment was one of the first high vertical resolution records analyzed that had evidence of IWISC. This instrument was deployed at 34.5° S, 26.9° W and revealed unexpected complexity of the semi-diurnal tide vertical structure. The data provides further evidence of IWISC in southern hemisphere oceans, and is one of just a few records where IWISC is identified just poleward of the critical latitude.

The evidence of IWISC in this record is shown in figure 2.28. Each color band represents a time series of rotary PSD for the indicated center frequency and depth band. There is a region in the plot indicating enhanced IWISC energy. The depth range of maximum enhancement appears between 100 and 143 meters. There appear to be two or three 'events' at these depths during the time period from 160 to 210 days.

As this instrument does not cover deeper depths, it would be speculation to quantify a vertical scale of IWISC energy, but the qualitative visual representation would suggest responses with vertical scales well less than 100 meters; it would be fair to say the scale is on the order of 50 m. In this record, there is correspondence in the peak energy time periods between IWISC and the inertial frequency.

In figure 2.29 the inertial frequency band is shown for this instrument. There are a few clear peak events that dominate the inertial energy over the whole record. Of interest are the events form 160 days to 230 days. Compare the timing and depth of this energy with the peak IWISC events. The IWISC peaks appear near this inertial energy, although they seem to precede them.

There is a very plausible explanation for the apparent inertial lagging of IWISC. The initial increase in inertial energy is at the same time as the IWISC peak energies. This energy level is dominated however, by the subsequent inertial peak energy associated with the forcing event. Furthermore, it is reasonable to assume that the depth of mixed water is steadily deepening during these significant events. This reduction in the buoyancy does not reduce the observed inertial horizontal velocities, but it would negate a process that depended upon significant baroclinic vertical structure. To reiterate, the

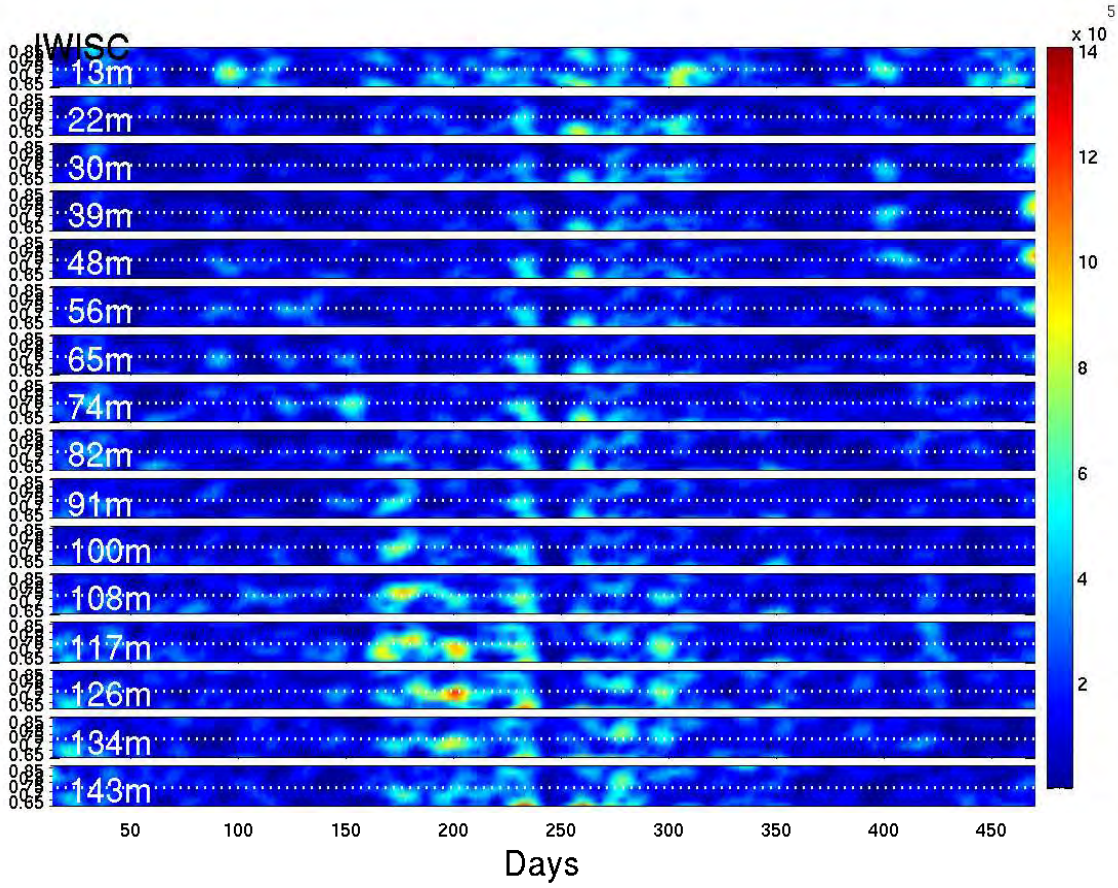

Figure 2.28. Time series of clockwise rotary PSD for the IWISC frequency band of the moored ADCP instrument as part of the Deep Basin (ACM13 WOCE component) experiment. Dotted white line indicates IWISC frequency. During the time period of 160 to 210 days enhanced IWISC energy is seen at lower depths. Other peak energy (days 220 to 300) is likely associated with inertial events, and is not peaked at the IWISC frequency. See Figure 2.7 and its accompanying description for further details of how the PSD time series were constructed.

observed IWISC peak energy in this record is coincident with increased inertial energy, though not at the exact time and depth of peak inertial energy.

For the M_2 frequency band (Figure 2.30) some interesting features are very clear. The spring neap cycle is quite distinct, yet the peak magnitudes vary considerably over the depth coverage. Perhaps the most striking feature is the lack of a consistent vertical structure. The variation in peak values is complex and could not be characterized with a single depth or a short record length. For instance, if you had a single current meter at 50m and deployed it at day 150 for two hundred days, you would completely miss peak M_2 energy levels at this location. This in itself is a clear warning against short

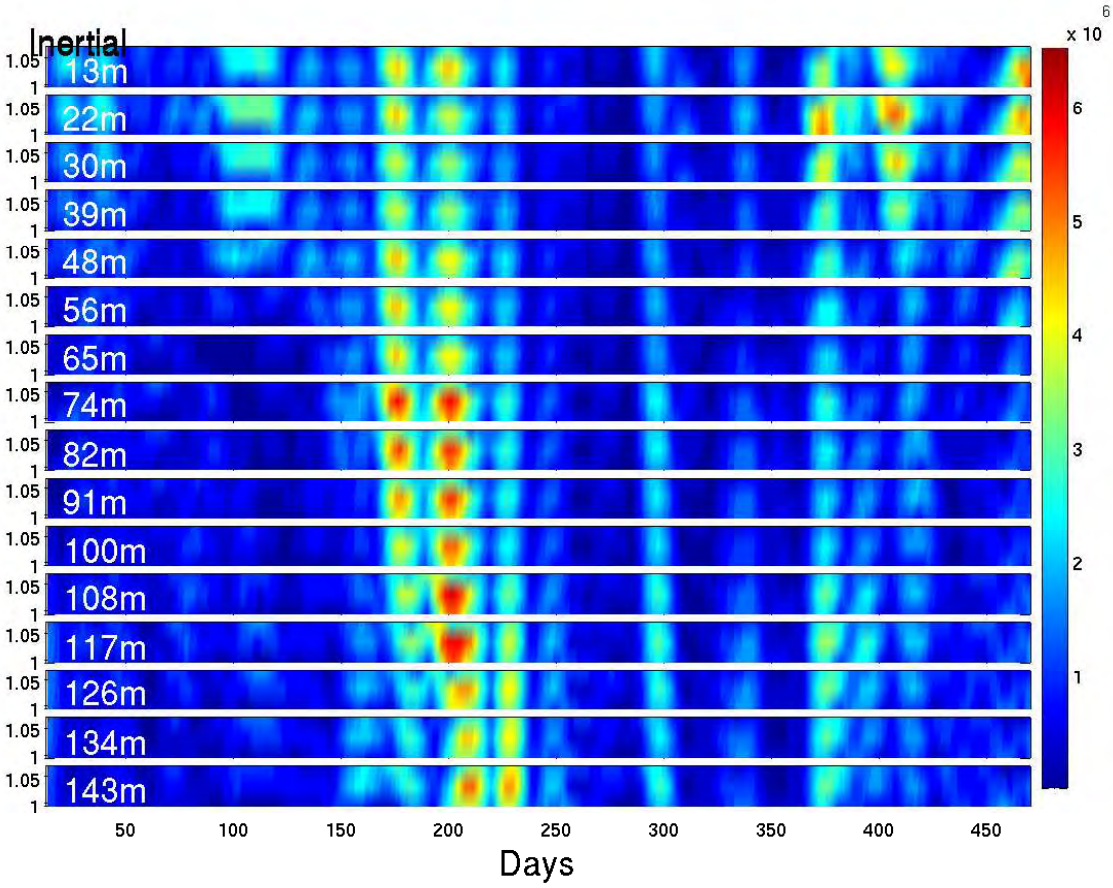

Figure 2.29. Time series counterclockwise rotary PSD for the inertial frequency band of the moored ADCP instrument as part of the ACM13 WOCE component. See Figure 2.7 and its accompanying description for further details of how the PSD time series were constructed.

term deployments even when observing baroclinic tidal features which are often regarded as having less temporal variability in structure than what is observed here.

In relating this semi-diurnal internal tide energy to IWISC evidence there are two major points. First, the existence of distinct semi-diurnal energy is not a predominant identifier of possible IWISC energy (e.g., Figure 2.11). However, in comparing the two (Figures 2.28 and 2.30), it is instructive to examine a single depth bin. The three principal IWISC peaks in the 117 meter bin occur over a time period of approximately 40 days (day 170 to 210). This roughly corresponds to the duration of three spring/neap cycles. In the semi-diurnal energy at the same depth, there are three spring/neap cycles evident.

The second interesting observation is the appearance of a drop off in semi-diurnal tide energy above 100 meters for the forty day time period (170 to 210 days) where IWISC peak energy is observed

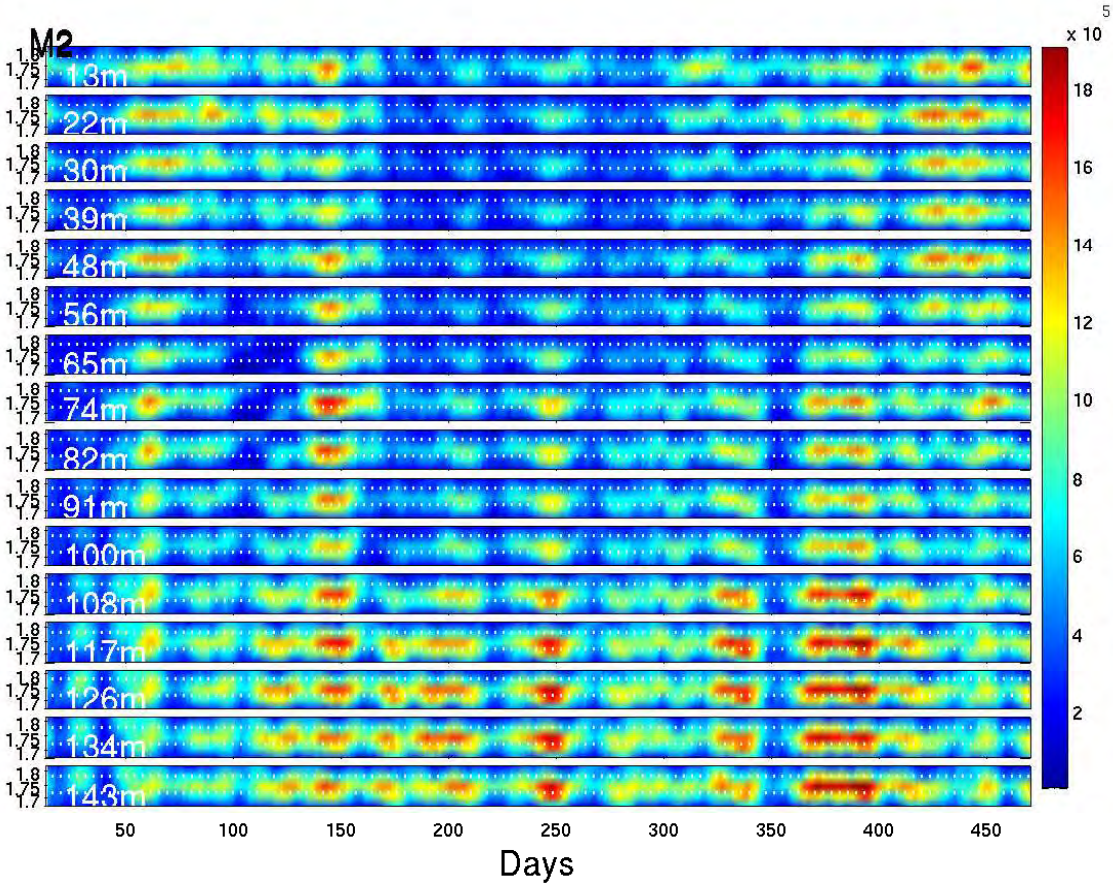

Figure 2.30. Time series of total (cyclonic and anti-cyclonic) PSD for the M_2 frequency band of the moored ADCP instrument as part of the ACM13 WOCE component. Dotted lines indicate M_2 (lower) and S_2 within each depth band. See Figure 2.7 and its accompanying description for further details of how the PSD time series were constructed.

below 100 m. Though not quantitatively conclusive, the lack of semi-diurnal energy is suggestive. There is inertial energy, but low tidal, and no IWISC. This is in contrast to the depths just below, where there is IWISC, inertial, and semi-diurnal energy. Conversely, there are other depth and time locations in this record where there is no IWISC, yet inertial and tidal energies are evident.

With the specific case examined here, it is quite clear that the depth dependence of IWISC in general can be constrained by multiple factors. If many observations like this ADCP record were available, with a greater depth range, and at many latitudes, a more detailed construction of IWISC depth dependence could be created. Of principal benefit would be the analysis of semi-diurnal vertical structure during time periods that have IWISC energy.

If such data were available, and a depth average of semi-diurnal vertical energy were compared with IWISC energy at depth, it is conceivable that one could explain in figure 2.27 the apparent depth dependence of IWISC peak energy. It is a relevant problem, and beyond the scope of available data. Fortunately, enough existing data was available to reveal a viable and realistic view of this problem.

In summary, the ADCP data at this location has yielded evidence of IWISC with vertical scale less than either of the other interacting waves. IWISC events were observed with vertical extent on the order of 40 meters.

2.4 Discussion of Variability

There are two likely classes of mechanism that could result in the observed energy at the interaction frequencies $M_2 - f$ and $M_2 + f$. One class exchanges energy in an irreversible way. The other is reversible under coordinate transformations. A semantic issue arises when one process is described as advection. In the analysis of moored current meters, the non-energy exchanging process that is examined is a periodic vertical displacement of primarily horizontal inertial currents by the semi-diurnal internal tide.

In a displacement following frame with purely linear waves that do not interact, energy would not be apparent at the interaction frequencies. If these waves interacted in a non-linear way, the resulting energy would be apparent in both reference frames.

Differentiating between these two mechanisms with point Eularian measurements is extremely difficult. The evidence does indicate that both of these mechanisms are possible, separately or in tandem. For instance, a pure periodic Doppler shift would have relatively equal energy distribution between the two interaction frequencies. The energy would also be dependent on the strengths of the horizontal currents.

Many of the records do not fit this model well. High variability has been demonstrated in each frequency band. A low bulk correspondence (Figure 2.6) between the two interaction frequency peak energies is another indication that periodic vertical Doppler shifting is an inadequate universal explanation.

The inability of the vertical periodic Doppler shifting model to completely explain the observed variability is not a conclusive argument for the existence of the energy exchanging process. Horizontal advection can be influencing these same frequencies. Complicated vertical structures of the input waves could significantly alter the observed energy.

These complications are all possible, but do not negate the indications of energy exchanging processes. Non-linear exchange of energy is both plausible and probable with the moored current meter evidence. Similar analyses in previous work have reached this conclusion for the sum $M_2 + f$ frequency.

Mihaly et al. [51] presents evidence of enhanced energy at the sum frequency. They also notice that the energy is not coincident between inertial and $M_2 + f$ frequency bands apart from seasonal time scales. As the observed structure of the M2 + f motion in their work appears consistent with internal wave theory, they conclude that the energy is permanently transferred from inertial and diurnal bands to the $M_2 + f$ band. A resonant process with short time scales would have coincident temporal variability in energy between bands. The authors surmise that the point measurements used in the analysis are not at the location of interaction, and that the product of the interaction propagated from the location of interaction into the measurement area.

A similar PSD peak is observed by van Haren et al. [88] at the $M_2 + f$ frequency. They make even stronger statements that the nature of the continuum internal wave spectrum is anchored at low frequencies by tidal harmonics and non-linear interactions between inertial and tidal energies. The specific mechanism generating the peaks such as $M_2 + f$ is not determined by the authors.

In direct contrast to these conclusions, Pinkel [67] proposes reversible vertical advection as a primary mechanism for creating the observed Eularian internal wave spectrum. The model is convincing and may explain numerous observations. It does not explain intermittent non-cotemporal peaks at the periodic Doppler shift frequencies as observed in this analysis of historic moored current meters.

Irregardless of dominant mechanism, the result remains that these energy peaks can no longer be ignored. Either underlying mechanism implies a significant change in the understanding of internal waves in the ocean.

2.5 Summary of Historical Data Analysis

The analysis of historical records has generated important result in the study of IWISC and the possible underlying mechanisms. These significant results include the following:

- A peak in spectral energy has been observed at the frequency of $M_2 - f$ over a broad range of depths and in numerous geographic locations throughout the worlds oceans.
- The IWISC energy is almost entirely in the cyclonic rotary component, rather than the anti-cyclonic component that dominates free internal waves.

- IWISC energy poleward of the critical frequency (where $f = M_2/2$) is outside of the free internal wave band.
- There is a corresponding anti-cyclonic rotary component energy peak at the frequency $M_2 + f$ in many of the records.
- Bulk observations of IWISC cyclonic peak energy poleward of the critical frequency ($f = M_2/2$) show a positive correlation (though not strong with R < .5) with the corresponding anti-cyclonic $M_2 + f$ energy peak.
- Energy at the IWISC frequency is episodic and in general is not directly correlated with observed energy at the semi-diurnal frequency.
- There is a weak (R < .2) positive correlation between bulk observations poleward of the critical frequency ($f = M_2/2$) of IWISC peak energy and inertial peak energy, with the strongest IWISC events usually associated with enhanced inertial energy.
- All interactant frequency bands (M_2, f, $M_2 - f$, $M_2 + f$) were found to exhibit horizontal correlation scales less than 10 km in one experiment where spatially-distributed time series were available.
- IWISC peak energy for mid-latitude records exhibits a depth structure, with maximum peak energy above a mesoscale background occurring near 1500 meters depth.

These significant results suggest the possible existence of an irreversible non-linear interaction between semi-diurnal internal tides and near-inertial internal waves. To resolve this possibility and clearly determine how inertial wave packets interact with the internal tides, higher resolution observations are necessary that will allow for the measurement of the waves vertical and horizontal wavenumbers and their evolution.

Chapter 3

Advection Analysis and Simulation

3.1 Single Sinusoid Vertical Advection Model

3.1.1 Introduction

This chapter addresses the question of how to discriminate, using Eulerian observations of oceanic variables, between (i) the passive Doppler-shift phenomenon of currents oscillating at one frequency (inertial waves) being advected vertically by currents oscillating at a second frequency (semi-diurnal tides), thus creating apparent energy at the sum and difference frequencies; and, (ii) the actual non-linear interaction of these two phenomena that drives oscillations (converting energy) into the interaction (sum and difference) frequencies. To identify the signature of advection without nonlinear energy transfer we have investigated several models containing a coordinate system that is vertically displaced. Testing a variety of analysis tools on these simulated velocities has assisted in the isolation of actual non-linear interaction in real ocean data records, and has provided invaluable insight into the advection signature when utilizing power spectra, bispectra, and other techniques.

Given the nature of inertial internal waves and their predominantly horizontal current orientation, it is natural to investigate what effects the distortion of the horizontal surfaces have on the wave field. One technique for examining data in this regard is the Semi-Lagrangian (S-L) inversion. This in general is the transition to a coordinate system that follows the gravest motion in one of the three dimensions. For our interest, this is the vertical advection by semi-diurnal internal tides. S-L inversions have been utilized to investigate finescale structure contamination observed in various locations by Desaubies and Gregg [16], Kunze et. al. [39], Sherman and Pinkel [79], D'Asaro et. al. [14], Pinkel and Anderson [68], Alford [2], and Pinkel [66] [67]. In a very recent publication, Pinkel [67] summarizes

the development and identifies three distinct scenarios where periodic (or stochastic) Doppler shifting should be addressed based on oceanic conditions. These are:

- Random Phase Distortion and Lateral Doppler Shifting
- Random Phase Distortion and Vertical Doppler Shifting
- Deterministic Phase Distortion and Vertical Doppler Shifting

In this scheme "phase distortion implies changes in the observed wavenumber/frequency structures due to coordinate advection. Periodic or stochastic Doppler shifting could also have an amplitude signature if the interactants have non-uniform spatial structures.

For our purposes here, the principal focus in the context of inertial wave interaction with the semi-diurnal internal tides falls into the third category. However, note it could be argued that lateral advection by inertial waves is a deterministic process that requires a separate investigation. A relevant application in the IWISC context of the Semi-Lagrangian inversion was done by Alford [2] to address the impact of vertical advection by internal tides on the fine-scale. Peaks in the velocity and shear spectra at Doppler shifted frequencies associated with the diurnal internal tide were removed through the S-L transformation.

The prediction model used by Alford involved a single sinusoid displacement signal which advected the vertical coordinate. A brief review of a similar model and examination of its limitations is necessary and is provided below. In addition, how does the inclusion of vertical structure for the displacement signal change the problem? Of comparable concern, what changes occur with the inclusion of multiple displacement signals? These questions become significant based on many observations. For instance, the observed vertical structure of the semi-diurnal tide in many locations indicates higher variability than just a predominant first vertical normal mode (see Chiswell [12]).

The S-L inversion with multiple displacement inputs has been successful in replicating the observed shear spectrum at a number of locations. For example, Sherman and Pinkel [79] use a Garret and Munk spectrum of displacement signals to self advect the GM spectrum and recover the features of the observed spectra for the higher wavenumber regime. This would indicate that the S-L transformation is a necessary step in identifying processes that actually exchange energy as opposed to energy that is based on the choice of observation frame.

The use of the single sinusoid advection model requires careful determination of the conditions under which it is viable. It has been determined in the work described below that the deterministic single sinusoid model has significant subtle details which are not trivial. The single sinusoid model applied to the advection of inertial waves by the semi-diurnal internal tide produces these results:

- it can yield realistic amplitudes of the sum and difference ($M_2 + f$ and $M_2 - f$) frequency waves in comparison to observations, and
- it indicates that the amplitude of motions at the sum and difference frequencies are equivalent.

In the following review and examination of several forms of the advection model it is shown that:

- the stationary nature of the model can lead to a mis-interpretation of the dynamics underlying the observed oscillations;
- the advection model yields motions that don't satisfy the internal wave consistency relations at the interaction frequencies (sum and difference frequencies);
- useful information could be obtained by retaining higher order terms in the model;
- including vertical structure in the advecting wave is pertinent and affects the result; and,
- extension to multiple deterministic displacement signals is non-trivial.

If vertical structure is specified, the prediction of the S-L inversion will have vertical variability. Similarly, a summation of advecting waves can lead to a beat frequency, and if the relevant signal to be advected has temporal variability of its own near this beat frequency, the amplitude of the advection product based on a simple model can be widely varying given a finite record.

Careful specification of the advecting signals characteristics leads to a useful model of observed advection variability, which then provides a framework within which to test techniques for discriminating simple advection from energy transferring processes in existing and future data. To reach this result, it is first necessary to briefly examine the deterministic single sinusoid model.

3.1.2 Deterministic Single Sinusoid Model Description

This simple model has been used successfully by the aforementioned authors, without the inclusion of vertical structure of the advecting signal. However, vertical structure is a ubiquitous aspect of the interacting waves in the ocean, so the model will be reviewed with vertical structure included. We implement vertical velocity in the simulations by specifying the horizontal velocity. This is to align the description with the more accurate horizontal currents available in oceanic current data sets.

There are two ways in which the vertical structure impacts the resulting solution. Since we have specified the horizontal solution, there is a paralization term in the corresponding solution for vertical velocity. The second influence is in the phase term of the solutions in each variable.

If the system of equations was solved for displacement, or vertical velocity, the vertical structure information would appear in a different way. However, through the parallelization relations, each of the dimensions would still be equivalent. This issue is an important detail when comparing simulations with a single sinusoid displacement and those with more complicated displacement structures. It is also important when comparing data to modeled waves.

If the displacement has vertical structure, as is the case with multiple component semi-diurnal internal waves of more than one mode, care must be taken in determining the relationship between modeled variables. Similar care needs to be exercised when examining data. If the measured displacement is used in an analysis, along with the horizontal currents at the same frequency, a consistency check is necessary. It would be easy to overlook the influence of the displacement vertical structure as well.

We begin the Semi-Lagrangian description with the inverted isopycnal following coordinate

$$\zeta = \overline{z(\rho)} \tag{3.1.1}$$

where ρ is the density and ζ is the new vertical coordinate. This is advected by a time dependent vertical displacement η, so the depth of the isopycnal is now

$$\hat{z}(\rho, t) = \zeta(\rho) - \eta(\rho, t) \tag{3.1.2}$$

A downward propagating inertial wave in the northern hemisphere can have its zonal velocity in the isopycnal coordinate described by

$$\mathcal{U}^f(\zeta, t) = \mathcal{U}_0^f e^{i(k_z^f \zeta - ft)} \tag{3.1.3}$$

where f is the inertial period, k_z^f is the vertical wavenumber, and $\mathcal{U}^f$ is the zonal velocity at the inertial frequency. We retain the notation of the z coordinate for clarity in the wavenumber, knowing that the wavenumber is determined by whichever vertical coordinate we originate with, in this case ζ. At this point an M_2 internal tide plane wave is introduced to heave the isopycnals. To evaluate the relationship between the two internal waves, one at the inertial frequency and the other at the semi-diurnal frequency, we introduce a solution for the internal tide in the zonal velocity (with the same inverted isopycnal frame as defined above)

$$\mathcal{U}^{M_2}(\zeta, t) = \frac{\mathcal{U}_0^{M_2}}{2}[e^{i(k_x^{M_2} x + k_z^{M_2} \zeta - \omega_{M_2} t)} + c.c] \tag{3.1.4}$$

The vertical displacement of the M_2 internal tide can now be introduced by the zonal momentum balance

$$u_t - fv = \alpha\eta_x \tag{3.1.5}$$

where u, v are the horizontal velocities, η is the displacement, f the inertial term, and α is the reduced gravity. This yields a coefficient for the displacement

$$\eta_0 = -i\frac{\omega_{M_2}^2 - f^2}{\alpha k_x^{M_2}\omega_{M_2}}\mathcal{U}_0^{M_2} \tag{3.1.6}$$

and the displacement solution

$$\eta = \frac{\eta_0}{2}[e^{i(k_x^{M_2}x + k_z^{M_2}\zeta - \omega_{M_2}t)} + c.c] \tag{3.1.7}$$

Substitution of the isopycnal following coordinate in eqn. 3.1.3 gives us

$$\mathcal{U}(\rho, t) = \mathcal{U}_0^f e^{i(k_z^f\hat{z} - ft)}e^{ik_z^f\eta} \tag{3.1.8}$$

Taylor expansion of the last term on the r.h.s.

$$e^{ik_z\eta} \approx 1 + ik_z^f\eta - \frac{(k_z^f\eta)^2}{2} \tag{3.1.9}$$

To zeroth order the solution for the periodic Doppler shifted inertial wave in Eulerian coordinates is

$$\mathcal{U}^f(z, t) = \mathcal{U}_0^f e^{i(k_z^f z - ft)} \tag{3.1.10}$$

The first order correction is

$$\mathcal{U}'(z, t) = \mathcal{U}_0^f\mathcal{U}_0^{M_2}\frac{k_z^f(\omega_{M_2}^2 - f^2)}{2\alpha k_x^{M_2}\omega_{M_2}}$$
$$* \left[e^{i(k_x^{M_2}x + (k_z^f + k_z^{M_2})z - (\omega_{M_2} + f)t)} + e^{i(-k_x^{M_2}x + (k_z^f - k_z^{M_2})z - (f - \omega_{M_2})t)}\right] \tag{3.1.11}$$

The second order correction is

$$\mathcal{U}''(z,t) = \mathcal{U}_0^f(\mathcal{U}_0^{M_2})^2 \frac{(k_z^f(\omega_{M_2}^2 - f^2))^2}{2(\alpha k_x^{M_2}\omega_{M_2})^2}$$
$$* \left[e^{i(2k_x^{M_2}x + (k_z^f + 2k_z^{M_2})z - (2\omega_{M_2} + f)t + \frac{\pi}{2})} + e^{i(-2k_x^{M_2}x + (k_z^f - 2k_z^{M_2})z - (f - 2\omega_{M_2})t + \frac{\pi}{2})} \right] \tag{3.1.12}$$

In the above, z is represents the zeroth order expansion of $\hat{z}$. This expansion is reasonable for low mode tides with depths much larger than the vertical displacement. However, as will be seen when two or more signals are utilized for the displacement, this 'self advection' expansion has far more stringent requirements than the ratio of displacement to wavelength. In addition, the assumption that local displacement is solely due to the gravest mode internal tide is convenient but not consistent with many observations which indicate significant variability in the vertical structure of semi-diurnal internal tides.

A very interesting result from eqn. 3.1.11 is that the inclusion of the semi-diurnal vertical structure has resulted in the structure associated with the two parts of the first order displacement solution being asymmetric. To illustrate this, compare the two phase terms in the first order correction for $t = 0, x = 0$:

$$R_z = \frac{(k_z^f + k_z^{M_2})}{(k_z^f - k_z^{M_2})} \tag{3.1.13}$$

This ratio of the sum frequency solution phase over the difference frequency phase will be approximately one when the inertial vertical wavenumber is much larger than the semi-diurnal vertical wavenumber. For semi-diurnal vertical wavenumbers that are only 'larger' than the inertial, there will be a distinct difference in the vertical structure of the two parts of the solution.

A significant impact of differing vertical structures is the possibility of asymmetric vertical profiles of amplitude between the two parts of the solution when considering sums of the solutions. For instance a solution with one $k_z^{M_2}$ associated with a mode one scale summed together with a solution based on a $k_z^{M_2}$ with a smaller scale will result in vertical patterns of enhancement/cancellation for each part of the solution. The nodes of these periodic envelopes will not be in alignment. A Eulerian measurement of the patterns could observe asymmetric amplitudes between the two frequencies in this case.

In models that do not consider vertical structure (such as Alford [2]) the amplitudes of the sum and difference frequency solutions are equivalent at all depths. One of the assumptions in the method is based on the vertical scale of the displacement in relation to the vertical scale of the inertial. It is evident now that including vertical structure is a necessary part of the description when extending the

simple model to more than one solution, even if the criteria of scale separation as needed for the single sinusoid displacement is satisfied.

It should be noted that the second order correction occurs at frequencies $(f - 2M_2)$ and $(f + 2M_2)$. Higher order corrections will result in sum/difference frequencies containing additional harmonics of M_2. The amplitude of the second order is dependent upon squared vertical structure terms. The second order could prove useful in identifying the advection process under observational conditions that resolve these short vertical wavelengths.

An estimate of the amplitudes at the summation and difference frequencies can be made with the following values:

$$\begin{aligned} \mathcal{U}_0^f &= .1\ (m/s) & \mathcal{U}_0^{M_2} &= .1\ (m/s) \\ k_z^f &= 2\pi/400\ (1/m) & k_z^{M_2} &= 2\pi/4000\ (1/m) \\ \omega_{M_2} &= 1.4 * 10^{-4}\ (1/s) & f &= 9.2 * 10^{-5}\ (1/s)(40deg) \\ N &\approx 5.2 * 10^{-3}\ (1/s) & \alpha &= \tfrac{\Delta\rho}{\rho_0} g \approx .01\ (m/s^2) \end{aligned} \tag{3.1.14}$$

We can express the first and second order amplitudes in terms of $k_z^{M_2}$ with the dispersion relation

$$k_x^{M_2} = \frac{\sqrt{\omega_{M_2}^2 - f^2}}{\sqrt{N^2 - \omega_{M_2}^2}} k_z^{M_2} \tag{3.1.15}$$

the first order amplitude is now

$$\mathcal{U}_0^f \mathcal{U}_0^{M_2} \frac{k_z^f \sqrt{N^2 - \omega_{M_2}^2} \sqrt{\omega_{M_2}^2 - f^2}}{2\alpha k_z^{M_2} \omega_{M_2}} = 0.02 \tag{3.1.16}$$

and the second order

$$\mathcal{U}_0^f (\mathcal{U}_0^{M_2})^2 \frac{(k_z^f)^2 (N^2 - \omega_{M_2}^2)(\omega_{M_2}^2 - f^2)}{2(2\alpha k_z^{M_2} \omega_{M_2})^2} = 0.002 \tag{3.1.17}$$

These estimates are constructed with specific values of M_2 and f vertical wavelengths representing the largest expected values. It would be prudent in any analysis using estimates derived from the single vertical displacement model to include at a minimum the inertial vertical structure associated with the location of the measurements and not a general estimate, as this term has a one to one impact on the amplitude.

The single sinusoid advection model (like that in Alford [2]), in which there is no vertical structure for the semi-diurnal tide, can be a useful estimate of vertical advection amplitudes measured in a Eulerian frame. However, it has been shown here that with the inclusion of the displacement vertical structure, the summation ($M_2 + f$) and difference ($M_2 - f$) phases differ with depth. This is potentially a useful discriminant in identifying advection in observations.

A second order solution to the advection model has been described above. The second order solution occurs at summation and difference frequencies between twice the semi-diurnal and the inertial. The amplitude of the second order has a squared dependence upon the vertical structure, and is found to be about one order of magnitude less than the first order under reasonable coefficient and wavenumber values. In records where a peak at $2M_2 + f$ is identified, it could be a unique identifier of the advection process if there is no significant $2M_2$ harmonic peak. Traditionally accepted non-linear processes within the internal wave field are unlikely to contain an interaction frequency not directly associated with the principal interacting free waves.

3.2 Extension of the Deterministic Displacement Advection Model

We have found that there is a substantial difference between a single periodic signal and one with multiple periods when considering periodic, reversible advection. However, it is necessary to extend the single sinusoid model to include multiple frequencies, since most of the data we have tested for vertical reversible advection signatures does not occur in regions where the semi-diurnal tide has a single frequency signal. The goal is to identify advection in the context of these deterministic signals that are often the most energetic waves in the internal wave band. If these semi-diurnal internal waves are also interacting non-linearly, the observed interaction frequency amplitudes will contain energy due to both Eulerian reference frame distortion and non-linear exchange of energy. A single sinusoid deterministic model is only a rough estimate to achieve this goal, and as such is unsatisfactory.

There are three major assumptions underlying the deterministic single sinusoid model. These assumptions may be accurate in some limited oceanic locations, but are unlikely to be valid globally. The assumptions are as follows:

- uniform stationary inertial motion,
- single low mode displacement signal, and
- constant amplitude displacement.

We have shown that vertical structure is very important for the displacement signal when creating an advection description. Addressing multiple displacement signals is the next obvious step. The semi-diurnal band contains multiple constituents which combine to create spatial and temporal variability. The spring/neap cycle is one of the major features. This cycle has periodicity which is comparable to the duration of the inertial peak energy events observed in the ocean. That fact alone makes the inclusion of multiple displacement signals absolutely necessary to characterize advection signatures if comparison is to be made with oceanic observations.

The predominantly low mode internal tide assumption is based upon the differing group velocities of generated structures. It is assumed that because the lowest mode propagates horizontally faster than the next mode, and so on, the majority of the open ocean any distance from generation sites is dominated by low mode internal tides. Observations in many open ocean locations however, reveal significant complexity in the vertical structure of the internal tide. In the research done by Hendry [34] using MODE data, roughly half the M_2 energy is established as deterministic, and required the first three modes to resolve. Dewitt et. al. [17] found complex vertical structure of the internal tide 100 km from its generation site in the North Atlantic, with some depths having peak modal energy at mode four. At Station Aloha in the North Pacific (believed to be in a beam of semi-diurnal tidal energy emanating form the Hawaiian Islands by Merrifield et al. [50]), Chiswell [12] found that three or four modes were necessary to account for semi-diurnal baroclinic tidal motion, with the second mode being most energetic. In the Western Equatorial Pacific, Feng et. al. [23] account for 40-60 percent of the semi-diurnal band across four moorings using the first few modes.

Given the extensive evidence indicating significant variability in the semi-diurnal tide in all major ocean basins, a single frequency, low mode displacement signal is not a good representation of reality. As a result, the vertical structure of two displacements is considered in the next model example. This will introduce a vertical variability resulting from the superposition of displacement signals.

Vertical structure will create amplitude variability spatially. Beat cycles will create amplitude variability temporally. But what about actual time dependent amplitudes, such as might be created by the refraction of the internal tides by mesoscale currents? This is far more difficult to address in a simple way. We will examine briefly how time dependent amplitude terms in the displacement signals will change the resulting expansions. Further descriptions incorporating time dependence more formally may be developed in the future.

To examine multiple displacements, we begin with two displacement signals advecting a single wave solution. For simplicity, only one dimension is utilized. The advected signal:

$$F(z,t) = Ae^{i(k_z^A z - \omega t)} + c.c. \tag{3.2.1}$$

The two functions representing displacements:

$$\begin{aligned} \Psi^B(z,t) &= B(t)e^{i(k_z^B z - \sigma^B t)} + c.c. \\ \Psi^C(z,t) &= C(t)e^{i(k_z^C z - \sigma^C t)} + c.c. \end{aligned} \tag{3.2.2}$$

We will advect the coordinate with the displacements via

$$z'(z,t) = z + \Psi^B + \Psi^C \tag{3.2.3}$$

There is an obvious difference in the formalism as compared with the single sinusoid case. The above equation can produce spatial and temporal variability arising from two simple input plane waves. Also, it is no longer easy to represent the input displacement functions in the new coordinate system. To illustrate:

$$\hat{\Psi}^B(z',t) = B(t)e^{i(k_z^B(z' - \Psi^B - \Psi^C) - \sigma^B t)} \tag{3.2.4}$$

$$\hat{\Psi}^B(z',t) = B(t)e^{(k_z^B z' - \sigma^B t)}e^{-ik_z^B(\Psi^B + \Psi^C)} \tag{3.2.5}$$

where the hat represents functions transformed to the new coordinate system. Focusing on the second exponential, expand in a multivariate Taylor series about $z = 0, t = 0$

$$\begin{aligned} e^{-ik_z^B(\Psi^B+\Psi^C)} &= e^{-ik_z^B(B(0)+C(0))}[(1)_{0th} \\ +k_z^B(B(0)(k_z^B z - \sigma^B t) - iB'(0)t + C(0)(k_z^C z - \sigma^C t) - iC'(0)t)_{1rst} \\ -\frac{ik_z^B}{2}((B(0)k_z^B z - (B(0)\sigma^B + iB'(0))t)^2 \\ +(C(0)k_z^C z - (C(0)\sigma^C + iC'(0))t)^2)_{2nd}] \end{aligned} \tag{3.2.6}$$

The first result arising from this description is the remaining amplitude and phase change at zeroth order. To replicate the result from the single sinusoid advection, we need the condition:

$$B(0) + C(0) = 0 \tag{3.2.7}$$

That is a rather severe restriction on the input functions. In terms of yielding a zero order Taylor expansion term equalling one, the requirement is:

$$\Psi^B + \Psi^C = 0 \tag{3.2.8}$$

The Taylor expansion will be the most successful when expanded about extinction points in the (z, t) plane that arise from the superposition of the input waves. It is not safe to assume that the method used in the single sinusoid case is a proxy for multiple inputs. Upon inspection, even simple time dependent amplitude functions will directly affect the result.

Beyond this point a constant amplitude displacement (no time dependence) will be utilized. Under a constant amplitude, the points about which the expansion is made require careful treatment. For instance, we could assume that the simple case

$$e^{(\Psi^B+\Psi^C)} = e^{\Psi^B} e^{\Psi^C} \approx 1 + h.o.t. \tag{3.2.9}$$

is valid, yet it will only be correct under the restrictive condition when the expansion location results in

$$\Psi^B = \Psi^C = 0 \tag{3.2.10}$$

Given these restrictions, the original function can be reasonably expanded about the case

$$Z = \hat{\Psi}^B(z', t) + \hat{\Psi}^C(z', t) = 0 \tag{3.2.11}$$

This results in a simple expression

$$\hat{F}(z', t) = Ae^{i(k_z^A z' - \omega t)} e^{ik_z^A Z} \tag{3.2.12}$$

which can be expanded to

$$\hat{F}(z', t) = Ae^{i(k_z^A z' - \omega t)}[(1)_{0th} + (ik_z^A Z)_{1rst} - ((k_z^A Z)^2)_{2nd}] + h.o.t. \tag{3.2.13}$$

The ratio of successive terms in the expansion when phase averaged results in

$$k_z^A(B + C) \ll 1 \tag{3.2.14}$$

The first order solution is

$$\hat{F}_{1rst} = ik_z^A A e^{i(k_z^A z' - \omega t)}(\hat{\Psi}^B(z', t) + \hat{\Psi}^C(z', t)) \tag{3.2.15}$$

This is now a linear summation of the single sinusoid solutions for B and C displacement signals under the conditions above regarding the self advection and the condition on Z. Clearly those conditions introduce complexity into the estimation process. The most significant difference with respect to the single sinusoid model advection model is the dependence on temporal and spatial information to accurately predict the advection amplitude. Explicitly stated, a measurement at a single point can be made, and modulation of the resulting amplitude of the Doppler shifted frequency can result from the summation of the input displacements. This occurs with no change in the magnitude of the input amplitudes.

Let me restate this important point a different way: with advection from two (or more) waves, the amplitudes of the motions at the periodic Doppler shifted summation and difference frequencies will have substantial temporal variability even when the individual amplitudes of the input advecting waves are constant. Obviously, this temporal variability should be reduced somewhat with temporal averaging; however, in the case of inertial internal waves, the intermittency time scale of these waves, being similar to (or smaller than) a spring-neap cycle, suggests that temporal averaging will be insufficient to mitigate the temporal variability at the Doppler shifted frequencies.

Figure 3.1 shows a clear distinction between single coordinate displacement vs. multiple displacement models. The case with two displacement signals, each having separate vertical structures, heavily modifies the distribution of energy. There are significant modulations in the energy in a given band across the depth range for the case with multiple displacement.

In the vertical profile of PSD (Figure 3.1) and in the single depth PSD (Figure 3.2) we have plotted only a single plane wave with vertical wavenumber and inertial frequency. Gaussian white noise with SNR of 10 is added to the wave. The coordinate displacements have semi-diurnal frequencies and vertical sinusoidal structure. The displacement signals only operate on the coordinate system, and are not added to the analyzed plane wave.

Single depth spectra for the case with single displacement and for one with multiple displacements are presented in Figure 3.2. A very interesting result that can be seen is the significant broadening of the spectral peaks when multiple displacements are involved (corresponding to the lower panel). This effect is especially noticeable at the IWISC frequency peak. The highest magnitude of the 'peak' (which is more of a broad elevation) is now distinctly red-shifted. If this scenario were observed with a single Eulerian point, it would be difficult to determine what process had created the energy distribution. Even more problematic for insightful analysis would be the inclusion of many other signals, as is the case with the oceanic internal wave band.

As we are interested in characterizing observations consisting of multiple advecting inputs, it would be prudent to simply create time series of deterministic advected inertial internal wave solutions advected by multiple displacements associated with the semi-diurnal internal tide. Given the simple, one dimensional example in figures 3.1 and 3.2, highly variable distributions of advected energy signatures are not unexpected, and may be considered the norm. It is apparent that establishing the boundaries of that variability is a necessary step in identifying what techniques will be useful in distinguishing between advected energy observed in an Eulerian coordinate system and true nonlinear energy transfer.

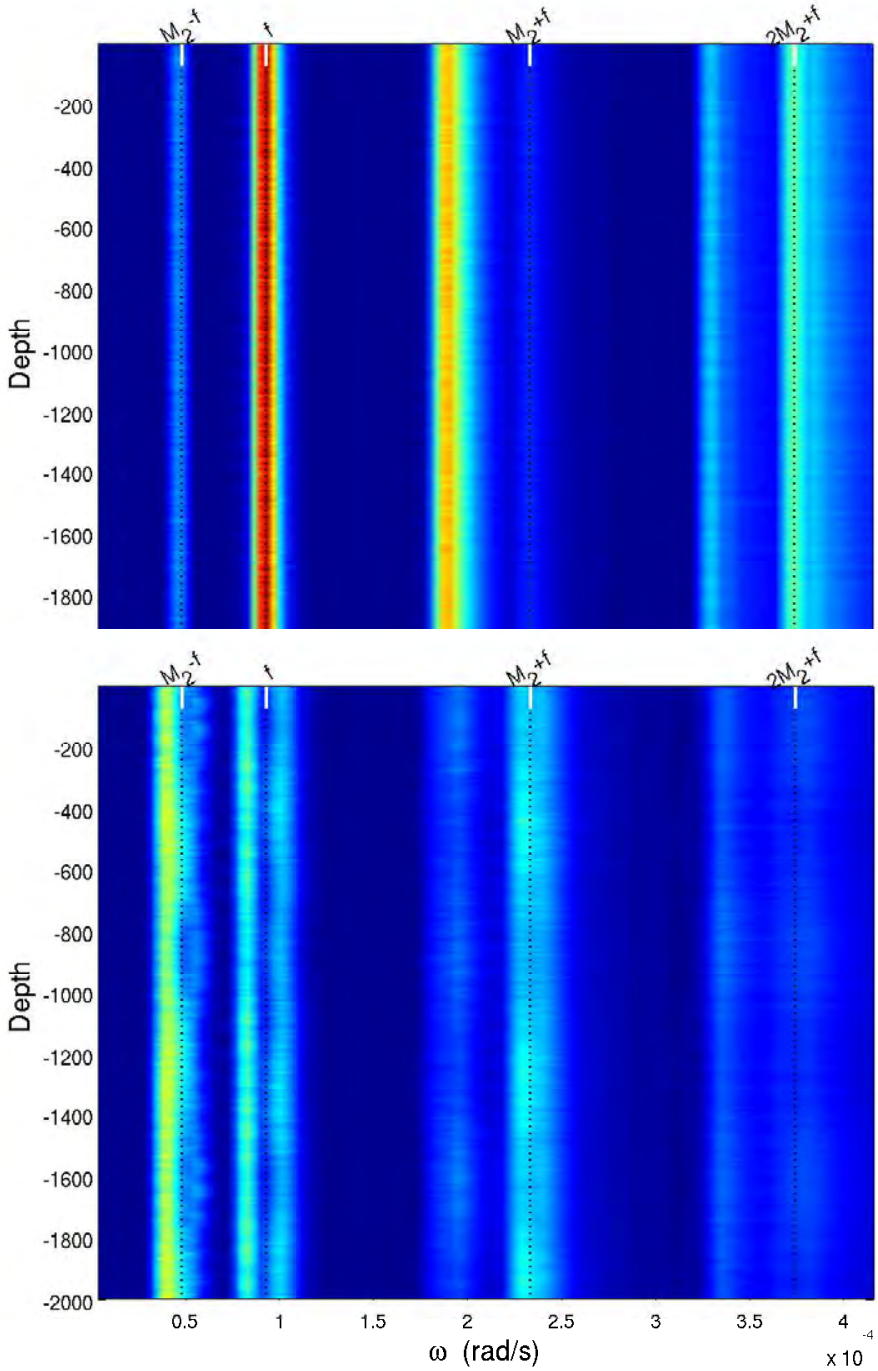

Figure 3.1. Vertical profile of PSD $((m^2/s^2)/(rad/s))$ for simple inertial frequency vertical plane wave ($L_z = 140m$) under periodic vertical coordinate displacement. The top panel has M_2 coordinate displacement structure with $L_z = 1000m$ and 75 meter amplitude. Bottom panel displacements are M_2 and S_2 vertical plane wave structures. Bottom panel M_2 has $L_z = 1000$m and 70m amplitude; S_2 has $L_z = 600$m and 50m amplitude. The inclusion of multiple frequencies in the displacement results in a vertical modulation envelope for the interaction frequencies and a relative broadening of the interaction bands. This figure only depicts the coordinate shifted inertial signal.

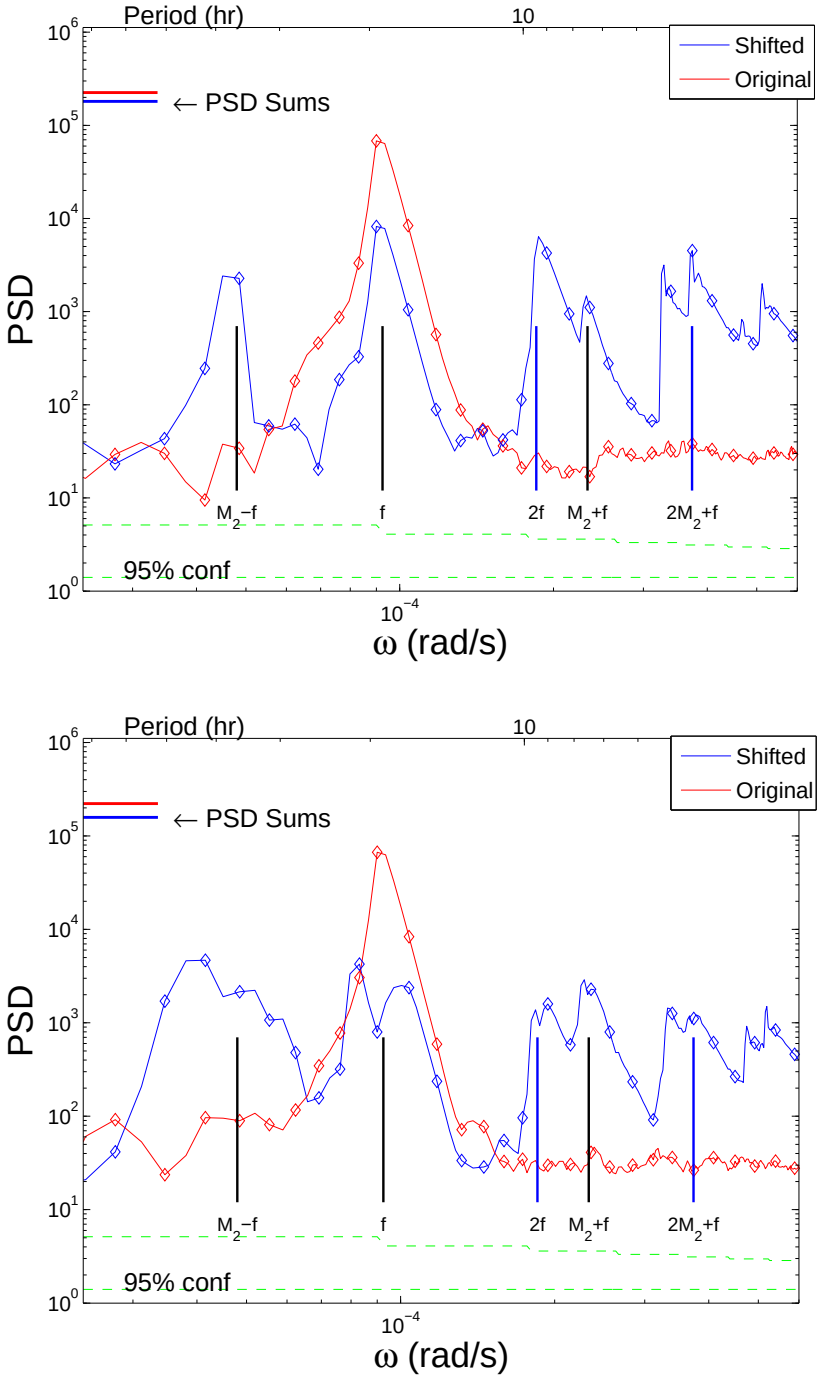

Figure 3.2. Single depth (600m) PSD for the spectral depth profiles in figure 3.1 with the original signal in red. Indicated in the upper left is the sum PSD across all frequencies. The top panel, with only M_2 displacement, has narrow peaks at interaction and harmonic frequencies. The bottom panel, with both M_2 and S_2 displacement, has broader, less defined peaks especially at the difference frequency $M_2 - f$. 95% confidence intervals for each independent PSD estimate are indicated by the dashed green lines at the bottom; the diamond symbols indicate the frequency intervals between independent PSD estimates.

3.3 Description of Multiple Deterministic Advection Model

It has been demonstrated above that even two simple displacement signals with vertical structure will produce a complex coordinate transformation. Given this, careful consideration must be made to include the influential displacements when attempting to recreate a velocity field that has been subject to reversible vertical advection. For the case of inertial interaction with semi-diurnal internal tides, that means modeling the dominant constituents that make up the semi-diurnal band. If the first four constituents are utilized, and a vertical normal mode description is desired with one mode per constituent, there results eight linear plane wave displacement signals.

Since even two displacement signals produce quite a complex analytical representation, we have chosen to accomplish the summation numerically to replicate a velocity field that might be expected to reasonably simulate the variability in real ocean observations. The simulated velocities, with and without advection turned on, will permit us to test analysis methods for discriminating simple advection from energy transferring non-linear interactions using Eulerian data.

A separate benefit of creating a plane wave summation model to vertically advect an inertial wave is the simplicity of switching from an idealized, stationary, infinite inertial internal wave to a more realistic 'packet' like inertial depiction. This is important, as both the vertical wavenumber and the spatial distribution of inertial energy have a significant impact on the amplitude of the advection signal.

A summation of linear internal gravity wave solutions is used to construct an advected velocity field. For a consistent derivation of the basic internal wave equation, examples can be found in the second chapter of Leblond and Mysak [41]. Their simulation is composed of plane wave solutions for two frequency bands; the inertial and the semi-diurnal. Consideration is also made regarding the temporal and spatial variability of observed inertial energy.

For the inertial band, one of the primary features emphasized in the model is the temporal variability associated with specific forcing events. In ocean velocity records, the inertial energy is highly dependent upon the location, strength, and duration of the wind forcing. This sets the"characteristics" of the energy, which then propagates as internal waves in a (presumably) slowly changing media. The amplitude of an interaction frequency associated with the inertial may have amplitude variability caused by many different physical processes. Propagation of the wave packet through Eulerian sensors will have temporal variability. Similarly, large scale horizontal advection can induce observed temporal variability.

Given that Eulerian measurement of the time variability of IWISC is dependent upon the temporal variability of the forcing and the advection of energy past a measurement point, establishing expected

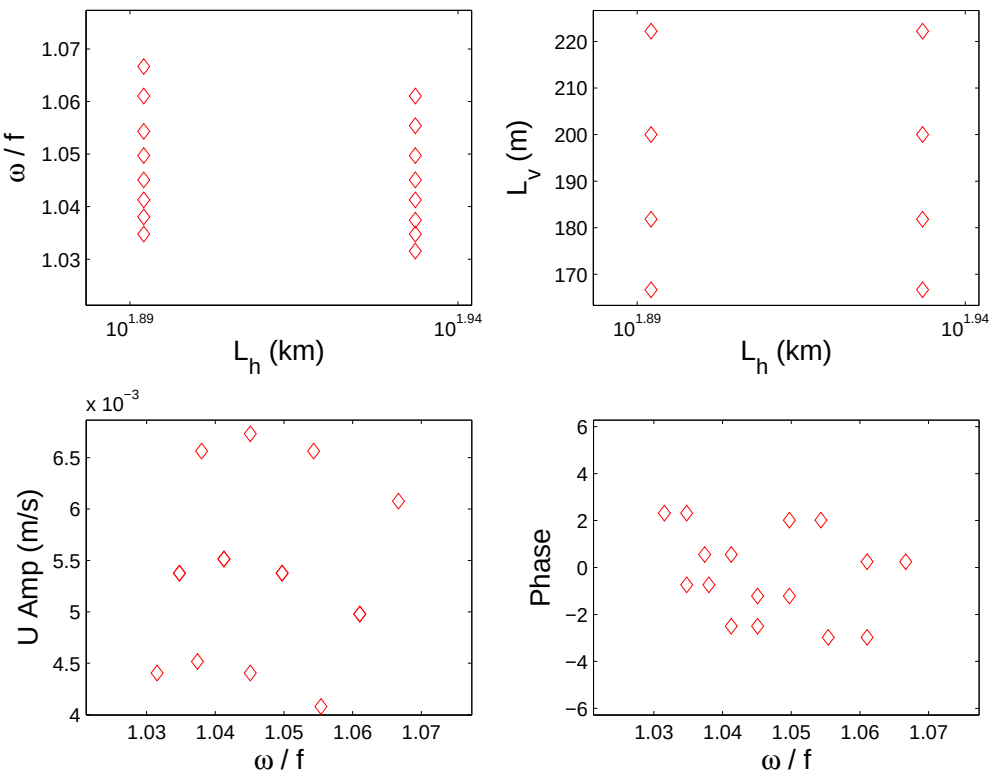

Figure 3.3. Wavenumber and frequency values for the inertial wave packet reconstruction utilized in the model are depicted in the top two panels. Amplitude and phase for each are indicated in the lower panels.

signatures of interaction with standard techniques will assist in the interpretation of observed features. We begin with an horizontally infinite, downward propagating, inertial internal plane wave with frequency $1.05f$. A three dimensional Hanning window is then applied in order to mimic an inertial wave packet. This wave is then decomposed into 12 three dimensional Fourier components which we find adequately replicates an inertial wave packet for the purpose of IWISC simulation. These wavenumber components correspond to slightly different frequencies according to the internal wave dispersion relation as shown in figure 3.3. The same figure also depicts the amplitudes and phases of the Fourier components. The wavenumbers and frequencies are shown in figure 3.4 in relation to contours of vertical group velocity.

In the following simulations we examine the consequence of latitudes above and below the critical frequency. Two latitudes are examined, 21° North corresponding to HOME data, and 40° North, a

latitude close to that of multiple historic current meter records in the North Pacific analyzed in chapter 2.

In figure 3.5 the time series amplitude is depicted for the inertial and semi-diurnal bands in the model. This is a single depth selection at 500m for the 21° N simulation. The time interval in the simulated data is 10 minutes. Fourier reconstructed curves were obtained with a band pass filter of ±3% around the respective center frequencies. Envelope curves were obtained by low pass filter (50 hrs) aplied to the total velocity magnitude.

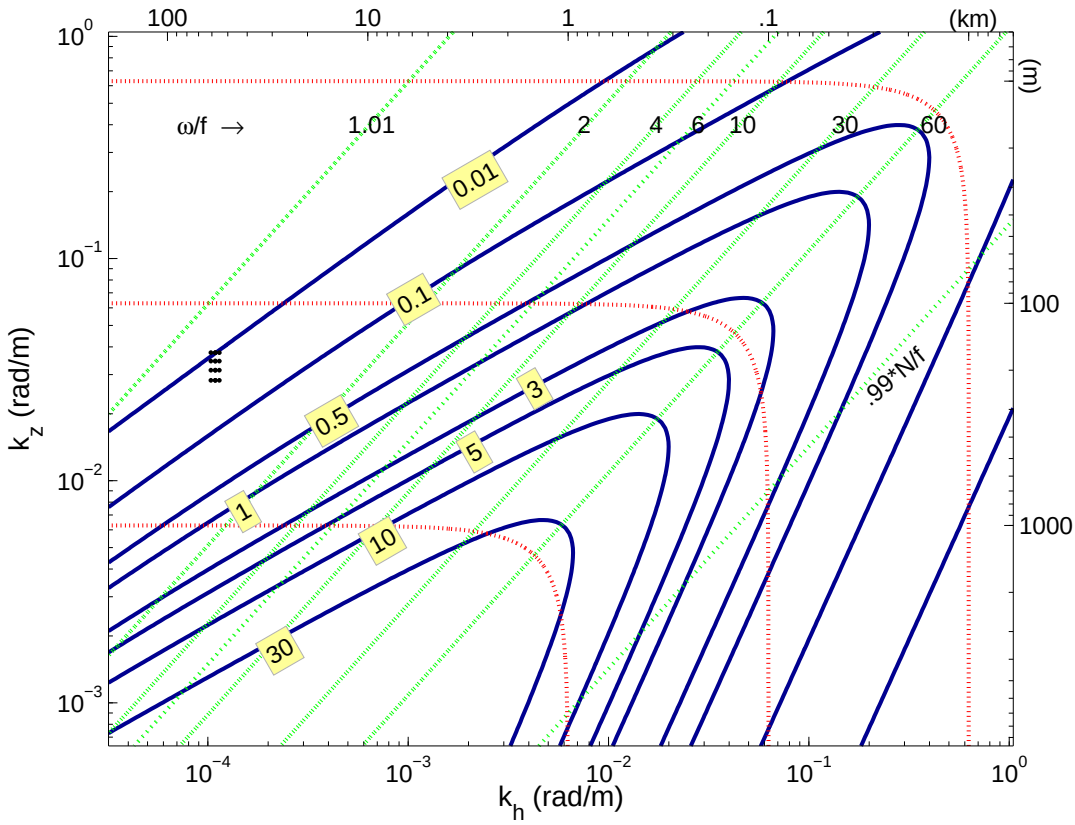

Figure 3.4. Internal wave vertical group velocity (cm/s) with inertial wavenumbers used in the synthetic model indicated with black stars located near $k_h = 1 * 10{-}4$ and $k_z = 3 * 10{-}2$. Lines of constant frequency are indicated in green. Constant total wavenumber is indicated in red. The buoyancy period for this simulation is 20 minutes.

The inertial curve in the top panel of figure 3.5 does have envelope variability not unlike observed oceanic records. The modeled inertial energy is propagating downward, hence the steady increase over the full 90 days. To simulate a very localized three dimensional inertial wave packet, which would

be more ‘event’ like, and hence closer to the observed peak energy inertial waves forced from storm systems, orders of magnitude more inertial input wavenumbers would be required. This may be useful in the future, but negates the utility of modifying the simulation on a regular basis due to computational restrictions.

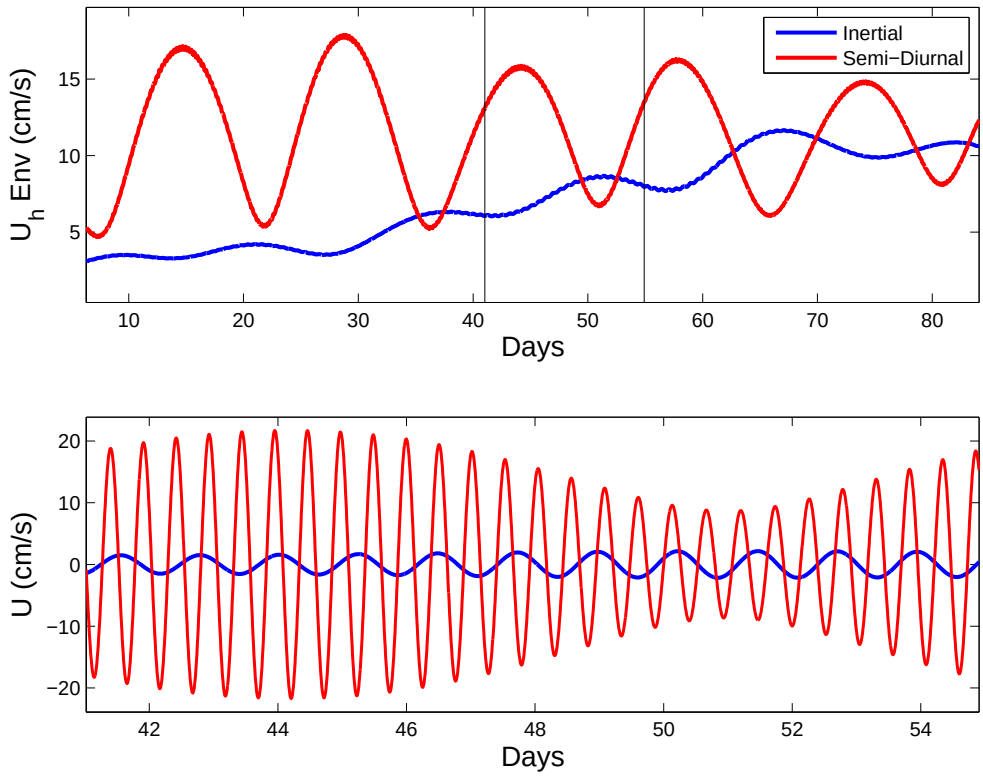

Figure 3.5. In the top panel amplitudes of horizontal velocity are Fourier reconstructed for the inertial and semi-diurnal bands at a selection depth of 500m for the plane wave summation model. A snapshot of the indicated time period for each band is shown in the bottom panel. See text for further description.

The model has constant stratification and no boundaries. We have used a reasonable vertical wavelength for the inertial of between 140 and 200 meters. Observed values may vary significantly from this, but for most regions, the scale separation between the inertial vertical and semi-diurnal tide’s lowest modes (assumed to contain the bulk of semi-diurnal energy) is large enough to allow for a substantial inertial vertical wavelength range. This implies that in constructing the semi-Lagrangian time series, we need to evaluate the summation of input solutions over at a minimum the vertical scale which is the inertial scale plus the maximum displacement of the semi-diurnal tide.

The semi-diurnal is represented by the first four constituents, whose relative amplitude ratios are taken for the latitude, longitude, and time period from the TPXO6.2 tidal model [20]. Each of the four solutions ($M_2S_2N_2K_2$) has been constrained to an "equivalent depth scale" of 4000 meters, in order to roughly recreate the structure of the first mode semi-diurnal tide in an ocean of 4 km depth. For each tidal constituent, both an upward and a downward propagating plane wave is input to replicate a modal structure. The internal wave consistency relation [56] has been adhered to in creating the "mode" structure.

Neglecting higher semi-diurnal internal tide modes is an important step in isolating the specific reversible advection signature. However, the construction lends itself readily to higher modes, multiple modes, or modes spread between tidal constituents. It would be beneficial to conduct future experiments to examine the variability under those differing situations. Especially with high resolution data sets to constrain the model input structures. A simulation like this may prove useful near topographic source regions of the internal tide, where higher modes will be influential in the distribution of interaction energy.

To simulate the vertical advection of inertial motion by the semi-diurnal tide, we calculate the displacement associated with the tidal solution and use the displacement to "advect" the inertial wave. These Eulerian time series are then combined into one velocity record and given Gaussian white noise with a SNR of 20.

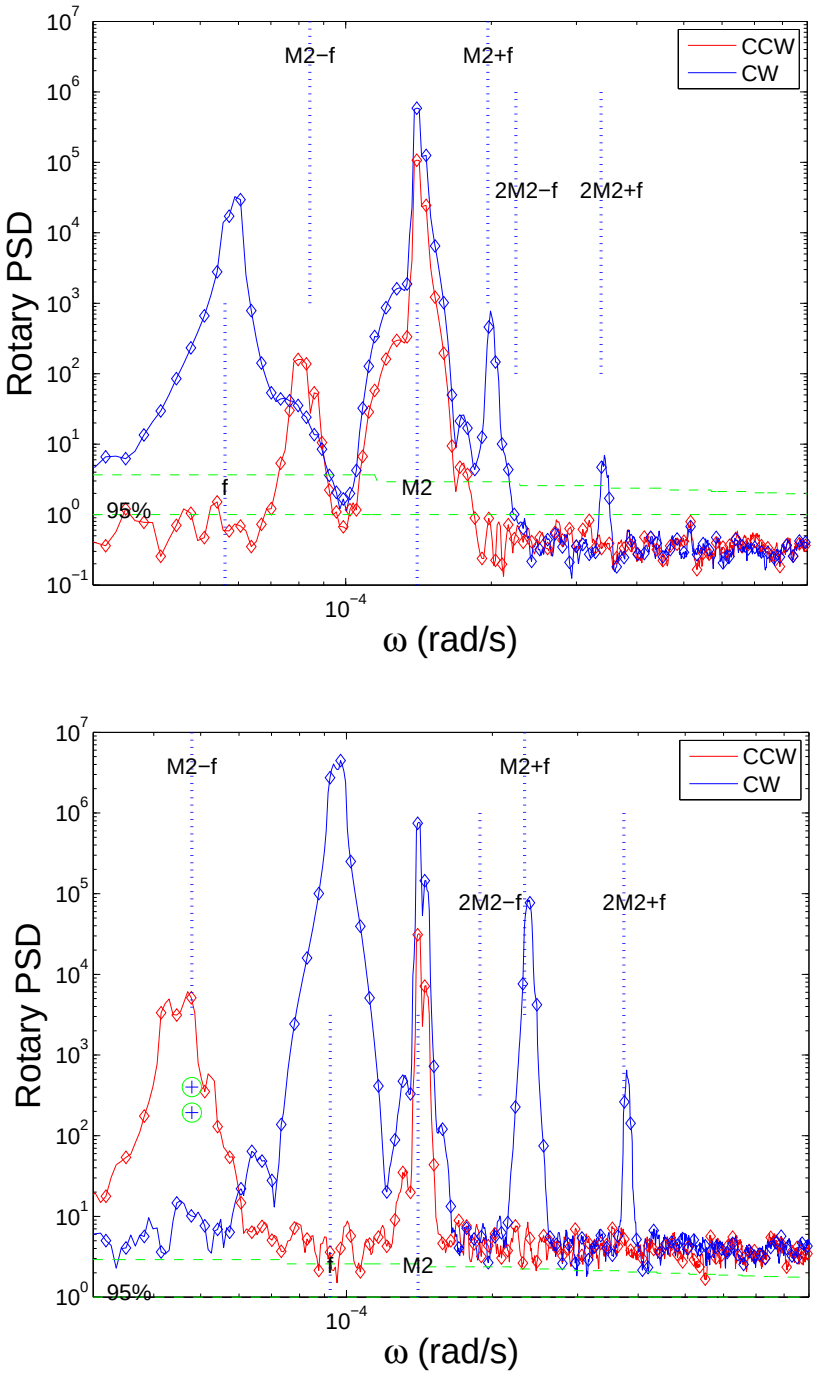

Figure 3.6. Spectra for two latitude ranges of the Synthetic Model. On the top is the model corresponding to the HOME mooring A2 at 21 degrees north. On the bottom is a model for 40 degrees north. Notice that for latitudes equator-ward of +/- 28.9 degrees latitude, the IWISC (difference frequency $M_2 - f$) interaction band occurs in the internal wave range. The record lengths are 90 days long. Independent PSD estimate 95% confidence intervals are indicated by the dashed green lines at the bottom; the diamond symbols indicate the frequency intervals between independent PSD estimates.

The spectra of the synthetic time series are shown in figure 3.6 for two latitudes, 21° N and 40° N. The peaks associated with the advection mechanism in this regard are the $M_2 - f$ (IWISC) and $M_2 + f$ frequencies. Note that the $M_2 - f$ frequency moves from super inertial at latitudes equator-ward of 28.9 degrees to sub inertial at higher latitudes.

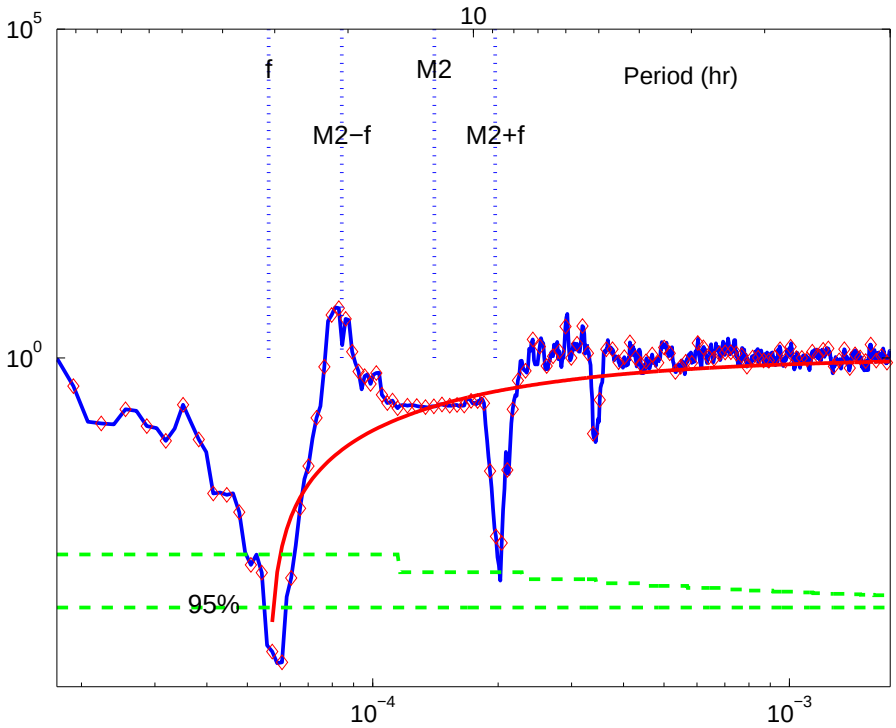

Figure 3.7. Consistency relation for the simulated velocity record created for 21° N latitude. Both sum ($M_2 + f$) and difference ($M_2 - f$) advection signature frequencies occur in the free internal wave regime. These two frequencies bands show deviation from theoretically predicted consistency ($(\omega - f)/(\omega + f)$). Independent PSD estimate 95% confidence intervals are indicated by the dashed green lines; the diamond symbols indicate the frequency intervals between independent PSD estimates.

There are other dynamics such as barotropic motion and forced oscillation that could produce similar deviations from consistency at frequencies in this range. As a test for non-linearity vs. advection however, it is insufficient. Resonant non-linear interaction can exchange energy among consistent internal waves. Other non-linear mechanisms could result in forced motion, violating consistency. Though consistency breaking could help in the characterization of reversible advection, the goal of decisively identifying non-linear mechanisms in a velocity field that has advection signatures associated with the

non-linear interactants still remains. This remains central to characterizing IWISC and potential sum frequency ($M_2 + f$) energy exchange.

Energy exchanging non-linear signatures will remain in both Eulerian and Lagrangian frames. However, reversible advection will disappear with a coordinate transformation to the advected frame. This motivates the S-L inversion technique used in previously mentioned studies. It is applicable to the IWISC problem as well, and we have applied it to existing data containing IWISC spectral signatures. To benchmark the utility of the S-L inversion, it has been tested against the plane wave summation model constructed in this section.

The details of the S-L inversion technique are;

- from model velocity field the band passed semi-diurnal vertical velocity is calculated,
- this semi-diurnal vertical velocity is then integrated in time to obtain displacement,
- a depth range of points bracketing the displacement depth at each time is selected,
- a PCHIP curve (Piecewise Continuous Hermite Polynomial) is fit to horizontal currents across the the selected depth range, and
- the curve fitting horizontal velocity value matching the displacement depth is obtained.

A comparison of model spectra, in both Eulerian and semi-Lagrange reference frames can be seen in figure 3.8. Clearly the S-L method reduces the energy within the interaction frequencies ($M_2 + f$, $M_2 - f$, $2M_2 + f$, $2M_2 - f$) to below statistical significance. This is the expected result, as we are effectively 'reversing' the reversible advection. However, as the S-L inversion is a 'reversible' advection process itself, the wave field now contains semi-diurnal energy and noise in addition to the inertial wave. This means that any horizontal currents in the field with high vertical structure will be affected. In other words, if there are any high vertical wavenumber flows, the S-L inversion will be redistributing energy in the spectra beyond the reversing of the reversible advection signature.

For the spectra in figure 3.8, there is a small peak at $2M_2$. This is due to the S-L inversion acting on the semi-diurnal signal. In essence, this is like a self advection product of semi-diurnal displacement acting on semi-diurnal horizontal flow.

This significant reduction in the reversible advection signature is seen in the PSD for the modeled velocity field at 40° N as well. Shear spectra is examined for each latitude, with the results from the 40° model shown in figure 3.9. The rotary shear PSD has a higher dependence on local vertical structure, and yields results with higher variability between interaction frequencies than the rotary

velocity PSD. The highest vertical wavenumber structures in the model are the summation interaction frequency structures. These have vertical wavelengths not less than a hundred meters with the chosen model inputs. For this analysis, five meter shear was utilized. In the rotary shear PSD figure, there is a distinct shear peak at the difference frequency which is removed in the S-L inversion. The shear at $M_2 + f$ is weaker, but is removed as well.

It has been demonstrated here that the S-L inversion technique effectively removes energy at advection interaction frequencies from Rotary PSD of currents and shear of the plane wave summation model. This technique uses semi-diurnal band passed vertical velocity to determine displacement. The very effective result from this technique would be hampered with displacement vertical structures of a higher mode and differing among constituents. With multiple displacements, there is a vertical scale associated with the enhancement/cancellation structure of the superposed vertical oscillations. If the displacement amplitude is of the same order as this scale, significant error could result from the S-L inversion.

The plane wave summation model has produced a velocity field that replicates significant features of observed oceanic velocities. This model uses displacement from four tidal constituents in the semi-diurnal internal tide to advect the vertical coordinate. The output is uniquely suited for testing techniques that should be able to differentiate between energy transferring processes and pure advection. The model is a result of investigating the single sinusoid advection model utilized in previous research. Our research determined that:

- vertical advection by itself produces oscillations at the interaction frequencies that violate internal wave consistency; the resultant motions are not free internal waves,
- higher order PSD peaks (harmonics of the interactants), when observed, can be a unique test of vertical advection,
- vertical structure of the input displacement signal produces phase asymmetry in the resultant advected signal between the sum and difference frequencies,
- multiple frequency displacements (semi-diurnal constituents) can broaden reversible advection spectra peak signatures,
- a S-L inversion methodology (to be later employed on observed data) was successfully tested on the plane wave summation model significantly reducing the spectral signature of reversible advection, and
- the S-L inversion itself can redistribute spectral energy.

To recap the accomplishments in this section, a realistic plane wave summation model was constructed which is easily adapted to local or regional observed parameters. The modeled semi-diurnal internal tide depends upon time, Lat/Lon, and the users choice of vertical modes. The inertial oscillations can be tuned to match observed vertical wavelength and amplitude, with a three dimensional packet like structure. The output is easy to analyse and visualize, yielding a comprehensive picture of the high spatial and temporal variability that could be expected in oceanic observations. This variability arises from simple linear plane waves and semi-diurnal vertical advection.

We have demonstrated that the S-L inversion technique can correct Eulerian current observations to yield spectral energy frequency distributions that do not have the advection spectral peaks in PSD. This validates the inversion as a tool for diagnosing vertical advection, but says nothing about identifying energy exchanging non-linear interactions. The modelled field is perfectly suited to test techniques which are designed to identify non-linear interaction. Bicoherence and bispectra have been found to be useful indicators of possible non-linear interactions as discussed in the next section. What needs to be determined is the sensitivity of these methods to vertical advection.

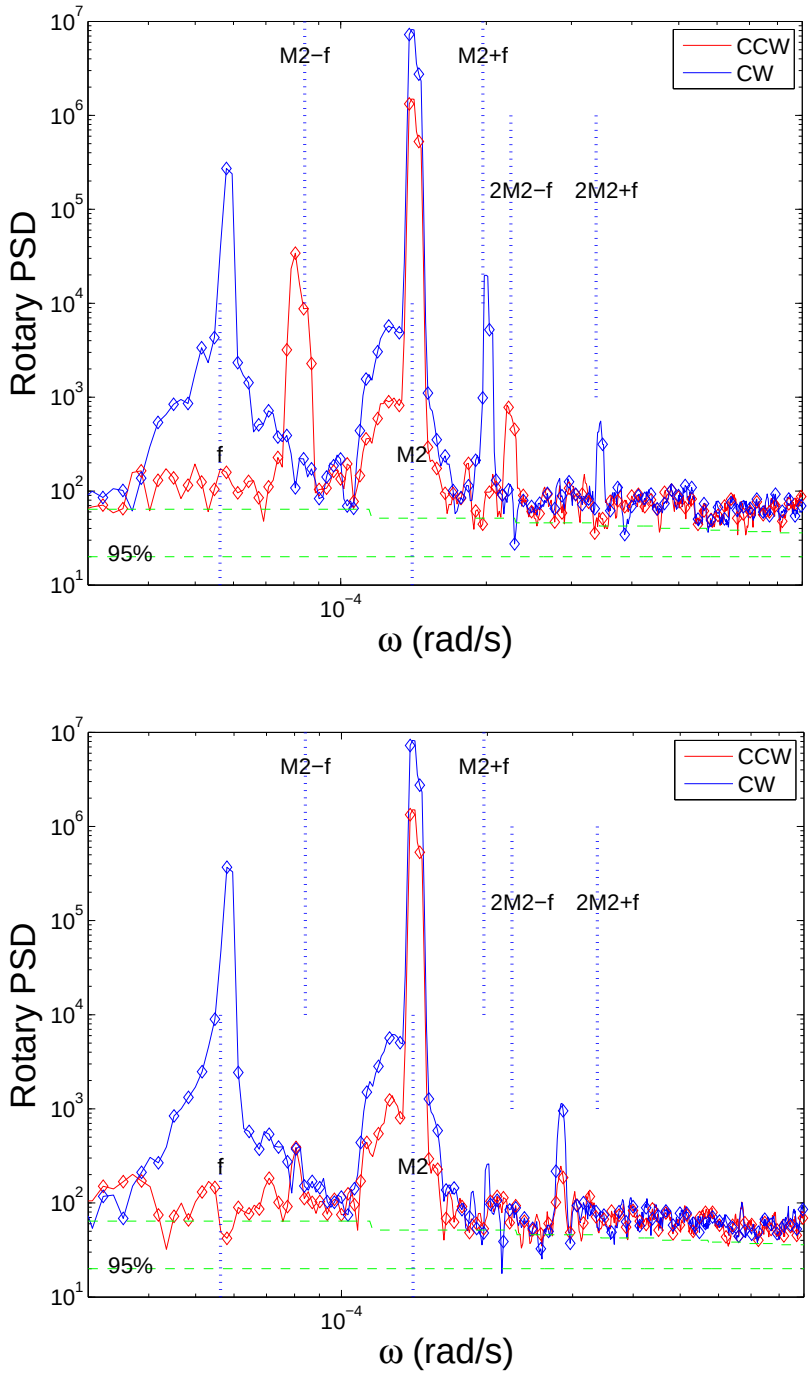

Figure 3.8. Rotary PSD $((m^2/s^2)/(rad/s))$ for the plane wave summation model at 21° N latitude. On the top is the PSD from the plane wave summation model with semi-diurnal displacement of the inertial motion. The bottom panel is the result of Semi-Lagrange (S-L) inversion of the modeled data. The S-L inversion is described in the text. Independent PSD estimate 95% confidence intervals are indicated by the dashed green lines at the bottom; the diamond symbols indicate the frequency intervals between independent PSD estimates.

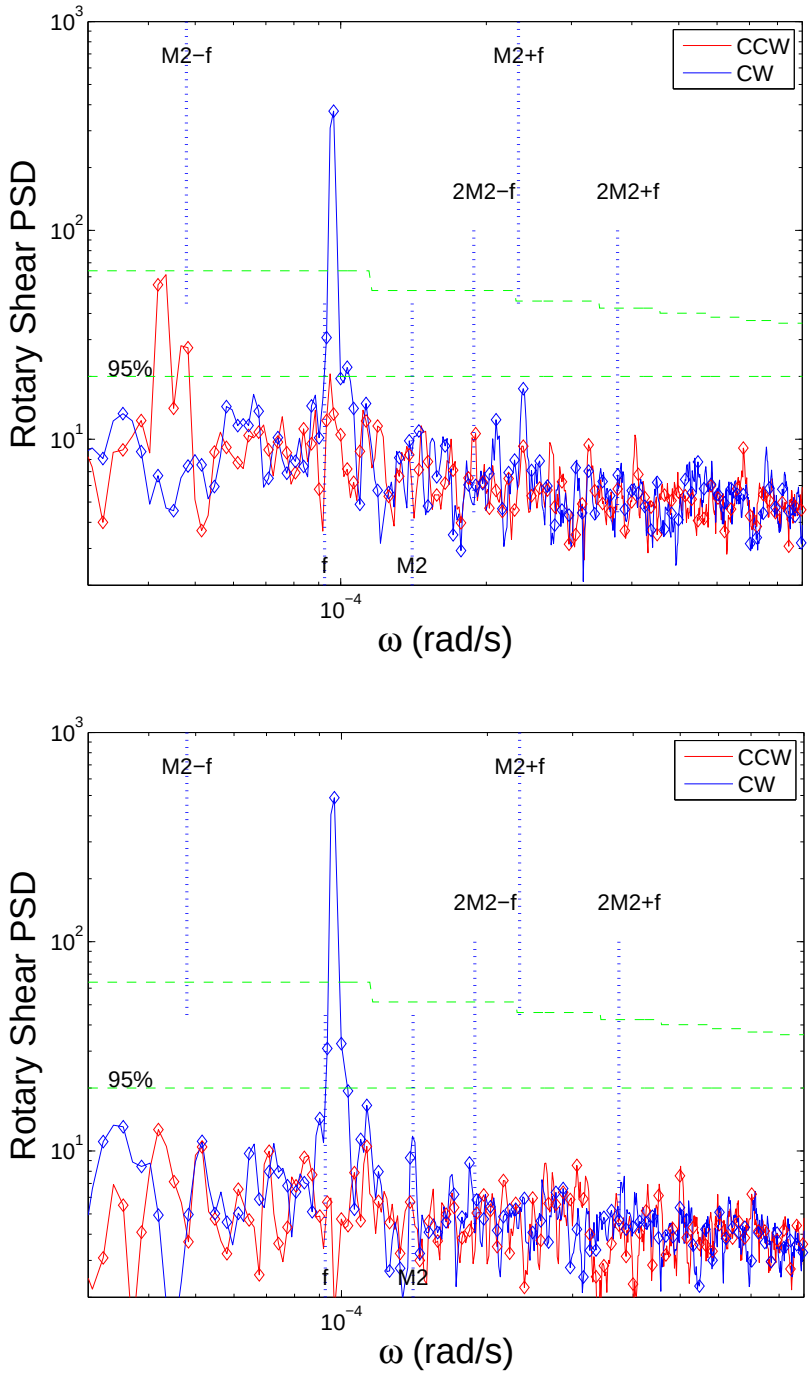

Figure 3.9. Rotary shear spectra $((1/s^2)/(rad/s))$ for the plane wave summation model at 40 degrees corresponding to the data used in figure 3.8 displaying PSD. In the bottom panel, after the S-L inversion, the shear associated with the IWISC interaction band has been diminished. Dashed green lines indicate 95% confidence interval.

3.4 Evaluation of Bispectra and Bicoherence for Delineating Non-linear Interactions

Powerful tools for determining non-linear interaction among observed oscillations in a time series are the higher order spectral analysis techniques of bispectra and bicoherence. These techniques have been utilized successfully in oceanographic applications to identify nonlinear energy transfer following the seminal work by Hasselmann, Munk, and MacDonald [32]. Bispectra became a integral tool in the description of shoaling surface gravity waves with the pioneering work of Elgar and Guza [22].

The bispectral technique was extended to internal waves, but without the same apparent success seen in surface wave interactions. Neshyba and Sobey [59] found bispectral evidence of internal wave non-linearity in the Arctic Ocean from temperature data collected at Ice Island T3 (85° N). Their evidence indicates two sets of interactions, one type between three internal waves and another between two internal waves and a zero frequency structure. However, they can not conclusively determine the interacting waves due to lack of wavenumber information. McComas and Briscoe [49] investigate the technique in the context of broader internal wave non-linear interaction and address why there had been little conclusive application.

The application of bispectra to investigate internal waves was perhaps maligned for its inability to enlighten the underlying mechanisms which create the internal wave spectra and its representations, specifically the GM spectra. A quote from McComas and Briscoe [49]: "Computations using a Garrett and Munk spectral model demonstrate the futility of bispectral analysis for indicating ocean internal wave interactions." Indeed, multiple complexities are pressent when interpreting higher order statistics of the internal wave band and they can lead to assumptions that have little evidentiary substance. In several recent cases (examples in the following dicsussion), the tool has proven successful when applied to specific situations, but not as a general diagnostic. Clearly a statistical measure that relies heavily upon multiple realizations (such as bispectral analysis) will be inadequate to elicit useful interaction information from an empirical broadband spectral description such as GM, almost by definition.

A more pressing issue arises in McComas and Briscoe [49], and that is the subject termed "kinematic contamination", sometimes referred to as a simple advection mechanism or reversible advection. With bispectral analysis, true nonlinear interactions can have the same signature as simple advection when viewed in an Eulerian frame. It has been speculated that simple advection explains some of the common empirical spectral representations in the ocean and atmosphere [67] [36]. With these considerations in mind, a close look at the difference between the advective mechanism and energy exchanging

non-linear processes is necessary for interactions that may occur to semi-diurnal tides and near inertial internal waves in the context of bicoherence/bispectra.

There has been recent renewed interest in the application of bispectra analysis to internal wave non-linear interactions. With the advent of high resolution numerical models, bispectra could be an important tool in establishing the non-linear interactions that determine the internal wave spectrum. Furuichi et. al. [26] analyzed the output of a high resolution two dimensional model and found interaction results supporting the Parametric Subharmonic Instability (PSI) mechanisms enhancement at the PSI critical latitude (28.9°). Carter and Gregg [7] recently identified near inertial peaks in bicoherence, specifically at possible subharmonic interaction frequencies.

One difficulty in the application of bispectra and bicoherence to the specific interaction between inertial waves and the semi-diurnal internal tide with a spring/neap cycle concerns the "inability" to resolve the independent frequencies given the short inertial event durations. The window length required (14 days) to adequately resolve the internal tide constituents is typically longer than a peak inertial event. Usually, the intermittency of the inertial events is such that in any given length of data, there will be few windows containing information from the peak inertial event. Averaging all windows in this situation results in diminished bicoherence.

A method that has been found to be more successful in extracting information from intermittent signals than Fourier analysis is wavelet analysis. The use of wavelet transforms in bispectra analysis is a proven approach in turbulent dynamics to identify non-linear interactions where one or more of the components has a time dependent amplitude envelope. As an example, wavelet bicoherence has been used in the aeromechanical field to identify nonlinear interactions in turbulent flow by Gurley [30]. A following section deals briefly with the application of wavelet rotary bispectra to the IWISC problem. New approaches developed here illuminate specific details in the flow fields.

The analysis of internal wave band processes is particularly suited to rotary decomposition. Rotary bispectra and bicoherence were developed for oceanographic applications by Yao et. al. [94] in 1975. This methodology was applied to wind forcing of the upper ocean by the same authors [95]. Twenty years later, Liu et. al. [45] incorporated wavelet transforms into rotary spectral analysis to analyze time localized inertial activity in Lake Michigan. The presentation of wavelet bispectra and bicoherence here is in line with extending these techniques to understand better the specific interaction between inertial and semi-diurnal internal tides.

More generally, the rotary bispectra/bicoherence analysis and visualization developed here can provide useful insight into potential sources of indicated interactions in complicated flow regimes.

Furthermore, rotary wavelet bispectra/bicoherence, though a new method, should prove invaluable in the future for identifying internal wave interactions of limited duration.

3.4.1 HOME C2 Mooring

Many observations have been analysed for the characteristic signature of IWISC in rotary PSD (for instance, see section 2.3). Spectral energy peaks at sum and difference frequencies of the inertial and semi-diurnal tide suggest possible interaction between those frequencies. Yet simply making these claims from spectra is insufficient, as reversible advection can be redistributing the observed energy in the Eulerian frame. To identify advective processes, with the intention of inverting the coordinate system, data with more that one spatial point is necessary. These considerations restrict the available data considerably. However, some moored ADCP velocity records have the required resolution and data for coordinate transformation. This process has been achieved at HOME mooring A2 in chapter 4.

As it is prudent to incorporate multiple observations in any analysis, in this test of higher order techniques a separate mooring south of A2 will be considered. This strengthens the more complicated situation at mooring A2 and lessens the chance of identifying singular phenomena associated with that location. However, for this particular validation of techniques, other historic records could have been selected. We have selected the C2 mooring (see map 4.1) for its availability and to compare with the A2 mooring.

Data from the C2 mooring of the HOME project will be examined with bispectra and bicoherence techniques. The selected time series for analysis of this ADCP horizontal velocity data at mooring C2 is shown in figure 3.10. The instrument was located at 21° 37' N, 158° 51' W, and is described in [6]. At the top is displayed the raw horizontal velocity at a depth of 520 meters. Below is the reconstructed, band passed, inertial and semi-diurnal signals from the raw data. There is an inertial event evident in the final third of the selected time period.

In the implementation of bicoherence and bispectrum specific choices of window type and size can alter the resulting bispectra and bicoherence, as alluded to earlier, and as is also common in Fourier spectral analysis. For the purposes of investigating signals that interact and are on the lower frequency range with respect to the window length, specific trade-offs must be made. In the following analysis, we utilize the following methods:

- identify a time period that includes specific inertial event,
- include 3 spring/neap cycles (to improve statistical reliability),

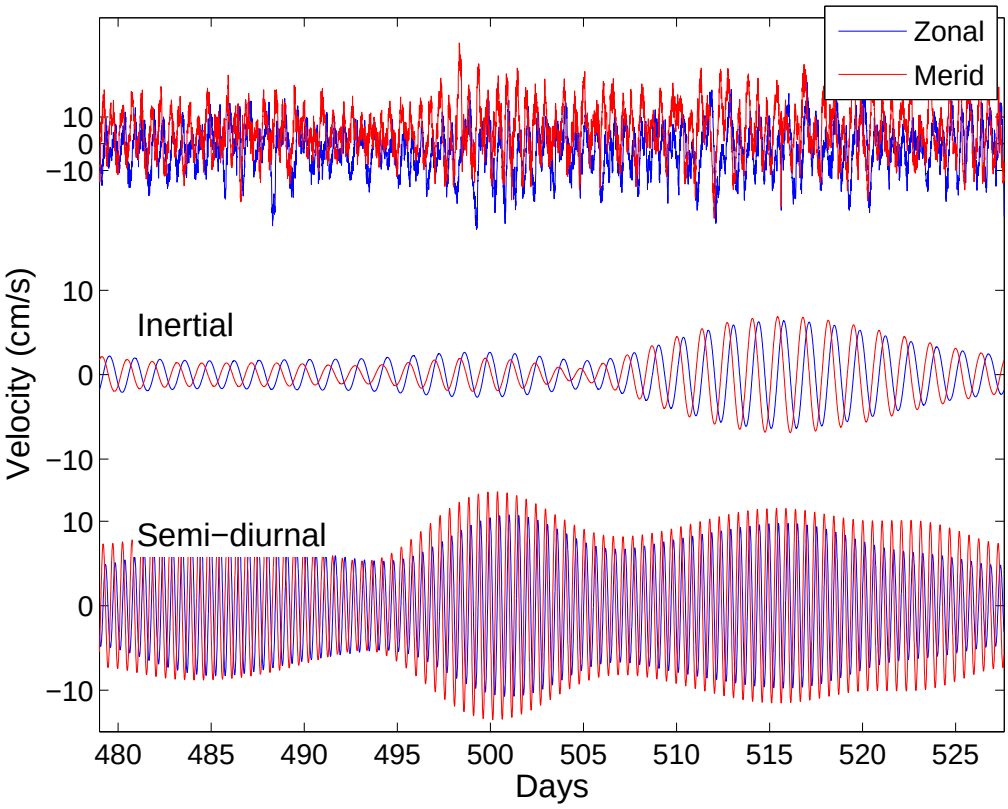

Figure 3.10. Selected time segment with IWISC energy of ADCP horizontal velocities from the HOME C2 mooring at 520 meters. Velocity data is in the upper series, with reconstructed, band passed, inertial and semi-diurnal signals below. Days begin January 1, 2002 with day 480 being April 24, 2003.

- use tapered Hanning window (to minimize spectral leakage),
- select window length of one spring/neap cycle (to ensure resolution of semi-diurnal tide constituents), and
- position windows (with overlap 25% to 60%) to encompass inertial event and peak tidal energy.

The bispectrum is constructed from an average of triple product of the Fourier constituents. Under the conditions outlined, there are typically three to five windowed sections in the analysis. A useful product assisting the interpretation of this method is to construct a rotary power spectral density plot utilizing the Fourier transforms from the same windowed sections that are used in the bispectrum/bicoherence. By checking this spectrum, the impact of window type, size, and placement, can be evaluated visually. Rotary PSD is shown in figure 3.11 for the selected C2 mooring data (figure 3.10).

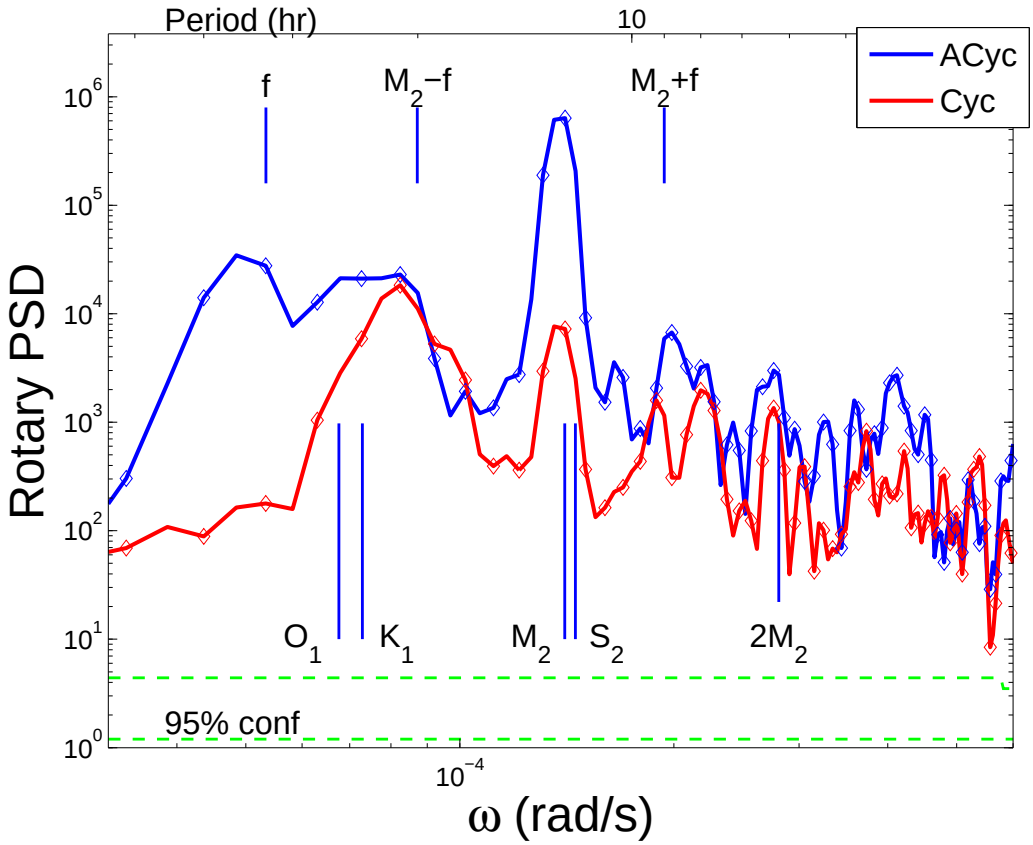

Figure 3.11. Rotary PSD $((m^2/s^2)/(rad/s))$ for the horizontal velocity time series depicted in figure 3.10 of the HOME C2 mooring at a depth of 520 meters. Of note is the significant enhancement of cyclonic energy at the IWISC $(M_2 - f)$ frequency. Independent points identified with diamond symbols. Dashed green lines indicate 95% confidence intervals.

The rotary PSD shows significant enhancement of cyclonic energy at the IWISC frequency $(M_2 - f)$. This is the strongest cyclonic signal, exceeding the semi-diurnal internal tide cyclonic energy. As $M_2 - f$ for this latitude is within the internal wave regime, it can be noted that there is obvious consistency breaking. There is a sum $(M_2 + f)$ peak as well in this record.

Peaks in the spectra as shown are one of the first indicators of potential non-linear interactions. In Mihaly et. al. [51], an observed summation frequency peak similar to the C2 rotary PSD, motivates even the title "Evidence for nonlinear interaction between internal waves of inertial and semi-diurnal frequency". Likewise, van Haren et. al. [88] attributes the sum peak to non-linear interaction. A separate claim is made by Pinkel [67] of simple vertical Doppler shifting being the underlying source of the peaks such as these. Clearly it can not be determined from power spectra alone, and this is where

higher order techniques have been traditionally effective in other fluid dynamics situations. This is what motivates our examination of the bispectrum and bicoherence in the low frequency internal wave regime for the horizontal ADCP data at HOME mooring C2.

In figure 3.12 the bispectrum of the selected C2 time series is shown. The bispectrum itself is a product of spectral coefficients at two frequencies and the coefficient at their sum/difference frequency. Peaks in the bispectrum represent an 'in phase' relationship between these three frequencies, with the respective amplitude product. There are three frequency axis on the figure. Each axis represents one of the frequencies in the calculation. Axis in the rotary representation proceed from cyclonic to anti-cyclonic, with zero frequency in the center. Labels and reference lines are color coded, with red for the cyclonic and blue for the anti-cyclonic. Reference lines correspond to a slightly blue shifted inertial (typically $1.04 * f$), an average semi-diurnal frequency SD ($\frac{M_2+S_2}{2}$), and the two interaction frequencies.

Using this representation, a specific peak can be quickly identified with its associated frequencies, and the rotary nature of the spectral component. Relevant peaks in the bispectrum and bicoherence for this example have been labeled in this way:

- A → (anti-cyclonic semi-diurnal, anti-cyclonic inertial, anti-cyclonic sum (SD+f))
- B → (anti-cyclonic semi-diurnal, anti-cyclonic inertial, cyclonic difference (SD-f))
- C → (cyclonic semi-diurnal, anti-cyclonic inertial, cyclonic difference (SD-f))
- D → (cyclonic semi-diurnal, anti-cyclonic inertial, anti-cyclonic sum (SD+f))

The location indicated at [A] represents the amplitude product between the anti-cyclonic semi-diurnal rotary velocity, the anti-cyclonic inertial rotary velocity, and the anti-cyclonic rotary velocity with a frequency at the semi-diurnal plus the inertial (what we have been calling the sum ($M_2 + f$) frequency). This corresponds with the sum peak indicated in the rotary PSD figure 3.11. The elevated bispectra alone would seem to indicate non-linear interaction in a traditional interpretation. The second location labeled [B] represents the three components; anti-cyclonic semi-diurnal, anti-cyclonic inertial, and cyclonic rotary velocity at the difference frequency between the semi-diurnal and inertial (the IWISC frequency). At this location as well, there is a clear bispectral peak, which would be indicative of some form of interaction.

The locations labeled [C] and [D] represent similar interactions, but with the anti-cyclonic semi-diurnal replaced with a cyclonic semi-diurnal. There are faint indications of bispectral enhancement at these points, but clearly more than a order of magnitude below the primary peaks. It is a consistent expectation to have indications at these points as the semi-diurnal internal tide has both anti-cyclonic

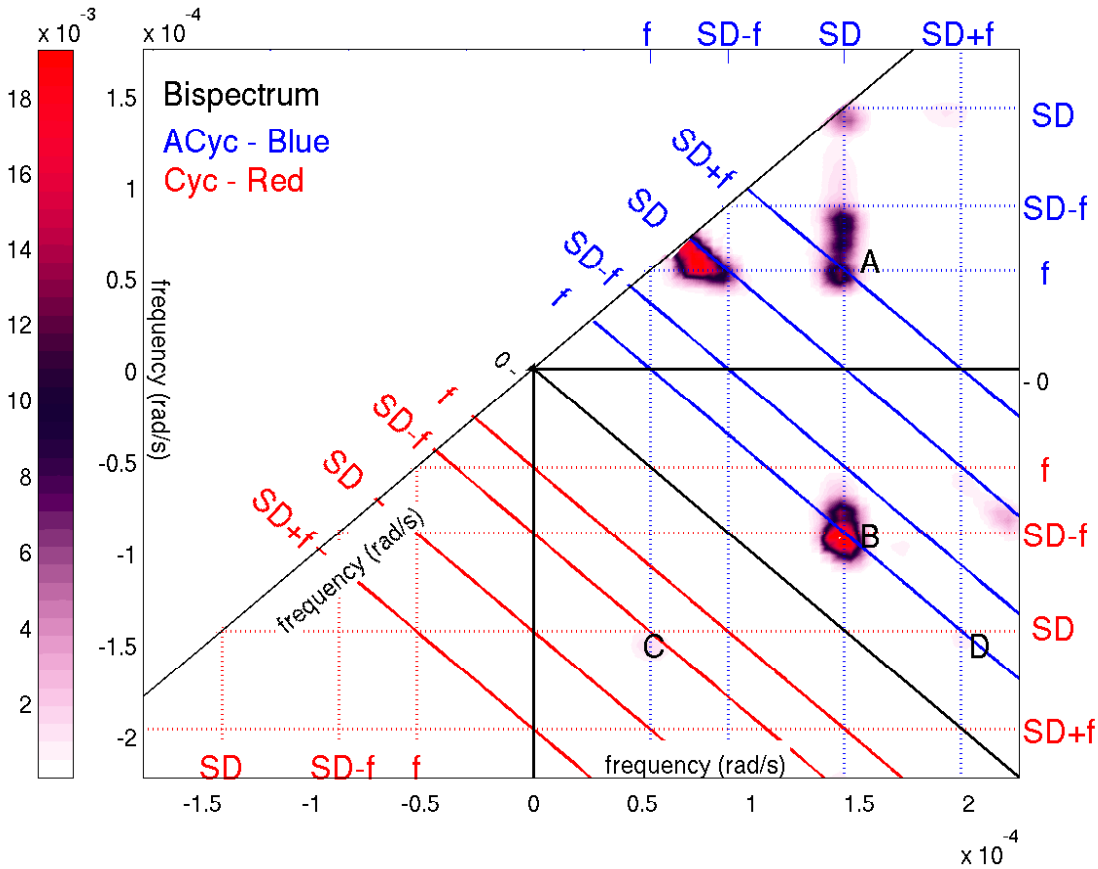

Figure 3.12. Rotary bispectrum of the HOME C2 ADCP horizontal velocities at a depth of 520 meters for the time period indicated in figure 3.10. SD indicates average semi-diurnal frequency. There are three frequency axis which range from cyclonic (red) through zero frequency to anti-cyclonic (blue). Elevated bispectrum indications are then associated with the three frequencies indicated on the respective axis. Labeled interaction points are described in the text.

and cyclonic rotating components consistent with the theoretical internal wave consistency relation. The cyclonic signal is near an order of magnitude below the clockwise as can be seen in the rotary PSD (figure 3.11).

The bispectrum indicates which in phase triple products contain maximal energies. This alone does not guarantee coherent interaction. Taking the bispectrum and normalizing by the triple product of the magnitudes produces the bicoherence. For this selected record, the bicoherence is shown in figure 3.13.

The elevated bicoherence values are an interesting suggestion of some active process at this depth and location. There are significant bicoherence peaks at some of the interaction frequencies suggested

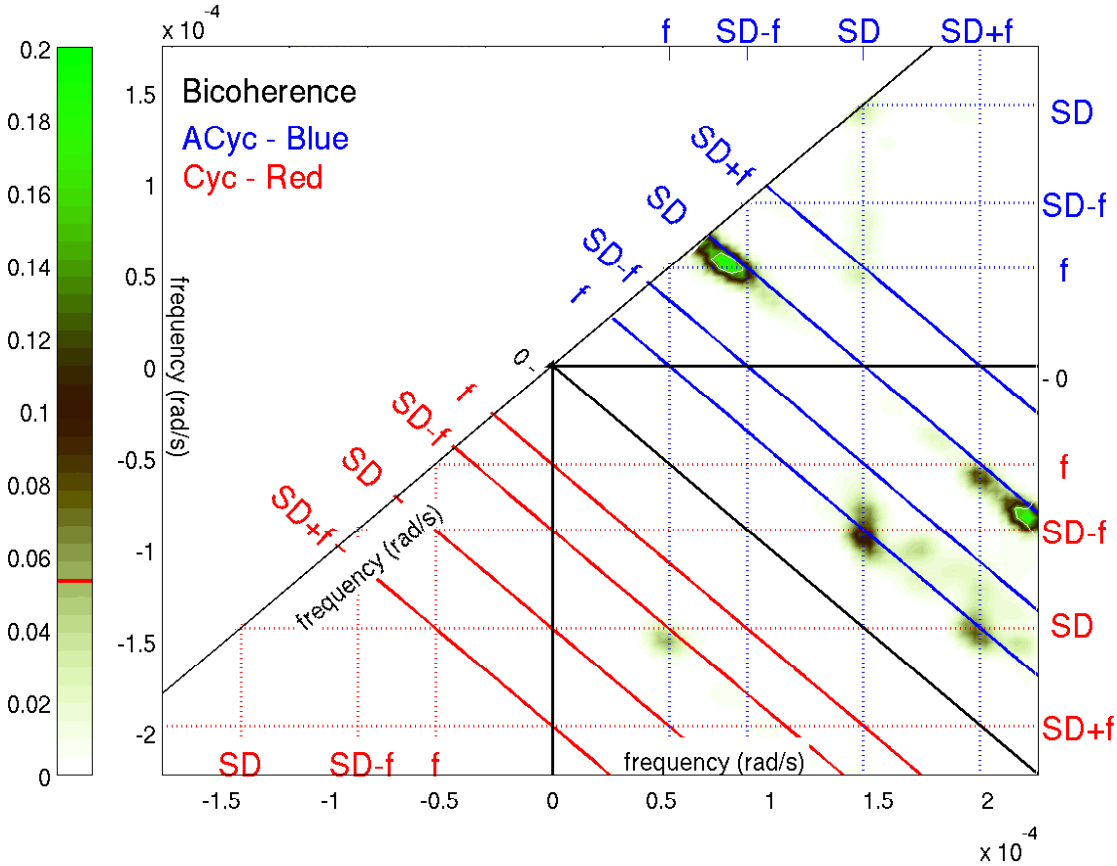

Figure 3.13. Rotary bicoherence of the horizontal ADCP velocities at HOME mooring C2 with a depth of 520 meters for the time period indicated in figure 3.10. There are coherent indications at the interaction points of interest. These points are discussed in the text. There are three frequency axis which range from cyclonic (red) through zero frequency to anti-cyclonic (blue). Elevated bicoherence indications are then associated with the three frequencies indicated on the respective axis.

by the rotary PSD and indicated in the bispectrum, most notably at the IWISC associated triple point. There are other bicoherent frequency triplets as well. For determining specific processes the bicoherence and bispectrum need to be examined together. For instance, there is elevated bicoherence at the triple point SD (anti-cyclonic), $2SD$ (anti-cyclonic), and $SD - f$ (cyclonic). Without the bispectrum, which did not indicate much activity at this point, undue significance might be attributed to this triple point and some interaction process.

Harmonics of the internal tide can be frequently found in observed rotary PSD, originating from different sources like topography (e.g., van Haren et al. [88]). We have found in general, that it is not unexpected to see combinations including tidal harmonics to show bicoherence. The bispectrum can

then be utilized to determine the relative importance of the energy in the prospective interaction. For the case of SD (anti-cyclonic), $2SD$ (anti-cyclonic), and $SD - f$ (cyclonic), the bispectum elevation is far below the interactions we are interested in, i.e. those directly between the inertial and semi-diurnal bands.

3.4.2 Plane Wave Summation Model

To better understand what is the connection between bispectra/bicoherence and the possible mechanisms, whether non-linear or simple vertical displacement of horizontal currents, the plane wave summation model constructed in earlier sections can be analyzed. There are three comparisons shown.

- Case I → model described in sec 3.3 with inertial wave vertically heaved by the semi-diurnal internal tide.
- Case II → Semi-Lagrangian inversion of modeled data used in the first case.
- Case III → inertial and semi-diurnal tide inputs without vertical displacement.

Case I

To keep the comparison in context with the C2 mooring, the plane wave summation model has been utilized with a latitude of 21° N. The time series of horizontal velocity selected for analysis with bispectra/bicoherence is shown in figure 3.14 with the reconstructed, band passed inertial and semi-diurnal tide.

Rotary PSD for this selected time series is shown in figure 3.15. The method of analysis remains the same as used to calculate PSD for the C2 mooring data.

In the bispectrum of the 21° plane wave displacement model (figure 3.16) there are four distinct elevated regions associated with the displacement interaction. These frequency triple points correspond to the sum and difference frequencies between the semi-diurnal and the inertial internal waves. There are two sets of interactions (with a sum and difference pair each), one corresponding to the clockwise semi-diurnal and another with the counter-clockwise. As expected, the two elevated frequency triplets associated with the cyclonic semi-diurnal are of a lesser magnitude, just as indicated by the rotary PSD (Figure 3.15). The input semi-diurnal waves are calculated to match internal wave theory, hence the cyclonic semi-diurnal reduced energy and subsequently reduced bispectrum..

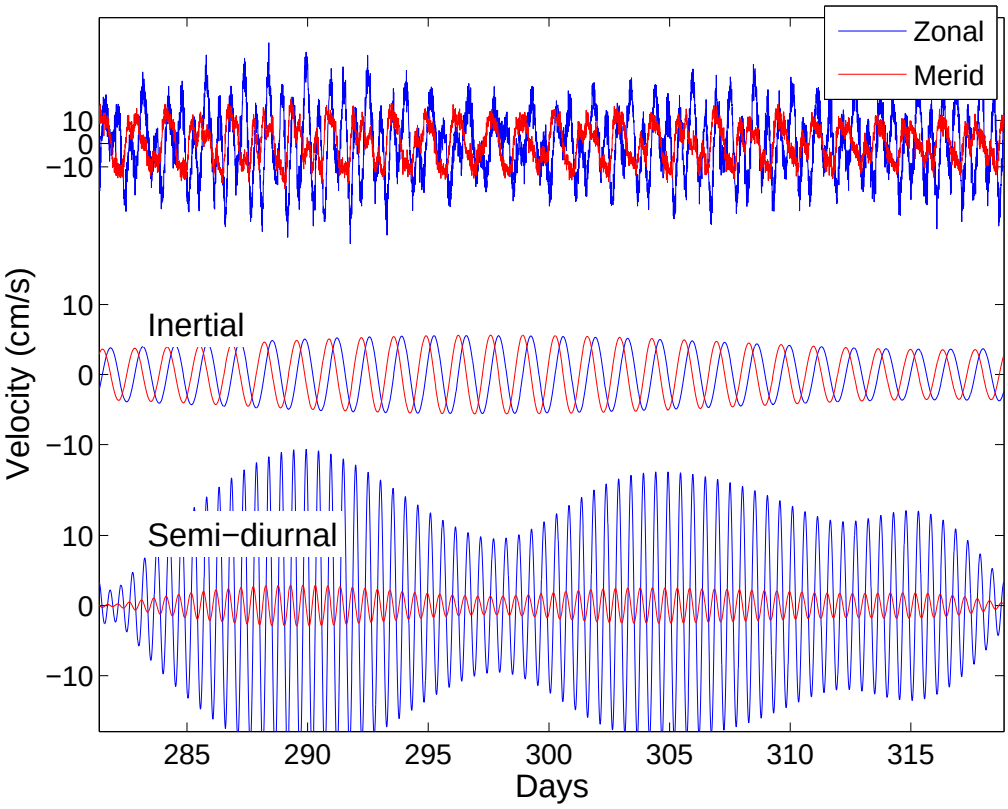

Figure 3.14. Plane wave summation model with vertical displacement of inertial currents at 21° latitude. Modeled data is in the upper series, with reconstructed, band passed, inertial and semi-diurnal signals below.

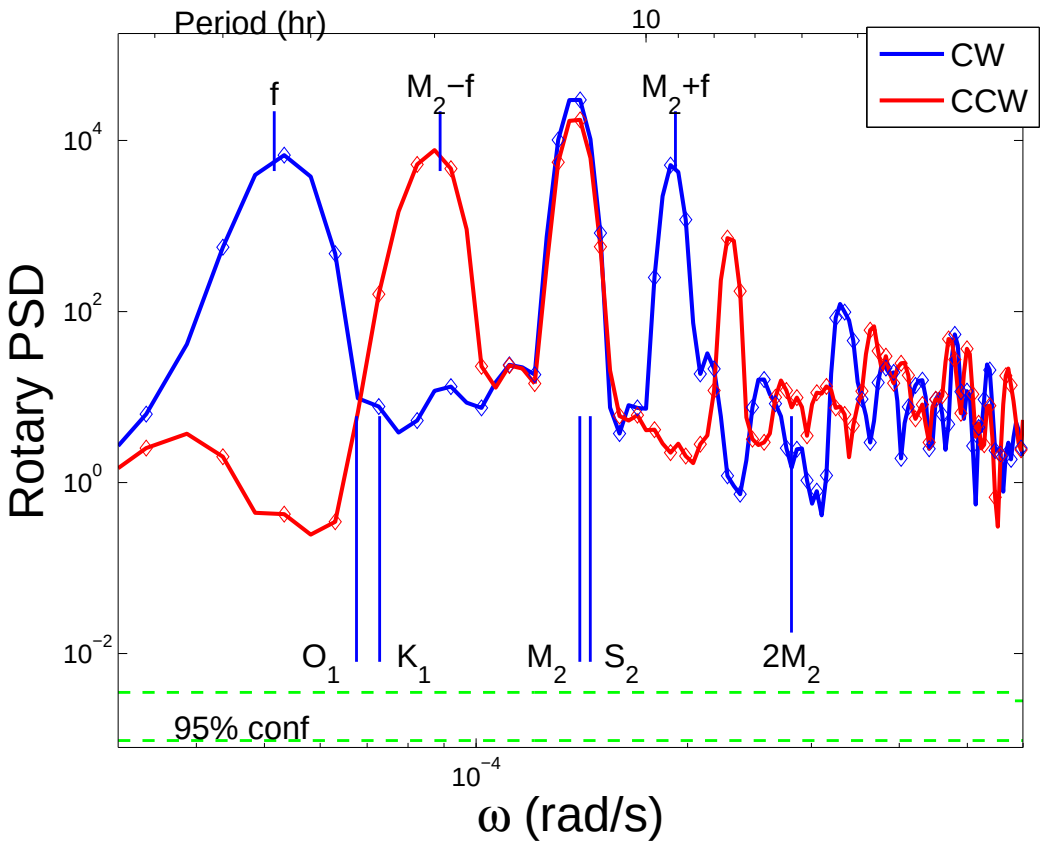

Figure 3.15. Rotary PSD $((m^2/s^2)/(rad/s))$ for the 21° plane wave model time series indicated in figure 3.14. There are significant peaks at the interaction frequencies between the inertial horizontal currents and the semi-diurnal internal tide. This is a result of the vertical displacement of the inertial by the semi-diurnal. Independent points identified with diamond symbols. Dashed green lines indicate 95% confidence intervals.

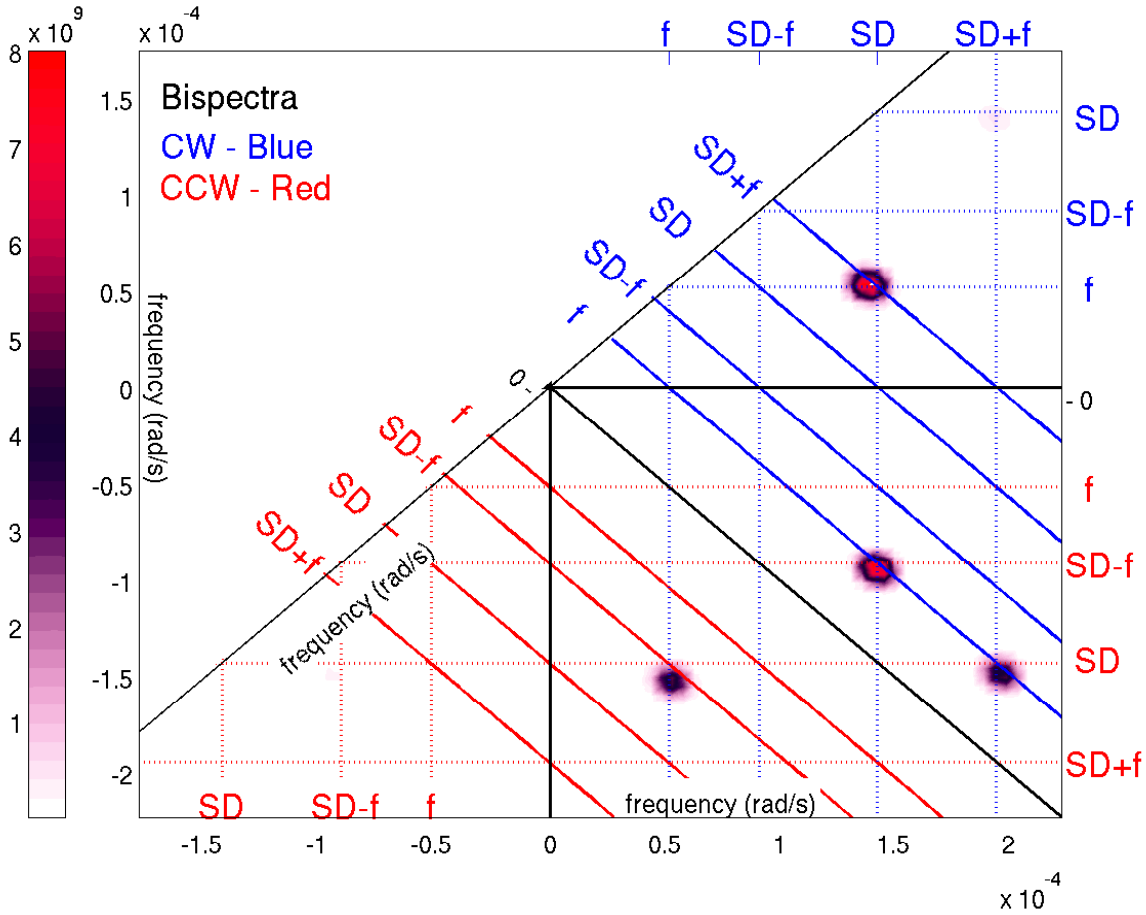

Figure 3.16. Bispectrum of the selected time series indicated in figure 3.14. There are peaks at the interaction triple points associated with the inertial and semi-diurnal internal waves in the modeled record. There are three frequency axes which range from cyclonic (red) through zero frequency to anti-cyclonic (blue). Elevated bispectrum indications are then associated with the three frequencies indicated on the respective axis.

It is important to note that no energy exchanging process was utilized to construct the model. The model consists of inertial waves who are calculated in a reference frame determined by the modeled semi-diurnal displacement. This isolates reversible advection and does not move energy into the interaction bands ($M_2 \pm f$) in the displacement following frame. The elevated bispectrum at the interaction points in Figure 3.16 indicate the bispectrum is not uniquely differentiating processes that exchange energy and periodic reversible displacement.

The bicoherence for this time series indicates that these same four frequency triples are significant (figure 3.17). The interpretation of having elevated bicoherence and elevated bispectrum at a triple point would be that there is a non-linear process active. Yet the model does not contain irreversible energy exchange.

In examining the C2 mooring record, it was shown that reliance on either bispectra or bicoherence exclusively can cloud the view of what interactions are important. Both calculations are important for understanding the record. Yet now we have demonstrated that the non-energy exchanging displacement of horizontal currents can yield a positive indication of non-linearity. This is a considerable result for the application of bispectra and bicoherence to internal wave spectral analysis. It is potentially important for any data where periodic Doppler shifting (reversible advection) is present.

3.4.3 Case II

To emphasize the model result, and to validate the analysis method, the same time series was Semi-Lagrange inverted in the vertical to 'recover' the input model internal waves. This procedure can be easily accomplished for the model case where vertical velocity is a recorded function. We choose to use the same procedure as used in the C2 mooring of taking the modeled vertical velocity and band passing for the semi-diurnal. This is done, as opposed to using the models semi-diurnal vertical velocity, to emulate how the bispectra and bicoherence analysis appears when applied to real data. The difference is only in the added Gaussian noise and the error associated with the band pass filter. The extracted vertical velocity is integrated to displacement, and then used for coordinate transformation.

The rotary PSD for the S-L inverted model horizontal velocities is indicated in figure 3.18. The Semi-Lagrange technique has reversed the advection and there is no significant rotary PSD energy at the interaction frequencies. The result is an expected one and verifies that the coordinate transformation is reversible for the predominantly horizontal inertial currents.

In figure 3.19 the bispectrum for the Semi-Lagrange inverted model record is shown. There are bispectral peaks at a few frequency triplets, with a apparent maximal peak located at the triplet associated with the sum frequency $SD + f$. The peak magnitude is approximately $5x10^5$ as indicated on

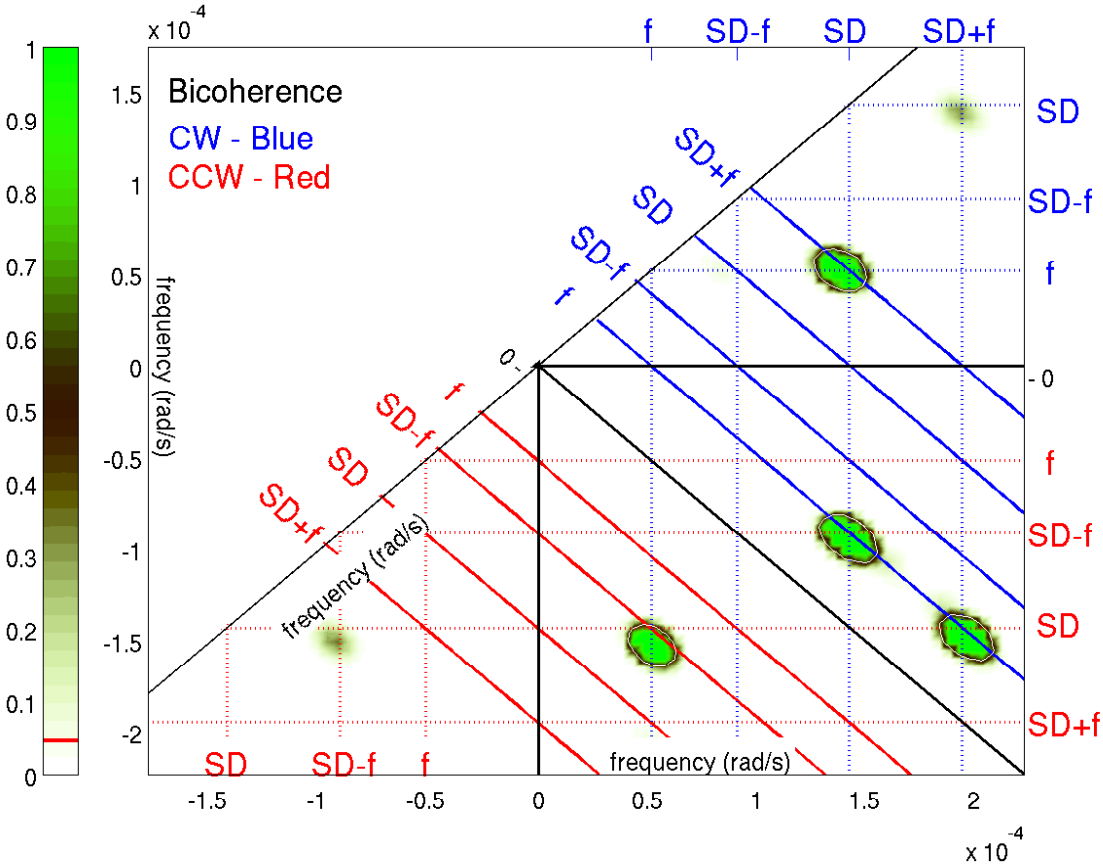

Figure 3.17. Bicoherence of the selected time series indicated in figure 3.14. The principal frequency triples associated with the vertical displacement of inertial horizontal currents by the semi-diurnal internal tide all show high bicoherence. There are three frequency axes which range from cyclonic (red) through zero frequency to anti-cyclonic (blue). Elevated bispectrum indications are then associated with the three frequencies indicated on the respective axis.

the colorbar. The same peak in figure 3.16 is approximately $8x10^9$, four orders of magnitude above the inverted record.

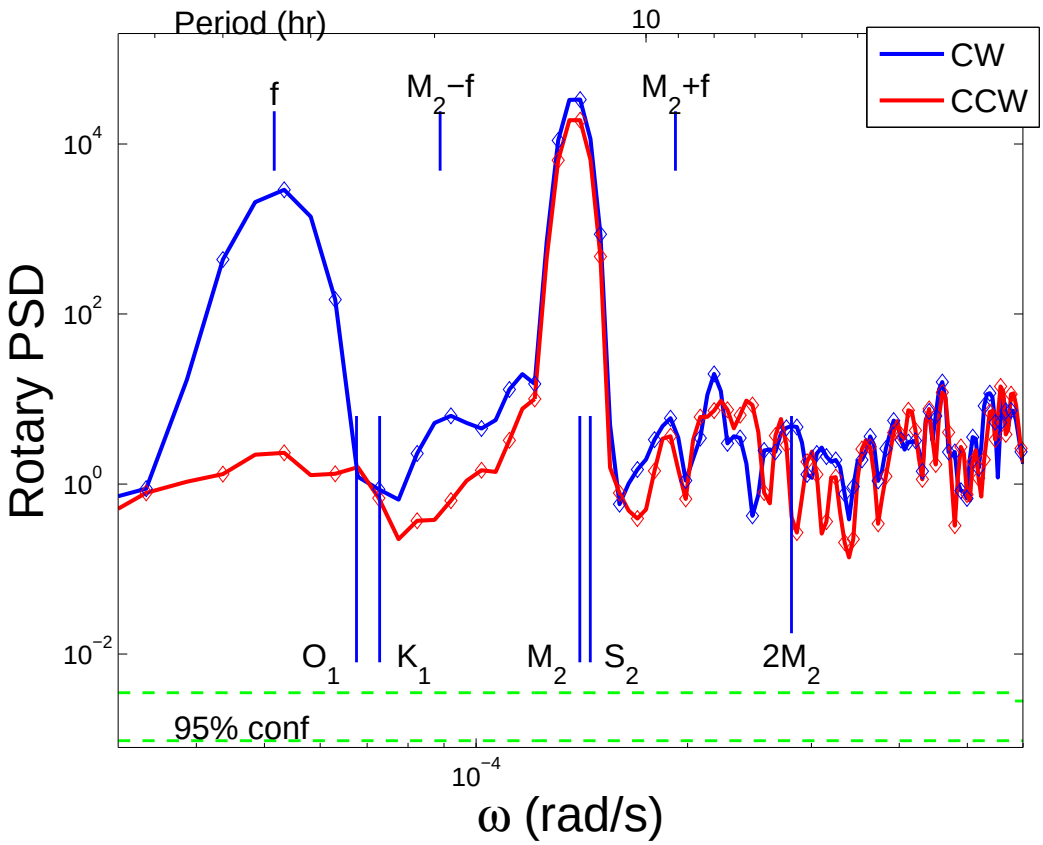

Figure 3.18. Rotary PSD $((m^2/s^2)/(rad/s))$ for the time series indicated in figure 3.14 after Semi-Lagrange inversion of the vertical coordinate. Spectral peaks indicating the reversible advection of the inertial wave by the semi-diurnal displacement, as indicated in Figure 3.15, have been removed by the S-L inversion. Independent points identified with diamond symbols. Dashed green lines indicate 95% confidence intervals.

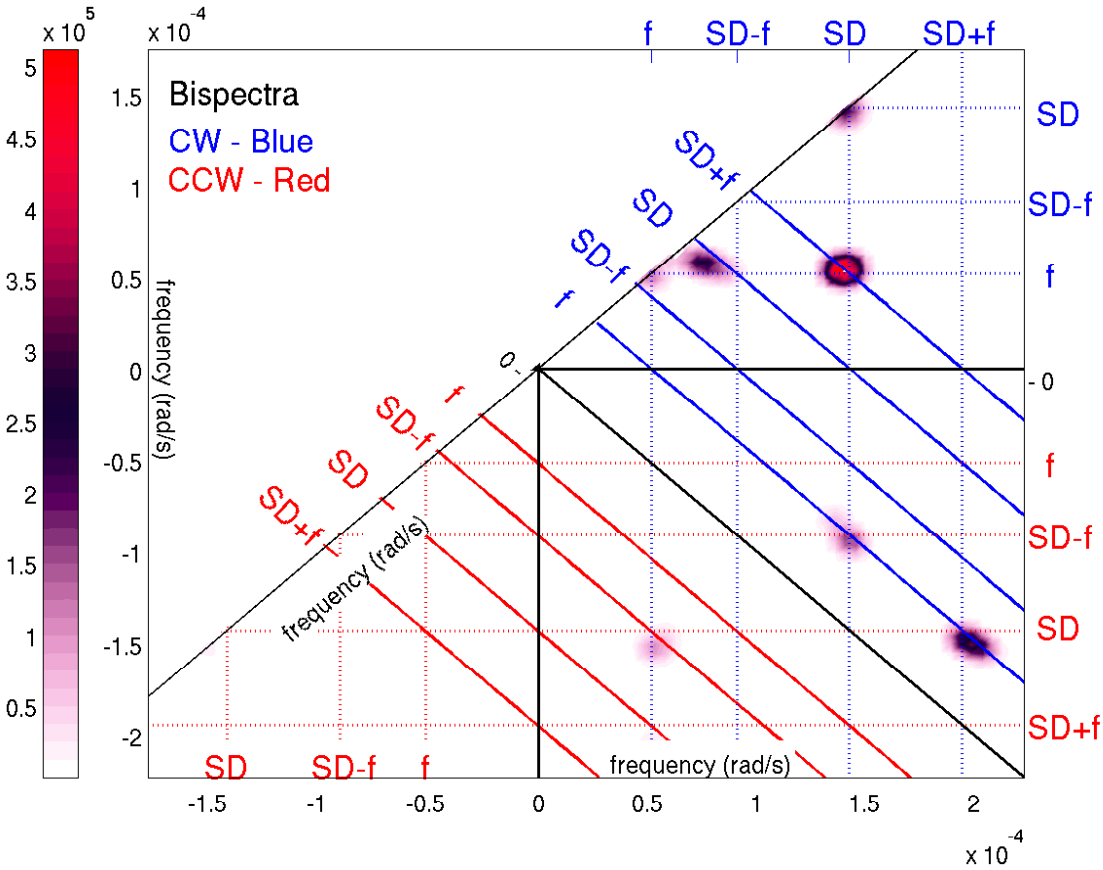

Figure 3.19. Bispectrum of the 21° semi-diurnal displacement model after Semi-Lagrange inversion. As compared with Figure 3.16, the magnitude of the interaction triple points has been significantly reduced (notice the multi-decadal drop in scale maximum). There are three frequency axis which range from cyclonic (red) through zero frequency to anti-cyclonic (blue). Elevated bispectrum indications are then associated with the three frequencies indicated on the respective axis.

More important is the bicoherence, which in figure 3.20 indicates there is very little energy associated between any frequency triplets. There is a coherent triplet at the location characterized by cyclonic semi-diurnal internal tide in the sum frequency. However there is relatively little bispectra associated with that point.

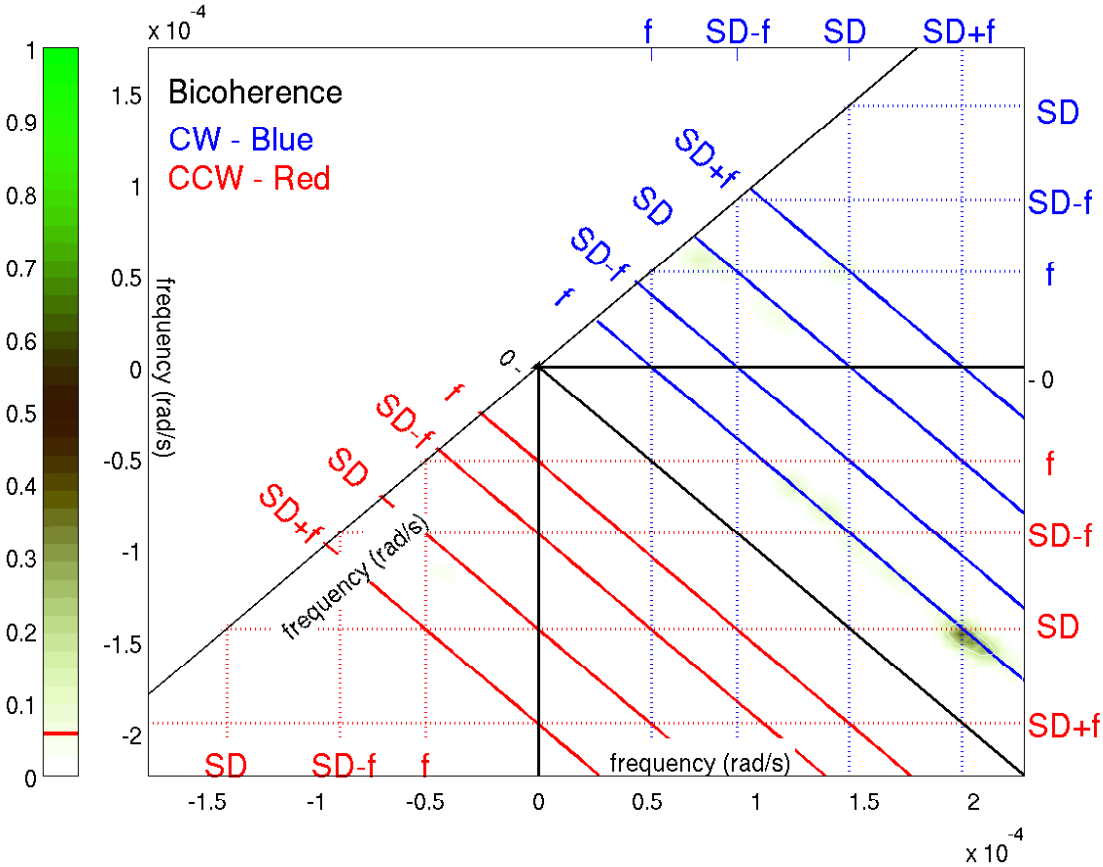

Figure 3.20. Bicoherence of the 21° semi-diurnal displacement model after Semi-Lagrange inversion. In comparison to Figure 3.17, the bicoherence before S-L inversion, there is very little bicoherence. There are three frequency axes which range from cyclonic (red) through zero frequency to anti-cyclonic (blue). Elevated bicoherence indications are then associated with the three frequencies indicated on the respective axis.

3.4.4 Case III

We can verify to what level the bispectra indications are possibly distorted by the inversion process. In figure 3.21 the bispectrum is shown for the modeled velocity field without any displacement of the inertial wave. This means that the inertial and semi-diurnal internal wave constructions were added without any interaction. The equivalent Gaussian noise (snr 20) was then applied to the velocity field and the bispectrum calculated. For this record the bicoherence is completely at the noise level, and is not shown.

The peak levels in the Semi-Lagrange inverted bispectrum compare very favorably with this control case. The maximal peak in the Semi-Lagrange case (Figure 3.19) is approximately double the peaks in the control. This is a very favorable indication that with the appropriate displacement record, the Semi-Lagrange inversion efficiently removes from the bispectra and bicoherence non-energy exchange associated interactions.

The control case also demonstrates that, given any record with significant peaks in the PSD, there can be associated bispectral peaks simply due to the magnitudes of the interacting PSD peaks. These are not erroneous, yet with the error calculation and in conjunction with the bicoherence will not give false indications of interaction.

3.4.5 Summary of Bispectra and Bicoherence Evaluation

A very significant result here is the inability of bispectra and bicoherence to decisively identify non-linear interactions which exchange energy from reversible advection. In the context of IWISC characterization, this means a record must be inverted to the displacement following coordinate before using the bispectrum and bicoherence to identify energy exchanging non-linearity.

Bispectra and bicoherence were successful in identifying interactions in the horizontal currents from the HOME mooring C2 ADCP. The analysis indicated the need for both the bispectrum and the bicoherence to identify interactions of interest. The methods were tested against a model which has only reversible advection. The bispectrum and bicoherence identified the reversible interaction. The result of these test indicate that to identify energy exchanging non-linearity successfully in the presence of reversible advection, a Semi-Lagrangian inversion is necessary.

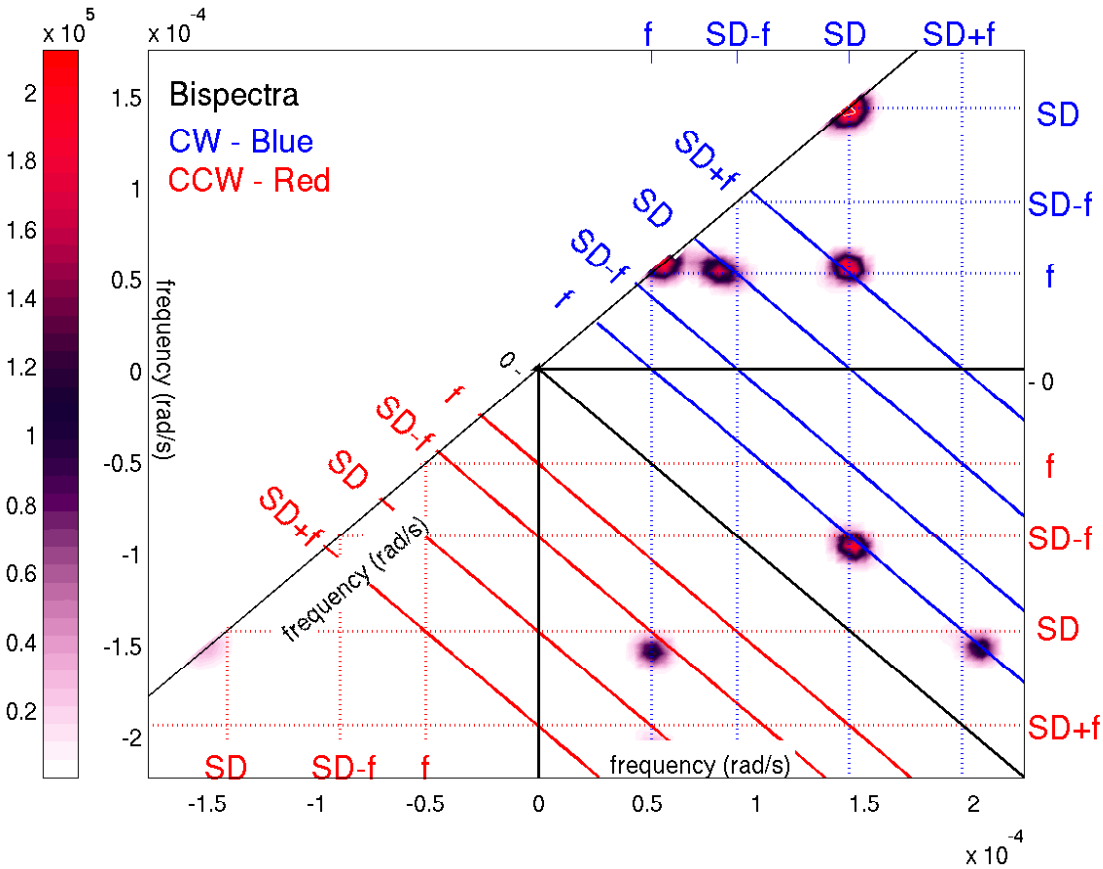

Figure 3.21. Bispectrum of the 21° model with no displacement of the inertial by the semi-diurnal. Compare with Figure 3.19 which is the bispectrum of the S-L inverted model with displacement. There are three frequency axes which range from cyclonic (red) through zero frequency to anti-cyclonic (blue). Elevated bispectrum indications are then associated with the three frequencies indicated on the respective axis.

3.5 Rotary Wavelet Decomposition

In previous sections some limitations of Fourier methods became evident, especially when trying to analyze a 'event' that has amplitude variability on the same time scale as the desirable windows. So a trade off between spectral leakage and temporal isolation arises. This can be addressed with multiple tapers, normalized windows, and various other techniques. However, a well developed technique for investigating this type of data exists.

An established method of analyzing signals that contain elements with time dependent amplitude envelopes is wavelet decomposition. This allows a much higher resolution of events temporally. The

technique is robust and well developed in related fields, particularly signal analysis in communications. It has yet to be widely adopted for oceanographic uses, but has a been successfully applied in a number of geophysical regimes.

A seminal application of wavelet analysis to near inertial motion was done by Liu and Miller [45]. They introduce a rotary wavelet decomposition to isolate inertial energy events. Related use of wavelets has matured in the area of tidal analysis as described in Flinchem [24] and more recently Jay [38]. At higher frequency ranges in the internal wave band, Lien et. al. [44] utilized wavelet decomposition to identify turbulent events. In regards to other geophysical flows, atmospheric gravity wave event dynamics have been analyzed with wavelet decomposition successfully by Zhang et. al. [98].

We have decomposed the 21° latitude plane wave summation model velocity field described in the previous section using wavelet techniques. Frequency b-spline wavelets were selected for the specific properties of scale/frequency matching and to make interpretation of the analysis match traditional and well established representations. This is a robust complex wavelet of the form:

$$\psi(x) = B_w^{1/2}\left(sinc\frac{B_w x}{m}\right)^m e^{i2\pi\omega_c x} \tag{3.5.1}$$

where m is an integer order parameter ($m \geq 1$), B_w is a bandwidth parameter, and ω_c is the center frequency. The key advantage of this wavelet over other complex wavelets is its natural translation from scale to frequency space.

After obtaining the coefficients, we can proceed to use these to construct a rotary wavelet PSD (figure 3.22). A discussion of error estimates used here can be found in van Milligen et al. [89]. The rotary wavelet PSD figure resembles its Fourier counterpart, only it appears highly averaged across bands. The following spectra and higher order spectra use two transforms taken one and a half days apart during a time period and depth in the 21° latitude model with inertial displacement where IWISC energy is elevated.

The wavelet rotary PSD has resolved the IWISC peak. The peaks are broader than in similar spectra using Fourier methods. That is the principal trade off with using wavelet analysis in this way. To examine features with very short duration there is a loss of spectral resolution. In the wavelet PSD example we can see that the sum interaction peak is 'buried' in the very broad semi-diurnal peak. However in this example, for signals like IWISC which are cyclonic, the resolution is good as there are no nearby cyclonic energies.

The rotary wavelet decompositions were used to construct a plot of the consistency relation (cyclonic/anti-cyclonic) in Figure 3.23. There is a large deviation from the theoretical curve at the IWISC frequency.

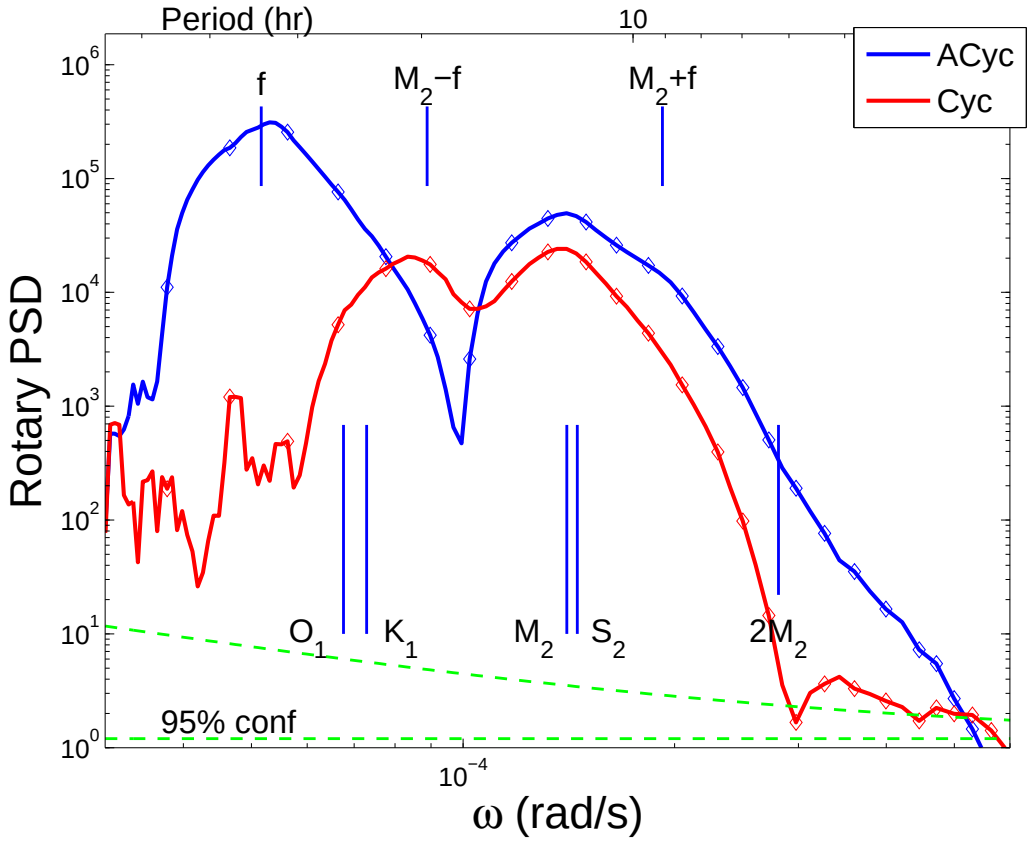

Figure 3.22. Rotary wavelet PSD $((m^2/s^2)/(rad/s))$ for the 21° latitude model with inertial waves displaced by the semi-diurnal waves as described in section 3.3. Spectral peaks indicating the reversible advection of the inertial wave by the semi-diurnal displacement, as indicated in Figure 3.15, have been removed by the S-L inversion. Independent points identified with diamond symbols. Dashed green lines indicate 95% confidence intervals.

The sum $(M_2 + f)$ band is inconclusive. As seen in the PSD (Figure 3.22) where the semi-diurnal peak obscured the sum interaction peak, there is no clear information in the consistency plot for $M_2 + f$.

The primary constraint we have observed on the Fourier bicoherence estimates usefulness in this oceanic context with non-stationary sources in the low frequency internal wave band is the overwhelming contribution to the expectation value from a very few records. This creates a deceptive situation, and can be illustrated using wavelet analysis. To see the difficulty, and illustrate how wavelets can capture temporal detail, it is instructive to examine time series of wavelet decompositions.

A time series of rotary wavelet decomposition coefficients is shown in figure 3.24. The decomposition is of the inertial displacement model at 21° latitude. Variability is resolved within the spring/neap

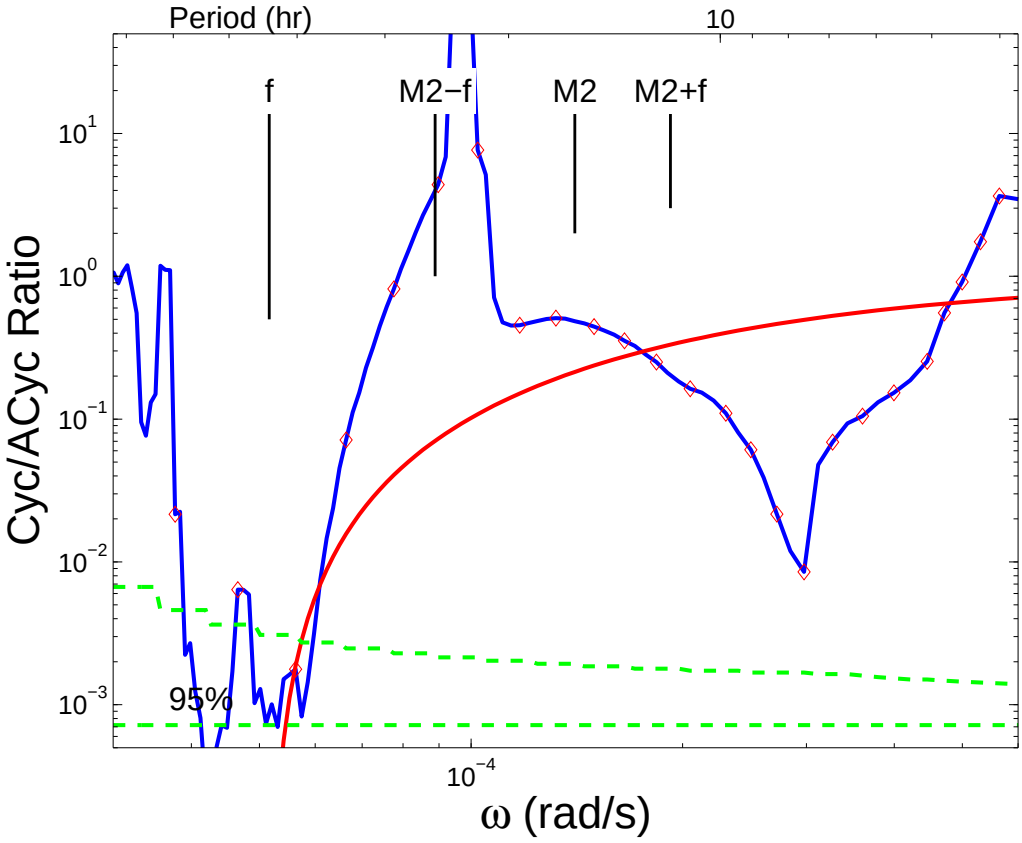

Figure 3.23. Consistency relation (cyclonic/anti-cyclonic) using wavelet analysis for the 21° latitude model corresponding to Figure 3.22. Near the IWISC frequency there is significant deviation from the theoretical curve ($(\omega - f)/(\omega + f)$). Independent points identified with diamond symbols. Dashed green lines indicate 95% confidence intervals.

envelope and within the inertial wave train. The difference frequency is well resolved in the cyclonic time series. At the sum interaction frequency in the anti-cyclonic, there is elevated wavelet amplitudes, but no clear separation visible between semi-diurnal amplitude and elevated $M_2 + f$.

There is a separate benefit in using wavelet transforms and that is to resolve the spatial/temporal variability of the inertial wave packets encountered in observations. The time series of coefficients shown in Figure 3.24 indicate the temporal resolution of the method. Individual semi-diurnal total amplitude variations are evident within a spring/neap cycle. This type of resolution can be very useful in examining inertial waves. They are event like signals in many oceanic current records with peaks in energy being observed at an Eulerian point rising and falling within a few days.

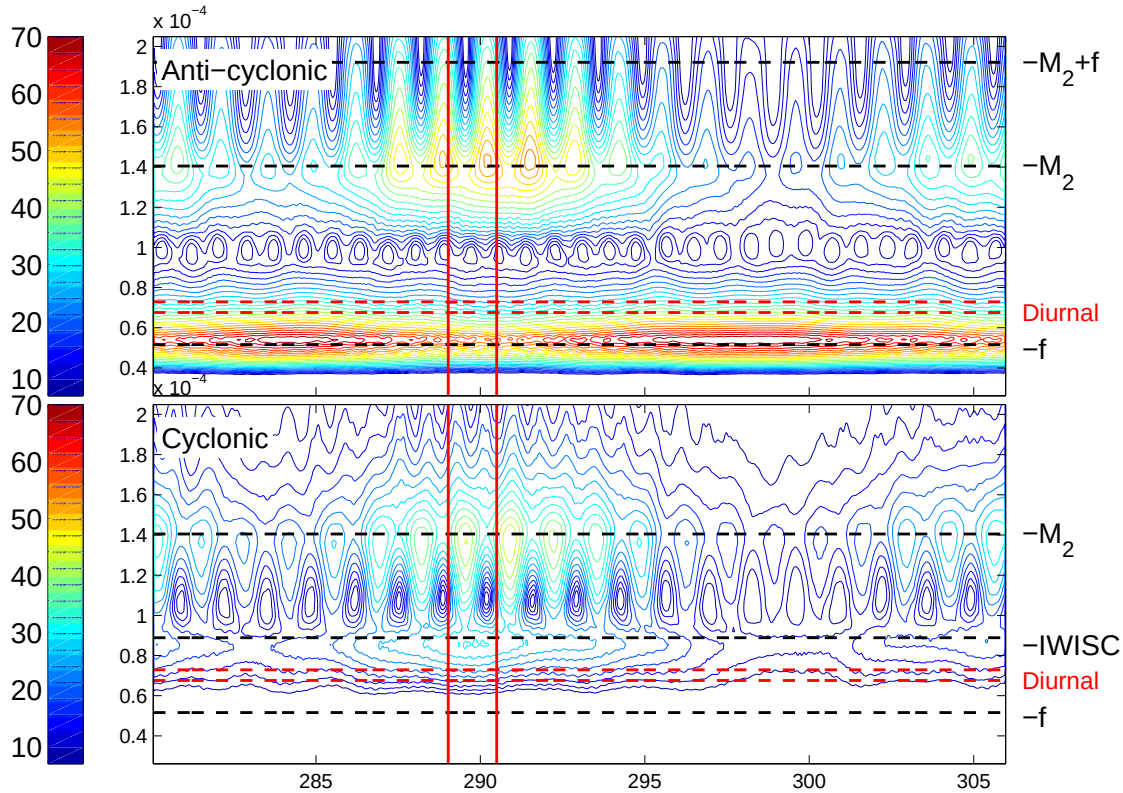

Figure 3.24. Frequency B-Spline wavelet decomposition of velocity for the plane wave summation model as described in the text for 21° latitude with displacement of the inertial waves by the semi-diurnal. The top panel is the clockwise wavelet time series and the bottom panel is the counter-clockwise. Contour color levels are indicated on the left. Transform times used in the rotary wavelet PSD (Figure 3.22) and wavelet bispectral analysis (Figures 3.28 and 3.28) are indicated by red dotted vertical lines.

Band passed coefficient time series can be displayed with depth to reveal the changing vertical structure of specific wave bands. A vertical section of clockwise rotary wavelet inertial amplitude is depicted in figure 3.25. There is a single vertical section overlaid on the left showing the vertical structure within the inertial wavetrain. The corresponding model input average wavelength is indicated. A theoretically estimated vertical group velocity of $.01cm/s$ for a wave at frequency $1.05f$ is also depicted. Packet phase information is clearly resolved, with upward phase velocity.

A time series of rotary clockwise wavelet decomposition at the semi-diurnal frequency is shown in figure 3.26 for the 21° inertial displacement model. The corresponding barotropic amplitude envelope

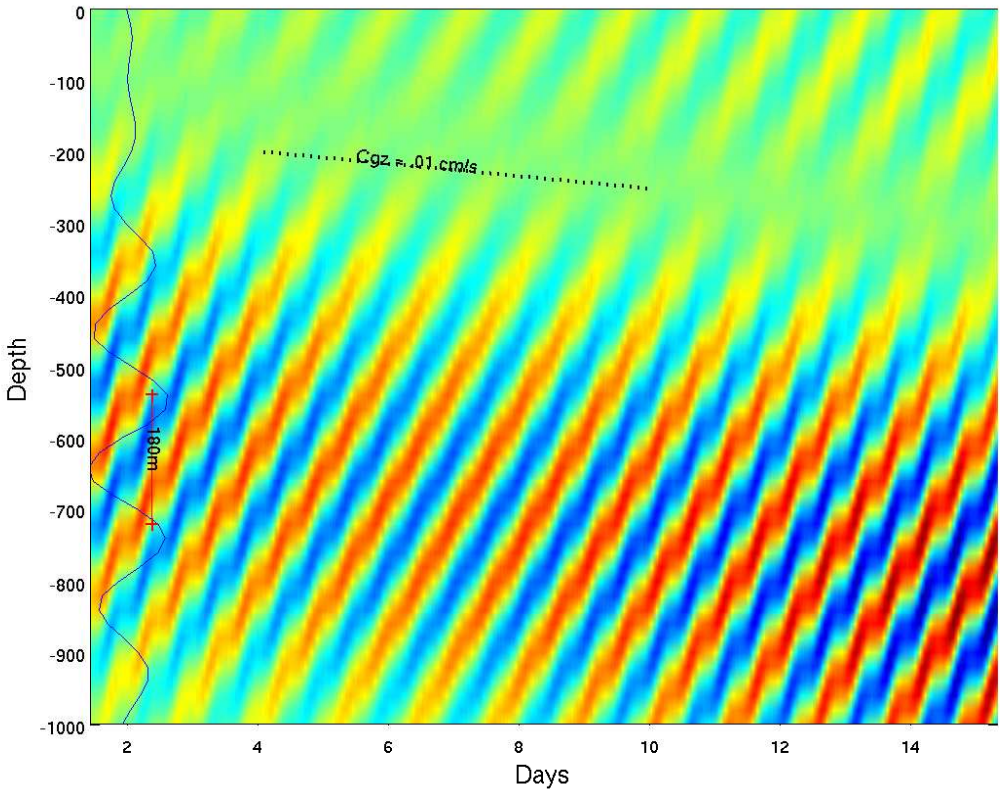

Figure 3.25. Anti-cyclonic rotary wavelet amplitudes of inertial frequency at depth over a 14 day section of the plane wave sum model at 21° with the inertial displaced by semi-diurnal waves. A single time vertical structure is overlaid on the left. The theoretical group velocity indicated upper center. Model description is in section 3.3

from constituents used to create the modeled internal tide is overlaid on the bottom. An interesting feature of this wavelet visualization of vertical structure is that you can see the upward phase propagation of the anti-cyclonic rotary velocity amplitude as the dark color. In lighter color, signifying lower amplitude, the cyclonic amplitudes seem to be visible with downward phase propagation.

For the wavelet bispectral analysis, two transforms were selected during elevated inertial, tidal, and interaction band wavelet amplitude. These are shown in Figure 3.24 as the two red vertical lines. The arrangement of wavelets used in the bispectral calculation can be represented like this:

$$B_{rx}(\omega_1, \omega_2) = \int_t W_{\pm}(\omega_1, \tau) W_{\pm}(\omega_2, \tau) W^*_{\mp}(\omega, \tau) d\tau \tag{3.5.2}$$

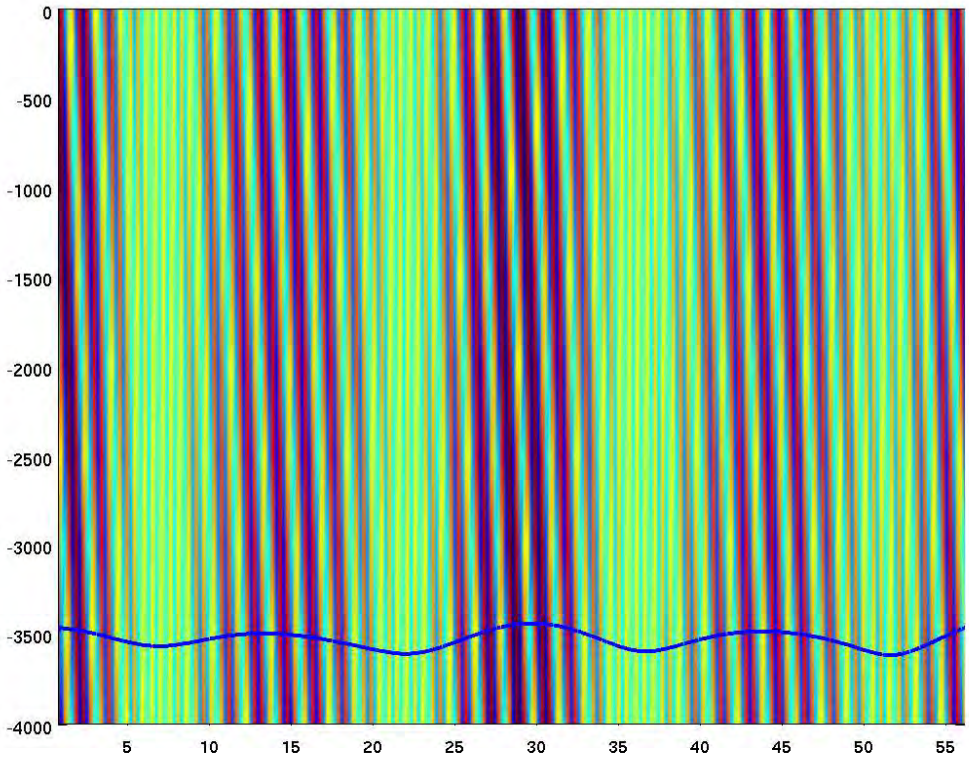

Figure 3.26. Anti-cyclonic and cyclonic rotary wavelet amplitudes at the semi-diurnal frequency at depth for the plane wave sum model at 21° with the inertial displaced by semi-diurnal waves. Curve on the bottom is the lowpass amplitude envelope of the barotropic tide values used in the model for setting the semi-diurnal properties. Model description is in section 3.3

where B is the bispectra, ω_1 and ω_2 the two input frequencies, ω the interaction frequency, W is the wavelet, and τ the time variable. For this calculation, the frequency sum rule is followed so that

$$\omega = \omega_1 \pm \omega_2 \tag{3.5.3}$$

The bispectra subscript (rx) indicates rotary cross-bispectra. The rotary wavelet bispectra and bicoherence can be considered as the cross wavelet bispectra between rotary velocity components. To visualize this, a single transform vector of complex velocity amplitudes is constructed mimicking a complex Fourier decomposition from individual wavelet rotary transforms and displayed in the same manner as the Fourier analysis.

The wavelet bispectra is normalized by the product of each transform's magnitude to yield the rotary wavelet bicoherence. A discussion of wavelet bispectra, and the associated error estimates used here can be found in van Milligen et al. [89]. There is an error associated with each wavelet decomposition component that can be approximated by $N^{-1/2}$ (where N is the number of realizations), representing the integration of the total record time. An additional error is associated with the scale of each decomposition component, i.e., how many independent kernel 'widths' will fit in the record at a given wavelet scale.

To summarize, we have incorporated rotary wavelet analysis (as in Liu et. al. [45]) with wavelet bispectra and bicoherence (e.g., van Milligen et al. [89]; Gurley et al. [30]) and presented the resulting wavelet rotary bispectra and bicoherence in a frequency equivalent format to the Fourier techniques used in the previous section.

Figure 3.27 shows the bispectrum for the 21° model. There is very good comparison with the corresponding bispectrum calculated using Fourier methods show in Figure 3.16. In the wavelet analysis, there has been a reduction in spectral resolution, which is evident in the far larger regions of elevated bispectrum. But the center of these regions lies on the triple points associated with the interaction between the semi-diurnal tide and inertial waves. Peak amplitudes between the Fourier and wavelet analysis are quite similar.

The rotary wavelet bicoherence is shown in Figure 3.28 for the same model. There is similarity with the corresponding Fourier bicoherence (Figure 3.17). However, the level of bicoherence between respective peaks is more variable, and the locations associated with the sum $(M_2 + f)$ interaction frequency are diminished. There are two factors which contribute to this: the sum frequency is contaminated by semi-diurnal energy in this wavelet decomposition (as seen in the wavelet rotary PSD, Figure 3.22), and the choice of two wavelet decompositions separated by 1.5 days could influence the bicoherence estimate for the sum frequency.

In this section a new wavelet tool for identifying interactions has been developed and compared with existing Fourier methods. The rotary wavelet bispectra and bicoherence analysis is shown to identify the inertial displacement model interaction signature associated with IWISC. This method could be useful in data where one or more of the signals are of short duration. The trade off is in loss of spectral resolution.

For wavelet analysis of currents, it has been demonstrated that vertical time series of band passed wavelet coefficients reveal spatial and temporal structure that could not be resolved with Fourier methods. This could prove desirable in the analysis of inertial wave, which have peak energies that appear as short term events in many oceanic current records.

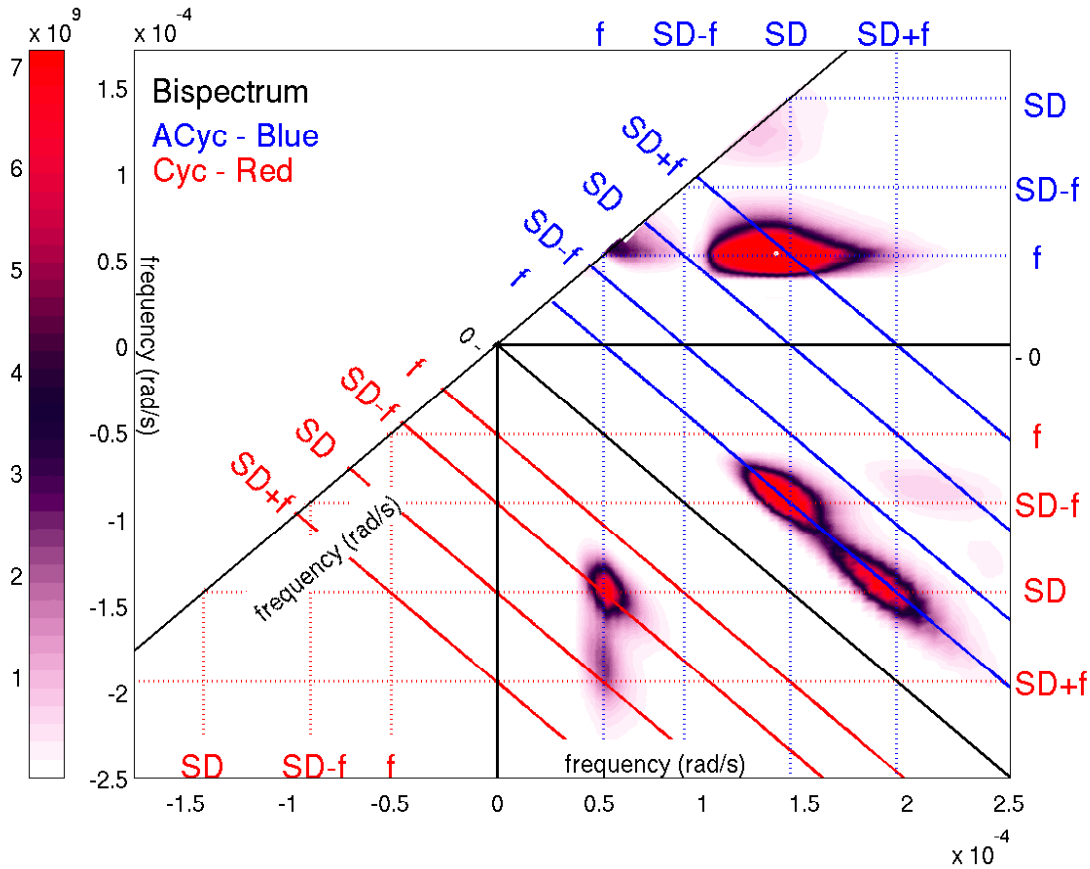

Figure 3.27. Rotary wavelet bispectrum for the inertial displacement model at 21° described in the text (section 3.3). There are peaks at the interaction triple points associated with the inertial and semi-diurnal internal waves in the modeled record. There are three frequency axes which range from cyclonic (red) through zero frequency to anti-cyclonic (blue). Elevated bispectrum indications are then associated with the three frequencies indicated on the respective axis.

3.6 Summary of Advection Analysis and Simulation

The simple model where a single sinusoid vertically advects a horizontal inertial current has been examined and extended to multiple displacements. This resulted in the following:

- vertical advection by itself produces oscillations at the interaction frequencies that violates internal wave consistency; the resultant motions are not free internal waves,
- higher order PSD peaks (harmonics of the interactants), when observed, can be a unique test of vertical advection,

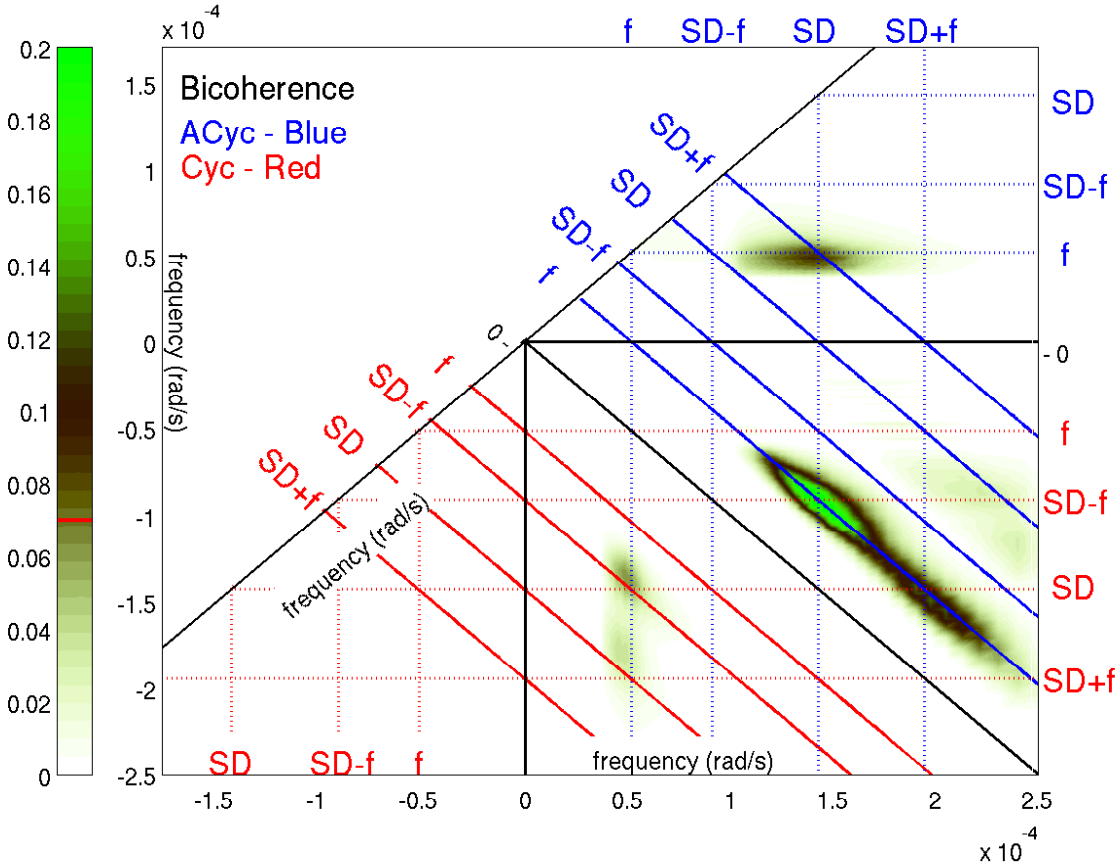

Figure 3.28. Rotary wavelet bicoherence for the inertial displacement model at 21° described in the text (section 3.3). The frequency triple associated with IWISC shows significant elevated bicoherence. There are three frequency axes which range from cyclonic (red) through zero frequency to anti-cyclonic (blue). Elevated bispectrum indications are then associated with the three frequencies indicated on the respective axis.

- vertical structure of the input displacement signal produces phase asymmetry in the resultant advected signal between the sum and difference frequencies,
- multiple frequency displacements (semi-diurnal constituents) can broaden reversible advection spectra peak signatures,

These results motivated the construction of an inertial displacement model with multiple semi-diurnal tidal constituents. This model has produced a velocity field that replicates significant features of observed oceanic velocities.

The inertial displacement model was used to test analysis techniques with the goal of identifying whether reversible advection could be discriminated from energy exchanging interactions. Significant results include:

- a Semi-Lagrange (S-L) inversion methodology was successfully tested on the inertial displacement model significantly reducing the spectral signature of reversible advection,
- the S-L inversion itself can redistribute spectral energy,
- bispectra and bicoherence analyses identifies reversible advection as an interaction with no distinction from energy exchanging non-linearity, and
- wavelet rotary bispectra and bicoherence are created and are consistent with the Fourier analysis tools.

Chapter 4

Analysis of HOME A2 Moored ADCP Velocities

4.1 HOME Experiment and Data

The analysis of historical mooring records made it clear that a higher vertical resolution than was available from among these data was needed to further elucidate the nature of the interaction between semi-diurnal internal tide motion and inertial waves. In practical terms, this means moored ADCP records. However, the availability of moorings with ADCP coverage of more than the upper 500 meters is very limited. Greater depth coverage is desired given the analysis of the depth dependence of IWISC shown in section 2.3.7, where the distribution of buoyancy scaled peak energy at the IWISC frequency is shown to be maximal near 1500 meters. Few experiments exist with ADCP coverage to 1000 meters or more. Fortunately, in the recent Hawaii Ocean Mixing Experiment (HOME), a mooring was deployed with three ADCPs covering more than 1000 meters of depth with current measurements. The verified data from this mooring became available after the current investigation of IWISC had begun

High vertical resolution of the full 3-D current vectors is necessary to help in the discrimination between advection and non-linear energy exchanging interactions. The primary reason is the need to characterize the vertical velocity of the semi-diurnal internal tide signal. Vertical velocity is used for conversion to a coordinate system that follows the displacement of the water column by the semi-diurnal internal tide. Of course, the data containing suitable vertical velocity also needs to have evidence of the interaction between the inertial and semi-diurnal internal tide. The confluence of these features was found in the A2 mooring deployed in the Kauai Channel during the HOME experiment.

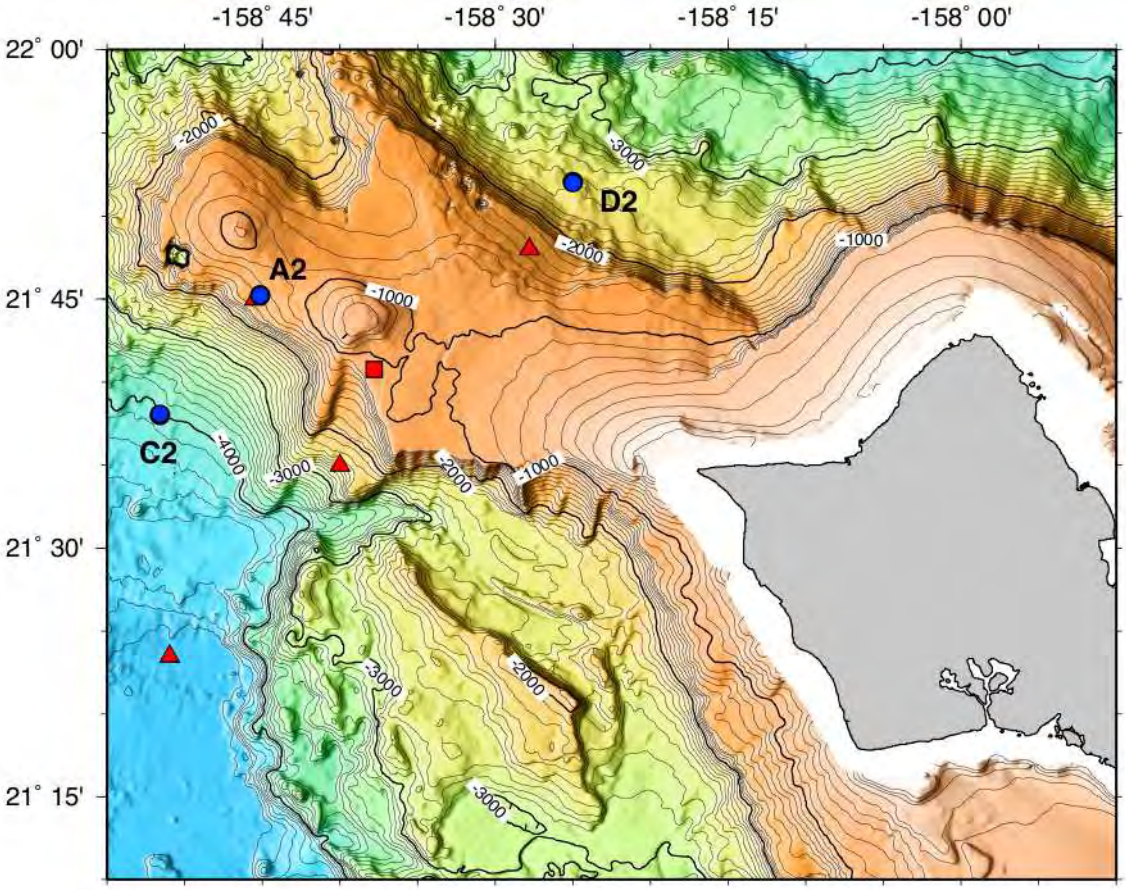

Figure 4.1. Location of Hawaii Ocean Mixing Experiment (HOME) moorings in the Kauai channel. The focus of this chapter is on ADCP data from the A2 mooring. Mooring C2 data was used as well. Map courtesy of D. Luther.

HOME was a directed effort to quantify the energy conversion from the barotropic tide to mixing at the Hawaiian ridge (see Rudnick et. al. [77]). A combination of new observations, numerical modeling, and historical data re-analysis was employed to determine the amount and pathways of tidal energy conversions. One important goal of the experiment was to produce a high resolution measurement of the activity directly above the ridge in the Kauai Channel. In previous modelling work (see Merrifield et. al. [50]), barotropic tide forcing was shown to produce beams of internal tide energy at mid-depth over the ridge, leading to the proposed mooring location.

The A2 mooring was deployed from November 2002 to June 2003 at the location indicated in figure 4.1. A description of the data, and discussion of quality control and processing, is contained

in the Oregon State University technical report COAS-2005 [6]. The depth at the mooring location is 1329 meters. Carter et al. [8] employed the A2 mooring data to validate the accuracy of a high resolution numerical model of the internal tide, and A2 data was used by Carter and Gregg [7] to evaluate near-diurnal waves at this location.

4.1.1 Impact of Observations

The obvious question that arises when considering any data set for its utility in investigating the IWISC phenomenon is whether there is a clear indication of energy at the interaction frequency $M_2 - f$ (at 1.19 cpd, or $8.71 * 10^{-5}$ rad/s for this latitude). To examine IWISC energy, the rotary velocity and rotary velocity shear have been analysed for power spectra and averaged across a 7 bin depth range. In figure 4.2 there is a pronounced peak in PSD at the IWISC frequency in the cyclonic rotary velocity. In Figure 4.3 there is an even more provocative peak in shear PSD in the cyclonic at the IWISC frequency.

Peak energy in PSD at these frequencies in other datasets has been interpreted as possible non-linear interactions (Mihaly et al. [51], van Haren [88]). The pronounced enhancement of shear at the IWISC frequency further suggests a role for IWISC variability in the non-linear cascade of energy to smaller scales.

This shear information is doubly interesting, as the depth range for this vertical average overlaps an energetic portion of a topographically generated semi-diurnal internal tide beam. The traditional expectation is that this type of internal tide beam would exhibit enhanced shear. While there is some shear at the semi-diurnal, the IWISC band shear is elevated above this.

As a comparison, figure 4.4 depicts the same data as figure 4.3 after vertical coordinate transformation (Semi-Lagrange inversion or S-L) based on the observed semi-diurnal tide vertical velocity. The transformation process is describe in section 3.3, and will be discussed later in this chapter. It is sufficient here to state that the IWISC shear has not diminished suggesting a process other than reversible vertical advection by the semi-diurnal internal tide displacement.

Given the energy distribution indicated by these figures, it is unlikely that a simple vertical advection mechanism is the dominant source of enhanced IWISC energy at these depths. This evidence is a unique indication of possible non-linear interaction in the internal wave field. In the analysis of historical moored current meter records in chapter 2 the origin of energy at the interaction frequencies associated with inertial and semi-diurnal internal waves was ambiguous. Using the high resolution data available from the A2 mooring, we have established ample evidence of IWISC activity that can not be explained by the simple vertical displacement scenario. The analyses presented in this chapter establish this significant result.

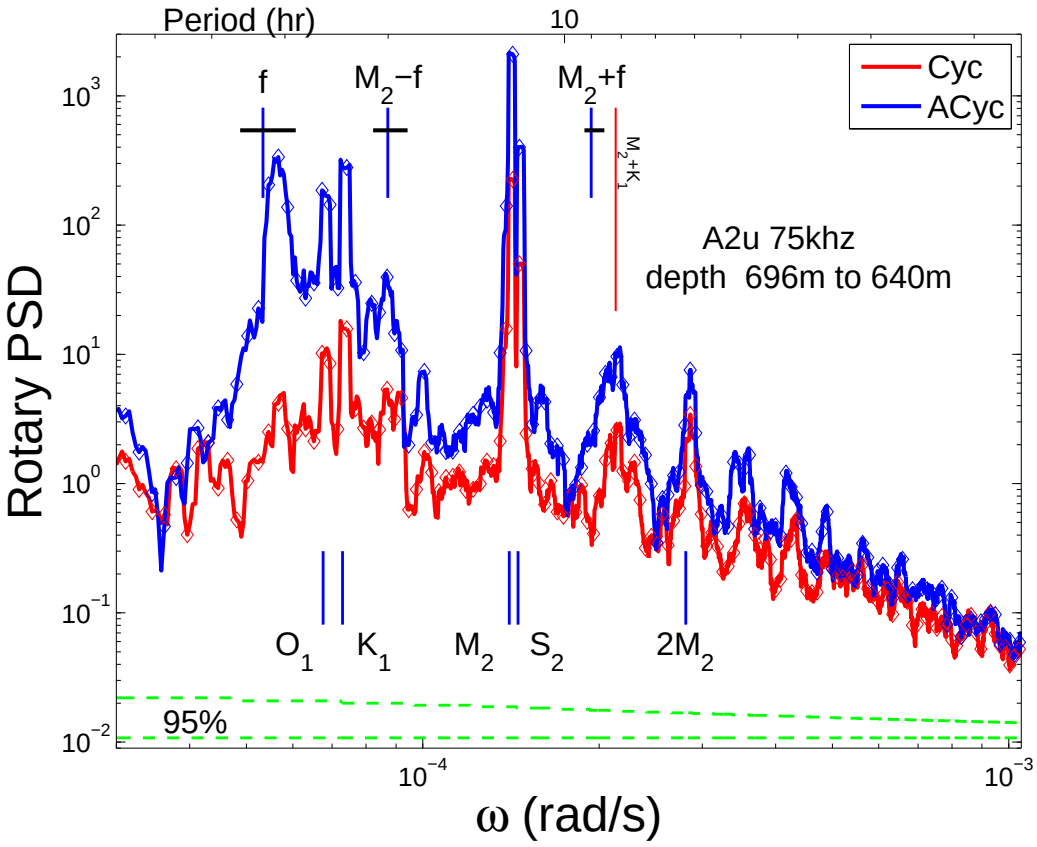

Figure 4.2. Horizontal rotary velocity PSD $((m^2/s^2)/(rad/s))$ from the HOME mooring A2 upper long range ADCP for the 7 bin depth range between 696m and 640m. There is enhanced energy at the IWISC $(M_2 - f)$ and $M_2 + f$ frequencies. Dashed green lines indicate 95% confidence interval, diamonds indicate frequency intervals between independent PSD estimates.

In an ideal world, the available data would cover horizontal ranges, include complete information on the large scale background flow, have continuous coverage of buoyancy at all depths, etc. Such data is not available at this time; however, progress is possible with the unique records at A2. Important features of the data for the study of IWISC include:

- Almost full depth range, yielding necessary vertical structure information.
- Temporal range covering many inertial events.
- Significant variability in internal tide structures.
- Data allowing for the extraction of semi-diurnal displacement from ADCP measurements.

Along with these important features, there is IWISC evidence as seen in figure 4.2, and at other depths discussed later in this chapter. ‘Events of enhanced IWISC energy occur at different times across these

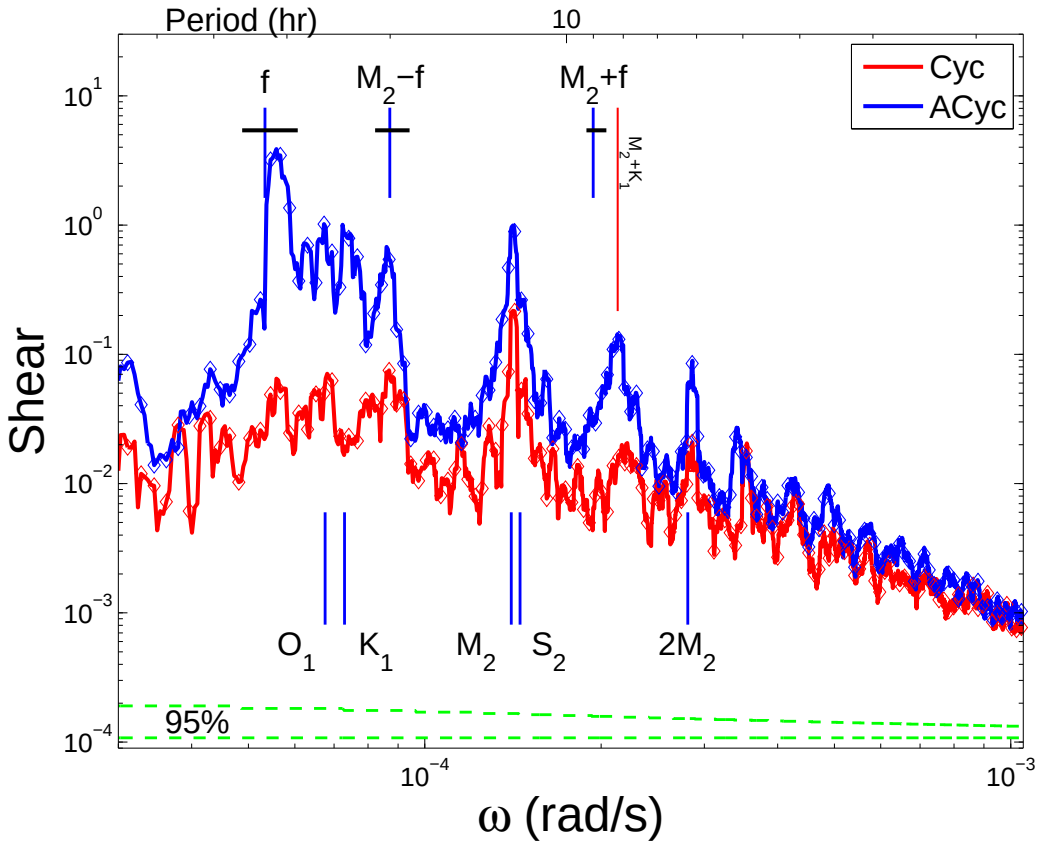

Figure 4.3. Companion display to figure 4.2 showing shear PSD ($(1/s^2)/(rad/s)$) for the 7 bin depth range between 696m and 640m. There is significantly enhanced shear at the IWISC ($M_2 - f$) frequency. Dashed green lines indicate 95% confidence interval, diamonds indicate frequency intervals between independent PSD estimates.

various depths. The data permit a distinctive illumination of the very complicated question concerning what mechanism or mechanisms are responsible for the observed IWISC energy.

4.2 Observational Context

In the examination of historical moored current meter data, the identification of IWISC was roughly dependent on the existence of inertial energy, semi-diurnal internal tide energy, and the energy of other variability in the interaction bands (such as sub-inertial eddies or energetic internal waves). The analysis was also dependent on the structure and variability of the two input energies. At the location of mooring A2 in the Kauai Channel, a multitude of processes are active that influence each of these considerations. This highly active site requires careful examination of many details influencing the nature of the IWISC phenomenon.

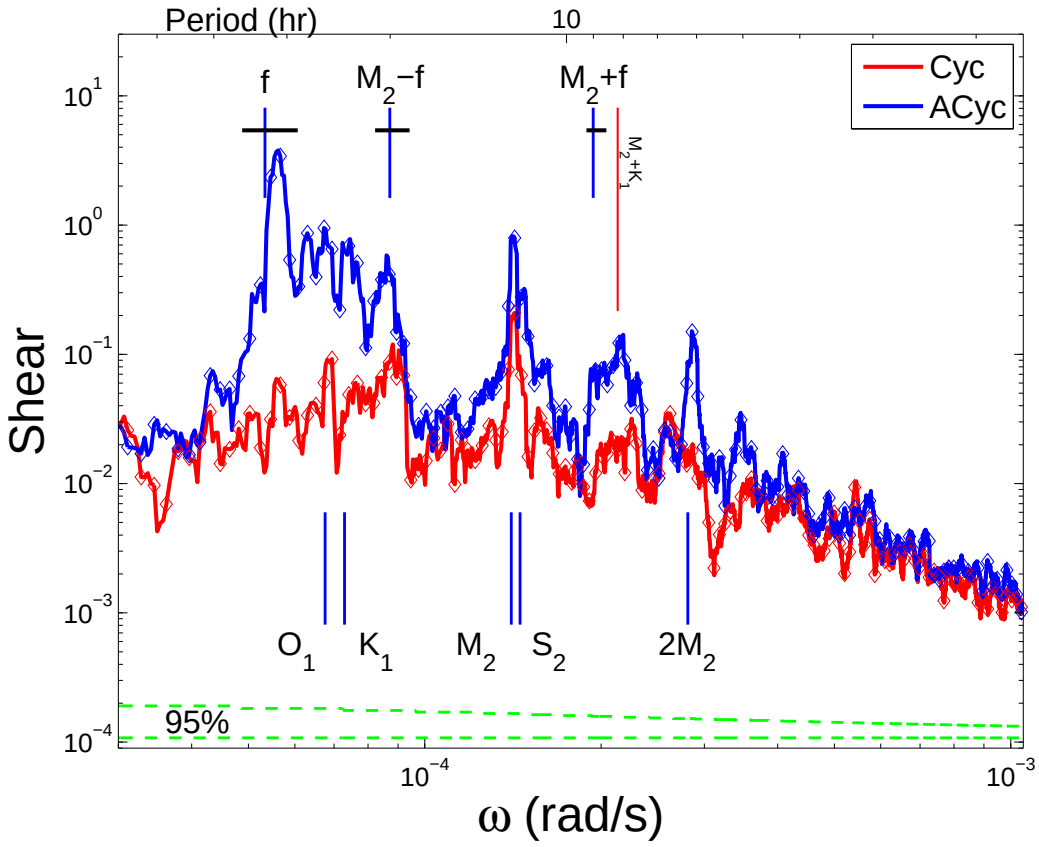

Figure 4.4. Shear PSD ($(1/s^2)/(rad/s)$) for the 7 bin depth range between 696m and 640m after the data has been Semi-Lagrange inverted using the semi-diurnal displacement (see text for details). In comparison to Figure 4.3, there remains significantly enhanced shear at the IWISC ($M_2 - f$) frequency. This suggests there are other processes than simple vertical advection of inertial waves by the semi-diurnal tide. Dashed green lines indicate 95% confidence interval, diamonds indicate frequency intervals between independent PSD estimates.

Large segments of the record contain significant background (low frequency) shear flow. The difference frequency band ($M_2 - f$; 1.19 cpd for this latitude) is near diurnal processes which might 'leak energy into it at times. The sum band ($M_2 + f$) is potentially impacted by tidal harmonics or other diurnal contaminants with harmonics at a frequency near $M_2 + K_1$. Inertial energy has high temporal variability throughout the records. The semi-diurnal tide itself is a summation of coherent beam structures emanating from multiple ridge slopes that are impacted by mesoscale advection.

4.2.1 Background and Diurnal Flow Structures

At the A2 site the inertial internal wave band may be influenced by a number of low frequency and diurnal flow features. This could have an impact on the determination of interaction processes. Two

influences are of particular concern, the diurnal tide which is very near in frequency to both the inertial and IWISC frequencies, and the low frequency background meridional flow. Figure 4.5 illustrates this complex situation. Two depth levels are represented, one at 440 m from the upper ADCP, and one at 776 m from the lower ADCP. This figure of time series of the frequency of the maximum inertial wave PSD was constructed using the following method:

- a double tapered Hanning window is constructed with half width less than 20 days;
- rotary Fourier PSD is computed daily from windowed data sections;
- time series of anti-cyclonic PSD from three depth bins bracketing the two central depths of 440 m and 776 m are smoothed with a 21 day moving average filter;
- the three time series around each central depth are averaged at each time step; and,
- the frequency corresponding to the maximum near-inertial PSD estimate at each timestep is recorded.

There is a trade-off as the closeness of the diurnal tidal band, and its variable amplitude, present a problem for observed inertial frequencies exceeding approximately $1.1f$. There are instances in the record where the diurnal energy is elevated and 'leaks into the band selected for the inertial waves. If the inertial wave peak is relatively weak, the predominant energy for any window containing diurnal elevated energy is contaminated, and yields an incorrect value for both peak frequency and energy.

At the top of Figure 4.5 is the 15 day average background meridional flow for each depth. There is a large eddy that appears to influence the inertial band at the upper depth during the time period between day 380 and 430. The eddy extends in depth far enough to influence the upper bins of the lower ADCP instrument as well. The colored crosses indicate the frequency of the peak PSD value in the inertial band for a rotary transform of the total record at the respective depths. The estimate of peak inertial band frequency based on the total record is dominated by the energy associated with the eddy event at the upper depth.

This analysis illustrates another significant source of variability that could potentially impact IWISC identification. Partitioning a record based on inertial events is problematic if there is significant background flow modifying the peak inertial frequency. Horizontal advection introduces multiple complexities into determining energy distribution among interacting structures. This is further complicated by the fact that it is a shear flow, and comparison between lower and upper depths during this time may not yield relevant comparisons.

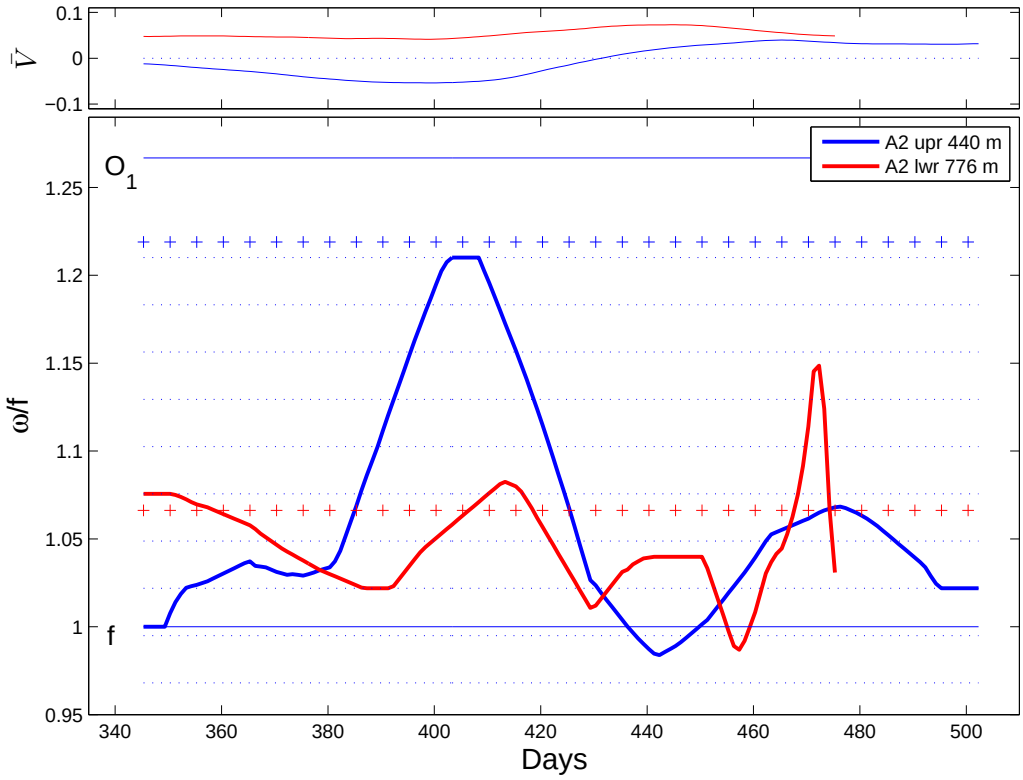

Figure 4.5. Frequency of the maximum PSD in the inertial wave band for an anti-cyclonic Fourier decomposition with double taper window applied daily to the A2 mooring ADCP data for two depths, 440 meters and 776 meters. At the two respective depths, the rotary PSD is averaged across three adjacent depth bins. Dotted reference lines indicate the frequencies of the Fourier constituents. Colored crosses represent the frequencies of the peak energies in the inertial band at both depths for the whole record . In the top frame is the 15 day average meridional velocity (m/s) for the two depths. Days are measured from Jan 1, 2002, 0000 GMT.

This analysis illustrates a significant source of variability that could potentially impact IWISC identification. Partitioning a record based on inertial events is problematic if there is significant background flow modifying the frequencies of near-inertial waves. Horizontal advection will complicate the determination of energy distribution among interacting structures from time periods of differing background flow. This is increased in difficulty by the fact that it is a vertically sheared flow, so that it may not be consistent to compare results between lower and upper depths.

One of the significant influences on the distribution and character of inertial and semi-diurnal energy interaction at this mooring A2 during the HOME experiment time period is likely the variability of the background meridional flow. Introduced at two depths in the discussion above, this flow is depicted in figure 4.6 for the full data length, and for all three ADCP instruments deployed. The meridional velocity was averaged with a fifteen day window at each day. In this figure, and subsequent figures, a black circle of variable radius has been used to represent the ratio of blanked data in the fifteen day window. The blanked data had a poor quality due to the noisy acoustic returns received from these depths and times. Areas of medium and high black circle density have little quality data. The most striking feature of the meridional flow is the complete shift from full depth shear flow during the first 120 days of the experiment to relatively uniform meridional flow during the remainder of the time. A definitive explanation for this observation has yet to be proposed. It is entirely possible that a large scale shift in flow occurs periodically or is a non-periodic normal dynamic range for the channel. Another explanation could be a large eddy interacting with the channel. Cursory investigations were made into weekly SSH maps of the region, but a conclusive dynamic link to large eddies around the Kauai channel were not obvious.

The second feature of note is the eddy-like structure entering the channel during the time period of 370 to 420 days (which obviously contributes to the sheared structure just emphasized). This flow structure appears to have an impact on the semi-diurnal internal tide beam (shown below). It is unclear whether this eddy is directly associated with whatever is creating the large scale vertical shear, or is completely independent of it. It was illustrated above how this eddy has significantly changed the energy distribution in the narrow inertial band. Subsequent figures will have the eddy velocity contour of 5 cm/s southward flow displayed to simplify the identification of potential eddy-related effects in other frequency bands.

There is a third feature which has been separately observed by the HOME surface radar installation which was operational for a portion of this time period (Chavanne et al. [9]). This is the eddy variability which is evident from 420 to 470 days, primarily above 250 meters. For the purpose of exploring interaction signatures between inertial and semi-diurnal structures, the eddy will not come into consideration. This depth range has significant data degradation preventing such analysis.

4.2.2 Vertical Time Series of Band-passed Velocity

As with the low frequency velocity, the A2 data set allows for the unique visualization of the evolution of the energy in frequency bands of interest as a function of depth over the course of the

deployment. Each depth vs. time series figure of specific band energy presented below is constructed using the following procedure:

- Extract the depth binned, sway and pressure corrected, ADCP velocity data for each instrument
- Apply mask removing additional contaminated data, as described in [6]
- Apply mask to edges of missing data
- Create daily data segments of 15 days length with an applied Hanning window
- Rotary decompose windowed velocity at each depth, for each day
- Calculate Fourier PSD and smooth
- Select peak values in PSD for each band of interest (bandwidths visually indicated in figure 4.2)
- Display with 2x2 two-dimensional smoothing filter applied in depth vs. time format

Each of the subsequent figures of band-passed energy at depth versus time utilize the same method. Color contours are independent and set for each figure individually.

Semi-diurnal

In figure 4.7 the sum of the power spectral densities of both components of horizontal velocity, band-passed for the semi-diurnal, is shown in depth versus time. Depths above 340 meters are shaded indicating reduced confidence in the data, corresponding to the degradation graphically represented in figure 4.6. This results in a significant un-answered question: "What is the upper extent of the semi-diurnal internal tide beam or beams? Fortunately, the 'core of the main observed beam is clear. This 'core is centered near 610 meters during many spring neap cycles.

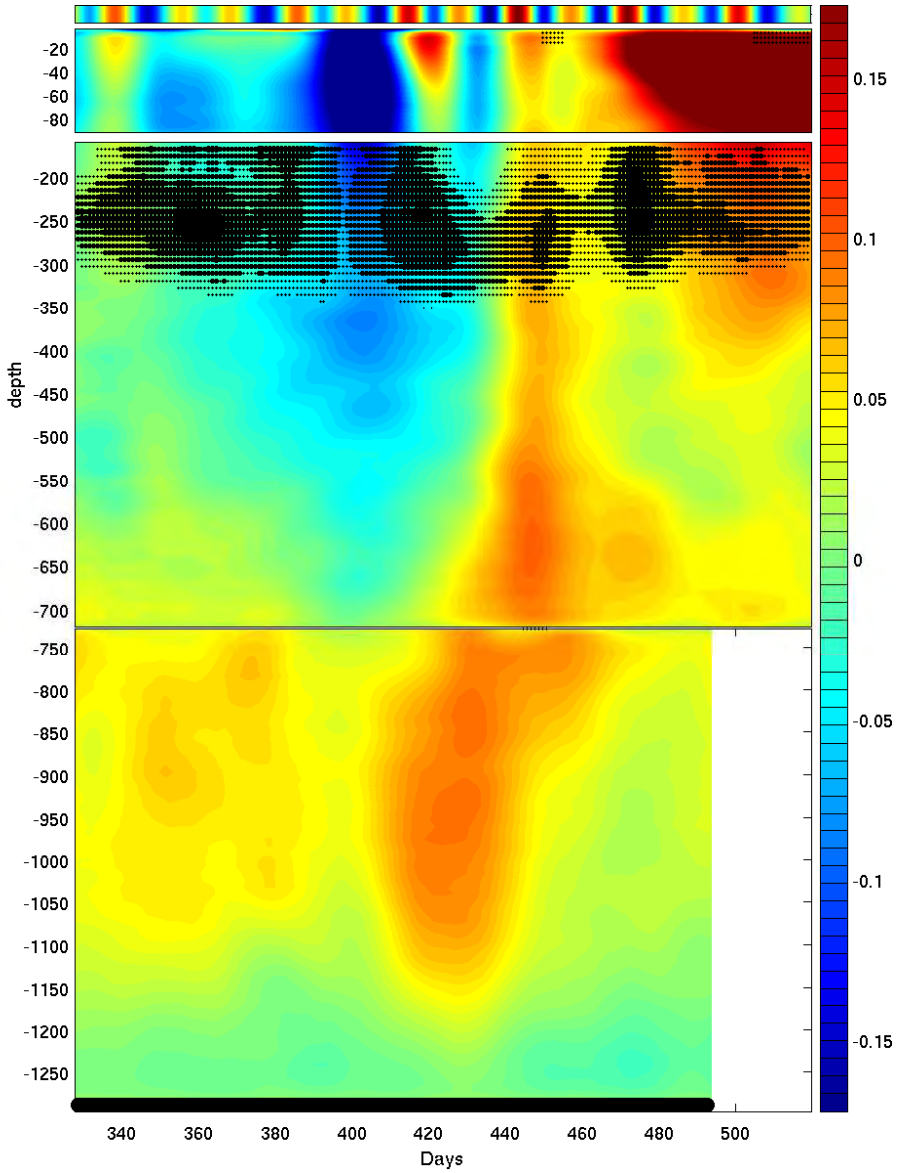

Figure 4.6. Vertical time series of ADCP fifteen day mean velocity (m/s) in the meridional direction for the A2 HOME mooring. Shaded regions represent ratios of blanked data in the calculation of the average at that point. Semi-diurnal barotropic tide amplitudes are indicate at the top, as calculated from TPXO6.2 model. Positive (red) indicates northward flow in meters per second. Days are measured from Jan 1, 2002, 0000 GMT.

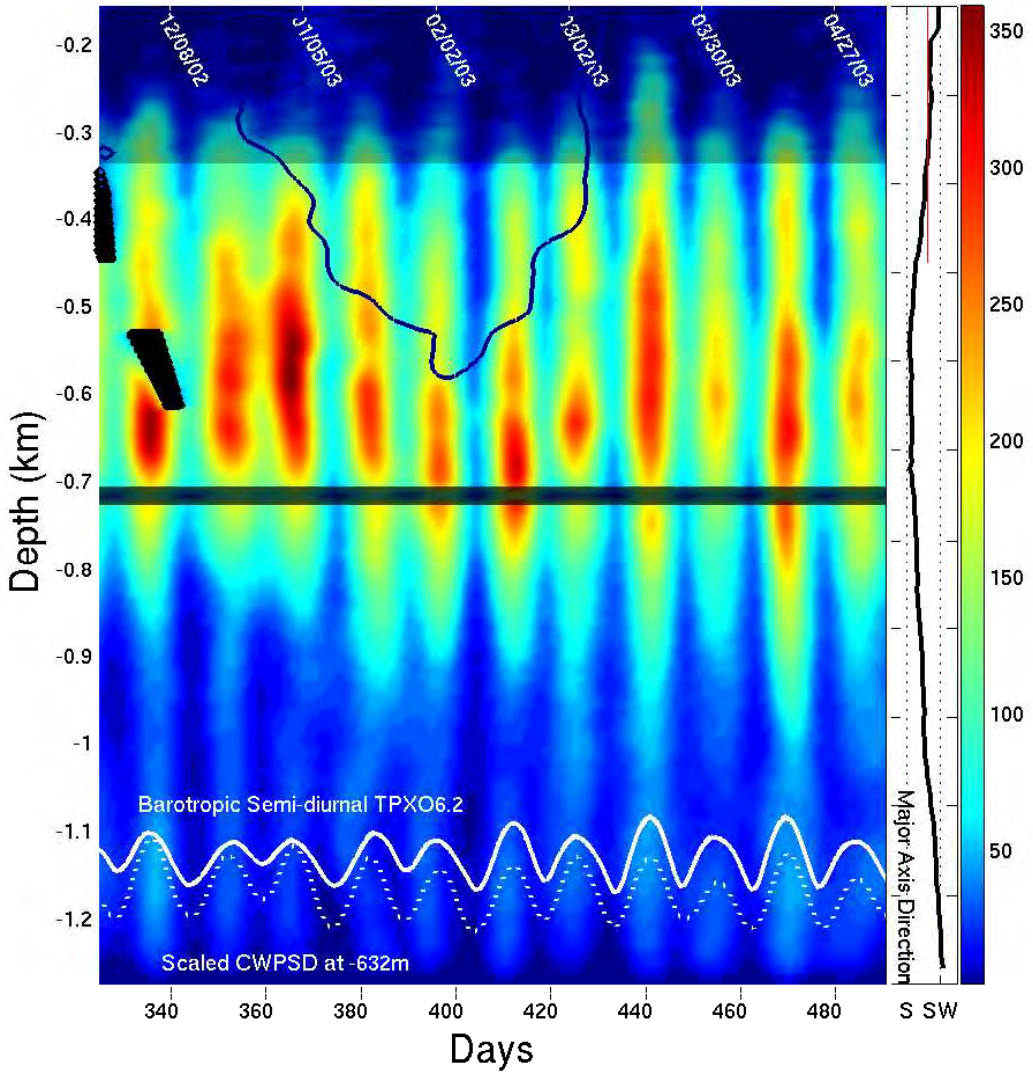

Figure 4.7. Time series of ADCP semi-diurnal band velocity PSD $((m^2/s^2)/(rad/s))$ sum of cyclonic and anti-cyclonic components vs. depth for the A2 HOME mooring. Above the thin blue contour is time depth location of southward background 15 day average meridional velocity that exceeds an amplitude of 5 cm/s. The solid white line represents the barotropic semi-diurnal sea level tide derived from TPXO 6.2 for this location. Dotted white curve is a scaled single rms time series of semi-diurnal horizontal current amplitude from depth 632 meters. First right hand panel indicates tidal ellipse major axis direction versus depth, with scale lines at 180° and 225° degrees indicated (South and Southwest, respectively).

A contour of the low frequency meridional velocity eddy is shown. Above the contour the meridional velocity exceeds five centimeters per second to the south. This appears to correspond with a deeper appearance of the semi-diurnal tide beam as it crosses the mooring location. A reasonable speculation is that beam energy is either advected southward by the eddy (since the beam is expected to be at a deeper depth to the north) or the beam is displaced downward via refraction during propagation through the eddy, resulting in the mooring seeing the beam at a lower depth during this time.

There are two sections of data removed from the records at 350 - 610 meters during the first 20 days of data. This is the result of an instrument software error, not a dynamic feature. At the overlap between the data from the two 75 kHz ADCPs (around 710 m) a data gap occurs. The first three bins of the upper instrument returned weaker current amplitudes than expected, probably due to contamination from acoustic reflections from hardware on the relatively motionless mooring line; the lower instrument only overlapped the first two bins of the upper instrument.

There is a remarkably good correspondence in relative timing and amplitude between the semi-diurnal barotropic sea level tide indicated by the solid white curve and the qualitative amplitude and envelope periodicity of the internal tide beam. To compare the observed spring/neap cycles within the beam with the modeled barotropic tide, a single depth of band passed semi-diurnal tidal currents has been selected and the data processed with the same low-pass filter as used on the TPXO6.2 model.

The dotted curve represents a single depth at 632 meters within the beam of total semi-diurnal PSD, scaled to compare with the barotropic tide. The alternating strong, then weak envelope structure during the record is especially clear in relation to the barotropic tide. The spring/neap cycle envelope peaks appear in close alignment visually, but a quantitative comparison is necessary.

A calculation of envelope peak lag can be done between the modeled spring/neap curve of barotropic sea level and the observed internal tide spring/neap cycles (dotted curve in figure 4.7). In the following table 4.1, each individual envelope maximum has been selected from the two curves and compared.

Table 4.1. Spring Neap Peak Times

TPXO6.2	337.3	354.9	367.4	384.9	397.8	413.9	427.3	442.6	456.5	471.3	486
Obs. 632m	337.6	353.8	367.7	383.8	398.3	414	427.3	442.7	457.1	471.8	486.4
Dif	0.3	-1.1	0.3	-1.1	0.5	0.1	0.0	0.1	0.6	0.5	0.4

If we neglect the two peaks in the observed data that precede the barotropic, the average lag is 7.4 hours. If we make a reasonable assumption that the beam vertical structure is mode three, a 7.4 hour lag implies a generation site approximately 25 kilometers from the A2 mooring, assuming the barotropic spring tide maxima have no lag over this distance. There is not enough information in this analysis to predict with confidence either the lag or the structure, but it is interesting that the outcome of this crude

analysis fits well with the beam as predicted by models like Merrifield et al. [50], where a significant beam-generating critical slope is located to the NNE 25 kilometers away. More detailed analyses, including explicit ray path calculations will be accomplished at a later date, since the origin of the internal semi-diurnal tide signal is not important to this work, just its vertical and temporal variability.

In figure 4.7, the first panel on the right indicates the major axis orientation of the internal tide ellipse for the semi-diurnal band. The calculation utilized data at each depth bin from day 330 to day 486. Within the peak energy region of the beam the axis is directed South. In depths descending from the beam the axis turns to the South-West. In the upper depths the barotropic modeled (TPXO6.2) major axis direction is indicated with a thin solid red line. This is oriented at 207°, roughly S by SW.

There is a suggestion that there are two distinct semi-diurnal internal tide beams crossing at this location at mid-depth. This can be seen in Figure 4.7 by the rotation of the tide ellipse to the southwest above the core and the appearance of a distinct 'second core around 400 m. The clearest indication of a second beam core occurs during the elevated semi-diurnal tide envelope centered at day 475. This core seems to extend in depth about 100 meters. Most times, the shallower and weaker core, which is likely generated a little farther from A2 than the beam centered at about 610m, appears to be overwhelmed and hidden by the vertical extent of the stronger, deeper internal tide beam. The change in the major axis direction discussed previously suggests a different origin site for the weaker beam, possibly more to the east and further away than 25 km (because of its position higher in the water column). The relative weakness of the second beam could be explained if the beam only grazes the A2 site. Other explanations abound. Again, all these speculations are subjects for future investigation.

There are two generation sites north of this location which possess the correct separation to produce such a structure. However, it is possible that this mooring was on the edge of the upper beam, and by advective mechanisms, recorded the beam with the variability shown. Also, as already stated, the full range of this second beam is not known, as the contamination prevents correct association of amplitudes at depths in the contaminated region.

Finally, note that Zilberman et al. [99] presented evidence of semi-diurnal internal tide generation at the bottom at A2. This process dominates the semi-diurnal internal tide in the 200 m right next to the bottom and produces predominantly a displacement signal. Careful inspection of Figure 4.7 (see also Figure 4.8) reveals occasional maxima in the PSD of the horizontal currents around a depth of 1150 m (e.g., see days 340, 442 and 473). This nascent third semi-diurnal tide beam at A2 must propagate off to the southwest per the direction of the major axis of the current ellipse previously discussed.

Before closely examining specific pieces of this rich data for possible IWISC interactions, a point needs to be made concerning the highly variable semi-diurnal tide structure displayed here. It can

be assumed that the generation is deterministic and locked to the barotropic tide (for example see Merrifield et al. [50]). This assumption seems to be supported by the similarity in the barotropic and baroclinic spring/neap cycle curves shown in figure 4.7. Such close correspondence in envelope amplitude between baroclinic and barotropic tides requires that the conversion of the semi-diurnal band at nearby abrupt topography occurs for multiple tidal constituents in concert (e.g., especially M2, S2, N2 and K2).

The close correspondence in envelope amplitude is improbable across the whole depth range, since each beam is generated at a separate critical slope of non-identical distance from the mooring. Each beam may then exhibit distinct phase and energy variability associated with the particular conditions at its origin and the environmental situation (e.g., distance; mesoscale/sub-mesoscale variations of density and current) through which it propagated before reaching A2

To examine the depth variability of semi-diurnal tide energy, a 28 day average of the output in figure 4.7 is displayed in figure 4.8 with three 100 meter vertical averages plotted at their respective center depths (solid white lines). Depths above 550 meters are clearly influenced by the strong semi-diurnal spring tides that precede and follow the eddy influence time period (approximately days 370-430). It is interesting that the lower curve shows a slightly increased energy during the eddy influence time period, further supporting the suggestion that beam energy is either advected southward by the eddy (since the beam is expected to be at a deeper depth to the north) or the beam is displaced downward via refraction during propagation through the eddy, resulting in the mooring seeing the beam at a lower depth during this time.

At the bottom of the figure is an average over all depths, which does not indicate significant shifts in semi-diurnal energy over the recorded time period. These averages are useful indicators of the depth variability of the semi-diurnal structures. Selecting a single depth, or narrow depth range, does not result in a complete picture of the energy variability.

Additional useful information about the semi-diurnal internal tide can be obtained by looking at individual spring/neap cycles. In figure 4.7, substantial vertical variability of PSD for each of the eleven spring/neap cycles is seen within the time coverage. Inside a single cycle there may be additional variations, even under the relatively strong averaging used in the figure. Any process such as IWISC that involves the semi-diurnal internal tide will be impacted by this variability.

To restate the problem, Eulerian observations of the semi-diurnal internal tides at a single geographic location, even with good vertical coverage, may be much less than ideal for studying non-linear interactions of the semi-diurnal tides due to variability associated with multiple source locations for the internal tide, as well as variability introduced by the effects of low-frequency shears. Even if the inter-

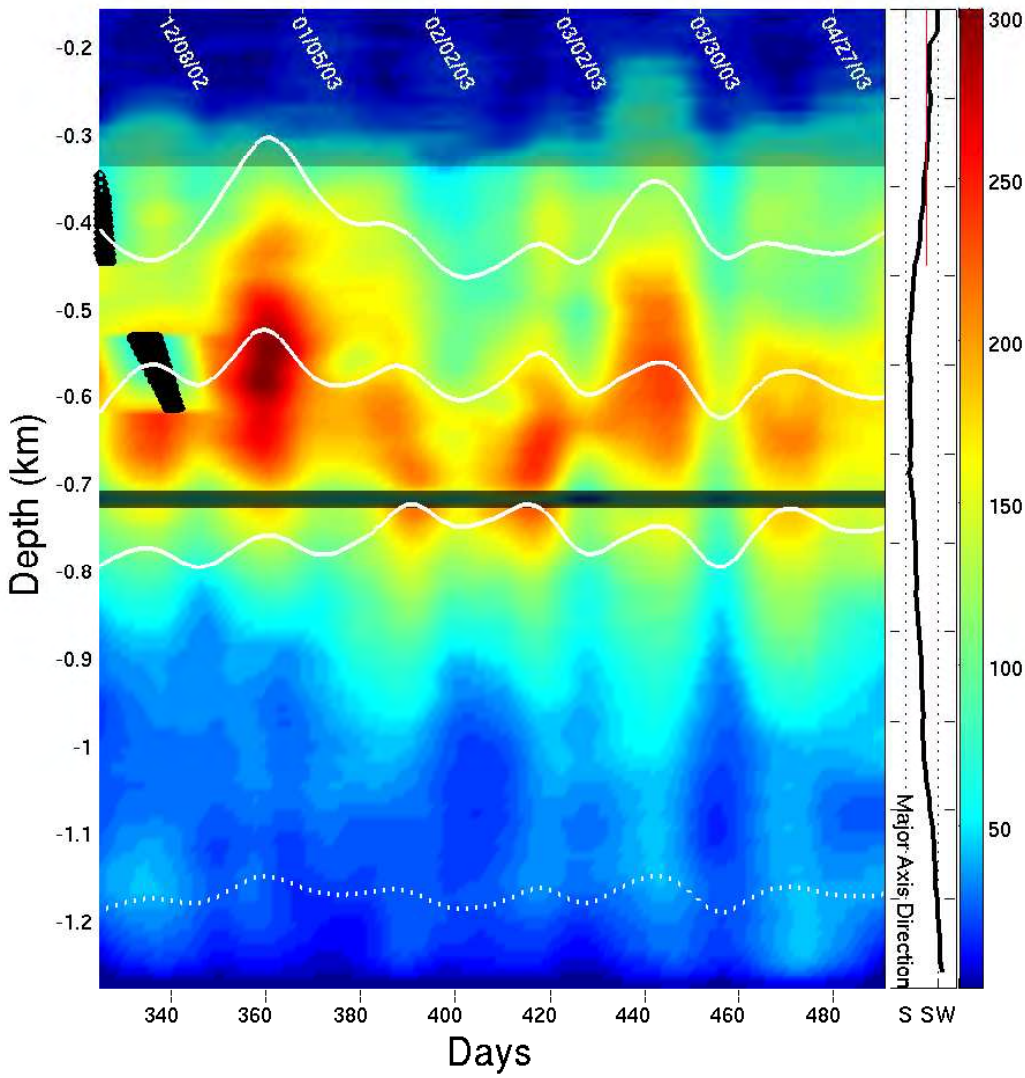

Figure 4.8. Semi-diurnal total PSD $((m^2/s^2)/(rad/s))$ from figure 4.7 after applying a 28 day moving average. Solid white curves indicate 100 meter depth averages plotted in their respective depth ranges. Bottom dotted curve is average of all depths.

nal tide beam is completely characterized by the deterministic barotropic tide, without knowledge of the beams horizontal structure, and accurate knowledge of the mesoscale background flow, the calculation of the time variability of the tidal energy and the tides interactions contains inherent unknowns.

For processes with time scales comparable to the spring/neap cycle, there are time periods within the data that show consistent features. Using the approach of comparing groups of similar spring/neap cycles may eliminate some of the questions about the impact of low frequency variability of the semi-diurnal energy at this location.

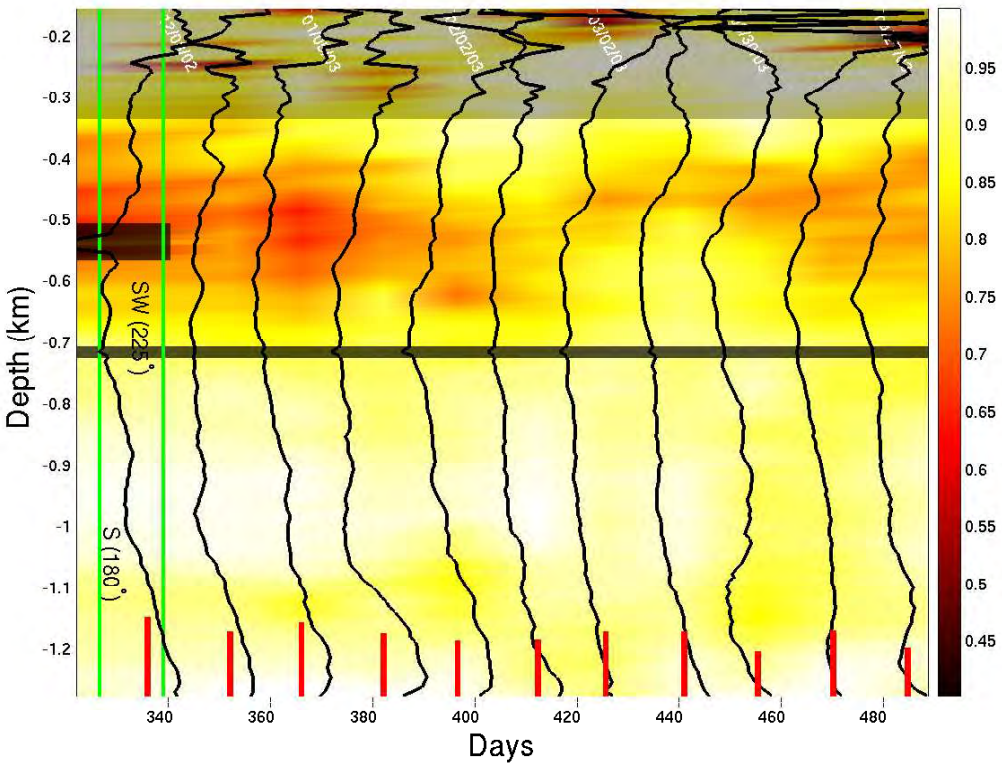

Figure 4.9. Major axis direction verses depth for each peak in the semi-diurnal spring neap cycle for the A2 mooring. There are eleven periods, with the center of the spring/neap envelope peak indicated by the day location of the red bar. The red bar indicates relative peak height of the spring neap envelopes corresponding to the main beam near 600 meters depth. The background field is smoothed eccentricity with darker colors indicating a more circular flow. The two green lines correspond to the major axis direction of the leftmost phase. Subsequent phases have the same relative angle.

An analysis of major axis orientation and eccentricity for each spring neap cycle is shown in figure 4.9. Each of the eleven recorded spring/neap cycles are analyzed and displayed with eccentricity verses depth, major axis orientation verses depth, and a bar graph with relative peak strength of the individual cycles in red.

An interesting and significant result shown by this figure is the region between the proposed two beams, one centered near 600m and the other above at 400m. This region is identified by lower eccen-

tricity (darker shading), indicating more circular motion. There appear to be multiple vertical structures that are not oriented in the same direction as indicated by the changes in major axis orientation over a given depth range. This lends additional support to the two beam conjecture.

These indications of high variability accentuate a problem when analysing the internal tide to look at interactions. When considering the interaction of these signals with other internal waves, at what point should the switch be made between deterministic demodulation vs. more generalized analysis which identifies temporal variability? In a short window of time, there is an expectation of significant variability. But it has been shown here that over the whole record of half a season, mesoscale features are at work on multiple time and space scales, and treating the internal tide as a variable process throughout is necessary, unless outside information is known or modeled.

Diurnal Internal Tide Variability

At this location there is significant temporal and spatial variability of the diurnal tide. The energy in this band is on the same order as the nearby frequencies, most importantly the inertial frequency and the interaction frequency at IWISC. This confluence of specific bands complicates analysis of any one specific frequency. For the purpose of identifying the interaction between the inertial and semi-diurnal bands, an examination of the diurnal is necessary to see its influence on the inertial and IWISC bands.

In figure 4.10 the time series of band-passed total velocity PSD is shown vs. depth. The figure clearly indicates a depth range of enhancement. There is no particularly clear beam or peak in total energy at a particular depth. Above 600 meters there is very little indication of a spring/neap cycle.

Below 600 meters the spring/neap signal is apparent, reaching towards the bottom with variations in the extent of enhancement. Above this depth there are periods of time when it appears to be predominantly diurnal internal tide energy, but inconsistent in time and depth. Some higher energy times and depths do not appear associated with diurnal internal tides.

Because energy in this band is spread among separate processes, a separate distinct identification of diurnal internal tide structures is possible by examining only the cyclonic rotary component of velocity. This will eliminate much of the broad banded inertial energy, as the inertial is predominantly anti-cyclonic. A plot of diurnal band cyclonic PSD is shown in figure 4.11.

With only the cyclonic component of rotary PSD, there appear fairly uniform weak spring/neap cycle patterns across all depths, though the region above 600 meters has some depths and times of reduced spring/neap energy. In comparison with the previous figure of total energy, it appears that the main diurnal beam center is deeper, and the energy appears to be separated into two beams.

One potential beam centered at 850 meters depth seems to correspond with a relatively uniform major axis direction. This 'beam' is not uniform in its magnitude or location from the beginning of the record to the end. There is more energy in the first half of the record at this depth. This could be associated with the background flow structure as show in figure 4.6.

The second beam is centered at a depth of 1100 meters. It has a separate axis orientation from the beam above, and is more uniform in magnitude throughout the record.

The information revealing the distribution of diurnal energy in depth and time can be summarily divided by the two depth ranges, above 600 meters and below. In the upper range, there is less distinction of diurnal internal tide activity, and the separation of this process from the inertial or IWISC could be difficult. However, this is also the depth range with much less overall energy. Subsequently, strong inertial or IWISC signals should be relatively unaffected by the diurnal.

Below 600 meters, the diurnal energy is considerably enhanced, leading to possible influence of nearby frequencies. At the same time, the diurnal is more periodic, and has a clear spring/neap cycle.

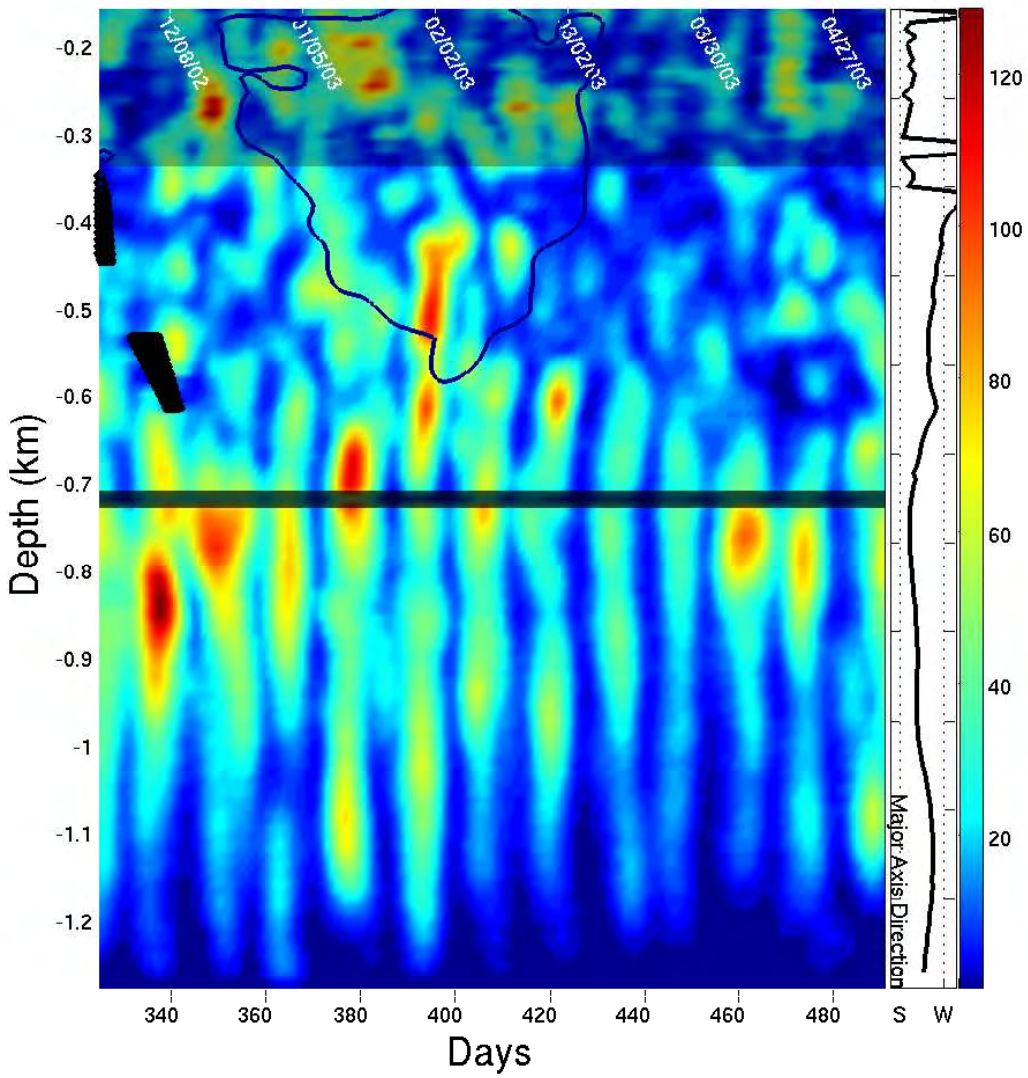

Figure 4.10. Time series of ADCP diurnal band velocity PSD $((m^2/s^2)/(rad/s))$ component sum vs. depth for the A2 HOME mooring. Above the thin blue contour is time depth location of southward background 15 day average meridional velocity that exceeds an amplitude of 5 cm/s. First right hand panel indicates tidal ellipse major axis direction verses depth, with scale lines at 180° and 270° indicated (South and West).

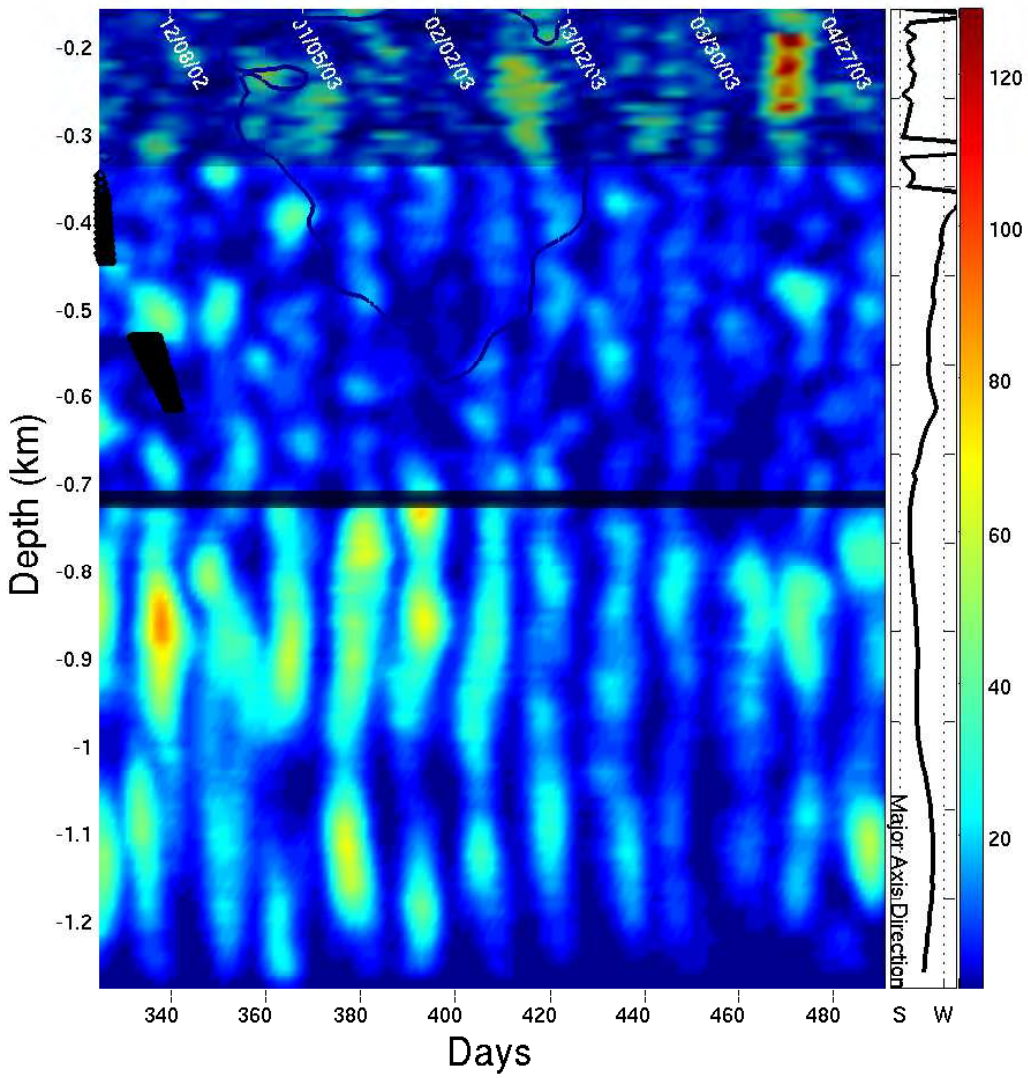

Figure 4.11. Time series of ADCP diurnal band cyclonic PSD $((m^2/s^2)/(rad/s))$ vs. depth for the A2 HOME mooring. Above the thin blue contour is time depth location of southward background 15 day average meridional velocity that exceeds an amplitude of 5 cm/s. First right hand panel indicates tidal ellipse major axis direction verses depth, with scale lines at 180° and 270° indicated (South and West). Color contour limits are independent for each figure.

Inertial

Characterizing the inertial energy at this location can be complicated by the nearness of the diurnal band and the eddy which impacts the upper depth levels during the first half of the record. A vertical time series of anti-cyclonic inertial PSD is shown in figure 4.12. Major axis direction is indicated by the black line in the second panel. Eccentricity exceeding .66, corresponding to a axis ratio of four thirds, are shown as the yellow colored depths in the second panel.

Inertial energy near f will have very low eccentricity, except near topography. At his location however, topography is near enough to be an influence. At the depths of enhanced eccentricity, the major axis direction is stable and in a similar direction as the diurnal. This could be an indication that the band itself is contaminated by diurnal energy at these depths.

The nearest topographic features are two rises, one to the North, and one to the East as seen in figure 4.1. To the North, the mount rises above the 900 meter contour, and the Eastern mount exceeds 700 meters. Both of these features are within 10 km. Some, or all, of the increased eccentricity could be due to these topographic features.

In figure 4.13 the inertial cyclonic PSD is shown. There is a definite event in the cyclonic inertial near 800 meters depth and centered on deployment day 480, a feature not evident in the anti-cyclonic inertial figure. There is not a strong indication of diurnal contamination in this figure, in comparison with the diurnal cyclonic time series. This evidence would tend to favor the near topography as a explanation of the elliptic inertial nature at depth.

In both of these inertial energy distribution figures, peak inertial PSD has more variability than would be expected of similar times series in the open ocean. There are events which occur at only certain depths, perhaps indicative of inertial wave packets being advected past this location. Little of the peak energy appears to be in storm generated downward propagating rays, as would be expected in the open ocean at similar latitudes.

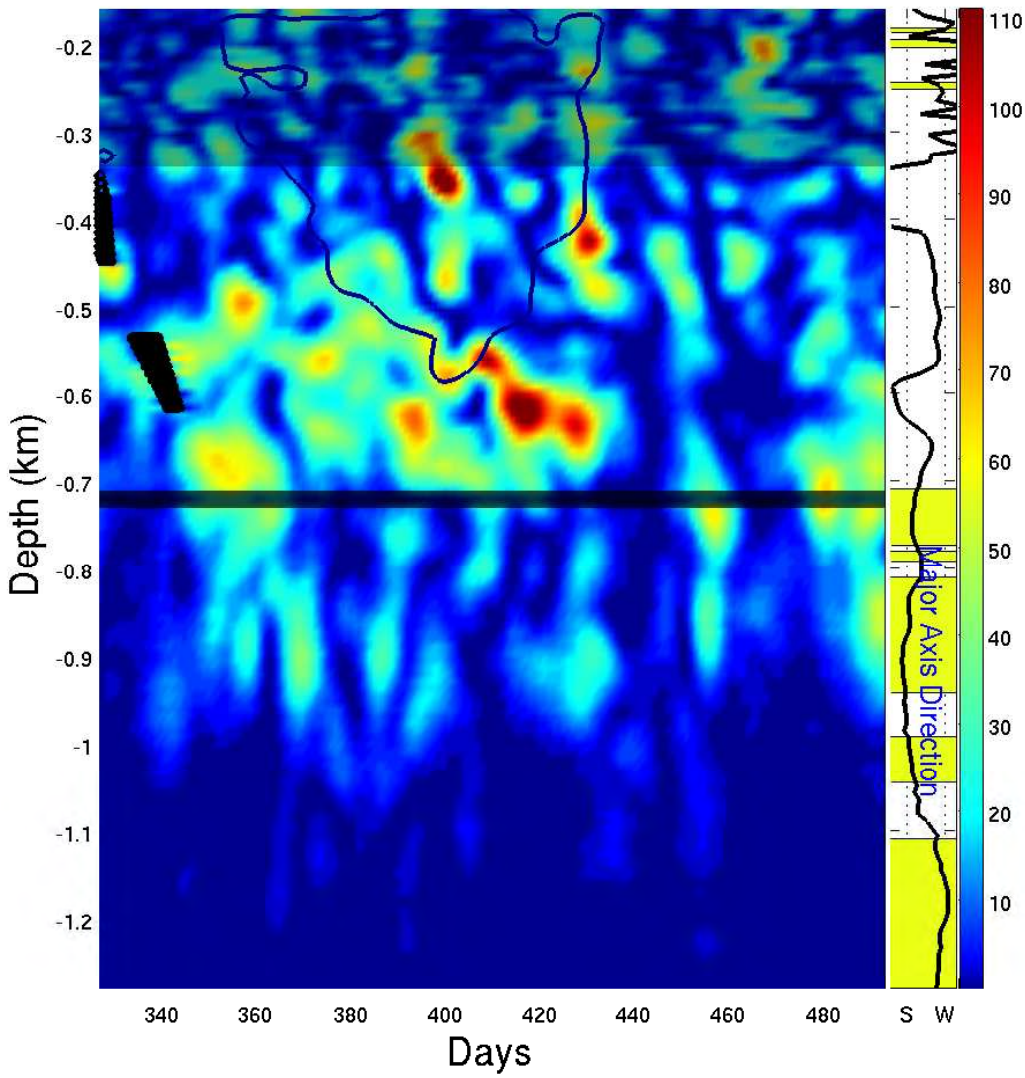

Figure 4.12. Vertical time series of ADCP inertial band anti-cyclonic rotary velocity PSD $((m^2/s^2)/(rad/s))$ for the A2 HOME mooring. Above the thin blue contour is time depth location of southward background 15 day average meridional velocity that exceeds an amplitude of 5 cm/s. First right hand panel indicates inertial ellipse major axis direction verses depth. Yellow shaded area shows depths where inertial eccentricity exceeds .66, indicating more elliptic motion.

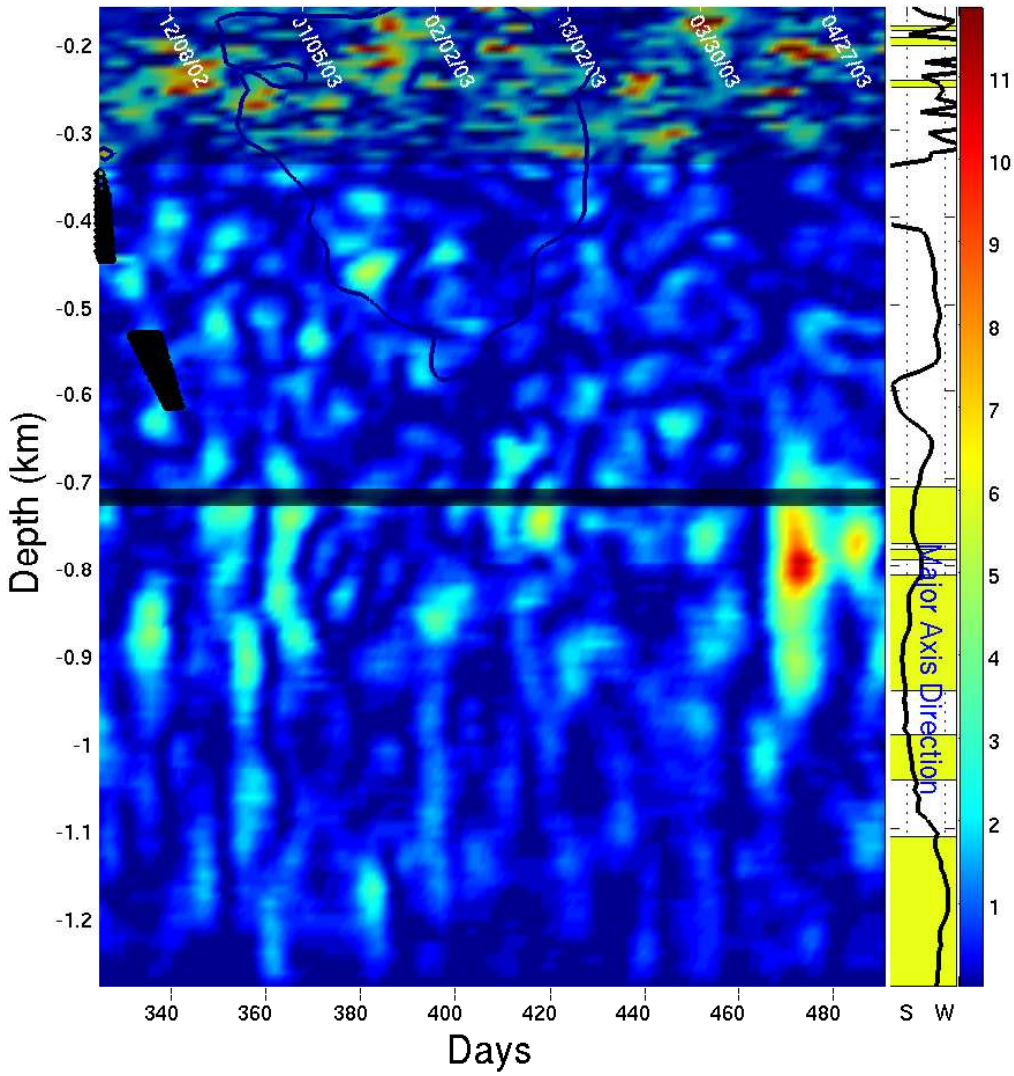

Figure 4.13. Vertical time series of ADCP inertial band cyclonic rotary velocity PSD $((m^2/s^2)/(rad/s))$ for the A2 HOME mooring. First right hand panel indicates inertial ellipse major axis direction verses depth. Yellow shaded area shows depths where inertial eccentricity exceeds .66, indicating more elliptic motion.

4.2.3 Power Spectra and Shear Spectra

To further understand the processes in the record, and to identify appropriate depth regions for more specific analysis, we begin the spectral analysis with full record rotary PSD and rotary shear PSD that have been depth averaged. In previous sections the distribution of energy in the depth vs. time was examined, and from those figures we would expect that plots of power spectra and related figures can vary depending on the time period and depth. Single depth measurements at this location can vary widely from nearby depths, and various time periods have significant energy at different frequencies. By selecting depth ranges with some similarity and averaging those, a more general characterization of the energy can be obtained, specifically leading to enhanced frequency resolution.

The following process was used for creating the figures: select the whole record from a single depth, apply a normalized five percent Tukey window, obtain the rotary Fourier decomposition, average across selected depth bins, and calculate the PSD. The resulting rotary PSD is then smoothed. Shear spectra are calculated in the same way, after obtaining the shear from adjacent depth bins. Bins have an eight meter separation.

Spectra for depth range 400 to 504 meters

In figure 4.14 thirteen depth bins are utilized in a depth range 'between' the upper and lower semi-diurnal beams. This enables a high spectra resolution which is particularly necessary to identify the feature near the band of $M_2 + K_1$, which is close enough to the interaction sum frequency $(M_2 + f)$ at this latitude to cause contamination.

In this spectra there is a clear peak at the IWISC frequency (cyclonic rotary velocity component at $M_2 - f$). With the increased spectral resolution due to vertical averaging, the IWISC peak is clearly separated from the cyclonic diurnal internal tide peak at K_1.

The black horizontal lines underneath the labels indicate the bandwidth used for amplitude comparisons between this data and the data that has been Semi-Lagrange inverted in the vertical. This comparison is made in section 4.5. The bands are calculated in this way:

- The frequencies are chosen to be $(M_2 + S_2)/2$, sometimes labeled SD, and $1.04 * f$, $fblue$
- 'Observed' center frequencies are calculated $SD + fblue$ and $SD - fblu$
- Percentage limits are selected to maximize band coverage across many depths and times
- Summation limits 5% below and 3% above

- Difference limits 6% below and 8% above
- Inertial limit is back calculated from difference limit

The only major time and depth where these limits are inadequate is during the eddy event in the upper depths. The inertial shift can exceed 15%, which poses a problem in separating it from diurnal energy. This peak can be observed in figure 4.14 just red of the O_1 peak and of the same magnitude as the expected inertial peak around $1.05f$.

In the second panel of the figure is the rotary shear power spectra. The highest anti-cyclonic shear is associated with the broad inertial band. Next in magnitude is the narrow semi-diurnal shear peak, then the band characterized by diurnal interaction with semi-diurnal components. The next major anti-cyclonic shear is at the interaction frequencies between the inertial and semi-diurnal. Both the sum ($M_2 + f$) frequency and IWISC ($M_2 - f$) have significant anti-cyclonic shear peak values.

In the cyclonic, the highest value is the narrow semi-diurnal peak. There is elevated cyclonic shear from the inertial to the IWISC frequency, with the diurnal tide and IWISC frequencies having the highest value. There is not clear separation in cyclonic shear between the IWISC and K_1.

In figure 4.15 the consistency relation is shown for the rotary PSD of velocity in figure 4.14. There is no significant deviation from consistency at the interaction frequencies. Deviation has been demonstrated at the sum and difference frequencies for a reversible advection based on the analysis of modeled inertial wave displacement in section 3.3.

In figure 4.16 the semi-diurnal and the sum frequency bands have been 'zoomed' for a closer examination. An interesting result is seen in the band associated with interactions between diurnal and semi-diurnal frequencies. There are at least two significant peaks, and possibly four separate peaks visible. Three of these appear to have probable interaction frequencies associated with them. Explanations of each peak, and possible dynamic processes involved, are beyond this analysis. However, this figure indicates that the band is complicated, and may contaminate the analysis of the $M_2 + f$ band.

Spectra for depth range 832 to 936 meters

A depth range in the lower ADCP instrument was selected that extends from below the main semi-diurnal beam. Thirteen bins were averaged and processed in the same way as the previous figures from the depth range 832 meters to 936 meters. The corresponding power and shear spectra are shown in figure 4.17.

The first major difference to notice in comparing the lower and upper depth ranges is in the inertial band. The lower depth range is below the influence of the background flow which blue shifted the

inertial for a considerable time in the first half of the record for the upper depth ranges. Now there is a clear 'well' between the inertial peak energy and the diurnal internal tide.

A second obvious difference is at the peak in the anti-cyclonic sum ($M_2 + f$) frequency. The peak itself it enhanced and there is a large reduction in the nearby peaks surrounding the frequency of M_2+K_1. A complete explanation of that band and its associated peaks has not been done for this record. However, with this lower record not having the blue shifted inertial, and also not having enhancement at the band slightly above $M_2 + f$, it is possible that some of the enhancement seen in figure 4.16 could be attributed to $M_2 + 1.15f$. This would be interaction of the semi-diurnal internal tide with the heavily blue shifted inertial during the background event which occurs in the first half of the record.

The cyclonic energy at the IWISC frequency is near the same value as in figure 4.14 for the upper depth range. This elevated energy at the IWISC frequency does not have a clear 'well' or gap distinguishing it from diurnal frequency energy nearby.

The shear spectrum in the lower panel of figure 4.14 has a significant enhancement at the IWISC frequency in the cyclonic component. This cyclonic shear at IWISC is among the highest for all cyclonic shear values. From both depth ranges there is evidence of shear at the IWISC frequency. This is an important observation, as it contributes to the idea of energy transfer from semi-diurnal internal tides and inertial energy into small vertical scale motion leading to dissipation.

There is also an enhancement at the inertial frequency of the cyclonic shear in contrast to the upper shear spectra. This could be attributed to the enhanced cyclonic inertial energy interacting with the semi-diurnal internal tide. The source of this anti-cyclonic shear peak at the IWISC frequency has not been conclusively determined.

Another feature of the lower rotary PSD is the overall cyclonic energy frequency distribution and especially the increase at the inertial frequency. This is quite different from the rotary PSD calculated previously for the upper bin range, and indicates motion that is not circular. The difference is very distinct in figure 4.18 where the ratio of cyclonic to anti-cyclonic is shown for the 832 to 936 meter rotary PSD.

The sum frequency ($M_2 + f$) deviates significantly from the consistency relation as well. This is in contrast to the corresponding consistency figure further up in depth.

4.2.4 Summary of General Observations at HOME Mooring A2

There is a rich collection of features in this record that have an influence on the investigation of IWISC. We have identified specific details at this site which are important considerations for the

analysis of internal wave interactions between the inertial and semi-diurnal frequencies. Important points include:

- shift in inertial frequency due to eddy influences in the upper depth ranges over the first half of the record,
- significant change in meridional full depth shear over the course of the record,
- multiple semi-diurnal internal tide beams evident,
- variability in amplitude and location of semi-diurnal internal tide energy,
- diurnal internal tide beam (or beams) seen,
- inertial energy distribution seen to be more variable than open ocean downward propagating storm generated inertial waves,
- inertial interaction with topography at depths below 800 meters,
- rotary PSD indicates energy at IWISC, $M_2 + f$ frequencies in upper and lower depths, and
- shear spectra indicates high shear at IWISC frequency.

Background meridional flow has contributed to the variability in energy distribution. Multiple beams of internal tide energy are evident. Inertial energy appears to be influenced by topography. These, and other considerations mentioned in the section, reveal the complex context necessary for investigation of IWISC.

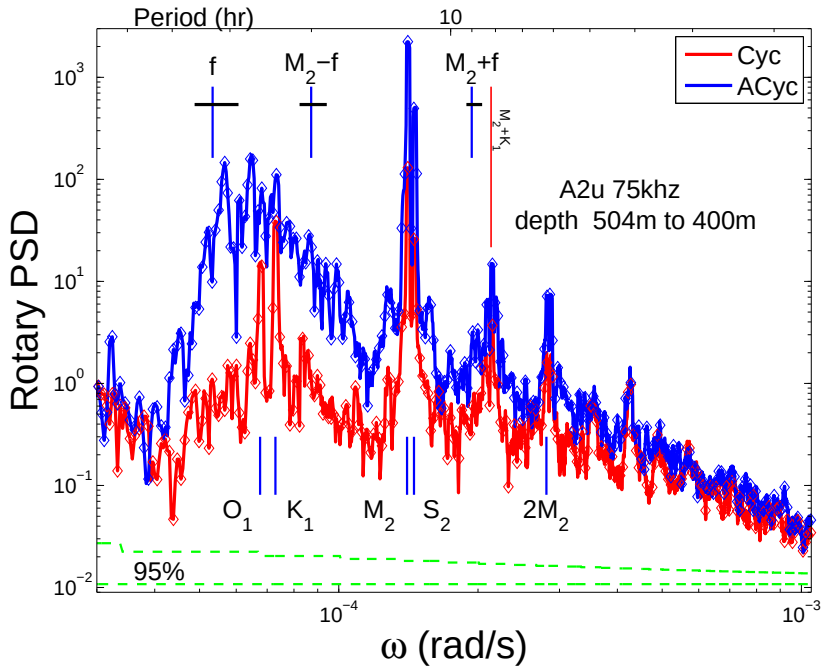

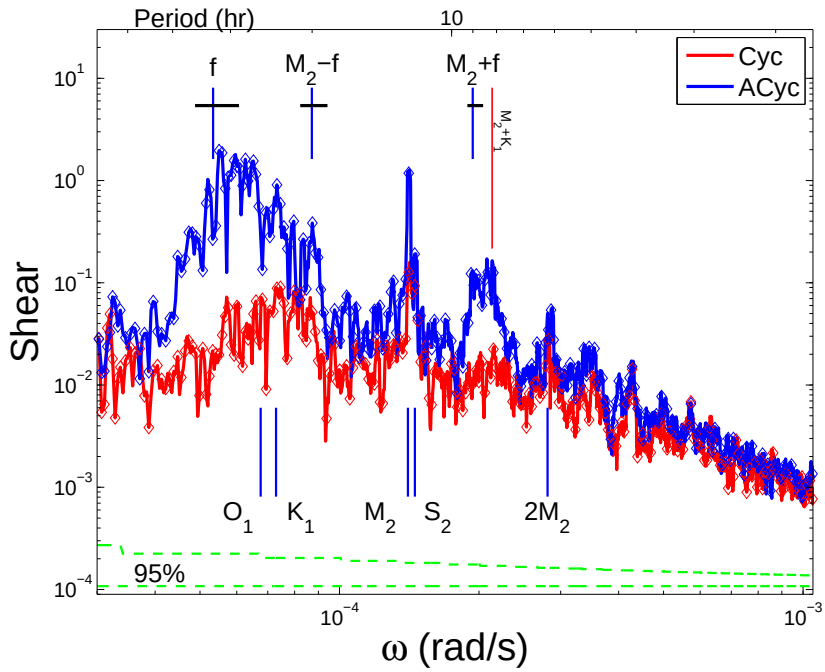

Figure 4.14. Rotary PSD $((m^2/s^2)/(rad/s))$ of the upper 75kHz ADCP from mooring A2 of the HOME experiment is in the top panel and rotary shear spectrum $((1/s^2)/(rad/s))$ is in the lower. The major tidal frequencies are indicated as well as the interaction frequencies. Sample is whole record encompassing data range between day 329 to day 500. Vertical average is 13 bins between 400m and 504m depth.

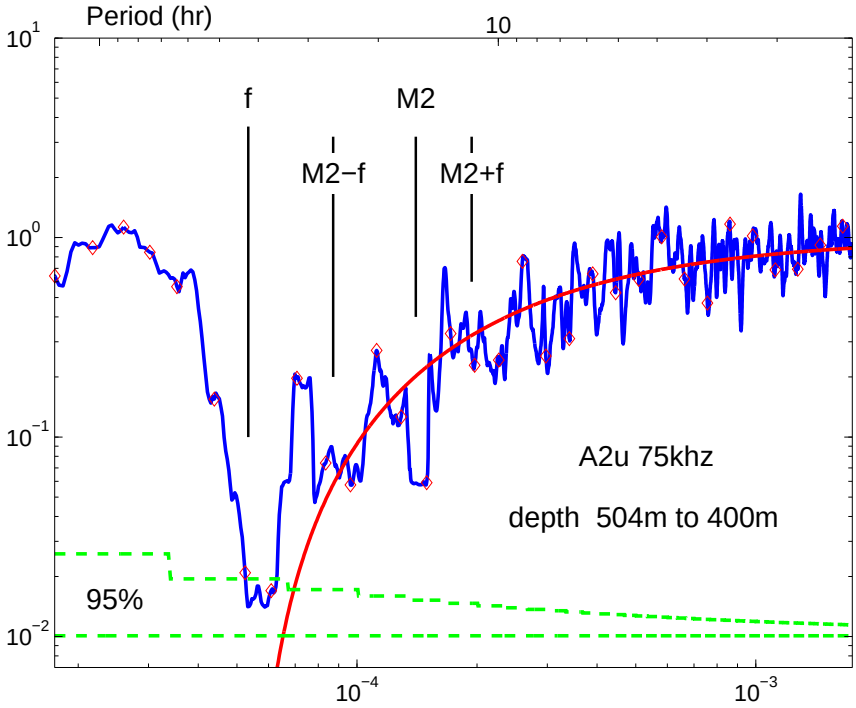

Figure 4.15. Internal wave consistency relation (ratio of cyclonic/anti-cyclonic) for the spectra in figure 4.14.

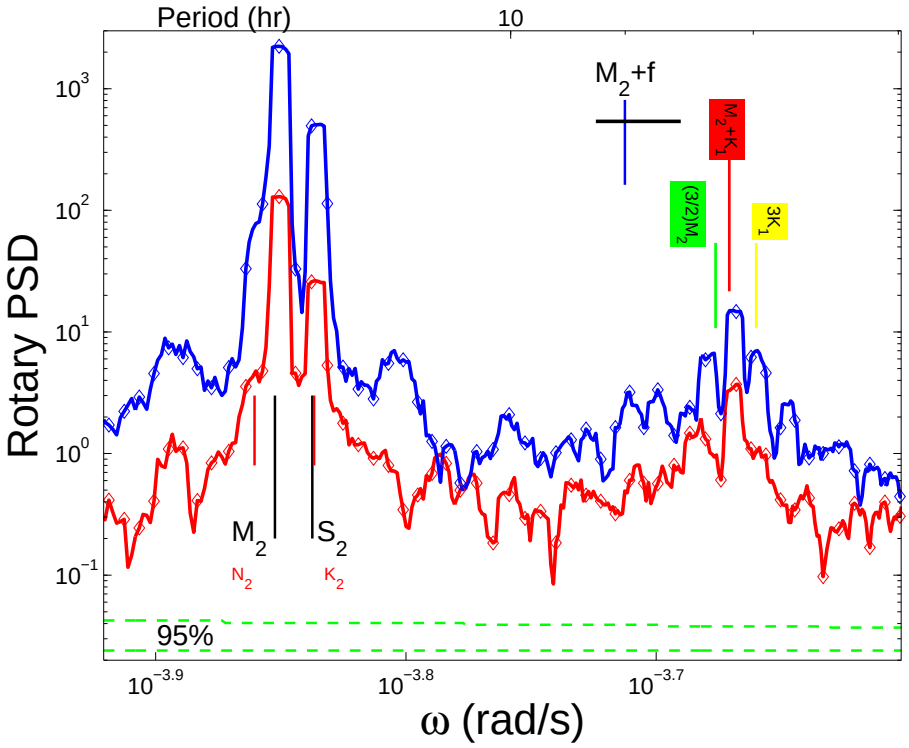

Figure 4.16. Expanded focus on the semi-diurnal band and the summation frequency band ($M_2 + f$) from figure 4.14. There are now four separate interaction frequencies identified in this figure. There is a band associated with diurnal constituents containing three nearby components, $\frac{2}{2}M_2$, $M_2 + K_1$, and $3K_1$. Visible but not distinct are other semi-diurnal components, N_2, and K_2. The black horizontal line beneath the sum frequency indicator is the bandwidth used for amplitude comparison between this data and a similar set that has been Semi-Lagrange inverted in the vertical.

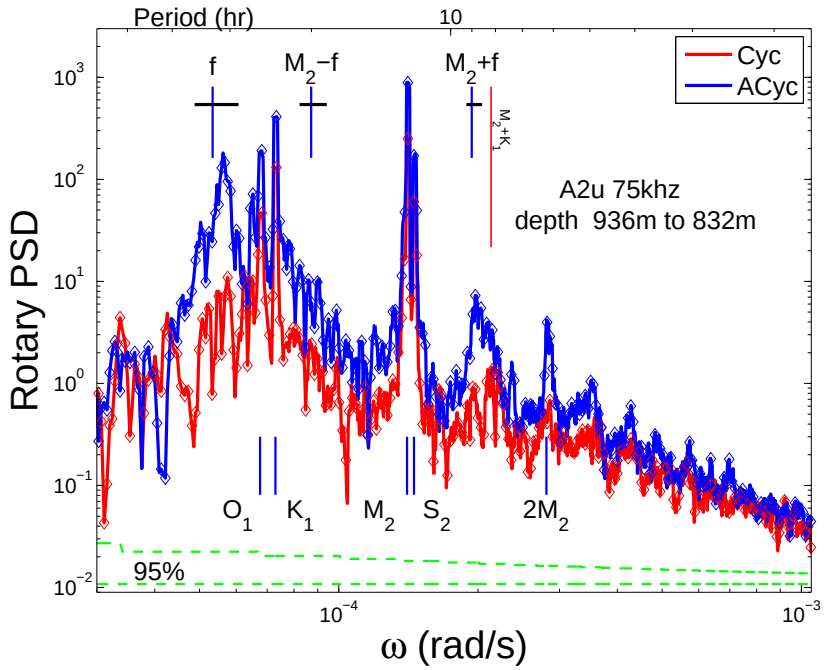

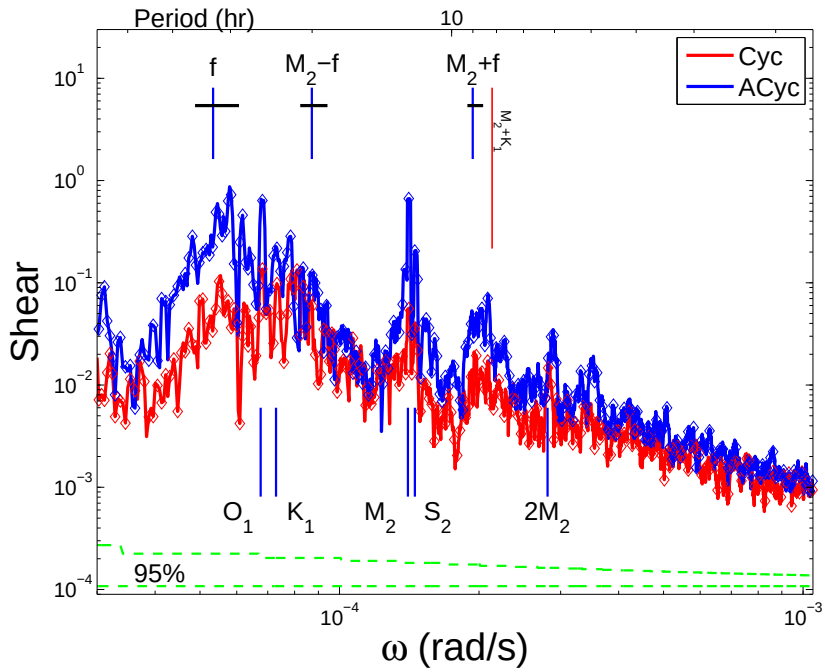

Figure 4.17. Rotary PSD $((m^2/s^2)/(rad/s))$ of the lower 75kHz ADCP from mooring A2 of the HOME experiment is in the top panel and rotary shear spectrum $((1/s^2)/(rad/s))$ is in the lower. The major tidal frequencies are indicated, as well as the interaction frequencies. Sample is whole record encompassing data range between day 329 to day 500. Vertical average is 13 bins between 832m and 936m depth.

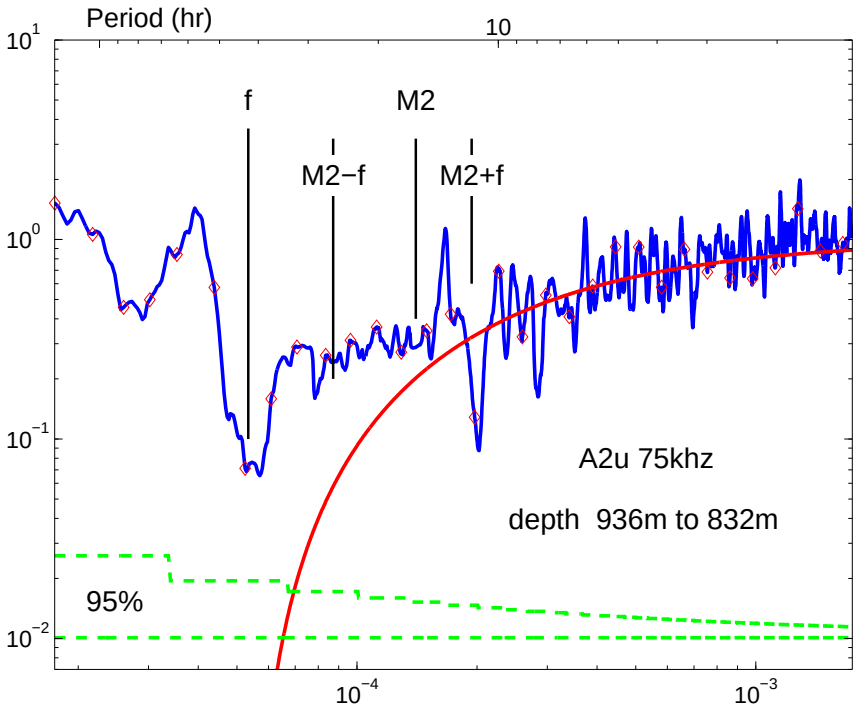

Figure 4.18. Internal wave consistency relation (ratio of cyclonic/anti-cyclonic) for the spectra in figure 4.17. There is significant deviation from the theoretical curve at the inertial band and higher near inertial frequencies. The sum $(M_2 + f)$ interaction frequency has deviated as well.

4.3 Vertical Velocity at A2

To differentiate between processes that exchange energy and those which are advection without energy transfer in the context of vertical advection, a transformation to Semi-Lagrangian (S-L) coordinates is necessary. To do a S-L inversion, there is a need for high resolution displacement. At this date, there are few long time period measurements in the ocean with vertical coverage and vertical velocity. The A2 mooring is one record where there are both. However, vertical velocity is an extremely tricky measurement. Here, the extraction of vertical velocity is successful in a narrow band. Capturing this universally across frequencies remains problematic.

In a recent paper, van Haren [87] compares ADCP vertical velocities to high resolution thermister data for locations on a shelf (Faeroe Shetland Channel), in the North Sea, and in the open ocean (Bay of Biscay). It was found that for the open ocean data there was good correspondence between ADCP vertical velocity and temperature data for frequencies well below the bouancy frequency. Data records did not cover multiple spring-neap cycles.

In the HOME A2 ADCP record it was discovered that the semi-diurnal vertical velocity signal was very strong and replicated the expected dynamics, apart from a significant contamination at the S_2 frequency. This contamination was successfully modeled, and removed from the signal. The resulting field was determined to be coherent over a broad depth range during the later half of the record. The background meridional shear during the first half of the record causes significant deviations from full depth range coherence in the vertical velocity. However, there are still coherent depth ranges within each instruments coverage during the time of shear.

4.3.1 Diel Migrator Contamination

Diurnal vertical migration of zooplankton has been observed in the oceans for decades. Following the advent of modern acoustic Doppler current profilers, diurnal vertical migration of zooplankton was studied closely in many locations. Typical migratory behavior sees the zooplankton descending to 'safe' depths at dawn and returning to the surface to feed at dusk. Early studies noted an increase in zooplankton within gull stomachs at night, indicating this behavior before direct in situ observations. An example of modern experimentation and discussion can be found in Rippeth and Simpson [75] regarding diel vertical migrators near the Hebridean Shelf. A more technical discussion of signal quality and migrators can be found in Moore and Stewart [52]. A clear distinction is made between signal quality and migratory periodicity for two classes of ADCP. In their post processing of data, recognition is made for potential error flagging of data influenced by migrators, up to 50% of the total

data. As a result, there was no one systematic data correction available to limit zooplankton influence. For near surface estuarian environs however, Ott [64] claims to observe reasonable vertical velocity in the presence of diel migrators without extended data correction.

We are concerned with recovering a narrow band vertical velocity centered at semi-diurnal frequencies from a record that is clearly contaminated with zooplankton migration. Our goal is to obtain displacement using the vertical velocity acquired from the ADCP for the semi-diurnal band. The first harmonic of the contamination falls directly on the S_2 frequency, and recovering this tidal constituent is necessary, as it sums with M_2, creating the spring/neap modulation of the band.

Modeling and Removal of Diel Migrators

The first step in processing this data is to recreate an ideal time series of zooplankton-only velocity. We begin with a correct time series of sunrise/sunset for the observed location. In this case we have used values for Honolulu from November 2002 onward corresponding to the HOME Kauai Chanel mooring deployments. The principal min/max values were accessed from the U.S. Naval Observatory Astronomical Applications Dept. A cosine fit was calculated for these values to construct the table of sunrise/sunset for the day coverage of observations.

An initial velocity time series was estimated with 30 minute smoothed spikes occurring at sunrise/sunset. This was compared to the C2 75kHz ADCP at depths above 400 meters, where zooplankton activity is enhanced. The HOME C2 mooring was chosen for this analysis to limit the influence of semi-diurnal beam energy in identifying zooplankton, and for its nearness to the A2 location. A set of recurring zooplankton peaks was observed to match this synthetic time series after the following adjustment: the modeled peak duration was increased to a Gaussian half width near 30 minutes. An example of the time series of vertical velocity is shown in figure 4.19.

To efficiently remove the peaks from the raw data time series, we multiply by the inverse fraction of the modeled zooplantkon amplitude. This has the advantage of easily adjusting the extent of spike removal. A simple function can be constructed for tapering off the contamination removal with depth. This process proved successful. More precise control can be introduced, but in this application has not proved necessary. Two more complicated schemes were tested, one where the spike amplitude removal was adjusted based on a moving average threshold, and another where there was smoothing of the spike removal area. However, for the application of recovering the narrow-band semi-diurnal vertical velocity, these had little or no effect.

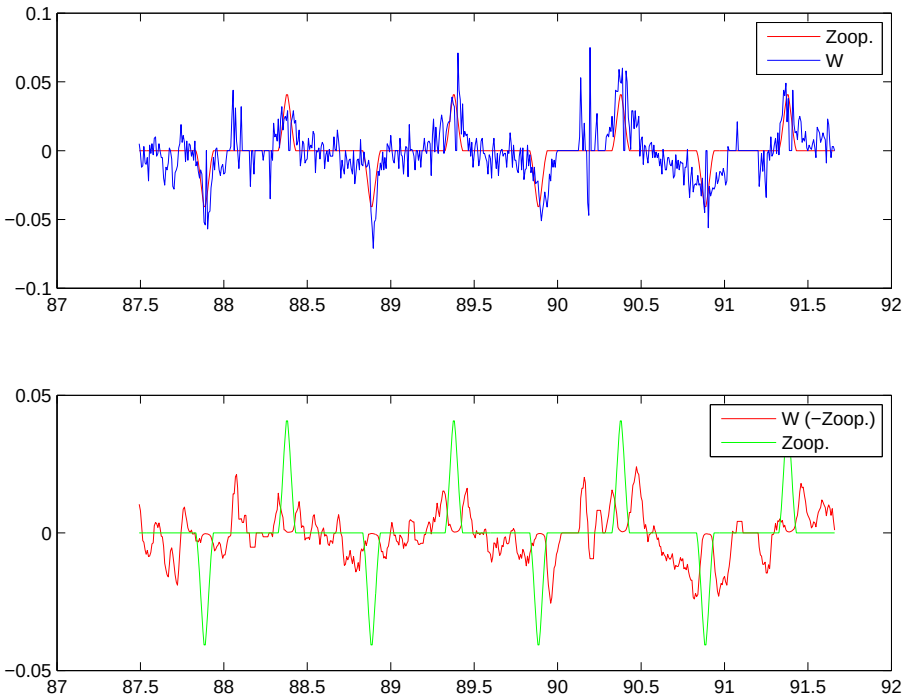

Figure 4.19. Comparison of raw vertical velocity (cm/s) and that with the zooplankton spike removed for HOME mooring C2 ADCP data. In the top figure, raw vertical velocity is shown for the 352m depth. On the bottom is the vertical velocity record with zooplankton removed. In both figures the times series of zooplankton vertical motion from the sunrise/sunset model is shown.

Results of Removal

What is clear in the figure 4.19 is that the synthesized series has captured the behavior of the main set of zooplankton velocity spikes. Over the whole record, there may be variations in the width of vertical velocity spikes associated with diel migrators, and we have chosen a model with widths slightly larger than necessary to account for this. It has been speculated that the sunrise peak could be wider, as zooplankton may be conserving energy by allowing gravity to account for some of their downward migration. Ott [64] may have observed this in the Juan de Fuca Strait. In this study of the HOME ADCP records, we qualitatively see the same phenomena at many times.

The application of spectral analysis on the zooplankton time series is shown in figure 4.20. The right side of the figure shows the calculated difference in the S_2 tide and the first harmonic of the zooplankton spikes. We can compare that to a spectra of the C2 ADCP for the 408m depth in figure

4.21. In the second panel of the figure there is a statistically significant reduction in the semi-diurnal S_2 tidal constituent by the removal of diel migrators. At the same time there is very little impact on the M_2 tidal peak, indicating the harmonic nature of the decrease in PSD. The comparison between the modeled spectra and that of the measured data is qualitatively revealing and quantitatively appropriate for the semi-diurnal band.

In an intermediate step, we discovered that ADCP signal recovery after a period of low signal contained spurious peaks. Since these low signal periods were coincident with mid-night zooplankton migration to upper depths, there was an increase in diurnal energy from this source. Specifically, it appeared that the ADCP recorded velocity calculations before a signal quality threshold was met. Upon increasing the blanking of data around low signal time periods, there was a decrease in diurnal spectral energy not associated directly with zooplankton vertical migrators. This analysis is consistent with the description of possible data correction given by Moore and Stewart [52]. For the purpose of vertical velocity recovery, the signal strength issue becomes marginal for bins that are closer to the instrument, yielding a broad depth range where there is no problem.

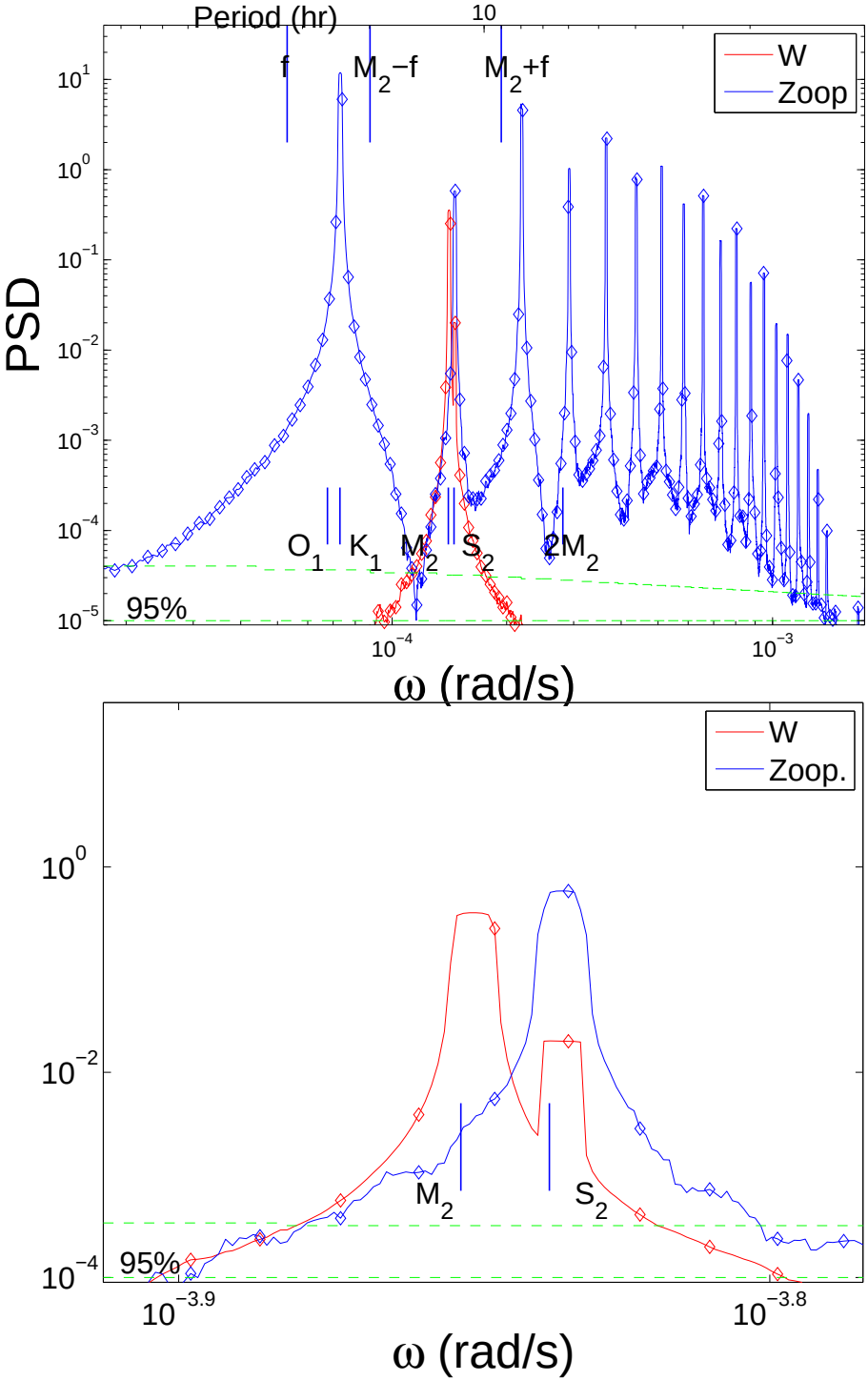

Figure 4.20. Vertical velocity PSD $((m^2/s^2)/(rad/s))$ for the zooplankton model and model $M_2 + S_2$ semi-diurnal tides in the top panel. On the bottom is a section of the same spectra constrained to the semi-diurnal band showing the uncontaminated semi-diurnal peaks and the level of the modeled zooplankton energy.

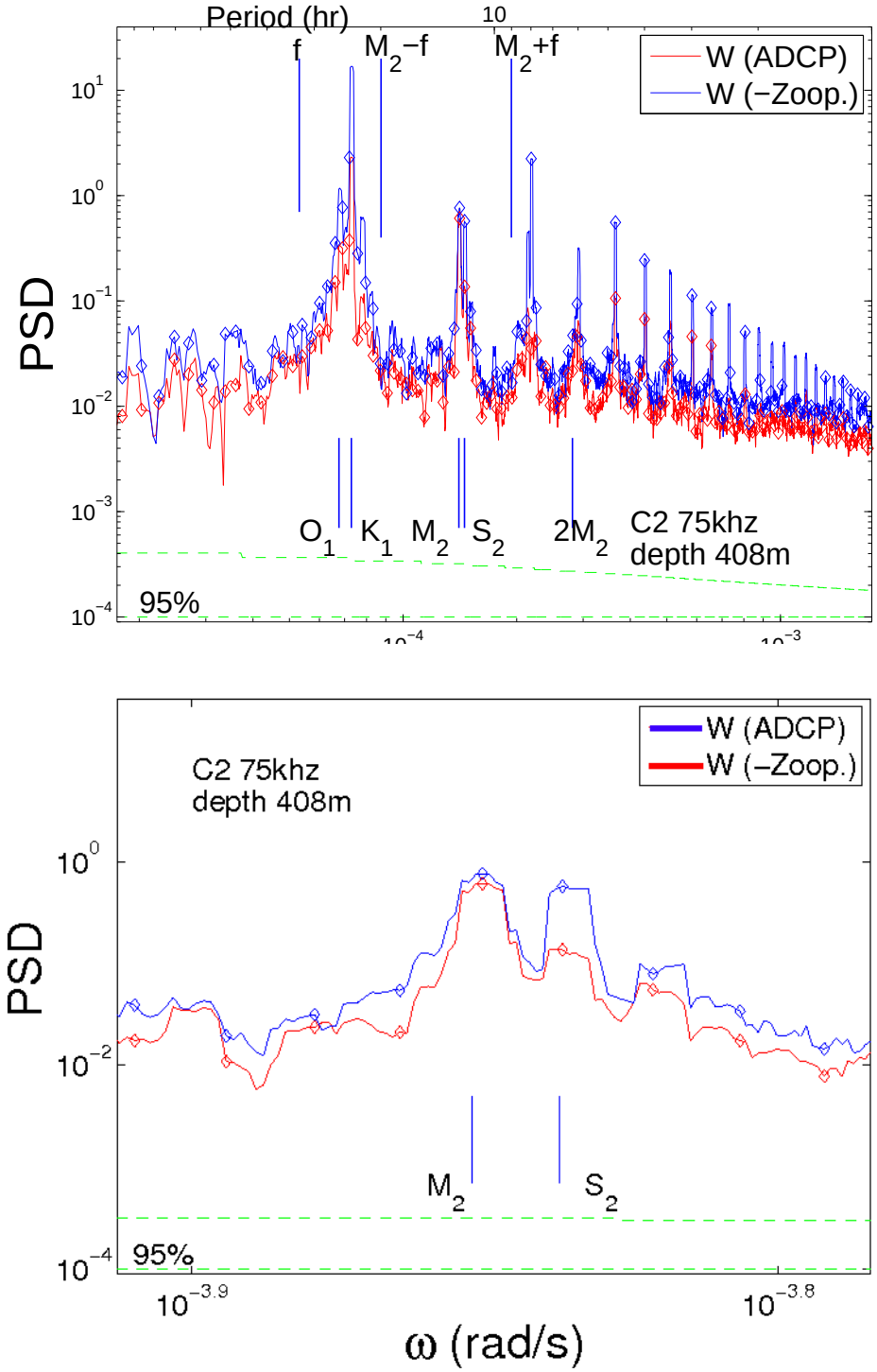

Figure 4.21. PSD $((m^2/s^2)/(rad/s))$ of vertical velocity from the C2 mooring 75kHz ADCP with the zooplankton removed and without from a depth of 408 meters. The second panel is expanded around the semi-diurnal tidal constituents. There is a good qualitative comparison with the modeled spectra in figure 4.20.

Another significant feature revealed by the migratory model is the apparent spring neap envelope phase shift seen in the ADCP vertical velocity (figure 4.22). It is apparent that the harmonic at the semi-diurnal frequency caused by the diurnal zooplankton migration acts as a separate modulator not unlike S_2. This creates enhancement and cancellation in a more complicated envelope than the internal tide spring/neap cycle. Removing the zooplankton influence at the semi-diurnal frequency can bring the vertical envelope structure into closer alignment with that as seen in the horizontal velocities. An example of this phenomena is shown in the constructed time series (figure 4.23). A clear shift in the phase of the envelope is seen in the vertical velocity time series which includes the zooplankton. This shift is similar to that seen in the ADCP record at various depths.

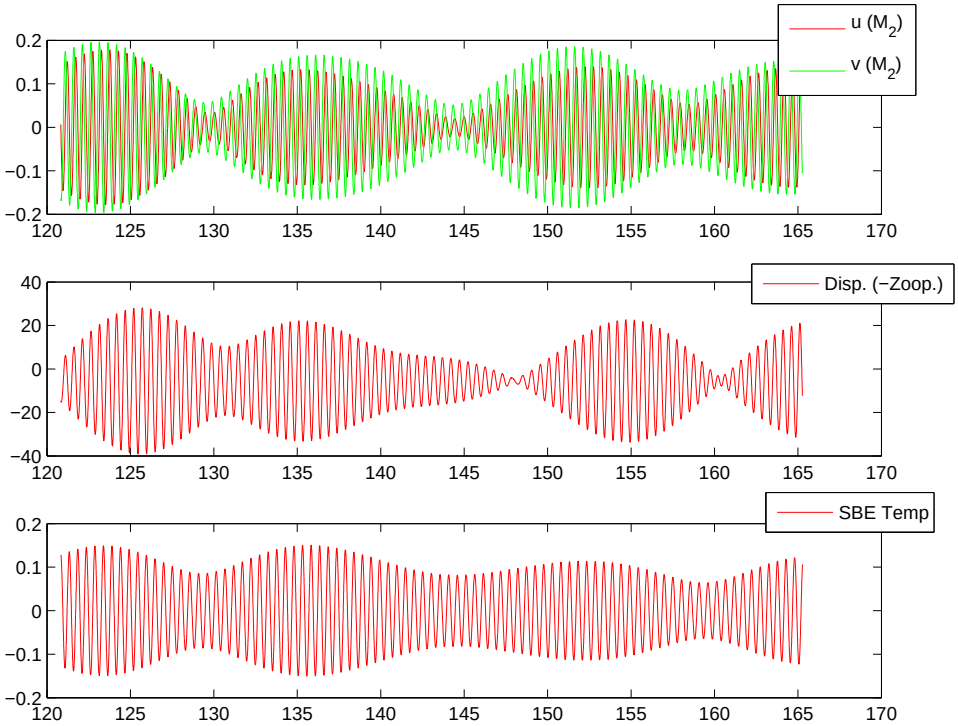

Figure 4.22. Comparison of times series in velocity (cm/s) and temperature (normalized, $C°$) that has band band-passed narrowly about the semi-diurnal tide for the 352m depth bin of the HOME C2 mooring. The upper panel is horizontal velocity. In the middle panel are the displacement (m) time series. On the bottom is a temperature time series from 680m.

A final consideration regarding removal of diel migrator is to what depth the removal should take place. At some depth, most of the harmonic spikes fall below noise levels, as the removal process

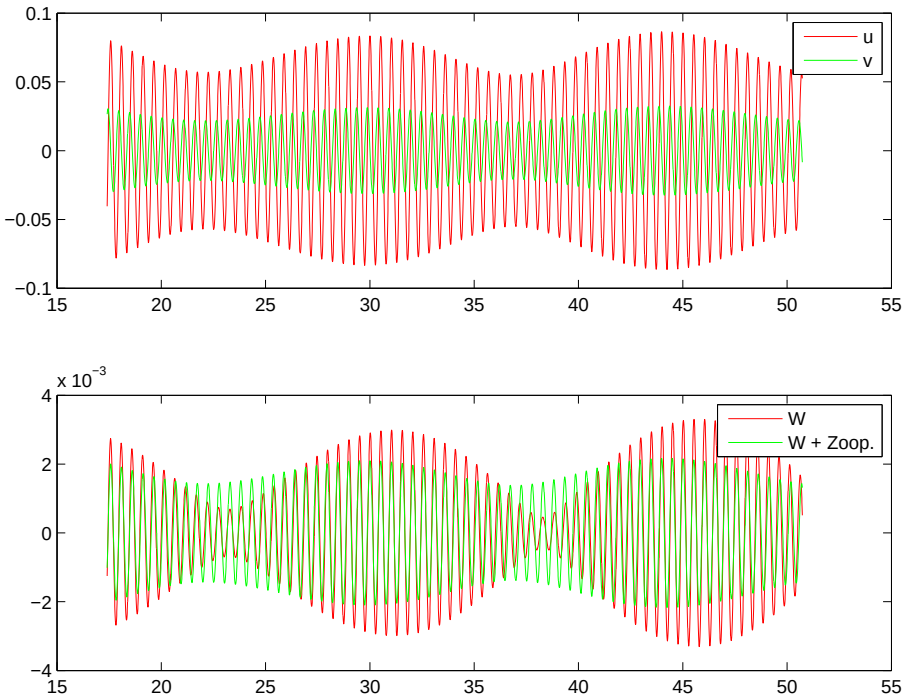

Figure 4.23. Comparison of times series in velocity (cm/s) derived from a simple model of semi-diurnal tide and zooplankton vertical migration. The top panel is horizontal velocity. The bottom panel is the vertical velocity, the green curve indicating the addition of the zooplankton signal.

adds more noise and removes viable velocity amplitude. To illustrate, in figure 4.24 the 'over' removal of zooplankton velocity spikes from the time series does not efficiently diminish diurnal harmonics. The nature of the diurnal signal at this depth needs to be characterized by a separate process, whether dynamic or biologic, and by a different time series signature with its respective spectra. This data analysis indicates that diel migrators contaminating S_2 do not 'swim' much farther than 600m at the locations of the HOME moorings, and for the temporal coverage of the deployments.

Under these considerations, the removal of diel migrators has a depth dependent component that reduces its effect, and by 700m, is very low in its reduction of the velocity spikes. What this leaves is a range in depth from near 600m, where migrators are still an influence, to 400m, where ADCP amplitude errors begin to influence the record, and where diel zooplankton migration effects can be efficiently reduced in the semi-diurnal band. This is for the HOME mooring design, and not indicative of a 75kHz ADCP at depths higher than this. The characteristics described here apply to the region

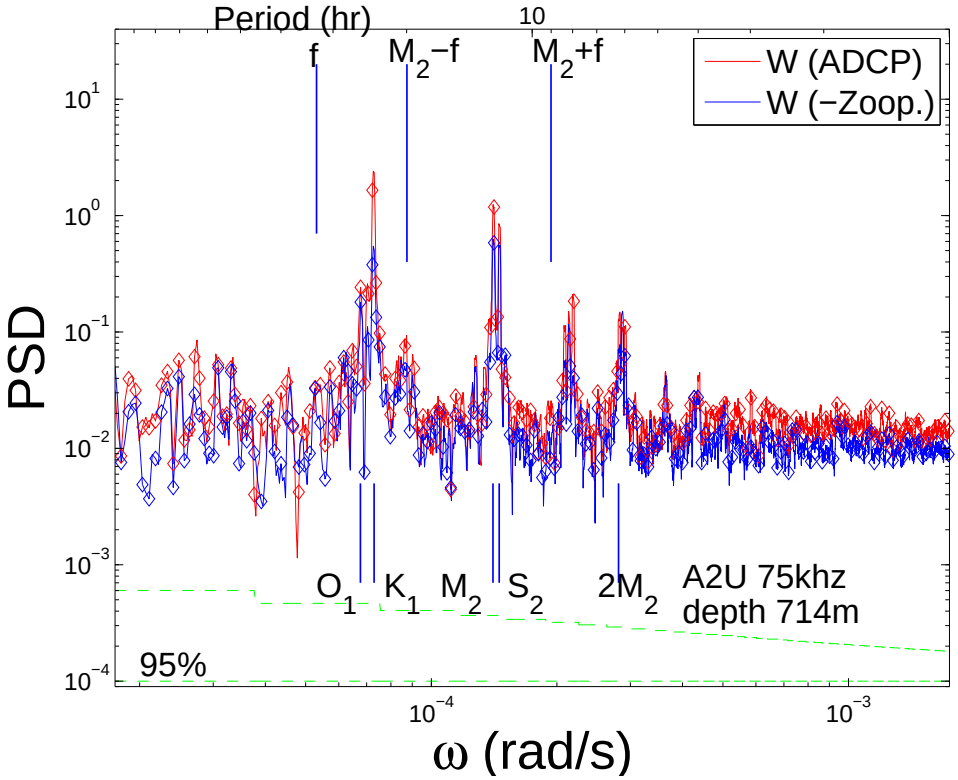

Figure 4.24. PSD $((m^2/s^2)/(rad/s))$ of vertical velocity from the 714m bin of the ADCP on HOME mooring A2. This is the upper instrument on the mooring located at 746m, and is upward looking. It is clear that the signal with the diel migrators removed is diminishing energy equally across bands, and is not selectively removing diurnal constituent harmonics. The remaining harmonics do not seem to be associated with the zooplankton harmonic 'spikes' in depths above this. This figure illustrates 'over' removal at a depth below most migration.

of the moorings (near Lat 22N Lon 158W) and are not indicative of other locations. The process as described does not identify or attempt to remove the effects of other possible diurnal or semi-diurnal signals.

4.3.2 Coherence of Vertical Velocity Through Depth Range

The S-L inversion technique requires vertical velocity with coherence across a broad enough depth range to encompass the expected displacements. This does not mean that incoherent vertical velocity is not suitable for inversion. However, in order to validate the technique and establish which vertical structure is active in the reversible advection or in a non-linear transfer, coherent vertical velocity across depth ranges beyond the expected displacement range is desirable. Even more suitable is a coherence

between widely separated depth ranges, indicating that the displacement signal is dominated by low mode structures.

Coherence of vertical velocity is of primary importance in the context of semi-diurnal vertical advection of inertial waves. If there is to be functional equivalence between isopycnal displacement and vertical velocity, broad coherent depth ranges will reduce possible associated error.

Fourier Coherence

To establish vertical velocity coherence, an analysis of the record between days 449 and 480 will be examined. In figure 4.25 the semi-diurnal band coherence is presented. This figure is a Fourier decomposition comprising five windows with 25% overlap. The exact proceedure is as follows:

- extract the depth binned, sway and pressure corrected, ADCP vertical velocity data for each instrument,
- apply mask removing additional contaminated data, as described in [6],
- apply mask to edges of missing data,
- remove diel migrator contamination as described above,
- use piecewise continuous Hermite polynomial interpolation across missing data,
- apply a 2.6 hour smoothing filter,
- Tukey taper a 14 day window, and
- calculate coherence for the semi-diurnal averaging across the time segment with 25% overlap.

A number of considerations are necessary in interpreting this coherence plot. The time segment without the large scale vertical shear identified earlier contains at most four spring/neap amplitude envelope peaks. The windowed segment to recover multiple constituents in the semi-diurnal band needs to be at a minimum 14 days. This leads to a situation where window placement has the potential to impact the coherence result. The times and overlaps used in creating this figure were carefully selected.

To read a coherence value from the chart, select a depth on either axis and follow the respective vertical or horizontal lines. The intersection of this reference line with the perpendicular depth lines contain the coherence associated with the two depths indicated on each axis. The figure is simply a

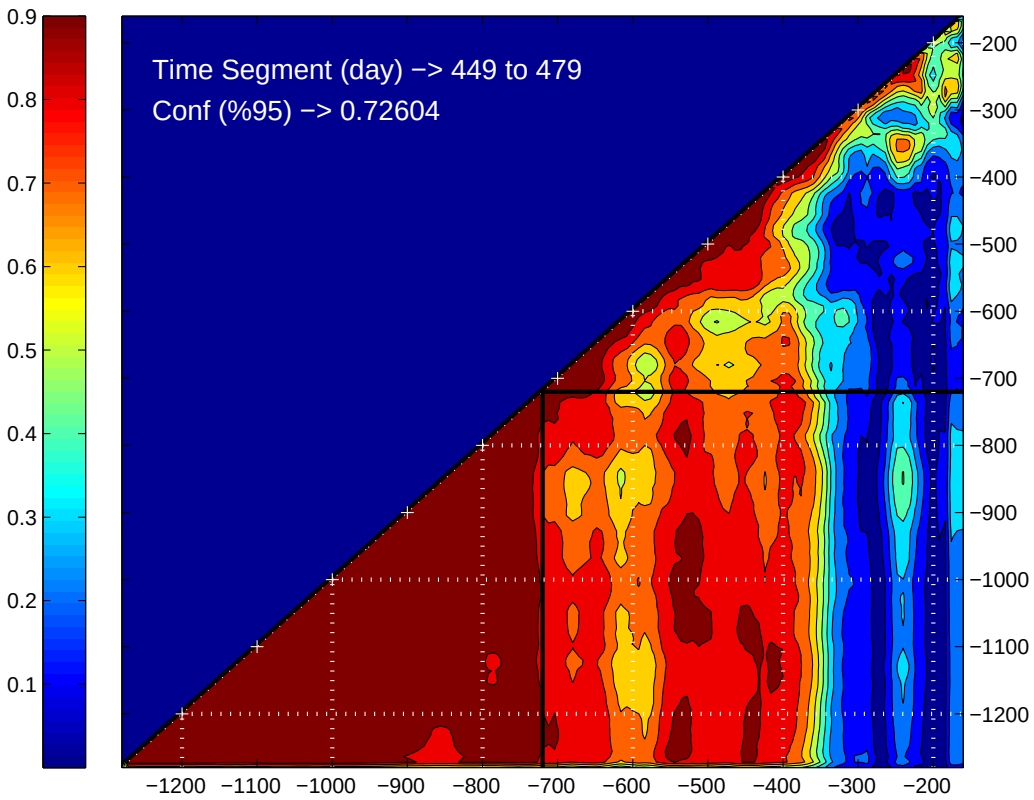

Figure 4.25. Coherence chart for the semi-diurnal band passed vertical velocity at the A2 HOME mooring for the time period of day 449 to 479 (beginning Jan 1, 2002). The separation of upper and lower ADCP coverage is indicated by the black line. This time period encompasses the highest vertical velocity coherence with depth in the A2 data.

convenient visualization of a matrix of coherence values. The black line indicates the depth at which the coverage switches from the lower instrument to the upper.

There has been no identification of data quality in this analysis. Since there was quite a bit of missing data above a depth of 320m, these depths should be viewed with caution. Below that there is a depth range of 350 to 400 meters where coherence values are at or above the 95% confidence interval in relation to much of the lower instrument depths, as well as the first few bins of the upper instrument. This is an interesting result in itself, considering the expected location of topographically generated beams impacting this mooring.

Where a beam is located, higher vertical structure would be expected within the beam, and the resulting lower coherence in the vertical velocity between depths outside of the beam and those in the

beam. If a comparison is made between what appears to be the center of the more energetic beam located at depth 600m in the rotary PSD (see figure 4.7) and the coherence at that depth, there is an interesting symmetry. The coherence in vertical velocity is generally high just below what would be the center as seen in horizontal velocity, and quite low above the center. Making a unsubstantiated assumption that this is a general feature, a second beam center would then be seen in coherence at depth 350 meters.

This is not conclusive, but if established more rigorously, the second beam description could be useful. This could be the case as the coherence drop indicating a possible beam center occurs where the data is still sound, and not in the region above 320m. Further analysis of this hypothesis is possible for future work.

The main beam during this time period covers the depth range from 500m to 770m with comparable amplitudes in horizontal rotary PSD. The vertical velocity coherence is very interesting here for two reasons. First, the transition between instruments occurs in this range, and the initial expectation was for a noticeable drop in coherence across instruments. Yet some of the highest coherence values cross this depth range. Second, it was expected under the assumption of a random Gaussian beam, that there would be a drop in vertical velocity coherence when nearing the center of the beam from below and above. This is not the case, but the precise structure that leads to this apparently conflicting result is not well established. It would possible to create such a beam with specific mode enhancement, and perhaps there is a fruitful course of investigation possible with this data in that direction for the future.

At the lower depths there are broad sections of enhanced coherence leading to a peak at around 1200 meters depth. This coincides with the lowest vertical mode and is the depth of the largest displacements. As a total depth range snapshot, the major features of this coherence map could be replicated by a full depth low mode semi-diurnal signal with two specific higher mode structures in the depth ranges of the beams.

During the time period of greatest background meridional shear the depth ranges of coherent vertical velocity shrink. Also the clear beam depths become less distinct. However, as can be seen in figure 4.26 for the high background meridional shear time period, there are broad ranges in depth with significant coherence.

As an example, follow the 800 meter line. The coherence is low from the bottom up to 1000 meters. Then the 800 meter bin is coherent up to a short break at 550 meters, then remains coherent until just above 400 meters. That yields two ranges, one of 450 meters, and another of slightly less than 200 meters. Even with displacements of 80 meters, these depth ranges would be adequate for determining displacement used in a coordinate inversion.

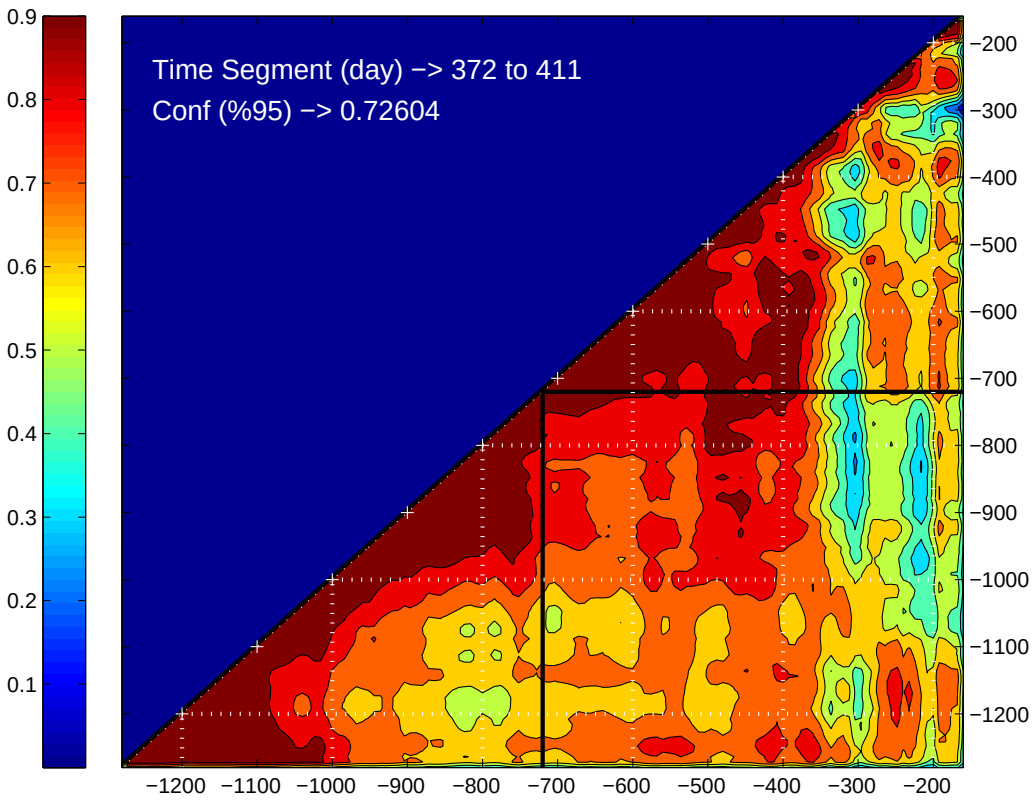

Figure 4.26. Coherence chart for the semi-diurnal band passed vertical velocity at the A2 HOME mooring for the time period of day 372 to 411 (beginning Jan 1, 2002). The separation of upper and lower ADCP coverage is indicated by the black line. The time period is indicative of the lowest vertical velocity coherence with depth from the A2 data.

Wavelet Coherence

The variability within the data introduces significant constraints to the coherence estimates. Background vertical shear limits the available time segment. Modulation via the spring/neap cycle constrains the windows and where they are calculated. Ideally, an analysis of each peak tidal envelope over tens of fortnights would reveal more accurate coherent structures. Separating each beam into its location in depth to account for advection could also lead to further insight. However, there is a separate analysis to be used as a check against the Fourier coherence.

We have used wavelet analysis to isolate event like signals temporally within modeled data (see section 3.5). With the same wavelet decompositions, we can make a comparison of wavelet derived

semi-diurnal coherence in relation to the Fourier analysis. The transform is explicitly stated in section 3.3. To compare with the previous figure, we select six realizations from the time segment used in the Fourier analysis and calculate the coherence.

There are a couple of major differences in the two analyses. First, the wavelet transform is integrated across the total record, not just the segment or window associated with the Fourier construction. Second, the time at which a particular transform is selected is of more importance than the window placement for the previous analysis. There are nearly a dozen wavelet kernel half widths available in this time segment at the semi-diurnal frequency. If six transforms were selected that corresponded to low internal tide activity, a lower/higher coherence could result, though not indicating energy significance.

We have selected each transform to obtain rough phase matching and to fall in a period of enhanced tidal envelope. A closer analysis of wavelet coherence between depth ranges is possible with this technique, with realizations compared between different phases and placement within the envelope. Comparison between the Fourier and wavelet methods reveals significant similarities in high coherence regions.

In figure 4.27 the wavelet coherence chart is presented. There is a similar coherent feature possibly below the upper beam. There is high coherence in the lower half of the lower beam. And the lower instrument overall is a region of higher coherence. All of these features are consistent with the Fourier description.

This technique could be valuable for analysis of ADCP records with limited sample time period. If the vertical velocity at a particular frequency needs to be extracted from a short (with respect to the desired frequency) record, this wavelet coherence mapping could be extremely useful in validating the vertical velocity.

4.4 Displacement and Semi-Lagrange Inversion

We have demonstrated that for simple plane wave constructions (section 3.3), reversible advection can produce the same signature as nonlinear interactions. Where it is applicable, a S-L inversion can remove the effects of the reversible advection. The resulting inverted record can then be analysed for non-linear interaction. To do the inversion, we first integrate the vertical velocity to find the displacement.

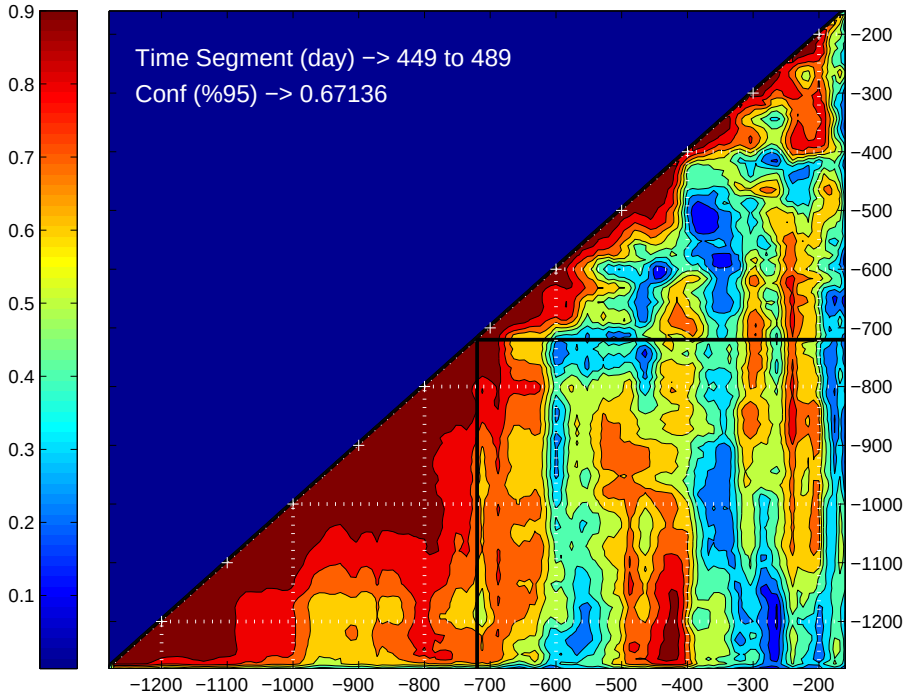

Figure 4.27. Wavelet decomposition of vertical velocity coherence in the semi-diurnal band for the A2 HOME mooring. The separation of upper and lower ADCP coverage is indicated by the black line. This figure is indicative of the second section of the deployment in regards to background mean flow, and corresponds to the Fourier coherence figure 4.25.

4.4.1 Displacement Series

Figure 4.28 shows the displacement at various depths over a time period corresponding to one of the peak tidal envelopes in the segment analyzed for vertical velocity coherence. The depth ranges with low coherence are evident on this plot as phase shifts. These shifts occur in ranges where the internal tide beams are enhanced. There is a separate displacement depth that is incongruent at the lower part of the upper beam. This cycle at 400 meters is at the depth indicated in the coherence figure where it switches from higher to lower coherence.

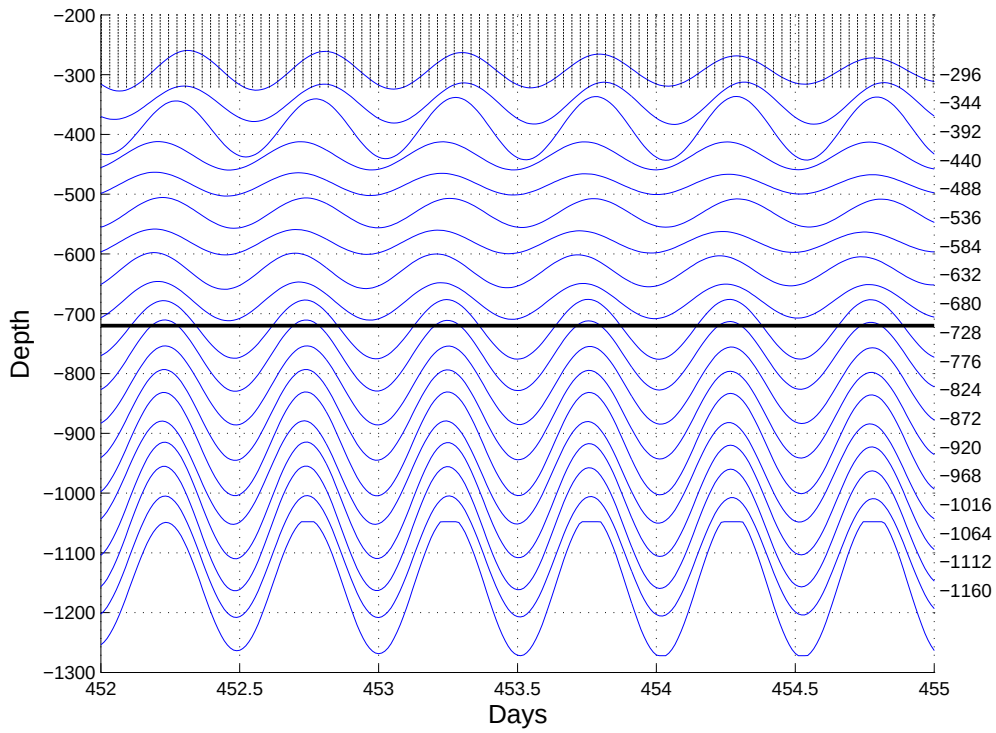

Figure 4.28. Calculated displacement vs. depth for a peak tidal spring/neap envelope during the time segment of the total A2 record with low large scale background shear. Shaded region represents area of poor data. Center line indicates depth where velocity coverage switches between instruments. Days from January 1, 2002.

4.4.2 Inverted Horizontal Velocities

The S-L inversion technique described in sec 3.3 can be applied to the displacement derived from the ADCP vertical velocity. In figure 4.29 the meridional velocity vs. depth is displayed for the matching depths and time period of the previous displacement figure. The velocity has been smoothed with a 1.33 hour MAF and scaled by 200 to visualize against the depth scale.

The strongest velocities are in the depth range of the main semi-diurnal internal tide beam. The semi-diurnal cycle is clearly evident at these depths. There is also evidence of the shock-like velocity spikes associated with diurnal periodicity at the depth range of 1000 to 1200 meters. This feature does not impact the semi-diurnal analysis.

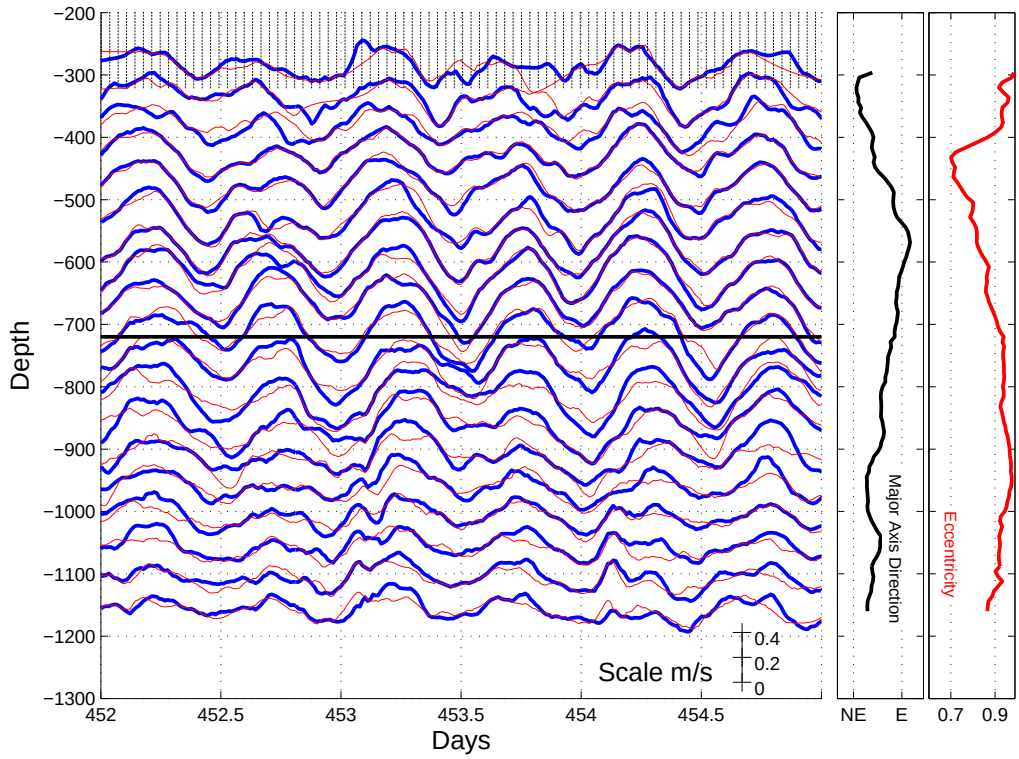

Figure 4.29. Semi-Lagrangian meridional velocities (blue curves) calculated with the displacements indicated in the previous figure. Original data in red. Velocities have been smoothed with a 1.33 hour moving average and increased in amplitude by 200 to match the depth scale. Shaded region represents area of poor data. Center line indicates a switch between instruments.

Further examination of the effect of the inversion can be seen in the power spectra. A PSD of this same enhanced tidal envelope (from day 450 to day 464) is shown in figure 4.30.

The solid curves are the S-L inverted rotary PSD values, and the dotted curves are from the original record. The coherence values showed variability below and above this depth range possibly indicating higher vertical structure in the vertical velocity and hence, displacement. Even with a potentially more complicated displacement structure, the inversion technique has not introduced major deviations from the raw values at tidal harmonics, and sums of those harmonics with other peak values. In the band we are focusing on, where the inertial is interacting with the semi-diurnal internal tide, the inversion has had no statistical reduction or enhancement on the IWISC ($M_2 - f$) or sum ($M_2 + f$) frequency bands. There is slight broadening of the $M_2 + f$ signal.

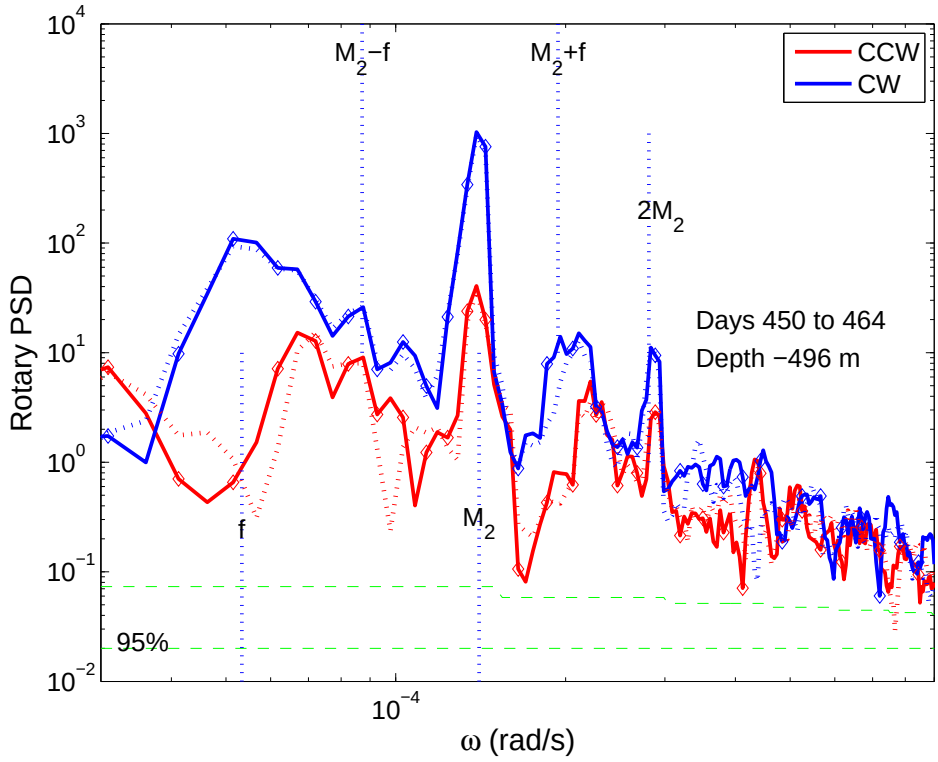

Figure 4.30. Horizontal velocity rotary PSD $((m^2/s^2)/(rad/s))$ of the single internal tide enhanced period selected for the previous figures of displacement. The solid curves are data that has been Semi-Lagrange inverted. The dotted curve is the original data.

Going to deeper depths during this same time period, we observe a different result. In figure 4.31 the inversion technique has reduced the sum $(M_2 + f)$ frequency peak by close to an order of magnitude. This reduction occurs at a depth of 928 meters, in a fairly uniform range of high coherence for vertical velocity as seen in figure 4.25.

What is striking about this PSD is that the difference frequency $(M_2 - f)$ has not been similarly reduced. All other major features remain intact between the inverted and raw PSD values. The inertial peak, as well as the semi-diurnal peak and its harmonics remain the same. Yet one of the principal indicators of vertical advection shows the inversion working, whereas the other is unaffected. With this type of analysis, an advection process based on a single sinusoid displacement will produce both frequencies in nearly equal magnitude. This spectra indicates that the process is not a simple reversible advection by a single sinusoidal displacement.

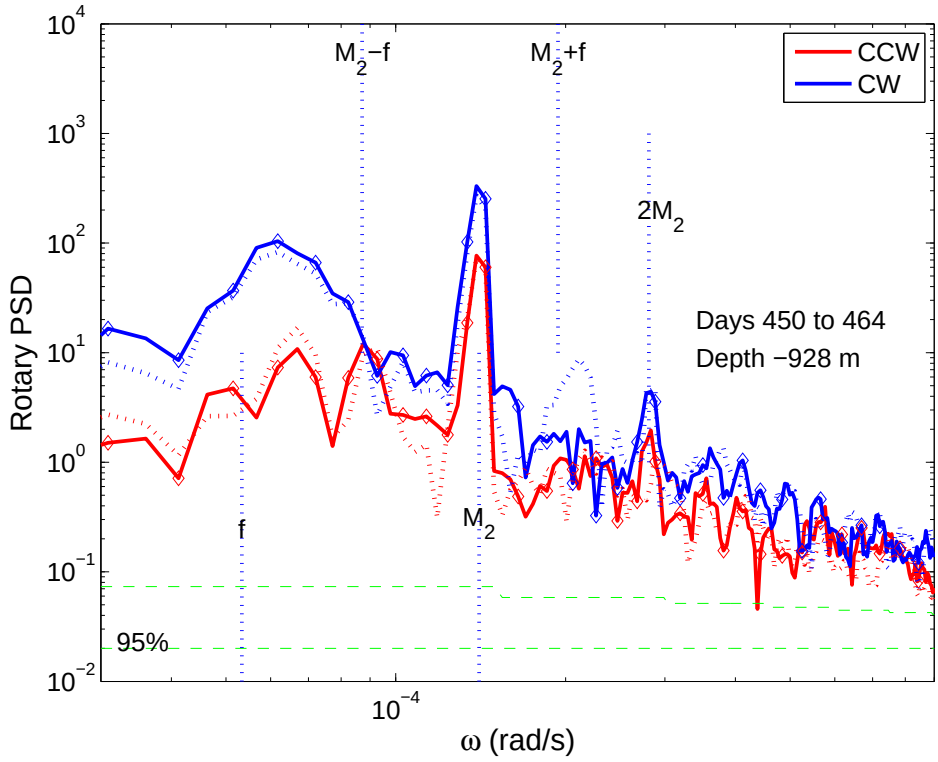

Figure 4.31. Horizontal velocity rotary PSD $((m^2/s^2)/(rad/s))$ of the single internal tide enhanced period selected for the previous figures of displacement. There is a significant diminishment of the energy in the $M_2 + f$ band. The depth is 928 meters on the A2 mooring. The solid curves are data that has been Semi-Lagrange inverted. The dotted curve is the original data.

4.4.3 Summary of A2 Semi-Lagrange Inversion

We have demonstrated that the vertical velocity from the A2 ADCP is useful in providing semi-diurnal displacement time series which can be utilized in a Semi-Lagrange vertical coordinate inversion. The inverted horizontal velocities have been checked with spectral analysis. The S-L inversion does not universally remove energy from the interaction bands as would be expected from single sinusoid reversible advection.

4.5 Vertical Profile of Interactant Peaks

In the observational context section a picture emerged of the variable energies in the frequency bands that will influence the IWISC band. There is a complicated depth distribution of energy for each of these bands. Comparisons of depth averaged spectrum between upper depth ranges and lower indicate differences in the interaction of semi-diurnal internal tide energy and the inertial energy.

To identify possible depth dependence or depth ranges with similarities and/or differences in the interaction signatures (spectral peaks at the IWISC and $M_2 + f$ frequencies), we have devised a single measure of the difference in peak energy within a band between the original data at a given depth bin and the data which has been S-L inverted. The intention is to differentiate between reversible advection and non-linearity.

If the S-L inverted data shows interaction peak energy removal at a given depth, and that depth is associated with a particular flow structure, a source of reversible advection could be determined with confidence. Likewise, in depth ranges where the S-L inversion does not reduce the interaction signature, it may be possible to identify non-linear interactions.

The calculation of interactant energy peak differences is calculated in this way:

- Fourier decompose the original and Semi-Lagrange inverted data sets for the time period form day 329 to day 495
- Subtract the narrow band average PSD of the original data from the S-L data for the interaction bands $M_2 + f$ and $M_2 - f$ for the cyclonic and anti-cyclonic rotary PSD respectively.
- Normalize the result by the maximum value in the viable data depth range (depths not impacted by contamination or diminished signal)
- Smooth the curve with a three depth bin RMA filter

This method was selected for its ability to demonstrate the relative effectiveness of the S-L inversion across a broad depth range. Since it is an abstraction of the absolute energy involved at any given depth bin, the quantitative importance of the result is obscured. For this reason, a calculation of relative peak height was made in conjunction with the difference.

The relative peak height is a measure of how far above a background band the peak value in a narrow band is, when they are both centered on the same frequency. The calculation can result in negative values if there is a 'valley' in the narrow band, or if there are higher peaks off center in the

broader band. The relative peak height is smoothed with the same three point running mean average as the peak difference calculation.

The two main depth profiles shown in figure 4.32 are the peak difference values, where blue indicates the IWISC frequency band and red the $M_2 + f$. Shaded regions are depths where the data has contamination or reliability issues. Negative values of the difference indicate depths where the S-L inversion is removing energy from the respective band. The filled markers on each curve represent difference values that have exceeded the 95% confidence interval. Negative values are the most likely locations where reversible advection is the dominant process creating the observed interaction energy peaks.

Periodic Doppler shifting of horizontal currents by vertical displacement can result in elevated energy at both of the interaction frequencies, as described in section 3.1.2. A S-L inversion of data, where periodic Doppler shifting (or reversible advection) is the sole mechanism creating the observed energy at the interaction frequencies, results in those peak energies being significantly diminished. Given this result, for depths such as 1000 meters, where the red and blue profiles are both negative, the case for reversible advection being the dominant mechanism is stronger. At other depths, it appears that advection is present, but in not a dominant process, as only one of the profiles is negative.

Values seen on the curves near zero or above indicate that the S-L inversion did not have an impact on the energy in the respective band at that depth. For these regions, it is necessary to examine the panel on the right, showing relative peak height. A low relative peak height indicates that the energy in the band is weak to begin with. In this case, the S-L inversion of a low relative peak would not be expected to have any significance. If the relative peak height is elevated at that depth, and the difference curve is near zero, this means that the S-L inversion did not remove energy from the band, and that the band has a significant peak.

Positive values of the difference indicate an increase in band energy due to the S-L inversion. The technique itself will redistribute energy, as examined in the analysis of modeled currents (see section 3.4). The interaction bands at these depth ranges are influenced by some process other than advection by the semi-diurnal displacement signal.

These possible situations can be divided into four categories with sub-explanations:

- Both bands have at least some energy significantly removed by the Semi-Lagrange inversion. [at depths of 560-575m, 660-730m, 940-970m: 13% of the depth range]

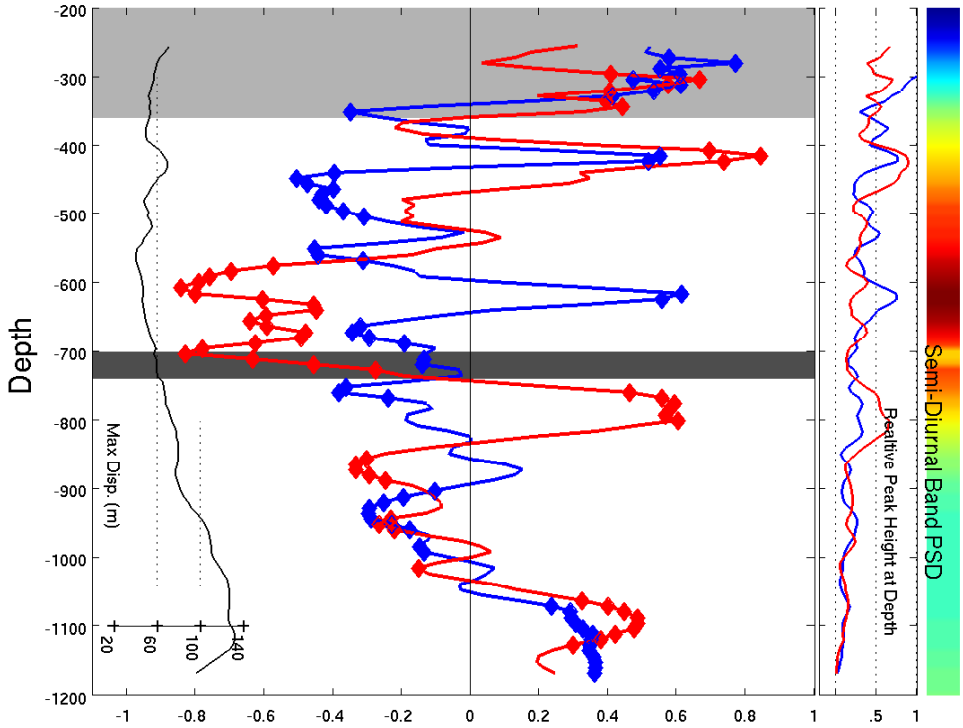

Figure 4.32. Vertical profile of the normalized difference in peak values at the interaction bands between the S-L inverted data and the original data. Blue indicates the difference band ($M_2 - f$) and red is the sum band ($M_2 + f$). Negative values of the main curves indicate regions where the S-L inversion has removed energy from the band, indicating vertical advection as the source of the observed band energy. Filled diamonds represent values exceeding 95% confidence. On the left is the depth smothed curve of maximum displacement over the entire record. The curves on the right indicate the relative strength of the band peak vs. depth. The far right colorbar is the clockwise bandpassed semi-diurnal energy vs. depth, with the peak value identifying the topographically generated internal tide beam at this location.

  - This situation has been associated with vertical displacement of horizontal currents being the source of the energy peaks in the interaction bands as examined in modeling section 3.3.

- One band has energy removed by the Semi-Lagrange inversion. [at depths of 440-510m, 540-560m, 575-660m, 730-780m, 850-940m, 970-1030m: 41% of the depth range]

  - One possible scenario is due to the asymmetric depth distribution of enhanced peaks at the interaction frequencies. This can occur with multiple periodic displacement advection (see modeling section 3.2).
  - Another possibility is that the Semi-Lagrange inversion is removing energy at both frequencies, while at the same time a separate process which yields energy at only one of the interaction frequencies is dominating its respective interaction band.

- The estimated energy differences are not statistically different from zero. [at depths of 360-400m, 510-540m, 810-850m, 1030-1050m: 13% of the depth range]
  - This could be the result of relatively weak energy at both frequencies.
  - Or, this result could be due to the existence of two processes. One being the introduction of energy into the interaction bands by non-linearity or horizontal displacement, the other being vertical displacement. In this case, the S-L inversion may have removed some of the energy at the bands, but it is not a statistically dominant mechanism.

- The Semi-Lagrange inversion has increased the energy in one band, with no reduction in the other, or increased the energy at both bands. [at depths of 250-360m, 400-440m, 780-810m, 1050-1180m: 33% of the depth range]
  - With this observation, vertical displacement is an unlikely source of the interaction peak energy.

The depth percentage by which the S-L inversion has some impact in reducing interactant peaks is 54%, a little over half the depth coverage. Yet only 13% is showing the S-L removing significant energy at both frequencies. Over the remaining 46% of the depth range the inversion technique is not reducing the interaction signatures. This finding is important, and indicates that arbitrarily applying a S-L inversion to correct for reversible vertical advection is not apropriate. The technique will give incorrect results if used indiscriminantly.

The maximum displacement profile is overlaid on the left of the figure. The highest displacements are near the bottom, and associated with a depth range of positive values in both the red and blue profiles of peak difference. These positive values were expected, due to the higher displacement input into the S-L inversion, and are not associated with high values of relative peak height.

On the far right of the figure, a depth profile of peak semi-diurnal energy is shown. The 'center' of the main beam is at 650 meters in this average. The center of the beam can vary depending upon the

time period examined. This figure represents most of the deployed time, and includes the period when background flow features appear to move the center of the beam deeper.

Despite the variability in vertical distribution of semi-diurnal internal tide energy, it is clear that at the depth range of the highest horizontal semi-diurnal currents, and in the core of the main beam, the S-L inversion is removing energy at the $M_2 + f$ frequency. This is not the case for the IWISC band.

In the core of the beam, the blue IWISC difference becomes positive. This occurs at a location of maximal relative peak height. At this depth, advection may play a part in the observed interaction peaks, but it is not the dominant process at the IWISC frequency.

The depth range just above the main beam shows little effectiveness of the S-L process. Above that is the second beam, as indicated in the analysis of section 4.2.2, and by the vertical velocity coherence in section 4.3.2. It appears that the S-L is removing IWISC energy until a depth of near 470 meters. Above that, in what is speculated to be the 'core' of the upper beam, the S-L is introducing energy into both interaction frequencies. This is in a depth range where the relative peak height for both bands is maximal.

This representation of the interaction peak energies suggests that there can be different processes involved even when the primary mechanism does not appear to be periodic Doppler shifting due to vertical displacement. By identifying these depths, further refinement to identify the mechanism can be done. Caution is necessary in interpreting these results. A negative indication from the S-L inversion in identifying advection does not mean the feature is non-linear. However, it does identify the most likely locations to find non-linearity.

We have demonstrated that relying on the S-L inversion to correct for observed energy at the interaction frequencies is not a simple or universal method. It will work for specific observations, although suitable data will need to be identified when applying the technique systematically.

4.6 Rotary Bispectra and Bicoherence

Bispectra and bicoherence are widely used to identify non-linear interactions. In section 3.4 there is a discussion of the techniques and their applicability to periodic Doppler shifting. It was discovered that bispectra/bicoherence alone can not universally distinguish between periodic Doppler shifting (reversible vertical advection) and energy exchanging non-linearity.

Consequently, in section 3.4 bispectra and bicoherence were used to analyze S-L inverted model data, where the interaction peaks in rotary PSD had been significantly reduced. There was a corresponding reduction in bispectra, and more importantly, the S-L inverted currents had no statistical

bicoherence at the interaction frequencies. That result encourages the use of these higher order techniques on the data that has been S-L inverted, and specifically here with data from the A2 mooring.

Depth regions have been identified where a S-L inversion does not effectively remove peak energy from the interaction bands as shown in figure 4.32. In these depth regions, there is a process (or processes) not associated with the vertical displacement of horizontal currents creating the peak energy at the interaction frequencies. Bispectra and bicoherence analysis of the inverted data can be used to identify the potential source of these peaks and their interacting frequencies.

To isolate higher order interactions involving inertial energy, a restricted time period of data will need to be analyzed. For the A2 mooring data, there are two reasons for this restriction. The first reason is the impact of the meridional background flow on the inertial discussed in section 4.2. Inertial energy above 650 meters is significantly blue shifted. Bicoherence and bispectra of a total record with these shifting sources will be inconclusive.

The second reason is due to the event like nature of inertial energy observed in this record. Events are typically less than two weeks in duration. Each event can have an independent phase associated with it. These events can thus interfere with each other in the averaging of the higher order calculation.

A segment of time will be analysed from the second half of the record corresponding to day 450 and ending at day 496 (from Jan 1, 2002). Figure 4.33 shows the peak difference after the S-L inversion for this time period. The values are normalized to the time period. Due to the normalized values, this figure will not have a direct comparison to figure 4.32, but there are significant similarities.

Two specific depths will be analysed. One depth is just below 400 meters in a depth region of the figure where the S-L inversion has not effectively removed the peak energies, and the relative peak height of both interaction frequencies is high. The other depth is near 800 meters in a depth region where the S-L is effectively removing energy from the sum ($M_2 + f$) frequency but is not diminishing the peak at the IWISC ($M_2 + f$) frequency.

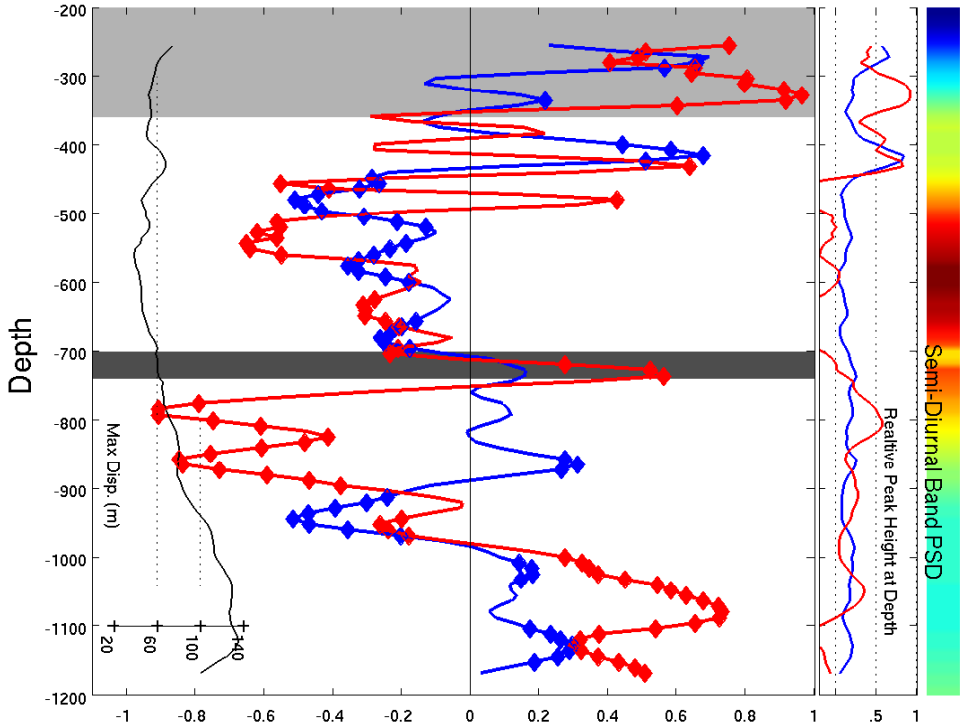

Figure 4.33. Vertical profile of the normalized difference in peak values at the interaction bands between the S-L inverted data and the original data. This figure represents data from the last third of the A2 mooring time coverage, and is constructed like figure 4.32.

One deviation to note in figure 4.33 that is not evident in figure 4.32 (representing the total record) is the apparent contradiction in the peak difference of the sum frequency at the 740 to 800 meter depth level. For the total record, the influence of the first two thirds of data is higher that the final third on the peak difference calculation. In that earlier time period, there was a significant background meridional shear which influenced this depth range. This appears to have impacted the semi-diurnal internal tide beam centered just above this depth range.

As the calculation is relative to the peak values corresponding to the time period of each respective figure, a deviation like that observed at the 740 to 800 meter depth level in the shorter record is not contradictory.

4.6.1 Analysis at 424 Meters

A selection of three spring/neap cycles in the second half of the record has been chosen at a depth of 424 meters to analyze with higher order techniques. The original time series along with an inertial and a semi-diurnal reconstructed demodulation of the horizontal velocities in this depth bin are displayed in figure 4.34. There are two inertial events within this section of time. The relative strength of the semi-diurnal tide is much higher that the inertial peak energy.

A comparison of the spectra can be seen between figure 4.35 which depicts the rotary PSD of the original velocities and figure 4.36 which is the data after S-L inversion. The spectra are constructed from the exact four windows of data used in the following bispectral calculation. As a check we can note that in figure 4.33 the S-L inversion is adding energy to both bands. In figure 4.35 there are energy peaks at the interacting frequencies and in the S-L inverted spectra (figure 4.36) these peaks are enhanced. The S-L inversion has introduced energy into the diurnal and $2M_2$ bands and removed energy from the inertial band.

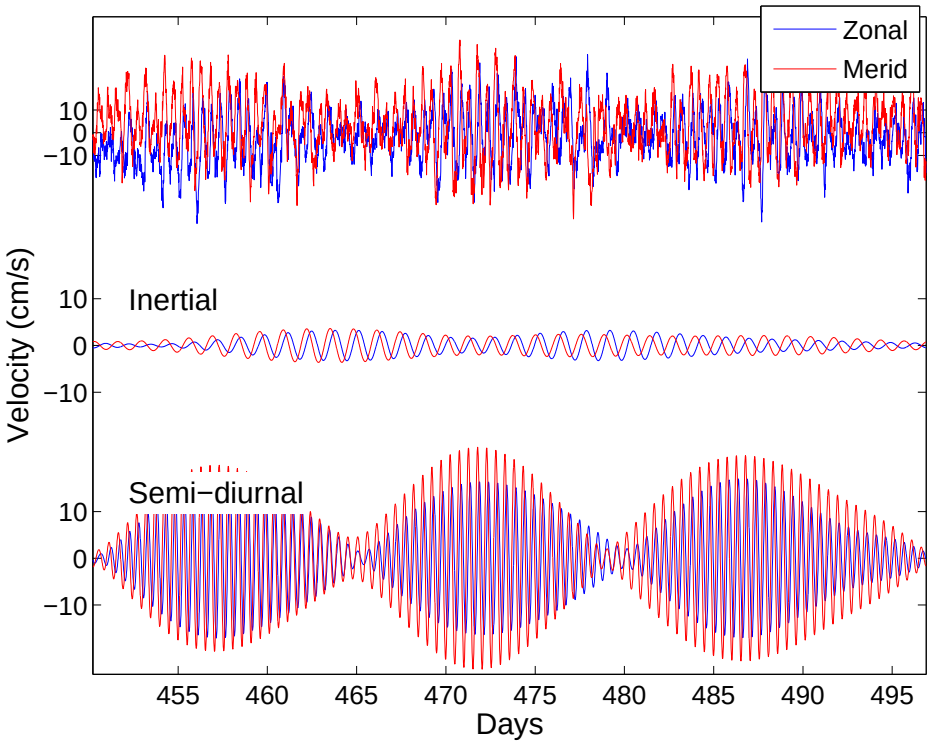

Figure 4.34. Horizontal velocity time series at a depth of 424 meters on the A2 mooring. The reconstructed, demodulated inertial and semi-diurnal horizontal velocities are depicted beneath the original data.

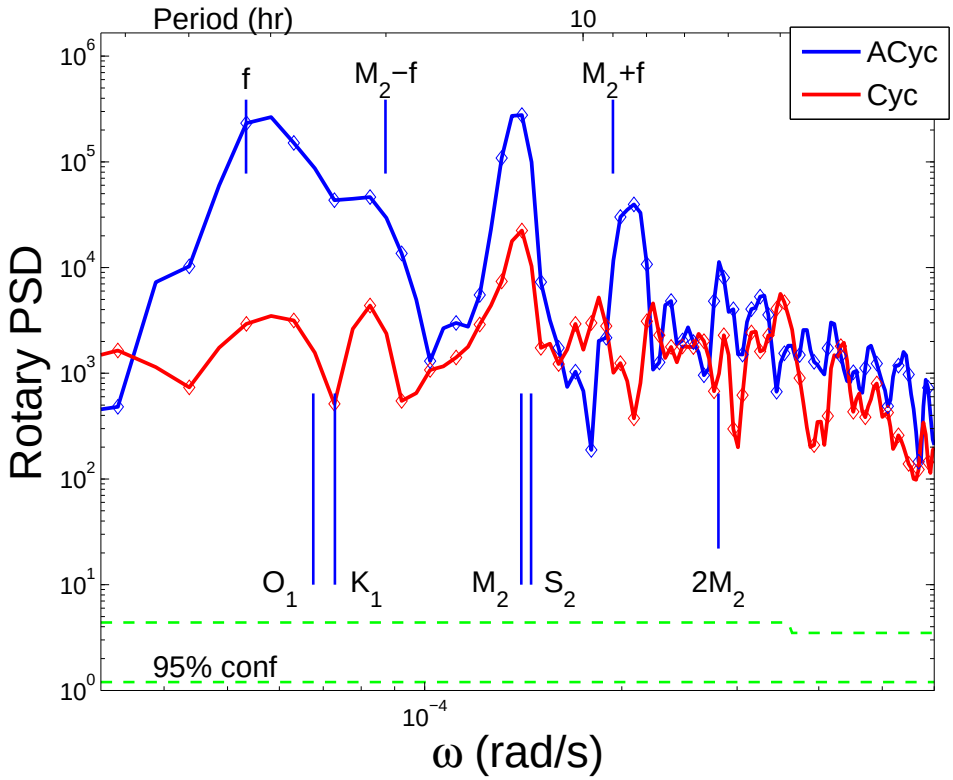

Figure 4.35. Rotary PSD for A2 at 424 meters of the time series shown in figure 4.34.

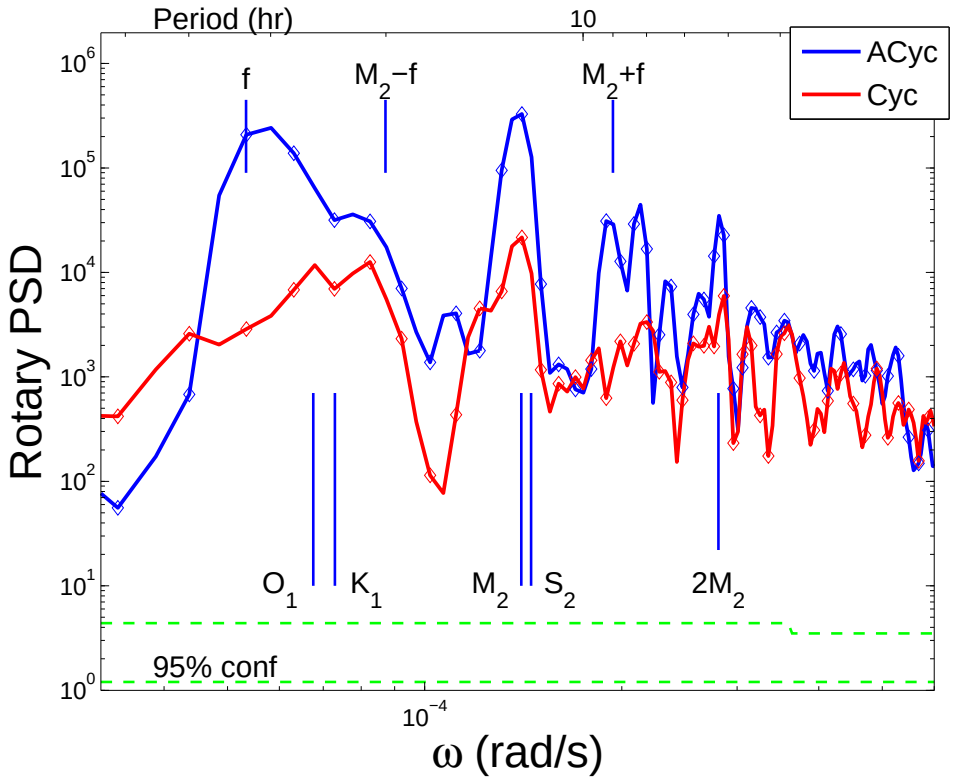

Figure 4.36. Rotary PSD for A2 at 424 meters of the S-L inverted data for the time period corresponding to figure 4.34. Peaks at the sum ($M_2 + f$) and difference ($M_2 - f$) frequencies have higher energy after the S-L inversion.

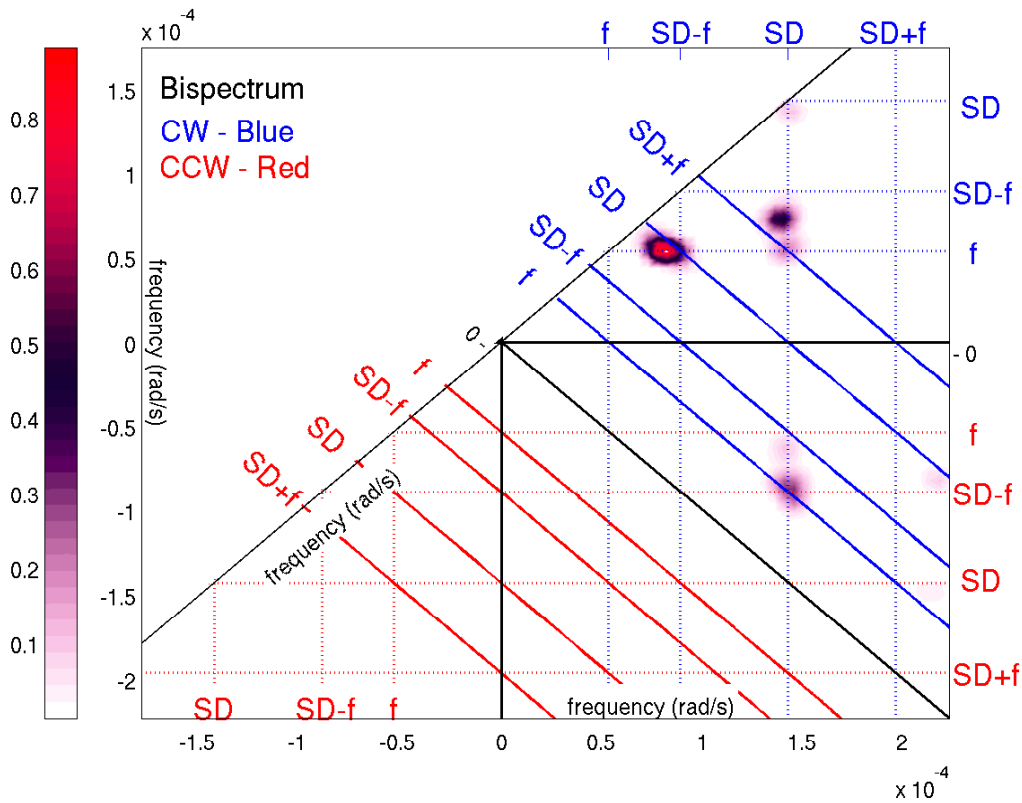

Figure 4.37. Rotary bispectrum for A2 at 424 meters. There are peaks in bispectrum associated with the two interaction frequencies. The IWISC ($M_2 - f$) is located at the intersection of cyclonic $SD - f$, anticyclonic SD, and anticyclonic f. The difference ($M_2 + f$) is located at the intersection of anticyclonic $SD + f$, anticyclonic SD, and anticyclonic f. Further discussion is in the text. Analysis technique described in section 3.4.

In figure 4.37 we have shown the rotary bispectrum of the original data. Details of the bispectra and bicoherence can be found in section 3.4. A further processing step was taken to filter interactions at higher frequencies than $M_2 + f$, specifically harmonic self interaction at the semi-diurnal frequency. In the figure, and subsequent bispectra/bicoherence, there are three axes, a horizontal, vertical, and diagonal. Each axis proceeds from cyclonic frequencies in red, through zero, to anticyclonic frequencies in blue. Dotted reference lines indicate the frequencies of interest. The label SD indicate the frequency $(M_2 + S_2)/2$, and the inertial value f, is blue shifted by three percent, representing a local (in depth) inertial frequency.

In figure 4.37 there are significant peaks in bistpectrum at points involving the interaction frequencies. There is a peak at the IWISC (cyclonic $M_2 - f$), which is located at the intersection of cyclonic $SD - f$, anticyclonic SD, and anti-cyclonic f. The difference (anti-cyclonic $M_2 + f$) peak is located at the intersection of anti-cyclonic $SD + f$, anti-cyclonic SD, and anti-cyclonic f. There is a separate peak involving anti-cyclonic $SD - f$, anticyclonic SD, and anti-cyclonic f. The origin of this interaction is unknown.

The rotary spectra indicate that the S-L inversion did not reduce the interaction peaks. There is little expectation then for the bispectrum of the S-L inverted data, however, an interesting point is observed in figure 4.38 which shows the corresponding bispectrum. The spectra indicated that the inversion added energy to both interaction frequencies. Energy was also added to the diurnal and first semi-diurnal harmonic.

The bispectrum of the S-L inverted data reveals an enhancement at only one peak, that associated with the IWISC. This can serve as an interesting point. The S-L inversion, of data that has no evident vertical displacement of horizontal currents, will effectively introduce such. For this depth, and this time period, with the displacement utilized in the S-L inversion, a asymmetric enhancement of bispectrum has resulted.

In conjunction with the bispectrum, a bicoherence plot is shown in figure 4.37. There is an elevated coherence at the IWISC associated point. The figure shows no significant coherence at the sum frequency. The very high coherence of the point associated with anti-cyclonic $SD - f$, anticyclonic SD, and anti-cyclonic f indicates possible semi-diurnal harmonic effects.

There is a visibly enhanced coherence at the point associated with the sum frequency with the S-L inverted bicoherence at this depth. It does not exceed the significance level, but is above the value in the non-inverted data.

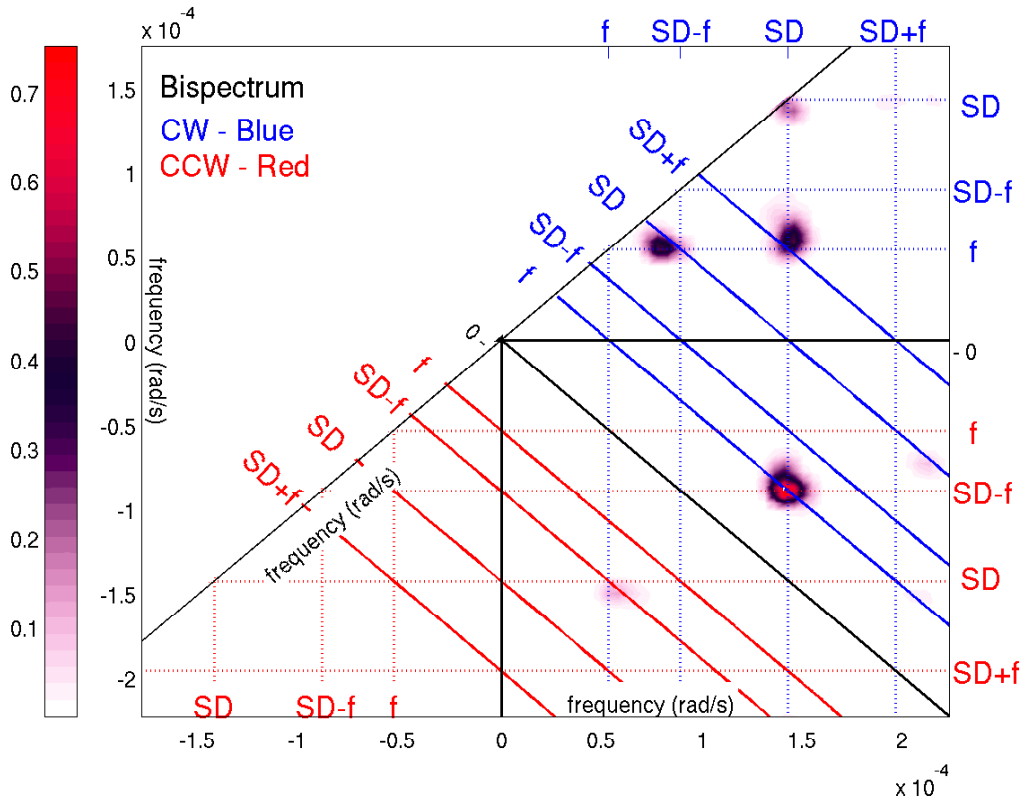

Figure 4.38. Rotary bispectra for A2 at 424 meters for the S-L inverted data. Enhanced energy remains at the interaction points as indicated in figure 4.37. Analysis technique described in section 3.4.

4.6.2 Analysis at 784 Meters

At the depths near 800 meters, the S-L technique is not removing energy from the IWISC band. For this time period it is removing significant energy from the $M_2 + f$ band. This can be seen in the following two spectra, which are constructed using the Fourier transforms utilized in subsequent bispectra/bicoherence figures. The analysis uses the same methods as in the preceding analysis at 400 meters.

The S-L inversion, though apparently effective at reducing the sum interaction peak, has not reduced the IWISC energy, and may have broadened that band. The cyclonic signal now exceeds the anti-cyclonic for part of the spectra near the IWISC frequency.

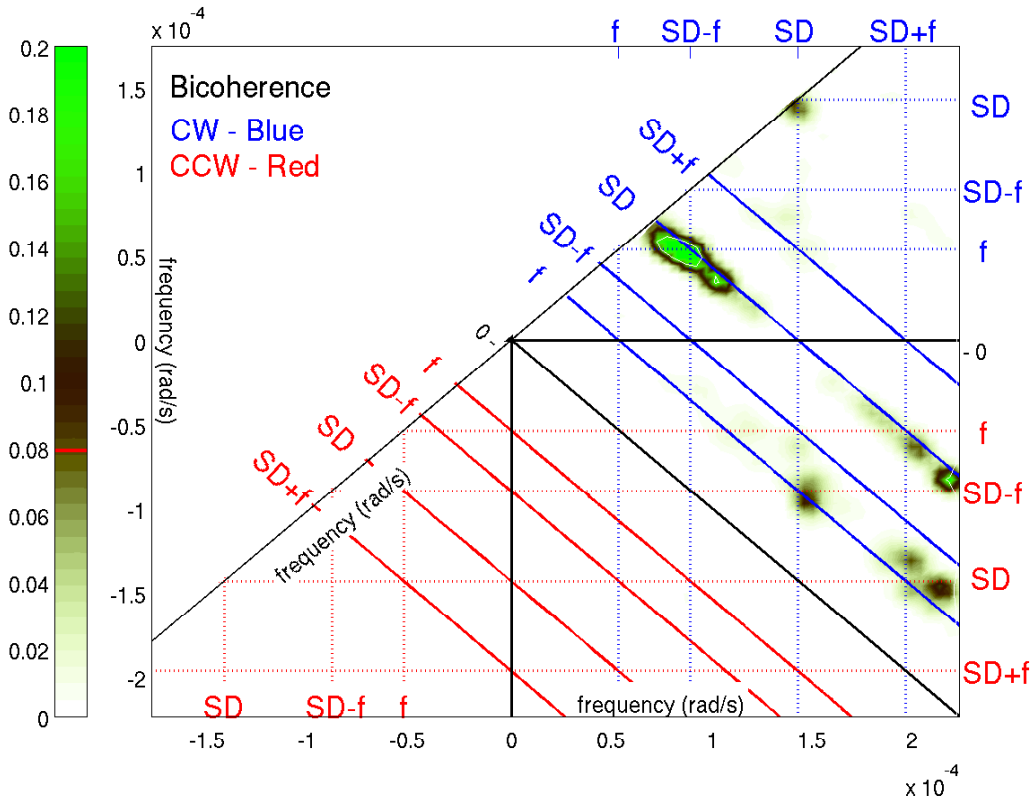

Figure 4.39. Rotary bicoherence for A2 at 424 meters. Significant coherence is indicated at the interaction point identified by cyclonic IWISC ($M_2 - f$) frequency, anti-cyclonic inertial frequency, and anti-cyclonic semi-diurnal frequency. Analysis technique described in section 3.4.

The bispectra for this depth (figure 4.43) shows enhancement at the IWISC and sum ($M_2 + f$) interaction frequencies. After the S-L inversion, there is a definite drop in the bispectra at the sum frequency, as seen in figure 4.44.

This drop in bispectra at the sum frequency is interesting as the IWISC seems to be unchanged. However, bispectra are not the complete picture, as there can be bispectral enhancement simply do to strong peaks in spectra. This leads to the corresponding bicoherence for this depth shown in figure 4.45.

There is elevated coherence at the IWISC and sum frequencies. These coherent features correspond to the enhanced bispectra locations in figure 4.43. There are other coherent frequency triplets. Only the triplet associated with the anti-cyclonic inertial frequency, anti-cyclonic semi-diurnal fre-

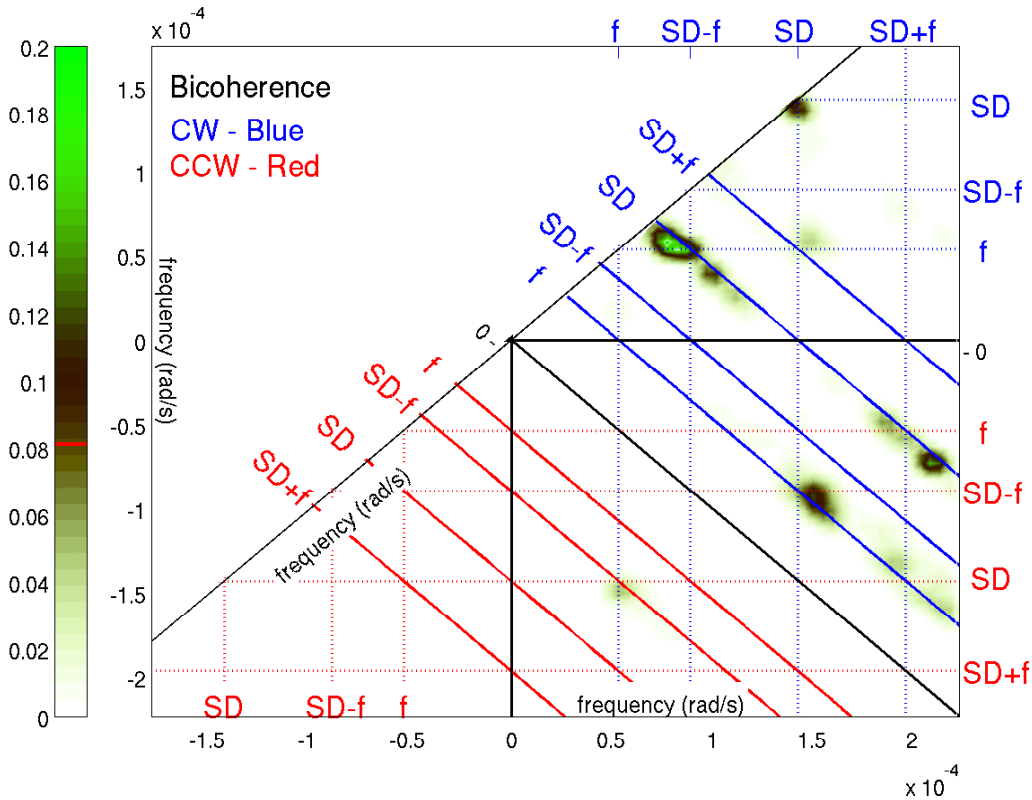

Figure 4.40. Rotary bicoherence for A2 at 424 meters for the S-L inverted data. Significant coherence remains at the location associated with the IWISC frequency as in figure 4.37. Analysis technique described in section 3.4.

quency, and anti-cyclonic IWISC frequency has corresponding enhanced bispectra. An analysis of this potential interaction feature has not been done, and may yield interesting results in the future.

The bicoherence after S-L inversion is shown in figure 4.44. The triple point associated with the sum frequency has now lost any significant bicoherence. However, the IWISC bicoherence is unaffected.

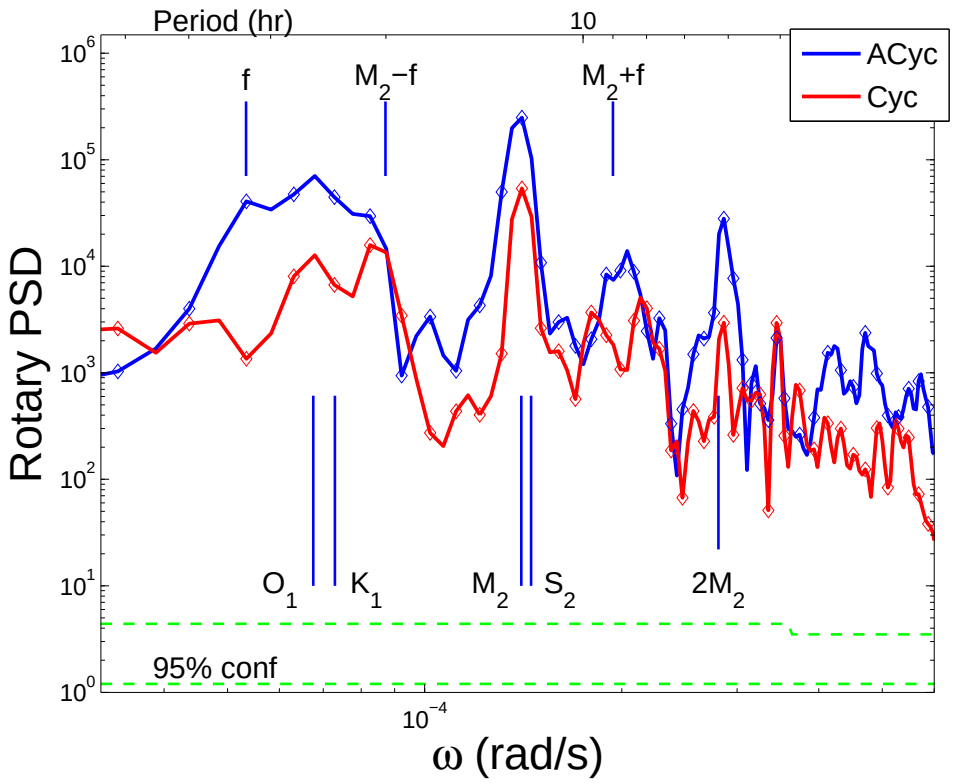

Figure 4.41. Rotary PSD for A2 at 784 meters. Peaks are evident at the interaction frequencies. The inertial is diminished as compared to the corresponding spectra for 424 meters (figure 4.35)

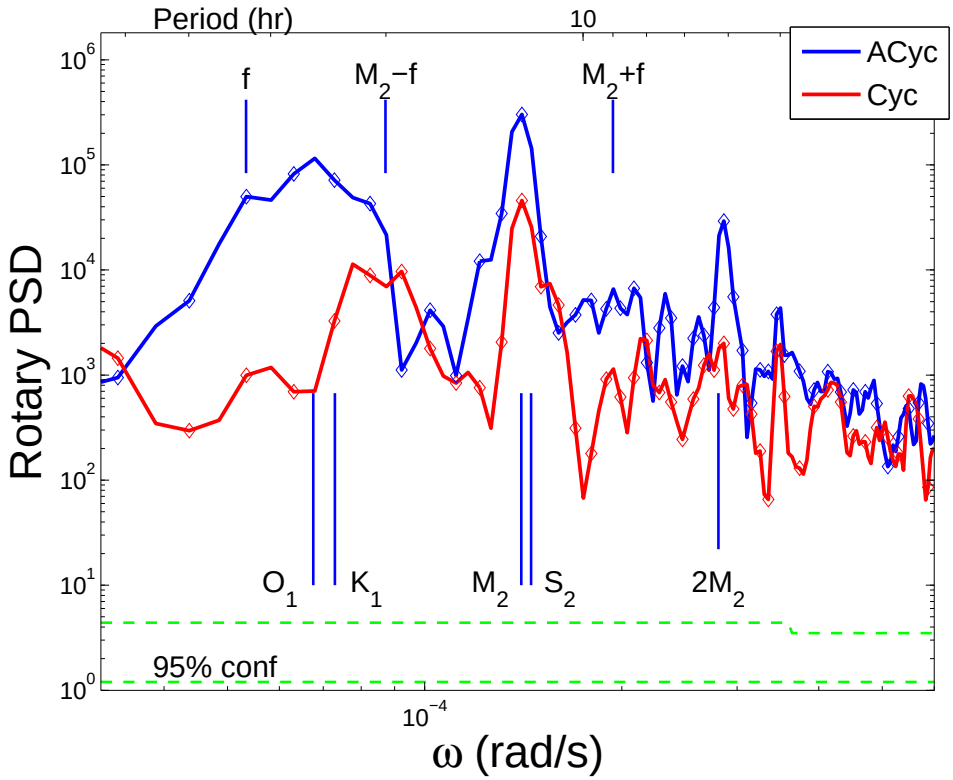

Figure 4.42. Rotary PSD for A2 at 784 meters for the S-L inverted data. The inversion has removed some of the energy at the sum ($M_2 + f$) frequency. There is not a corresponding drop in the IWISC energy.

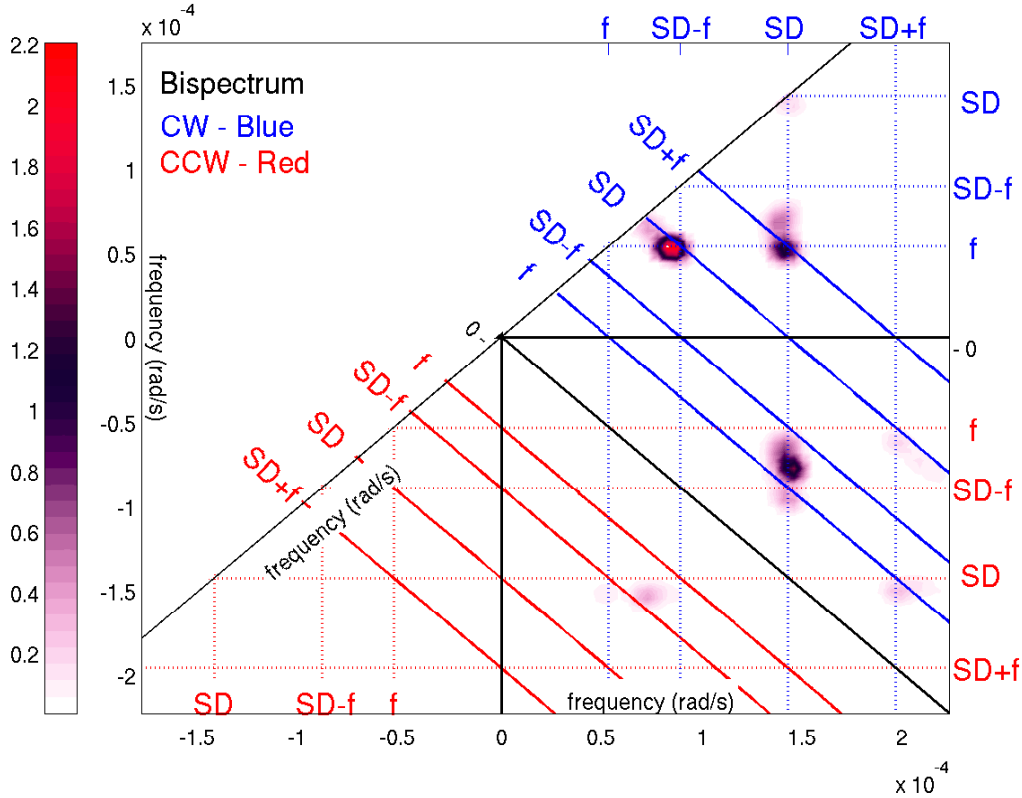

Figure 4.43. Rotary bispectra for A2 at 784 meters. There is enhanced bispectra at the IWISC and sum ($M_2 + f$) interaction frequencies. Time period and method correspond to the previous analysis at 424 meters. Analysis technique described in section 3.4.

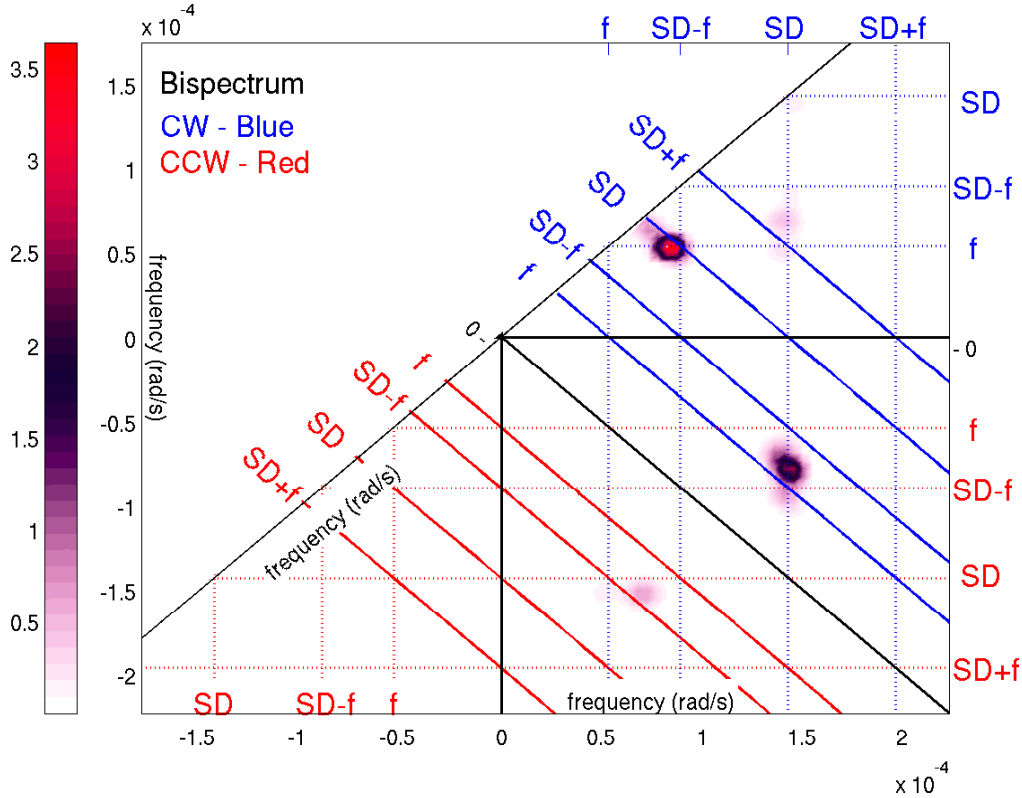

Figure 4.44. Rotary bispectra for A2 at 784 meters for the S-L inverted data. Bispectra at the sum ($M_2 + f$) interaction frequency has diminished as compared to figure 4.43. Time period and method correspond to the previous analysis at 424 meters. Analysis technique described in section 3.4.

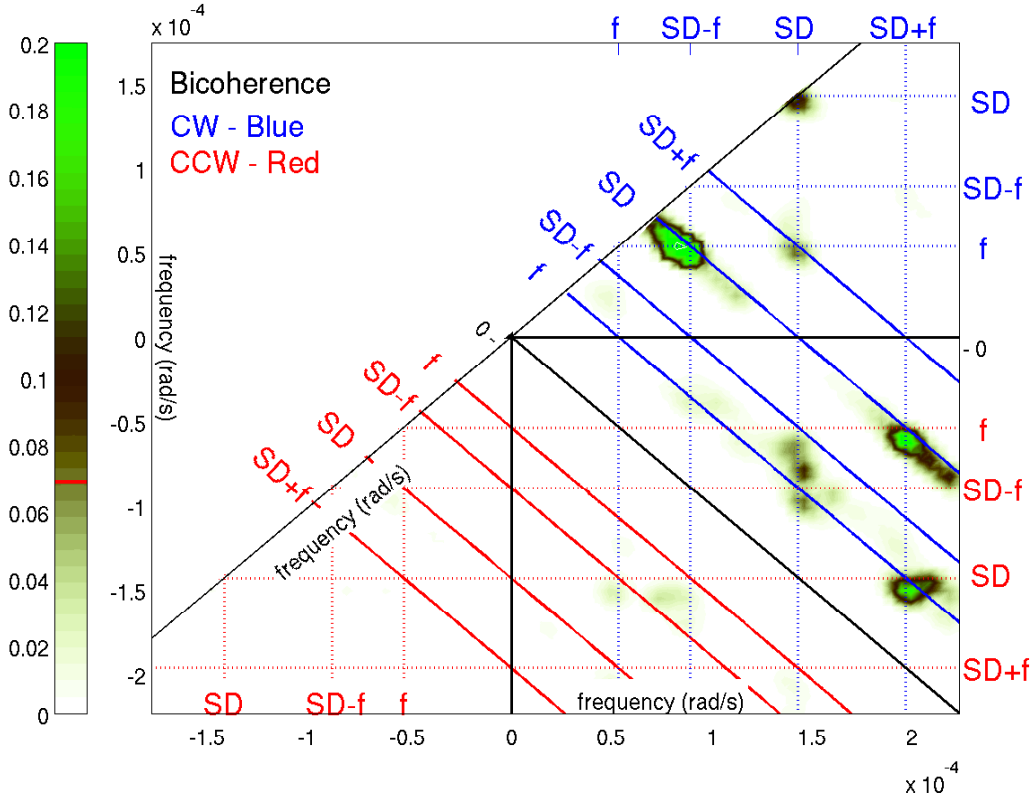

Figure 4.45. Rotary bicoherence for A2 at 784 meters. Elevated bicoherence is indicated at the IWISC and sum $(M_2 + f)$ interaction frequencies. Time period and method correspond to the previous analysis at 424 meters. Analysis technique described in section 3.4.

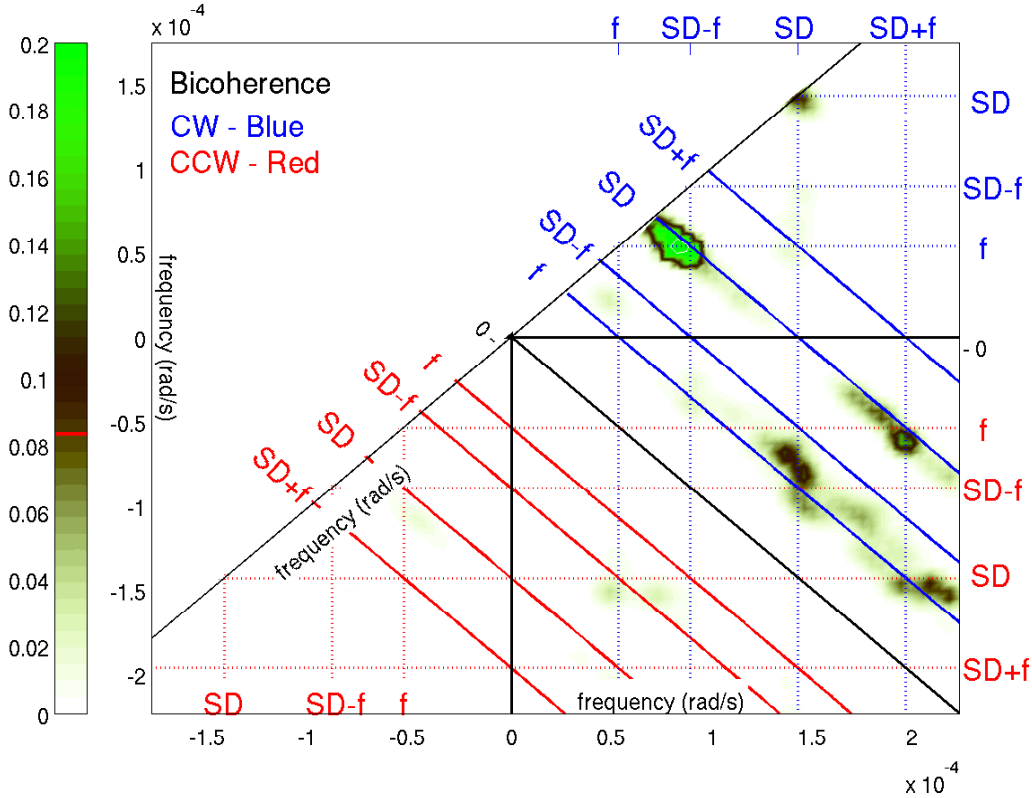

Figure 4.46. Rotary bicoherence for A2 at 784 meters for the S-L inverted data. Elevated bicoherence is indicated at the IWISC frquency. This indication supports a conclusion that reversible advection is not the source of the IWISC interaction at this depth. Analysis technique described in section 3.4.

4.6.3 Wavelet Rotary Bispectra and Bicoherence

Wavelet techniques offer the unique perspective of temporal localization. A rotary wavelet bispectra/bicoherence method was developed in section 3.5 that can take advantage of the temporal localization and identify possible non-linear interactions among frequency triplets even when one or more of the frequency bands are dominated by episodic events. At the 424 meter depth level analysed previously with Fourier transforms, an event is present that will be looked at with wavelet techniques.

The trade-off in using wavelet techniques is a loss in frequency 'sharpness'. This translates into broader areas of enhancement in the bispectra and bicoherence. This tool is very useful when the need to isolate an event out weighs the need to separate nearby frequency structures.

As the first step in this wavelet analysis, we present the coefficient time series in figure 4.47. The time period isolated in the figure falls within the data used in the Fourier analysis previously. The top panel is anti-cyclonic wavelet amplitudes, and the bottom cyclonic. Indicated in red vertical lines are the times of the two transforms used in the rotary PSD and in the bicoherence/bispectrum.

A semi-diurnal spring/neap cycle is clear, with individual semi-diurnal wave amplitude variation resolved within the envelope. Anti-cyclonic diurnal energy is not as regular. The diurnal signal is close in frequency to the inertial and the IWISC, with only a cursory examination would difficult to distinguish between these frequencies. However, we can get significant information by looking systematically at each.

For the inertial, there is energy from the beginning of the figure, then it diminishes slightly after day 467, then rising again. This falls during days 471 to 473, then rises again.

Moving up in frequency is the diurnal band. The two red dashed lines are O_1 and K_1. There are two time periods of elevated anti-cyclonic energy in the diurnal band. However, there is no corresponding energy in the cyclonic, which would be expected for a baroclinic internal tide, such as can be seen for the semi-diurnal. Some of this energy could be blue shifted inertial internal waves, which would have little cyclonic energy.

At the IWISC frequency band there is a clear rise in energy to a maximum at day 469, then a slower decrease back to very little energy. This IWISC energy corresponds to a time of increasing spring/neap semi-diurnal energy and fairly steady inertial energy. The amplitude of the semi-diurnal tide does not appear to be modulating the appearance of the IWISC energy.

By utilizing the wavelet transforms, we have isolated a IWISC event and avoided potentially conflicting energy at the diurnal frequency. As shown in the vertical time series of diurnal energy (figure 4.2.2) there are many depths and times when the cyclonic diurnal has energy. The method using Fourier

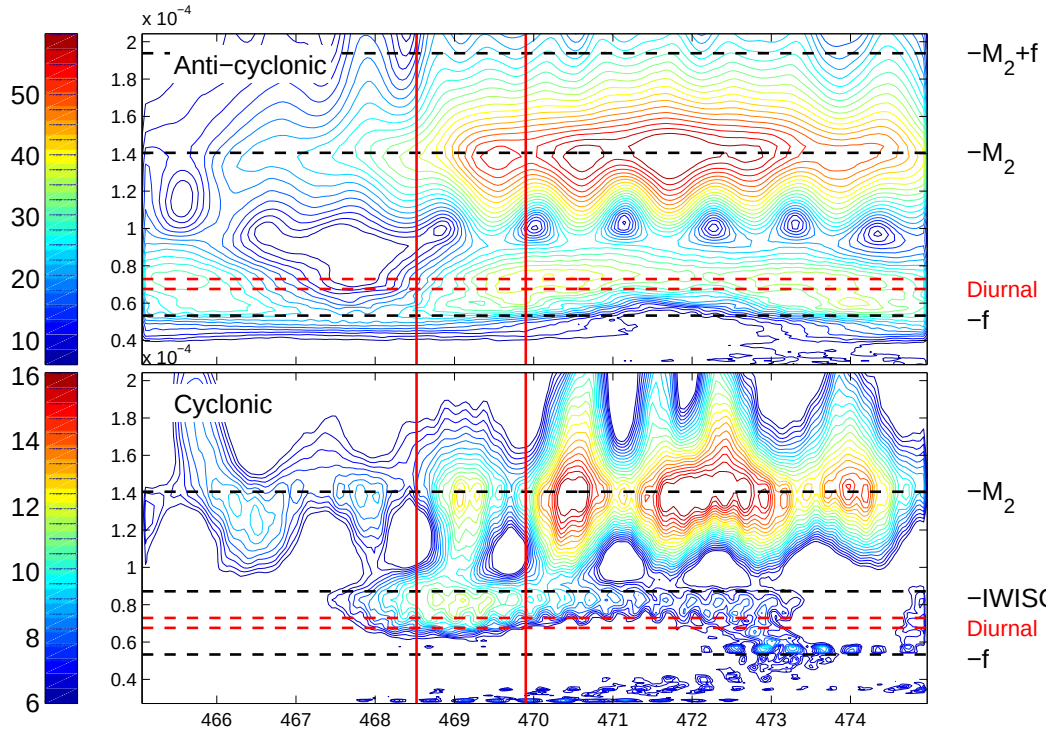

Figure 4.47. Wavelet rotary amplitude coefficient time series from the HOME A2 mooring at a depth of 424 meters. Temporal range is selected from within the time period of the corresponding bispectral analysis. Vertical red lines indicate center time of wavelet transforms used in bispectral/bicoherence analysis. Analysis technique described in section 3.4.

transforms involves analyzing a long enough record to achieve spectral separation, which would in this instance overlap with increased cyclonic diurnal energy. The diurnal signal would then distort the ability to isolate specific IWSIC event interactions.

In figure 4.48 the wavelet rotary bicoherence is indicated. There is an elevated value at the IWISC associated triple frequency vertex. Another coherent co-location involves the $SD + f$ (anti-cyclonic), SD (anti-cyclonic), and f (cyclonic) frequencies. Notice that there is not a significant level of bicoherence at the location associated with the sum $(SD + f)$ interaction triple point.

With the wavelet bicoherence in mind, we can examine the wavelet rotary bispectrum in figure. 4.49. There is an elevated bispectrum value at the IWISC associated triple point. There is no bispectrum peak evident at the location of the other bicoherent triple point identified earlier. The elevated

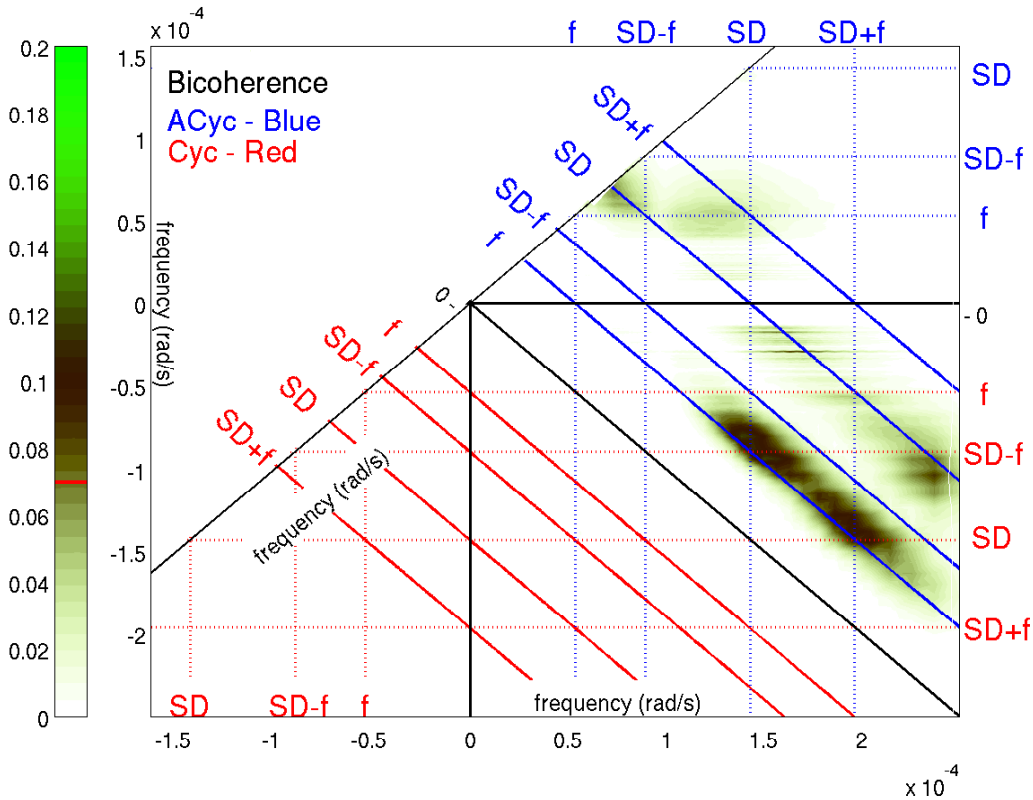

Figure 4.48. Wavelet rotary bicoherence utilizing the two transforms indicated in figure 4.47. There is elevated coherence associated with the IWISC interaction located at the frequencies $SD - f$ (cyclonic), SD (anti-cyclonic), and f (cyclonic). Analysis technique described in section 3.4.

bispectrum near the location of the sum interaction triple point does not have corresponding bicoherence.

We have performed this same analysis on the S-L inverted data. The result is equivalent to the Fourier methods in that there is increased spectra, bicoherence, and bispectra due to the inversion. Similarly, the S-L distorts heavily the diurnal band.

The primary significance of the wavelet analysis is in its usefulness to isolate temporally, frequency associated motion. Two main benefits of that property are: a) the ability to analyze processes that happen as events in time, and 2) to separate event dominated signals from near frequency neighbors to avoid spectral contamination. This is makes the rotary wavelet analysis quite powerful in the context of forced internal waves or non-linear interactions.

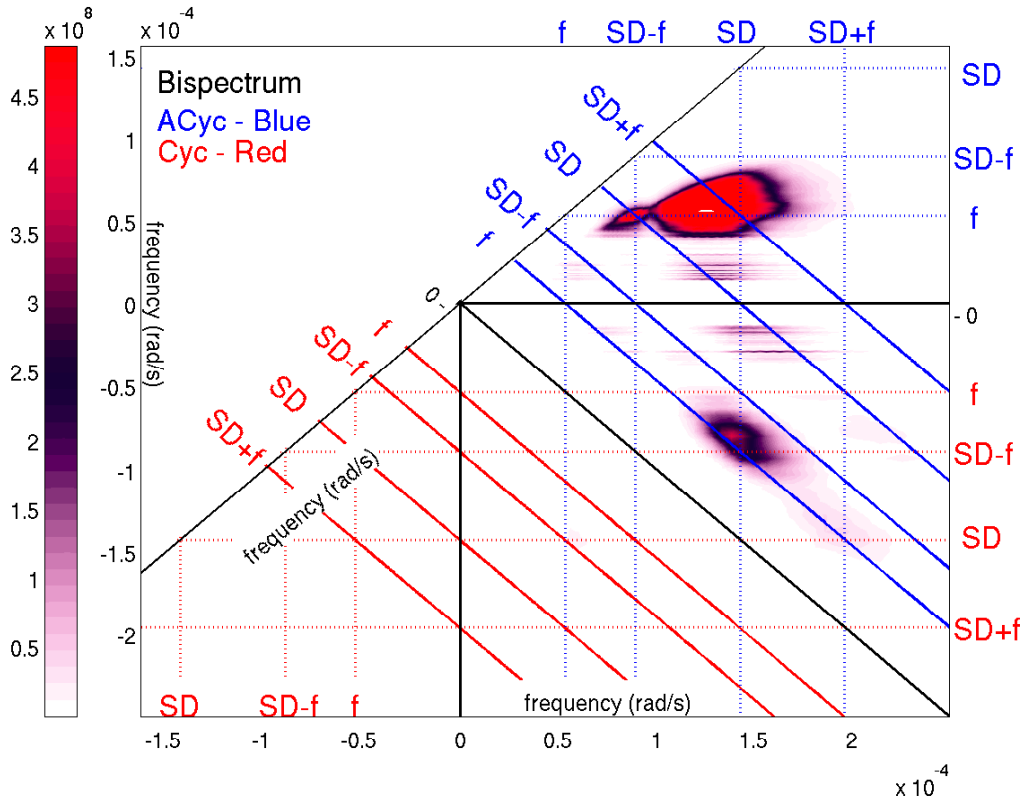

Figure 4.49. Wavelet rotary bispectrum utilizing the two transforms indicated in figure 4.47. There is an elevated bispectrum value associated with the IWISC interaction located at the frequencies $SD - f$ (cyclonic), SD (anti-cyclonic), and f (cyclonic). Analysis technique described in section 3.4.

We have specifically applied the rotary wavelet technique to HOME ADCP data and resolved IWISC associated interaction signatures from a localized time of IWISC enhancement. The method gives results consistent with the Fourier analysis, and is applicable to short duration event signals like the observed IWISC.

4.7 Summary of HOME Results

The HOME mooring A2 has provided a high vertical resolution data set to investigate the interaction between inertial internal waves and the semi-diurnal internal tide. The mooring was in a location with many overlapping processes. We have been able to investigate these features as they relate to IWISC and discover very interesting results. The foremost of those results is the evidence supporting

the theory that more than one process is responsible for the observed energy at the IWISC ($M_2 - f$) and sum ($M_2 - f$) frequencies.

To discover this, it was necessary to obtain accurate semi-diurnal displacement and use that in a Semi-Lagrange inversion of the data. This inversion recovers the 'reference frame' where any energy evident will be due to some other process besides vertical displacement of horizontal currents. For multiple location in depth, this inversion did not remove the energy at the interaction frequencies.

The expectation is that the spectral signature of reversible vertical advection process would be mediated by a coordinate transformation to one that follows the vertical 'heaving'. This is the Semi-Lagrange inversion, and after application to the HOME A2 moored ADCP data, there was not a universal reduction in those spectral signatures. By not mediating the reversible advection, we conclude that other processes are involved.

In depth regions of the horizontal currents that have IWISC evidence remaining after the S-L inversion, a bispectral/bicoherence analysis indicates interaction at the IWISC frequency. This is evidence of another process at this location redistribution energy to the IWISC frequency even in a reference frame following the displacement due to the semi-diurnal tide. We have not determined conclusively the nature of this process, and expect that this will be a significant research avenue in the future.

Though a conclusive case has not been obtained, the confluence of shear spectral evidence with elevated bispectra and bicoherence weighs in favor of a irreversible energy exchanging process. This would represent a path of energy from the source internal waves, as semi-diurnal internal tides and inertial waves, to motion within the internal wave frequency band at the IWISC and/or $M_2 + f$ frequencies. With the high shear observed, these motions would appear to be dissipative.

The analysis of HOME data resulted in the following in order of appearance within this chapter.

- Analysis of HOME ADCP record reveals IWISC frequency peaks in power spectra and shear.
- Significant variability of semi-diurnal energy in depth and time characterized.
- Semi-diurnal beam energy located in depth indicating at least two beams.
- The vertical velocity from the HOME mooring A2 ADCP records was corrected for diel migrator contamination at the semi-diurnal frequency. Vertical velocity at this band was extracted. Validation was possible due to the existence of two ADCP's on the mooring.
- Coherence in the vertical velocity between depths consistent with expected vertical structure, even between separate instruments.
- The vertical velocities were used in a Semi-Lagrange inversion of ADCP horizontal velocity.

- The Semi-Lagrange inversion reveals depth ranges where interaction peak energy is diminished by the inversion, and depth ranges where the energy peaks remain unaffected. This leads to the conclusion that both reversible vertical advection and other energy redistribution processes are present at this location.
- Bispectral analysis on Semi-Lagrange corrected ADCP velocity indicates non-linear interaction at IWISC.
- Wavelet analysis supports results from Fourier techniques.

The central result, that S-L inversion of the data does not correct universally the interaction signatures, was possible due to the high vertical resolution of data from this mooring. In the future, as similar data is collected, the analysis done here can be expanded.

Chapter 5

Conclusion

5.1 Discussion

Internal Wave Induced Sub/Super-inertial Currents are fascinating, complicated structures whose existence implies a new energy path from tidal and inertial internal waves directly to dissipative structures, independent of the assumed cascade of energy through the internal wave field from large to small scales. The research presented in this dissertation was able to use existing data to explore characteristics of IWISC motions, to provide a clearer understanding of the difficulty in distinguishing reversible from irreversible non-linear interactions, and to suggest additional areas of exploration for a more complete understanding of non-linear internal wave dynamics.

The analysis of IWISC opens up new possibilities concerning internal wave interactions and the path of energy from the wind and tides towards mixing. The first question addressed is about advection. This question was formulated at the beginning of this research into the IWISC context: ”Can vertical advection by the semi-diurnal internal tide account for the evidence indicating an interaction at the difference frequency between inertial waves and semi-diurnal internal tides?”

IWISC energy is not predominantly co-temporal with horizontal semi-diurnal internal tide energy as shown in section 2.3. If vertical advection by the semi-diurnal internal tide was the primary limiting factor, some relationship would be expected. This expectation was shown to be valid (see section 3.3) for a simple model where the vertical coordinate of the inertial wave was advected vertically.

Another expected relationship with vertical displacement as the primary factor was the nearly even distribution of periodically Doppler shifted energy between the IWISC frequency and the sum frequency ($M_2 + f$). In actual data, there was only a weak relationship between the two as seen in section 2.3, but not strong enough to be the sole explanation. A portion of the uneven distribution of

energy between the two Doppler frequencies can be attributed to vertical structure of the input inertial and semi-diurnal internal waves as shown in section 3.2.

The variability introduced by vertical structure can explain some of the variation between the two periodic Doppler shifted frequencies. Conversely, there are cases where the energy difference between the two frequencies cannot be explained by this variability, as shown in section 2.3. There are also periods of time when there is considerable energy (relative to other enhanced energy time periods) in the interaction frequency bands, yet the semi-diurnal tide is relatively weak. This could be attributed to current meters at depths where the vertical velocity is large and the horizontal velocity is reduced.

This situation where vertical velocity and the observed horizontal energy do not match could explain a number of observations. Additional data was analysed to check this possibility. Due to the strong relationship between temperature and vertical velocity, temperature has been widely utilized as a proxy for displacement. Peak energy periods in semi-diurnal temperature spectra were investigated for corresponding enhanced IWISC energy as shown in section 2.3. No direct relationship between temperature (as a semi-diurnal vertical displacement proxy) and enhanced IWISC energy was found.

Assuming irreversible non-linear forcing is the cause of IWISC, several plausible hypotheses can be imagined for why the particular datasets examined here do not yield a good correlation between the semi-diurnal forcing energy time series and IWISC enhanced energy periods, e.g.:

- Semi-diurnal displacement is a necessary component of the interaction, but the magnitude of observed IWISC may not be limited by the displacement amplitude. This would result in a decoupling of the semi-diurnal and IWISC.

- The structure of the semi-diurnal displacement may at times have variability that is not well resolved by the temperature and horizontal current data.

- Eulerian observation 'sees' limited extent of interaction process. For instance, the interaction may occur above or beside the instrument, then the interacting waves propagate away. When propagated or advected into the range of the instrument, the interactants no longer correlate with the IWISC and $M_2 + f$ energies.

Other possibilities may exist. To address these scenarios, data with higher vertical and/or horizontal resolution is necessary.

Higher resolution data from moored ADCP instruments was analysed for direct measurement of vertical velocity at semi-diurnal frequencies. That vertical velocity was found to be coherent through broad depth ranges (see section 4.3) and across two instruments. This information is particularly unique

to the location and design of the HOME project A2 mooring, but may lead to utilization of other moored ADCP vertical velocity records as direct measurements of vertical velocity in a narrow band.

A vertical coordinate inversion is possible with directly measured vertical velocity (see section 4.4). The Semi-Lagrangian (S-L) inversion removes energy seen at the periodic Doppler shifted frequencies for modeled records with vertical displacement of inertial internal waves by semi-diurnal internal tides (section 3.3). Application of this technique to observed horizontal currents at mooring A2 revealed depth ranges where the S-L inversion removed energy at the interaction frequencies, and depth ranges where it did not.

This surprising and important finding indicates that more than one process is involved in the heightened energy observed at the two frequencies, $M_2 - f$, and $M + f$. Bispectral analysis was employed on the inverted data to identify the nature of this interaction. The results of the analysis indicate a non-linear interaction (section 4.6). This analysis was bench-marked against a simple displacement model (section 3.4).

It has been demonstrated here that using spectral energy peaks and higher order products like bispectral analysis to determine non-linear interactions in fields showing significant periodic Doppler shifts can lead to inappropriate conclusions (section 3.4). These false positive identifications of non-linear interaction have been avoided here by precisely inverting the vertical coordinate system, and then using bispectral and bi-coherence analysis to determine the presence of non-linear activity.

Significant aspects of the nature of IWISC need further investigation. The role of horizontal advection has not been determined, as well as the impact it would have at these interaction frequencies. High vertical wavenumber structure in the semi-diurnal tides will have a significant impact on IWISC as well. Both of these concerns require data with better spatial resolution than is currently available in order to be addressed.

Given the preponderance of evidence, the energy at the IWISC and $M_2 + f$ frequencies can no longer be ignored. Even a small percentage of non-linear energy exchange from inertial waves and semi-diurnal tides to these frequencies can have a significant impact on the total internal wave energy budget. This small percentage when compared with other bands in the internal wave spectrum can not be neglected.

The interaction frequency $M_2 + f$ is often the next highest peak energy at frequencies greater than the semi-diurnal tides (for instance see figure 2.1). If half of that energy represented a periodic Doppler shift (reversible advection), the other half would still be the next highest energy peak in the internal wave regime. Many refinements to classic, empirically based theory establish a measured energy level at some arbitrary frequency near this based on observed averages. Refinement to the empirical de-

scription could be made by establishing what level of energy was due to reversible processes and what energy remained.

Determining the disposition of energy at these interaction frequencies, and their structures, would likely change the formulation of continuum models. Even if the energy is entirely due to measurement in an Eulerian reference frame, with no irreversible interaction, this represents an important change to the established spectral models as well, as Pinkels [67] pure advection formulation demonstrates. Inverting the field and correcting for reference frame motion would significantly diminish the energy at $M_2 + f$, and presumably at other related low order harmonic frequencies, which lowers any 'average' in nearby bands that are traditionally used for establishing a continuum model.

At the IWISC frequency, peak energy attributed to non-linear energy exchange represents a 'short circuit' in the established path of energy flow. At latitudes above critical, energy put into the internal wave band at inertial and semi-diurnal tide frequencies would be continuously leaking out of the free internal wave regime. This is fundamentally important for two reasons:

- Estimates of energy transferred into the internal wave regime have a dependence on measured inertial and semi-diurnal energies (see Müller and Briscoe [54]). The analysis done in this work indicates that not all of that energy goes into free internal waves.

- The resulting structures from the energy transfer into IWISC and $M_2 + f$ frequencies have potentially high vertical wavenumbers thus short vertical scales. This implies enhanced shear and subsequent mixing by these processes.

The first point is important for estimating global energetics, and for modeling internal waves. These global estimates are not precisely refined at this time. As more numerous and accurate data becomes available, refinements on the order of the energy transferred to IWISC will be important.

From a standpoint of mixing, IWISC represents an intriguing pathway. The process extends deep into the ocean where there is an identified need for diapycnal mixing (e.g., Munk and Wunsch [58]). There is a widely held view that the internal wave band supplies the energy necessary for this mixing, but all the mechanisms have not not been identified. IWISC could represent a process that continually bleeds off inertial internal wave energy as it propagates downward.

Given the potential importance of the process identified in this work, new efforts should be initiated to determine with greater accuracy the apportionment of energy into the interaction frequencies between inertial waves and the semi-diurnal tide. There are two main processes; periodic Doppler shifting without energy transfer, and non-linear energy exchange that does not fit the established theories. The periodic Doppler shifting needs to be examined closely, as it changes the currently accepted view

of the internal wave continuum. The non-linear energy exchange in IWISC exposes the importance of direct forcing in the low frequency internal wave band.

This non-linear exchange differs from established non-linear resonant triad interaction theory. It could be representative of a broad class of structures involved in non-linear exchange between other free internal waves and non-free motions. These interactions may be responsible for some of the expected energy redistribution which dictate the structure of the observed internal wave spectrum. This situation is unique in the study of internal wave non-linear dynamics as there is a preponderance of evidence, but no established theory motivating the search.

5.1.1 Observational Results

Reaching the conclusion that multiple processes are responsible for the observed energy at the IWISC and $M_2 + f$ interaction frequencies has been based on the following observational results:

- A peak in PSD has been observed at the frequency of $M_2 - f$ (the IWISC frequency) over a broad range of depths and in numerous geographic locations throughout the worlds oceans.
- The IWISC energy is predominantly in the cyclonic rotary component.
- IWISC energy poleward of the critical frequency is outside of the freely propagating internal wave band.
- Horizontal kinetic energy at the IWISC frequency is episodic and in general is not directly correlated with observed energy at the semi-diurnal frequency.
- There is a weak (R < .2) positive correlation between bulk observations of IWISC peak energy and inertial peak energy, with the strongest IWISC events usually associated with enhanced inertial energy.
- Bulk observations of IWISC cyclonic peak energy poleward of the critical frequency ($f = M_2/2$) show a positive correlation (though not strong, R < .5) with the corresponding anti-cyclonic $M_2 + f$ energy peak.
- All interactanct frequency bands (M2, f, M2-f, M2+f) were found to exhibit horizontal correlation scales less than 10 km in one experiment where spatially-distributed time series were available.
- IWISC peak energy for mid-latitude records exhibit a depth structure, with maximum peak energy above a mesoscale background occurring near 1500 meters depth.

- Analysis of HOME ADCP record revealed IWISC frequency peaks in power spectra of horizontal currents and their vertical shear.
- The vertical velocity from the well-instrumented HOME mooring A2 ADCP records was corrected for diel migrator contamination at the semi-diurnal frequency. Vertical velocity at this band was extracted. Validation was possible due to the existence of two long-range ADCP's on the mooring with overlapping fields of view.
- The vertical velocities were used in a Semi-Lagrange inversion of ADCP horizontal velocity.
- The Semi-Lagrange inversion revealed both depth ranges where interaction peak energy (at IWISC and M2+f) is diminished by the inversion thus implying that reversible advection dominated those signals, and depth ranges where the energy peaks remained unaffected. This leads to the conclusion that both periodic Doppler advection and other energy redistribution processes are present at this location.
- Bispectral and bicoherence analysis of Semi-Lagrange-corrected ADCP velocity suggests the presence of irreversible non-linear interaction at IWISC.

5.1.2 Analysis Tools

A number of tools and techniques were employed in the analysis of observed velocity fields. Some are novel applications of existing methods. Others are new tools used in specific applications.

- A hierarchy of vertical advection models has been created to establish if when and how vertical advection is a satisfactory explanation of IWSIC.
- The simplest model of a single sinusoid semi-diurnal internal tide displacement of an inertial internal wave replicates properties of the Eulerian observations such as a power spectral density (PSD) peak at the IWISC frequency; however, this model always yields an additional PSD peak at the sum ($M_2 + f$) frequency. Such a tight correlation between PSD at IWISC and $M_2 + f$ frequencies is not observed.
- Extending the displacement model to include multiple semi-diurnal vertical modes and frequency constituents results in temporal and spatial variability of IWISC not inconsistent with observed variability.

- Several analysis techniques were applied to the output of the model that employed multiple plane waves (simulating multiple vertical modes and frequency constituents) to vertically advect inertial currents, in order to provide insight into the utility of applying these techniques to real data.
- Bispectra and bicoherence analysis, used to identify non-linear interactions in many disciplines, **do not** distinguish between periodic Doppler shifting (reversible advection) and energy exchanging non-linearity.
- Semi-Lagrangian inversion is commonly used to remove reversible advection signals from Eulerian data. Applying such an inversion to the model output yielded the expected result, i.e., absence of any indication of the original advection, e.g.,
  - Semi-Lagrange inversion of modeled currents eliminated interaction frequency energy so that there were no longer IWISC or M2+f peaks in power spectra, bispectra or bicoherence.
- Wavelet rotary bispectral analysis was created here in an attempt to improve the identifications of interactions where one or more of the interactants is of short duration.

5.2 Hypothetical Non-linear Process Producing IWISC

Though conclusive observational evidence has not been obtained indicating the mechanism which produces a peak in energy at the IWISC frequency after the effects of vertical displacement have been removed, we have narrowed the possibilities, and can present an argument in favor of certain scenarios. At this time, we are looking at the interaction as a forced, nearly resonant direct non-linear interaction.

As a forced interaction, energy could be transferred rapidly, as is observed in time series where elevated inertial inertial energy corresponds in time with IWISC energy. The small vertical scale of IWISC energy would be match a forced interaction, as the vertical scale of the energy would be close to that of the inertial, which tends to be short.

The high intermittency of observed IWISC, and its lack of correspondence to either inertial or semi-diurnal horizontal currents could be accounted for with a direct, nearly resonant non-linearity. This can be explained as the dependence of the energy transfer on the vertical scale of the inertial wave packet and the magnitude of the displacement. As the observations are not highly accurate in these two quantities, isolating this dependence in the data will require future work.

The direct non-linearity would produce mixing directly for latitudes poleward of the critical frequency, leaving behind patches of fossil turbulence. Equator-ward of the critical frequency, there would

be included the radiation of free internal waves as well. To reiterate, this is a speculation based on observations and some simple theoretical constructions, and satisfactory development of this as a definitive explanation remains for future work. Even without this conclusive development, in the next section we examine what the possible impact of a non-linearity of this type would produce.

5.3 Hypothetical Energy Transfer

In this section, a hypothetical construction is discussed that illustrates the potential impact of IWISC on global transfer of energy out of the internal wave regime. For this construction a number of assumptions need to be made. Each is based on established theory and observational estimates. There are relationships without quantification that prevent this calculation from being more than a hypothetical estimate. This is additional motivation for the acquisition of appropriate new data that would more precisely determine vertical advection and non-linear energy exchange involving inertial waves and the semi-diurnal internal tide.

First we assume that the majority of inertial energy is input into the ocean as events associated with atmospheric forcing. For a given forcing event, there results a narrow-band group of free inertial internal waves propagating downward out of the mixed-layer. The waves in this group have slightly higher frequencies than the local inertial frequency (theyre slightly blue shifted) which permits the vertical propagation of each wave according to its characteristic as determined by the internal wave dispersion relation. This situation is illustrated in figure 5.1 with an inertial wave packet and its ray path in the Northern Hemisphere in a depth-latitude plane.

One of the results from analysis of the historical mooring records and more recent ADCP velocities is that advection alone cannot account for all the observed energy at the sum and difference interaction frequencies between inertial internal waves and the semi-diurnal internal tide. Estimating the energy lost to a particular process based on observed energy levels is speculative for the data that has been analyzed. For the rough calculation here, an estimate must be made of how much energy is transferred. A process that transfers three percent of the inertial energy has been selected. This is based on the IWISC peak in Figure 2.1 of the historical data analysis section. In that analysis, IWISC was 3.4% of the inertial energy.

A further assumption about the depth scale is also made. Two factors influence this, the maximum vertical displacement of the semi-diurnal internal tide, and the vertical extent of the inertial packet envelope. This scale is an idealized depth range over which a single Eulerian point measurement gathers information about the process. A value of 200 meters has been selected.

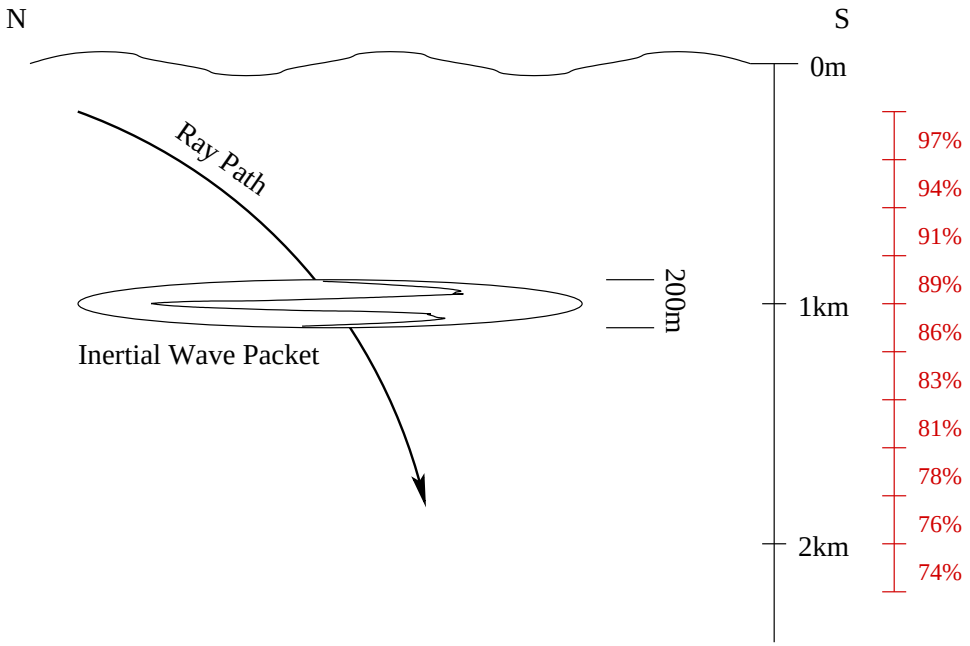

Figure 5.1. Visual representation of inertial energy lost at 200 meter intervals to a process with a three percent conversion rate. Within 1400 meters, one third of the inertial energy has been removed.

The postulation is now that as the inertial wave packet propagates downward a distance corresponding to its vertical extent it loses another 3% of its energy. For illustration purposes, an additional (unjustifiable) assumption has been made that the IWISC energy is predominantly derived from the inertial waves.

The percentage depth brackets in Figure 5.1 represent remaining total inertial energy after the conversion at that depth. The following logic motivates this representation; if there were a set relationship between inertial energy, semi-diurnal energy, and semi-diurnal vertical velocity that would allow for the estimation of remaining energy in the interaction frequencies (presumably representing the amount of energy actually transferred), a calculation of energy transfer percentage could be made. This would be applied to existing data and extrapolated in depth to estimate total energy transferred.

If such a method were available, it would be highly relevant to current research into oceanic energy budgets. The implication from this simple Figure is not inconsequential. Even with a relatively weak transfer process, by a depth of 1400 meters, 17% of the inertial energy has been transferred out of the internal wave regime. For sub-inertial IWISC in mid-latitude regions this is energy that has been removed to non-free wave structures, short-circuiting the expectation of energy transfer within the internal wave band to smaller scale waves.

There are a multitude of caveats and unknowns inherent in this postulation. Clearly, a process which depends upon semi-diurnal tide vertical velocity will not be continuous over a significant depth range due to minima and maxima in the vertical velocity profile. Another unknown is how the non-linear energy transfer rate depends on the amplitude of input energy. Other considerations need to be established before an estimate could be made with confidence. Given the significant potential impact on global internal wave energy, further investigation into the processes which generate IWISC is warranted.

IWISC is a significant phenomena both as a correction in identifying advected energy and as a potential pathway for the direct energy transfer out of the internal wave band both inertial and semi-diurnal energy. The work here has established evidence of these processes, and points to future work in determining the scope of energy redistribution.

Bibliography

[1] *Oregon state university buoy group's deep water archive - kepler.oce.orst.edu.*

[2] M. H. Alford, *Fine-structure contamination: Observations and a model of a simple two-wave case*, JOURNAL OF PHYSICAL OCEANOGRAPHY **31** (2001), no. 9, 2645–2649.

[3] ———, *Redistribution of energy available for ocean mixing by long-range propagation of internal waves*, NATURE **423** (2003), no. 6936, 159–162.

[4] M. H. Alford, J. A. MacKinnon, Z. X. Zhao, R. Pinkel, J. M. Klymak, and T. Peacock, *Internal waves across the pacific*, GEOPHYSICAL RESEARCH LETTERS **34** (2007), no. 24, L24601.

[5] A. M. Althaus, E. Kunze, and T. B. Sanford, *Internal tide radiation from mendocino escarpment*, J. Phys. Oceanogr. **33** (2003), no. 7, 1510–1527.

[6] T. J. Boyd, M. D. Levine, S. R. Gard, and W. Waldorf, *Mooring observations from the hawaiian ridge*, Tech. Report 197, Oregon State University, January 2005.

[7] G. S. Carter and M. C. Gregg, *Persistent near-diurnal internal waves observed above a site of m-2 barotropic-to-baroclinic conversion*, Journal Of Physical Oceanography **36** (2006), no. 6, 1136–1147.

[8] G. S. Carter, M. A. Merrifield, J. M. Becker, K. Katsumata, M. C. Gregg, D. S. Luther, M. D. Levine, T. J. Boyd, and Y. L. Firing, *Energetics of m-2 barotropic-to-baroclinic tidal conversion at the hawaiian islands*, JOURNAL OF PHYSICAL OCEANOGRAPHY **38** (2008), no. 10, 2205–2223.

[9] C. Chavanne, P. Flament, P. Klein, and K. W. Gurgel, *High-resolution observations of the interaction between a submesoscale anticyclone and a front*, JOURNAL OF PHYSICAL OCEANOGRAPHY (2008 - submitted).

[10] A. D. Chave, D. S. Luther, and J. H. Filloux, *Variability of the wind stress curl over the north pacific: Implications for the oceanic response*, J. Geophys. Res. **96** (1991), no. c10, 18,361–18,379.

[11] T. K. Chereskin, M. Y. Morris, P. P. Niiler, P. M. Kosro, R. L. Smith, S. R. Ramp, C. A. Collins, and D. L. Musgrave, *Spatial and temporal characteristics of the mesoscale circulation of the california current from eddy-resolving moored and shipboard measurements*, JOURNAL OF GEOPHYSICAL RESEARCH-OCEANS **105** (2000), no. C1, 1245–1269.

[12] S. M. Chiswell, *Vertical structure of the baroclinic tides in the central north pacific subtropical gyre*, J. Phys. Oceanogr. **24** (1994), no. 9, 2032–2039.

[13] WOCE Data Products Committee, *Woce global data, version 3.0*, Tech. Report 180/02, WOCE International Project Office, Southampton, UK, 2002.

[14] E. A. D'Asaro and M. D. Morehead, *Internal waves and velocity fine structure in the arctic ocean*, J. Geophys. Res. **96** (1991), no. c7, 12,725–12,738.

[15] A. M. Davies and J. X. Xing, *The effect of a bottom shelf front upon the generation and propagation of near-inertial internal waves in the coastal ocean*, JOURNAL OF PHYSICAL OCEANOGRAPHY **35** (2005), no. 6, 976–990.

[16] Y. Desaubies and M. C. Gregg, *Reversible and irreversible finestructure*, J. Phys. Oceanogr. **11** (1981), no. 4, 541–556.

[17] L. M. Dewitt, M. D. Levine, C. A. Paulson, and W. V. Burt, *Semidiurnal internal tide in jasin: Observations and simulation*, J. Geophys. Res. **91** (1986), no. c2, 2581–2592.

[18] R. R. Dickson, *Global summaries and intercomparisons: flow statistics from long-term current meter moorings*, Eddies in Marine Science, ch. 15, Springer-Verlag, 1983.

[19] B. D. Dushaw, B. D. Cornuelle, P. F. Worcester, B. M. Howe, and D. S. Luther, *Barotropic and baroclinic tides in the central north pacific-ocean determined from long-range reciprocal acoustic transmissions*, JOURNAL OF PHYSICAL OCEANOGRAPHY **25** (1995), no. 4, 631–647.

[20] G. D. Egbert and S. Y. Erofeeva, *Efficient inverse modeling of barotropic ocean tides*, Journal of Atmospheric and Oceanic Technology **19** (2002), no. 2, 183–204.

[21] G. D. Egbert and R. D. Ray, *Significant dissipation of tidal energy in the deep ocean inferred from satellite altimeter data*, NATURE **405** (2000), no. 6788, 775–8.

[22] S. Elgar and R. T. Guza, *Observations of bispectra of shoaling surface gravity-waves*, JOURNAL OF FLUID MECHANICS **161** (1985), 425–448.

[23] M. Feng, M. A. Merrifield, R. Pinkel, P. Hacker, A. J. Plueddemann, E. Firing, R. Lukas, and C. C. Eriksen, *Semidiurnal tides observed in the western equatorial pacific during the tropical ocean-global atmosphere coupled ocean-atmosphere response experiment*, J. Geophys. Res. **103** (1998), no. C5, 10253–10272.

[24] E. P. Flinchem and D. A. Jay, *An introduction to wavelet transform tidal analysis methods*, Estuarine, Coastal and Shelf Science **51** (2000), 177–200.

[25] L. L. Fu, *Observations and models of inertial waves in the deep ocean*, Rev. Geoph. Space Phys. **19** (1981), 141–170.

[26] N. Furuichi, T. Hibiya, and Y. Niwa, *Bispectral analysis of energy transfer within the two-dimensional oceanic internal wave field*, J. Phys. Oceanogr. **35** (2005), no. 11, 2104–2109.

[27] C. Garrett, *What is the "near-inertial" band and why is it different from the rest of the internal wave spectrum?*, JOURNAL OF PHYSICAL OCEANOGRAPHY **31** (2001), no. 4, 962–971.

[28] C. Garrett and W. Munk, *Internal waves in the ocean*, ANNUAL REVIEW OF FLUID MECHANICS **11** (1979), 339–369.

[29] C. Garrett and L. St Laurent, *Aspects of deep ocean mixing*, JOURNAL OF OCEANOGRAPHY **58** (2002), no. 1, 11–24.

[30] K. Gurley, T. Kijewski, and A. Kareem, *First- and higher-order correlation detection using wavelet transforms*, ASCE Journal of Engineering Mechanics **129** (2003), no. 2, 188–201.

[31] K. Hasselmann, *Feynman diagrams and interaction rules of wave-wave scattering processes*, REVIEWS OF GEOPHYSICS **4** (1966), no. 1, 1–32.

[32] K. Hasselmann, W. Munk, and G. MacDonald, *Bispectra of ocean waves*, Proceedings of the Symposium on Time Series Analysis (M. Rosenblatt, ed.), Wiley, 1963, pp. 125–139.

[33] D. Hebert and J. N. Moum, *Decay of a near-inertial wave*, J. Phys. Oceanogr. **24** (1994), no. 11, 2334–2351.

[34] R. M. Hendry, *Observations of the semidiurnal internal tide in the western north atlantic ocean*, Phil. Trans. R. Soc. London A **286** (1977), no. 1330, 1–24.

[35] T. Hibiya, Y. Niwa, and K. Fujiwara, *Numerical experiments of nonlinear energy transfer within the oceanic internal wave spectrum*, J. Geophys. Res. **103** (1998), no. C9, 18715–18722.

[36] C. O. Hines, L. I. Childress, J. B. Kinney, and M. P. Sulzer, *Modeling of gravity-wave tail spectra in the middle atmosphere via numerical and doppler-spread methods*, JOURNAL OF ATMOSPHERIC AND SOLAR-TERRESTRIAL PHYSICS **66** (2004), no. 11, 933–948.

[37] J. H. Hu and P. P. Niiler, *Nepac current meter and xbt data for the circulation in the northeast pacific thermocline: 42°n and 28°n, 152°w; july 1982 - october 1985*, Tech. Report 87-4, SIO, 1987.

[38] D. A. Jay and Tobias Kukulka, *Revising the paradigm of tidal analysis – the uses of non-stationary data*, Ocean Dynamics **53** (2003), no. 3, 110–125.

[39] E. Kunze, M. G. Briscoe, and A. J. Williams III, *Interpreting shear and strain fine structure from a neutrally buoyant float*, J. Geophys. Res. **95** (1990), no. c10, 18,111–18,125.

[40] J. W. Lavelle, E. T. Baker, and G. A. Cannon, *Ocean currents at axial volcano, a northeastern pacific seamount*, JOURNAL OF GEOPHYSICAL RESEARCH-OCEANS **108** (2003), no. C2, 3020.

[41] P. LeBlond and L. Mysak, *Waves in the ocean*, Elsevier, 1978.

[42] M. D. Levine, *A modification of the garrett–munk internal wave spectrum*, J. Phys. Oceanogr. **32** (2002), no. 11, 3166–3181.

[43] M. D. Levine and J. G. Richman, *Extracting the internal tide from data: Methods and observations from the mixed layer dynamics experiment*, **95** (1989), no. c2, 8125–8134.

[44] R. C. Lien, E. A. D'Asaro, and M. J. McPhaden, *Internal waves and turbulence in the upper central equatorial pacific: Lagrangian and eulerian observations*, J. Phys. Oceanogr. **32** (2002), 2619–2639.

[45] Paul C. Liu and Gerald S. Miller, *Wavelet transforms and ocean current data analysis*, Journal of Atmospheric and Oceanic Technology **13** (1996), no. 5, 1090–1099.

[46] D. S. Luther, J. H. Filloux, and A. D. Chave, *Low-frequency, motionally induced electromagnetic fields in the ocean 2. electric field and eulerian current comparison*, J. Geophys. Res. **96** (1991), no. C7, 12797–12814.

[47] J. A. MacKinnon and K. B. Winters, *Subtropical catastrophe: Significant loss of low-mode tidal energy at 28.9*, GEOPHYSICAL RESEARCH LETTERS **32** (2005).

[48] C. H. McComas and F. P. Bretherton, *Resonant interaction of oceanic internal waves*, J. Geophys. Res. **82** (1977), no. 9, 1397–1412.

[49] C. H. McComas and M. G. Briscoe, *Bispectra of internal waves*, JOURNAL OF FLUID MECHANICS **97** (1980), no. 1, 205–213.

[50] M. A. Merrifield, P. E. Holloway, and T. M. S. Johnston, *The generation of internal tides at the hawaiian ridge*, GEOPHYSICAL RESEARCH LETTERS **28** (2001), no. 4, 559–562.

[51] S. F. Mihaly, R. E. Thomson, and A. B. Rabinovich, *Evidence for nonlinear interaction between internal waves of inertial and semidiurnal frequency*, GEOPHYSICAL RESEARCH LETTERS **25** (1998), no. 8, 1205–1208.

[52] Andrew N. Moore and Douglas L. Stewart, *The effects of mobile scatterers on the quality of adcp data in differing marine environments*, Proceedings of the IEEE/OES Seventh Working Conference on Current Measurement Technology, 2003.

[53] E. G. Morozov, *Semidiurnal internal wave global field*, Deep Sea Res. **42** (1995), no. 1, 135–148.

[54] P. Müller and M. G. Briscoe, *Diapycnal mixing and internal waves*, Dynamics of oceanic internal gravity waves, II. Proceedings ‘Aha Huliko‘a Hawaiian Winter Workshop, 1999, pp. 289–294.

[55] P. Müller, G. Holloway, F. Henyey, and N. Pomphrey, *Nonlinear-interactions among internal gravity-waves*, REVIEWS OF GEOPHYSICS **24** (1986), no. 3, 493–536.

[56] P. Müller and G. Siedler, *Consistency relations for internal waves*, Deep Sea Res. **23** (1976), 613–628.

[57] W. Munk, *Once again: once againtidal friction*, Progress in Oceanography **40** (1997), no. 1-4, 7–35.

[58] W. Munk and C. Wunsch, *Abyssal recipes ii: energetics of tidal and wind mixing*, Deep Sea Res. **45** (1998), no. 12, 1977–2010.

[59] S. Neshyba and E. J. C. Sobey, *Vertical cross coherence and cross bispectra between internal waves measured in a multiple-layered ocean*, J. Geophys. Res. **80** (1975), no. 9, 1152–1162.

[60] Y. Niwa and T. Hibiya, *Numerical study of the spatial distribution of the m2 internal tide in the pacific ocean*, Journal of Geophysical Research **106** (2001), no. c10, 22,441–22,449.

[61] D. J. Olbers, *Nonlinear energy transfer and the energy balance of the internal wave field in the deep ocean*, JOURNAL OF FLUID MECHANICS **74** (1976), no. 2, 375–399.

[62] _____, *Models of the oceanic internal wave field*, Rev. Geoph. Space Phys. **21** (1983), no. 7, 1567–1606.

[63] D. J. Olbers and N. Pomphrey, *Disqualifying two candidates for the energy balance of oceanic internal waves*, J. Phys. Oceanogr. **11** (1981), 1423–1425.

[64] Michael W. Ott, *The accuracy of acoustic vertical velocity measurements: instrument biases and the effect of zooplankton migration*, Continental Shelf Research **25** (2005), 243–257.

[65] O. M. Phillips, *On the dynamics of unsteady gravity waves of finite amplitude, 1, the elementary interactions.*, JOURNAL OF FLUID MECHANICS **9** (1960), no. 2, 193–217.

[66] R. Pinkel, *Doppler sonar observations of internal waves; the wavenumber-frequency spectrum*, JOURNAL OF PHYSICAL OCEANOGRAPHY **14** (1984), no. 8, 1249–1270.

[67] _____, *Advection, phase distortion, and the frequency spectrum of finescale fields in the sea*, J. Phys. Oceanogr. **38** (2008), no. 2, 291–313.

[68] R. Pinkel and S. Anderson, *Shear, strain, and richardson number variations in the thermocline .1. statistical description*, JOURNAL OF PHYSICAL OCEANOGRAPHY **27** (1997), no. 2, 264–281.

[69] R. T. Pollard and J. F. Read, *Rrs discovery cruise 201, 23 mar-03 may 1993. south west indian ocean experiment (swindex)*, Tech. Report 240, Institute of Oceanographic Sciences Deacon Laboratory Cruise Report, 1994.

[70] H. Qi, R. A. De Szoeke, C. A. Paulson, and C. C. Eriksen, *The structure of near-inertial waves during ocean storms*, J. Phys. Oceanogr. **25** (1995), no. 11, 2853–2871.

[71] L. Rainville and R. Pinkel, *Propagation of low-mode internal waves through the ocean*, JOURNAL OF PHYSICAL OCEANOGRAPHY **36** (2006), no. 6, 1220–1236.

[72] R. D. Ray and D. E. Cartwright, *Estimates of internal tide energy fluxes from topex/poseidon altimetry: Central north pacific*, GEOPHYSICAL RESEARCH LETTERS **28** (2001), no. 7, 1259–1262.

[73] R. D. Ray and G. T. Mitchum, *Surface manifestation of internal tides generated near hawaii*, GEOPHYSICAL RESEARCH LETTERS **23** (1996), 2101–2104.

[74] _____, *Surface manifestation of internal tides in the deep ocean: observations from altimetry and island gauges*, Progress in Oceanography **40** (1997), no. 1-4, 135–162.

[75] Tom P. Rippeth and John H. Simpson, *Diurnal signals in vertical motions on the hebridean shelf*, Limnology and Oceanography **43** (1998), 1690–1696.

[76] D. L. Rudnick, *Direct velocity measurements in the samoan passage*, J. Geophys. Res. **102** (1997), no. C2, 3293–3302.

[77] D. L. Rudnick, T. J. Boyd, R. E. Brainard, G. S. Carter, G. D. Egbert, M. C. Gregg, P. E. Holloway, J. M. Klymak, E. Kunze, C. M. Lee, M. D. Levine, D. S. Luther, J. P. Martin, M. A. Merrifield, J. N. Moum, J. D. Nash, R. Pinkel, L. Rainville, and T. B. Sanford, *From tides to mixing along the hawaiian ridge*, Science **301** (2003), no. 5631, 355–357.

[78] F. Schott, *On the energetics of baroclinic tides in the north atlantic*, Ann. Geophys. **33** (1977), 41–62.

[79] J. Sherman and R. Pinkel, *Estimates of the vertical wavenumber–frequency spectra of vertical shear and strain*, J. Phys. Oceanogr. **21** (1991), no. 2, 292–303.

[80] H. L. Simmons, R. W. Hallberg, and B. K. Arbic, *Internal wave generation in a global baroclinic tide model*, Deep-Sea Research II **51** (2004), no. 25-26, 3043–3068.

[81] B. Sjoberg and A. Stigebrandt, *Computations of the geographical distribution of the energy ux to mixing processes via internal tides and the associated vertical circulation in the ocean*, Deep Sea Res. **39** (1992), 269–291.

[82] L. St Laurent and C. Garrett, *The role of internal tides in mixing the deep ocean*, J. Phys. Oceanogr. **32** (2002), no. 10, 2882–2899.

[83] H. M. van Aken, L. R. M. Maas, and H. van Haren, *Observations of inertial wave events near the continental slope off goban spur*, JOURNAL OF PHYSICAL OCEANOGRAPHY **35** (2005), no. 8, 1329–1340.

[84] H. van Haren, *On the polarization of oscillatory currents in the bay of biscay*, JOURNAL OF GEOPHYSICAL RESEARCH-OCEANS **108** (2003), no. C9, 3290.

[85] _____, *Bandwidth similarity at inertial and tidal frequencies in kinetic energy spectra from the bay of biscay*, DEEP-SEA RESEARCH PART I-OCEANOGRAPHIC RESEARCH PAPERS **51** (2004), no. 5, 637–652.

[86] _____, *Some observations of nonlinearly modified internal wave spectra*, JOURNAL OF GEOPHYSICAL RESEARCH-OCEANS **109** (2004), no. C3, C03045.

[87] _____, *A comparison between vertical motions measured by adcp and inferred from temperature data*, Ocean Science **4** (2008), 215–222.

[88] H. van Haren, L. R. M. Maas, and H. M. van Aken, *On the nature of internal wave spectra near a continental slope*, GEOPHYSICAL RESEARCH LETTERS **29** (2002), no. 12, 1615.

[89] B. Ph. van Milligen, E. Sanchez, T. Estrada, C. Hidalgo, B. Branas, B. Carreras, and L. Garcia, *Wavelet bicoherence: A new turbulence analysis tool*, Phys. Plasmas **2** (1995), no. 8, 3017–3032.

[90] M. L. Waite and P. Bartello, *Stratified turbulence generated by internal gravity waves*, JOURNAL OF FLUID MECHANICS **546** (2006), 313–339.

[91] C. Wunsch, *Internal tides in the ocean*, REVIEWS OF GEOPHYSICS **13** (1975), no. 1, 167–182.

[92] J. X. Xing and A. M. Davies, *Processes influencing the non-linear interaction between inertial oscillations, near inertial internal waves and internal tides*, GEOPHYSICAL RESEARCH LETTERS **29** (2002), no. 5, 1067.

[93] _____, *Nonlinear interaction between wind-forced currents and near-inertial oscillations and internal waves in nearshore frontal regions*, JOURNAL OF GEOPHYSICAL RESEARCH-OCEANS **110** (2005), no. C5, C05003.

[94] Neng-Chun Yao, S. Neshyba, and H. Crew, *Rotary cross-bispectra and energy transfer functions between non-gaussian vector processes i. development and example*, J. Phys. Oceanogr. **5** (1975), no. 1, 164–172.

[95] _____, *Rotary cross-bispectra and energy transfer functions between non-gaussian vector processes. ii. winds and currents off the oregon coast*, J. Phys. Oceanogr. **7** (1977), no. 6, 892–903.

[96] W. R. Young, Y. K. Tsang, and N. J. Balmforth, *Near-inertial parametric subharmonic instability*, JOURNAL OF FLUID MECHANICS **607** (2008), 25–49.

[97] W. Zenk, G. Siedler, B. Lenz, and N. G. Hogg, *Antarctic bottom water flow through the hunter channel*, JOURNAL OF PHYSICAL OCEANOGRAPHY **29** (1999), no. 11, 2785–2801.

[98] F. Zhang, S. E. Koch, C. A. Davis, and M. L. Kaplan, *Wavelet analysis and the governing dynamics of a large-amplitude mesoscale gravity-wave event along the east coast of the united states*, Quarterly Journal of the Royal Meteorological Society **127** (2001), no. 577, 2209–2245.

[99] N.V. Zilberman, M. A. Merrifield, G. S. Carter, D. S. Luther, M. D. Levine, and T. J. Boyd, *Time-variable conversion of barotropic to baroclinic m2 tidal energy at the kaena ridge, hawaii*, Eos Trans AGU (2009 - submitted), presented at AGU Ocean Sciences Meeting, March, 2008, Orlando, Fla.